รายงานวิจัยฉบับสมบูรณ์

โครงการ การควบคุมแบบอันตรกิริยา ของระบบหุ่นยนต์ที่ข้อต่อมีความยืดหยุ่น

โดย ผศ.ดร.พงศ์แสน พิทักษ์วัชระ

มีนาคม 2558

สัญญาเลขที่ MRG5580227

รายงานวิจัยฉบับสมบูรณ์

โครงการ การควบคุมแบบอันตรกิริยา ของระบบหุ่นยนต์ที่ข้อต่อมีความยืดหยุ่น

ผศ.ดร.พงศ์แสน พิทักษ์วัชระ จุฬาลงกรณ์มหาวิทยาลัย

สนับสนุนโดยสำนักงานคณะกรรมการการอุดมศึกษา สำนักงานกองทุนสนันสนุนการวิจัย

และ จุฬาลงกรณ์มหาวิทยาลัย

Abstract

Project Code: MRG5580227

Project Title: Interaction Control of Flexible-Joint Robot System

Investigator: Phongsaen Pitakwatchara, Chulalongkorn University

Email Address: phongsaen.p@chula.ac.th

Project Period: 24 months

One challenge of current robotic systems is the ability to work within the unstructured environment. To fulfill this requirement, intrinsically the robot must be controlled to perform tasks with the appropriate impedance behavior. This work concerns with the task space impedance control of a nonlinear flexible joint robot system. The proposed controller uses limited information of the angle and the current of the motors to regulate the end point compliance at the specified set point. In particular, the controller infers the transmitted torque to the robot from the cascaded flexible joint model and the motor current. This torque is then fed back to mitigate the effect of the motor inertia from deteriorating the desired impedance. Motor angles are employed to estimate the stationary robot link angles in real time. They are then used to constitute the gravity force, aiming at cancelling the robot gravity force, and the force developed according to the robot desired impedance characteristics. Asymptotic stability of this controller with the nonlinear flexible joint robot is guaranteed with additional damping. Simulation and experiments of the proposed control scheme on a two degrees-of-freedom cable-pulley driven flexible joint robot model are examined.

Keywords: flexible joint robot; task space impedance control; transmitted torque estimation; link angle estimation

บทคัดย่อ

รหัสโครงการ : MRG5580227

ชื่อโครงการ : การควบคุมแบบอันตรกิริยาของระบบหุ่นยนต์ที่ข้อต่อมีความยืดหยุ่น

ชื่อนักวิจัย : พงศ์แสน พิทักษ์วัชระ สังกัด จุฬาลงกรณ์มหาวิทยาลัย

อีเมล : phongsaen.p@chula.ac.th

ระยะเวลาโครงการ : 24 เดือน

ความท้าทายประการหนึ่งสำหรับระบบหุ่นยนต์ในปัจจุบันได้แก่การที่หุ่นยนต์สามารถในการทำงานในสภาพแวดล้อมที่มิได้มีการตระเตรียมไว้ล่วงหน้า เพื่อให้การทำงานลุล่วงไปได้ด้วยดี ค่าอิมพีแดนซ์ของหุ่นยนต์จะต้องได้รับการควบคุมอย่างเหมาะสม โครงการวิจัยนี้จึงได้ทำการศึกษาการควบคุมอิมพีแดนซ์ในปริภูมิการทำงานของระบบหุ่นยนต์ที่ข้อต่อมีความยืดหยุ่นแบบไม่เชิงเส้น ตัวควบคุมที่นำเสนอใช้ข้อมูลป้อนกลับที่จำกัดได้แก่ มุมและกระแสของมอเตอร์ขับในการควบคุมค่าอิมพีแดนซ์ ณ จุดทำงาน ทอร์กที่ส่งให้กับหุ่นยนต์สามารถคำนวณได้จากกระแสของมอเตอร์และแบบจำลองของหุ่นยนต์ที่คำนึงถึงความยืดหยุ่น ค่าที่คำนวณได้จะนำมาใช้ในการลดความเฉื่อยของมอเตอร์ขับที่รบกวนการควบคุมอิมพีแดนซ์ให้ได้ค่าที่เหมาะสม ส่วนมุมของมอเตอร์นั้นจะถูกใช้เพื่อประมาณค่าของมุมและความเร็วของข้อต่อหุ่นยนต์ ซึ่งจะนำไปใช้ในการชดเชยค่าแรงโน้มถ่วงและปรับค่าอิมพีแดนซ์ของหุ่นยนต์ให้เป็นไปดังต้องการ ความหน่วงเพิ่มเติมในระบบช่วยกำกับเสถียรภาพแบบเชิงเส้นกำกับของระบบควบคุม ตัวควบคุมที่พัฒนาขึ้นได้รับการยืนยันด้วยการจำลองและการทดลองการทำงานจริงของตัวควบคุมกับหุ่นยนต์ที่มีจำนวนองศาเสรีเท่ากับสอง ซึ่งข้อต่อมีความยืดหยุ่นและขับเคลื่อนผ่านระบบส่งกำลังด้วยรอกและเคเบิล

คำหลัก ระบบหุ่นยนต์ที่ข้อต่อมีความยืดหยุ่น การควบคุมอิมพีแดนซ์ในปริภูมิการทำงาน การประมาณค่าทอร์กที่ส่งผ่าน การประมาณค่ามุมของข้อต่อหุ่นยนต์

Executive Summary

This work develops a task space impedance control of the manipulator driven through the multi-stage flexible transmission unit. The controller regulates the stiffness and damping of the end effector at the specified position based on the available feedback signal of the motor angle and current. Motor angle is used to compute the estimation of the robot link angle and joint velocity based on the stationary elastic model. These values are employed in the traditional impedance control law. Optionally, the motor current might be used to determine the transmitted torque, which helps reducing the motor inertia. It can be shown that the controller effectively shapes the system potential energy to the one of the desired task space compliance.

A two degrees-of-freedom cable-pulley driven flexible joint robot as the embodiment of the manipulator driven through the multiple stages flexible transmission unit is regulated with the proposed controller. Detailed model of the robot is derived for the purpose of system simulation. From the experiments, the controlled system yields satisfactory results of displaying the desired impedance during general task execution. Therefore this practical controller will be helpful in accomplishing real-world manipulation of the flexible robot system.

1. Introduction

Current robotic systems are extending their capability to work in more unstructured and complex environment. For example, a laparoscopic surgical robotic system such as [1] typically works inside human abdomen which is packed with vital organs where their precise location and geometry are not known. Motion of the forceps is controlled and supervised by the skillful surgeon. Nevertheless, erroneous motion is possible for which the surrounding organs may be injured. Had the forceps be equipped with proper compliance, severity of the wound can be mitigated. As another example, a service robot system such as [2] among the others is able to perform general daily tasks e.g. serving a bottle of beer or frying a pancake. Again, the robot has limited and imprecise information about the environment it is interacting with. To successfully implement such tasks, the robot must possess appropriate compliance characteristics.

In the past, many efforts have been carried out in shaping the robot compliance to the desired values. General impedance control scheme was proposed by [3] and is widely applied. Commonly, the control laws are devised to achieve the desired impedance behavior especially for the rigid robots [4]. Later, the controllers have been modified to cope with flexible robots where their elastic behavior is typically viewed as undesirable dynamics that complicates the control problem.

Only few works attempted on controlling the impedance of the flexible joint robots compared to the regulation and tracking control. According to the simplified model of the flexible joint robot [5], compliance control with online gravity compensation based on the measurable motor angles and their derivatives, and the desired robot link angles is applied to a cable-actuated robot [6]. The proposed control law resembles the PD regulation control with constant gravity compensation [7]. Improvement of the response may be achieved by feeding back additional (non-collocated) signals, e.g. link angles or joint torques. Applying the singular perturbation analysis to the flexible robot model, the simplified tracking impedance controller using the measured joint torques and their derivatives, the robot link angles and their derivatives, and the desired end effector trajectory is implemented on the DLR-II arm [8]. Passivity approach has also been used in designing the highly robust and stable impedance controller with the feedback signals of the joint torques and thier derivatives as well as the motor angles and their derivatives for the desired robot end effector posture [9]. Sophisticated adaptive impedance controller based on the function approximation technique (FAT) where the motor dynamics is also taken into account is proposed [10]. Note that this controller requires the measurement of the robot link angles and their derivatives, the joint torques, the motor currents, and the external force, which is presumed to act precisely at the robot end effector.

However, novel manipulators treat their inherent flexibility as a boon, particularly to the tasks involving uncertainties and shock loads as frequently encountered in general service operation, for which interaction to the environment are inevitable. Physical spring is intentionally introduced [11] as the interface between the actuator and the equipped joint of the legged robot, for the main purpose

of temporarily storing and restoring the impact energy from walking and running. An important consequence is the lower effective impedance. [12] proposed the micro-macro actuation scheme for driving the robot. Basically, each joint is driven by two parallel motors. A small motor is installed at the joint as usual, but the large one is cleverly relocated to the base for which its actuation is transmitted to the joint via the elastic coupling and the cable drivetrain. With this actuation approach, the safety and the performance of the robot may be attained simultaneously. In recent work, physically controllable compliance elements such as the varible stiffness actuator [13], where a redundant actutator is employed to adjust the effective stiffness of the actuator through some mechanisms, are designed and applied to the robots. The DLR hand-arm manipulator [14] uses these advanced actuators and the embedded joint torque sensors, making it capable of adjusting the stiffness in a passive manner and reacting to the collision force safely.

This paper develops the task space impedance control of a nonlinear flexible joint robot system whereby only the motor angle and current measurement are available. In section 2, model of the nonlinear flexible joint robot, including the transmission and motor dynamics is derived. Based on this model and limited amount of feedback information, task space impedance control is developed in section 3 to accomplish the desired viscoelastic behavior at the specified set point. A prototypical two degrees-of-freedom (DOF) cable-pulley driven flexible joint robot with the proposed control law is simulated in section 4. The results are discussed. Section 5 concludes the study.

2. Modeling of the Nonlinear Flexible-Joint Robot

In the following, a simplified model of the nonlinear flexible joint robot system, in which the transmission and motor dynamics are included, is derived. First of all, the following assumptions are made.

Assumption 2.1 Rotors of the motors and of the transmitting elements, e.g. gears or pulleys, are geometrically symmetric about their rotating axes. This assumption makes the inertia matrix of the rotor represented in its body-fixed frame having the z-axis coincident with the rotor axis be a diagonal matrix of the form $I = \mathrm{diag}(a, a, b)$.

Assumption 2.2 Relative rotational motion of the rotor with respect to its stator dominates its rotational kinetic energy. This implies the rotational kinetic energy of the rotor may be determined simply by $T = \frac{1}{2} I_{rr} \omega^2$, where ω is the relative angular velocity of the rotor with respect to the stator and I_{rr} is the rotor inertia about its rotational axis r-r.

Assumption 2.3 Elasticity in the system is distributed in the transmission subsystem and concentrated at the joints connecting the actuator/transmission subsystem to the rigid link robot.

Assumption 2.4 The reducer in the transmission yields a constant, non-modulated, transmission ratio matrix. This assumption, which holds for majority of the robot drivetrains, simplifies the

drivetrain model development.

2.1. Rigid Robot Model

Assumption 2.3 implies the structural isolation between the robot and the actuator/transmission subsystems by the joint stiffness. Therefore, system modeling can be completed through (almost) separate analysis of these subsystems. Lagrangian formulation is the common method used in deriving the equations of motion of the robot because it yields directly the model in a compact matrix-vector form suitable for the controller design. The resulting joint space model is well studied, e.g. in [15], and hence will just be mentioned here;

$$\boldsymbol{M}(\boldsymbol{q})\,\ddot{\boldsymbol{q}} + \boldsymbol{C}(\boldsymbol{q},\dot{\boldsymbol{q}})\,\dot{\boldsymbol{q}} + \boldsymbol{g}(\boldsymbol{q}) = \boldsymbol{\tau}_{dr} + \boldsymbol{\tau}_{ext}. \tag{1}$$

With assumption 2.2, the translational and rotational kinetic energy of the rotor are decoupled. In other words, the former depends on the robot link angle $\boldsymbol{q}$ and link velocity $\dot{\boldsymbol{q}}$ while the latter depends solely on the rotor velocity $\dot{\boldsymbol{\theta}}$. Hence, for convenience, the translational kinetic energy of the rotors may be incorporated into the rigid robot dynamics Eq. 1.

As a consequence the joint inertia matrix $\boldsymbol{M}(\boldsymbol{q})$ is determined by

$$\begin{aligned}\boldsymbol{M}(\boldsymbol{q}) &= \boldsymbol{M}_l(\boldsymbol{q}) + \boldsymbol{M}_{vr}(\boldsymbol{q}) \\ &= \sum_{i=1}^{n} \boldsymbol{J}_{l,i}^{b}(\boldsymbol{q})^T \mathcal{M}_{l,i} \boldsymbol{J}_{l,i}^{b}(\boldsymbol{q}) + \sum_{j=1}^{m} m_{r,j} \boldsymbol{J}_{vr,j}^{b}(\boldsymbol{q})^T \boldsymbol{J}_{vr,j}^{b}(\boldsymbol{q}).\end{aligned} \tag{2}$$

For the n-link robot, $\mathcal{M}_{l,i}$ is the i^{th}-link inertia matrix

$$\mathcal{M}_{l,i} = \begin{bmatrix} m_{l,i}\boldsymbol{I}_3 & \boldsymbol{0} \\ \boldsymbol{0} & \mathcal{I}_{l,i}^{b} \end{bmatrix} \tag{3}$$

of which its mass is $m_{l,i}$ and its constant inertia matrix about the body-fixed frame located at the center of gravity is $\mathcal{I}_{l,i}^{b}$. $\boldsymbol{J}_{l,i}^{b}(\boldsymbol{q})$ is the corresponding link Jacobian matrix expressed in its own frame. For the m-rotors (of the motors or of the drivetrain elements), $m_{r,j}$ is the mass of the j^{th}-rotor and $\boldsymbol{J}_{vr,j}^{b}(\boldsymbol{q})$ is the translational portion of the rotor Jacobian matrix represented in its body-fixed frame having the z-axis coincident with the rotor axis. In general, m might not be equal to n. Additionally, the number of DOF of the robot N may be different from the number of robot linkages n.

$\boldsymbol{C}(\boldsymbol{q},\dot{\boldsymbol{q}})$ is known as the Coriolis/centrifugal matrix where its elements may be calculated directly from $\boldsymbol{M}(\boldsymbol{q})$ according to the following relationship;

$$c_{ij} = \sum_{k=1}^{N} \left(\frac{1}{2}\frac{\partial m_{ij}}{\partial q_k} + \frac{1}{2}\frac{\partial m_{ik}}{\partial q_j} - \frac{1}{2}\frac{\partial m_{jk}}{\partial q_i} \right) \dot{q}_k, \tag{4}$$

in which m_{ij} is the $(i,\,j)$-element of $\boldsymbol{M}(\boldsymbol{q})$. The gravity torque vector $\boldsymbol{g}(\boldsymbol{q})$ is governed by the gravitational potential energy $V_g(\boldsymbol{q})$;

$$\boldsymbol{g}(\boldsymbol{q}) = \left(\frac{\partial V_g(\boldsymbol{q})}{\partial \boldsymbol{q}} \right)^T. \tag{5}$$

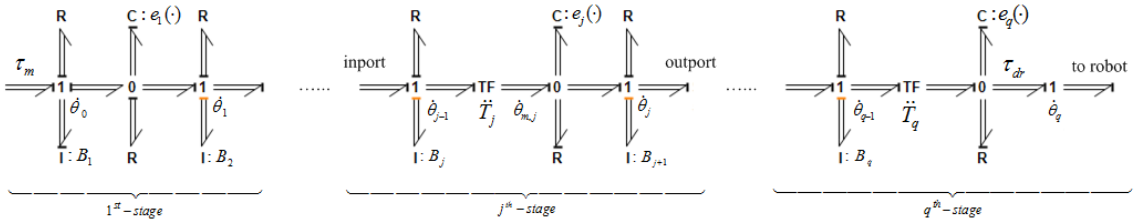

Figure 1: Multi-dimensional bond graph diagram of the transmission system displaying the interconnection between the lumped elements and the neighboring stages. Causality assignments conform to the cable-pulley elastic model of Eq. 152.

$V_g(\boldsymbol{q})$ is contributed by the mass of the links and the rotors according to

$$V_g(\boldsymbol{q}) = -\sum_{i=1}^{n} m_{l,i}\boldsymbol{g}^T\boldsymbol{p}_{Cl,i}(\boldsymbol{q}) - \sum_{j=1}^{m} m_{r,j}\boldsymbol{g}^T\boldsymbol{p}_{Cr,j}(\boldsymbol{q}), \tag{6}$$

where $\boldsymbol{g}$ is the gravitational acceleration vector. $\boldsymbol{p}_{Cl,i}(\boldsymbol{q})$ and $\boldsymbol{p}_{Cr,j}(\boldsymbol{q})$ are the position vector of the center of mass of the i^{th}-link and of the j^{th}-rotor, respectively. They depend on the robot posture.

Finally, the vector $\boldsymbol{\tau}_{dr}$ is the actual torque applied at the robot joint by the transmission unit and the vector $\boldsymbol{\tau}_{ext}$ is the reflected torque at the robot joint caused by the external force $\boldsymbol{F}_{ext}$. Their relation is due to the duality of the static force and velocity mapping as

$$\boldsymbol{\tau}_{ext} = J(\boldsymbol{q})^T \boldsymbol{F}_{ext}, \tag{7}$$

where $J(\boldsymbol{q})$ is the Jacobian matrix of the frame attached to the point of application of the external force. $J(\boldsymbol{q})$ and $\boldsymbol{F}_{ext}$ are expressed in the same frame.

2.2. Drivetrain Model

The drivetrain or the transmission system is the mechanism that transmits the power from the input power source to the remote system which receives the output power. For the robotic system, the drivetrain typically comprises of several parts as linkages, gears, belts, etc. in delivering the power. While the power is being transmitted through the mechanism, the power variables, i.e. the force/torque (effort) and the collocated velocity (flow) are often being modulated to amplify the output torque or to reduce the output velocity. Nonetheless, ideal transmission would preserve the power flow at any instant. Unfortunately, the actual system deviates from this ideal line due to the underlying impedance properties of the parts and matings. Therefore it is important to consider these dynamical effects to improve the validity of the model for the design of the control system.

Complicated structure of the drivetrain mechanism may be devised to yield the desired output motion. Nevertheless, it can in general be divided into multiple stages of the sub-transmission connecting in tandem. Each stage has the sub-mechanism to transmit the power to the next stage. The sub-mechanism itself may be constructed from a multitude of machine elements. However they can

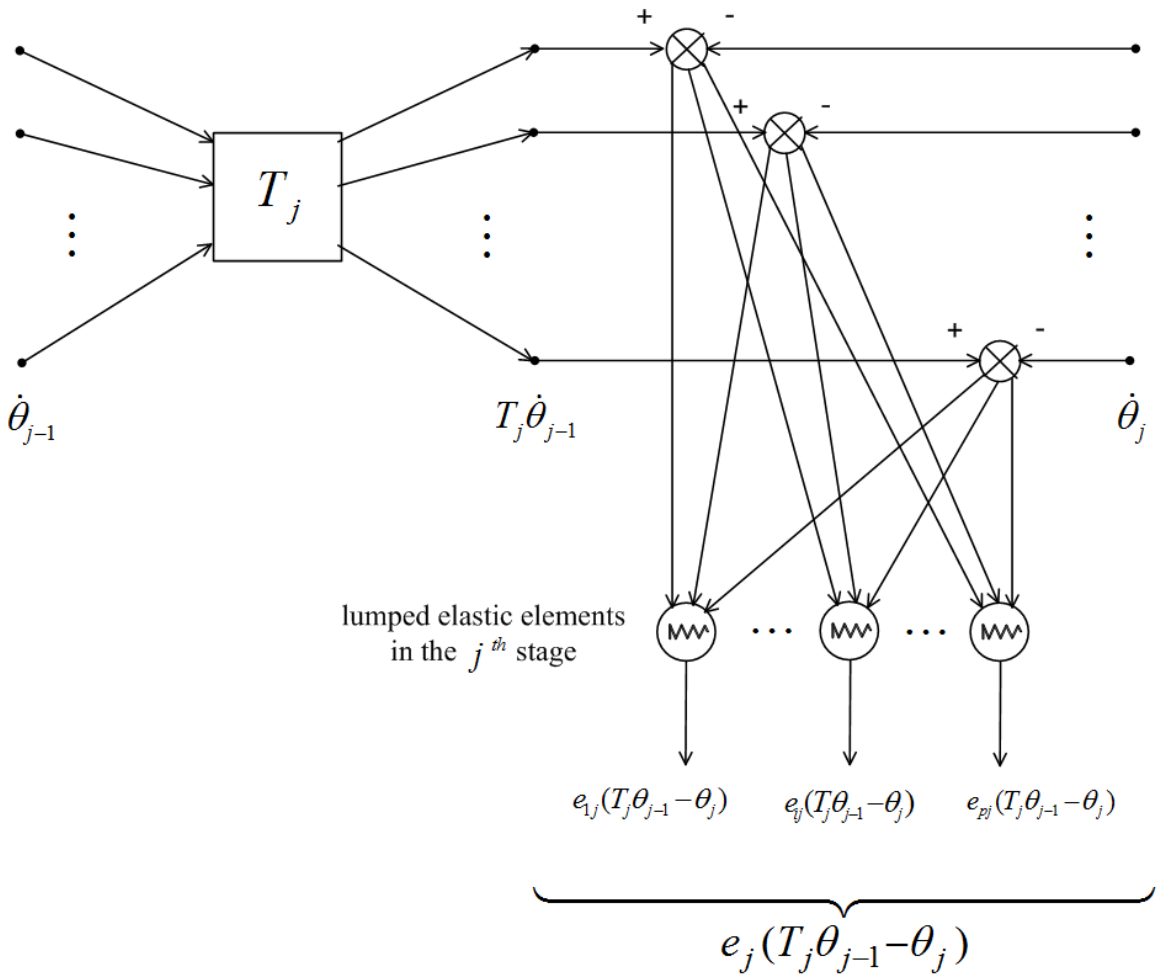

Figure 2: Signal flow diagram illustrating the elastic elements network of the j^{th}-stage transmission system according to Eq. 19 and the subscript notations.

be modeled using only three elemental behaviors of the inertance, the compliance, and the resistance, in conjunction with the nodes and the transformers. Bond graph technique [16] may be useful in the modeling process.

The ideal sub-transmission at each stage can be modeled as the transformer (the reducer) connecting the inport to the outport. To make the model be more realistic, lumped compliance and resistance elements should be included to capture the compliant and dissipative characteristics of the mechanism, as depicted in Fig. 1. At the inport and the outport of each stage, lumped inertance elements may be connected where the resistance may be introduced as well.

For the j^{th}-stage, if the constant transmission ratio matrix of the reducer $\boldsymbol{T}_j$ is assumed according to assumption 2.4, the modulated velocity vector $\dot{\boldsymbol{\theta}}_{m,j}$ after the reducer would be

$$\dot{\boldsymbol{\theta}}_{m,j} = \boldsymbol{T}_j \dot{\boldsymbol{\theta}}_{j-1}, \tag{8}$$

where $\dot{\boldsymbol{\theta}}_{j-1}$ is the p-dimensional outport velocity vector of the previous stage. Referring to Figs. 1

and 2, let the elastic potential energy at the lumped i^{th}-elastic element in the j^{th}-stage be

$$V_{e,ij}\left(\boldsymbol{\theta}_{j-1},\boldsymbol{\theta}_j\right)=\int_0^{\delta} e_{ij}\left(\boldsymbol{\theta}_{m,j}-\boldsymbol{\theta}_j\right)d\left(\boldsymbol{\theta}_{m,j}-\boldsymbol{\theta}_j\right)=\int_0^{\delta} e_{ij}\left(\boldsymbol{T}_j\boldsymbol{\theta}_{j-1}-\boldsymbol{\theta}_j\right)d\left(\boldsymbol{T}_j\boldsymbol{\theta}_{j-1}-\boldsymbol{\theta}_j\right), \quad (9)$$

where $e_{ij}\left(\boldsymbol{T}_j\boldsymbol{\theta}_{j-1}-\boldsymbol{\theta}_j\right)$ is the nonlinear elastic force of the i^{th}-elastic element in the j^{th}-stage, which depends on the generalized coordinates $\boldsymbol{\theta}_{j-1}$ and $\boldsymbol{\theta}_j$. Hence the total elastic potential energy is merely the sum of the potential energy of every elastic elements, i.e.

$$V_e\left(\boldsymbol{q},\boldsymbol{\theta}\right)=\sum_{j=1}^{q}V_{e,j}=\sum_{j=1}^{q}\sum_{i=1}^{p}V_{e,ij}. \quad (10)$$

Note that the total number of stages of the transmission system is q and the configuration of each stage may be described by p-generalized coordinates $\boldsymbol{\theta}_j$. In turn, the total number of DOF of the transmission system is pq, including the generalized coordinates at the inport. They are lumped into the vector $\boldsymbol{\theta}$. It should be mentioned that the outport generalized coordinates, $\boldsymbol{\theta}_q$, are the generalized coordinates of the robot, $\boldsymbol{q}$, corresponding to the input generalized torque $\boldsymbol{\tau}_{dr}$ applied at the robot joints.

The gravitational potential energy of the drivetrain is independent of its own generalized coordinates $\boldsymbol{\theta}$ acknowledging assumption 2.1. It has already been taken care of within the rigid robot model by $V_g\left(\boldsymbol{q}\right)$. On the same assumption, the translational kinetic energy of the drivetrain due mainly to the mass of the rotors, concentrated at the generalized velocity nodes, is not relevant to $\boldsymbol{\theta}$ and $\dot{\boldsymbol{\theta}}$, and it has been accounted with the kinetic energy of the rigid robot. Hence only the rotational kinetic energy T_r of the rotors are left and it is quite simple thanks to assumption 2.2;

$$T_r=\sum_{k=1}^{pq}T_{r,k}=\sum_{k=1}^{pq}\frac{1}{2}b_k\dot{\theta}_k^2, \quad (11)$$

in which b_k is the k^{th}-rotor inertia about its rotational axis and $\dot{\theta}_k$ is its spinning angular velocity. The equation implies the total number of the rotors be pq, for the rotors of the motors are counted in as well.

Lagrangian method is applied to derive the drivetrain model. Recall the Lagrangian formulation

$$\frac{d}{dt}\left(\frac{\partial\mathcal{L}}{\partial\dot{\boldsymbol{\theta}}}\right)^T-\left(\frac{\partial\mathcal{L}}{\partial\boldsymbol{\theta}}\right)^T=\boldsymbol{\tau}, \quad (12)$$

where the Lagrangian $\mathcal{L}$ is the difference of the kinetic and the potential energy. Substituting and evaluating the above formulation, equations of motion for the drivetrain subsystem may be obtained as

$$\boldsymbol{B}\ddot{\boldsymbol{\theta}}+\boldsymbol{c}\left(\dot{\boldsymbol{\theta}}\right)+\boldsymbol{e}\left(\boldsymbol{\theta}\right)=\boldsymbol{\tau}, \quad (13)$$

where $\boldsymbol{\theta}=\begin{bmatrix}\boldsymbol{\theta}_0^T & \boldsymbol{\theta}_1^T & \cdots & \boldsymbol{\theta}_{q-1}^T\end{bmatrix}^T$ is the vector of generalized coordinates of the drivetrain subsystem, composed of the p-generalized coordinates at each stage, successively arrayed starting from the

first stage (described by the coordinates $\boldsymbol{\theta}_0$) to the last q^{th}-stage (described by the coordinates $\boldsymbol{\theta}_{q-1}$). $\boldsymbol{B}$ is the diagonal inertia matrix

$$\boldsymbol{B} = \text{diag}\left(b_{11},\, b_{21},\, \ldots,\, b_{p1},\, b_{12},\, b_{22},\, \ldots,\, b_{p2}, \ldots,\, b_{1q},\, b_{2q},\, \ldots,\, b_{pq}\right), \tag{14}$$

containing the rotational inertia of the rotors about their rotational axes associated with the generalized coordinates. The subscript notation adopted here is the same as of the elastic force depicted in Fig. 2 that b_{ij} denotes the inertia of the i^{th}-rotor in the j^{th}-stage. Hence the first p-elements correspond to the inertia of the motors. $\boldsymbol{c}\left(\dot{\boldsymbol{\theta}}\right)$ expresses the major loss at the rotor bearings and is evaluated by the nonlinear vector function;

$$\begin{aligned} \boldsymbol{c}\left(\dot{\boldsymbol{\theta}}\right) \;=\; & \Big[\; c_{11}\left(\dot{\theta}_{10}\right) \quad c_{21}\left(\dot{\theta}_{20}\right) \quad \ldots \quad c_{p1}\left(\dot{\theta}_{p0}\right) \quad c_{12}\left(\dot{\theta}_{11}\right) \quad c_{22}\left(\dot{\theta}_{21}\right) \quad \ldots \\ & \ldots \quad c_{1q}\left(\dot{\theta}_{1(q-1)}\right) \quad c_{2q}\left(\dot{\theta}_{2(q-1)}\right) \quad \ldots \quad c_{pq}\left(\dot{\theta}_{p(q-1)}\right) \;\Big]^T, \end{aligned} \tag{15}$$

where $c_{ij}\left(\cdot\right)$ is the nonlinear viscous force developed at the bearing of the i^{th}-rotor in the j^{th}-stage.

$\boldsymbol{e}\left(\boldsymbol{\theta}\right)$ is the nonlinear vector function expressing the elastic forces according to the elastic potential energy in Eq. 10;

$$\begin{aligned} \boldsymbol{e}\left(\boldsymbol{\theta}\right) \;&=\; \left(\frac{\partial V_e\left(\boldsymbol{q},\boldsymbol{\theta}\right)}{\partial \boldsymbol{\theta}}\right)^T \\ &=\; \begin{bmatrix} \boldsymbol{T}_1^T \boldsymbol{e}_1\left(\boldsymbol{T}_1\boldsymbol{\theta}_0 - \boldsymbol{\theta}_1\right) \\ -\boldsymbol{e}_1\left(\boldsymbol{T}_1\boldsymbol{\theta}_0 - \boldsymbol{\theta}_1\right) + \boldsymbol{T}_2^T \boldsymbol{e}_2\left(\boldsymbol{T}_2\boldsymbol{\theta}_1 - \boldsymbol{\theta}_2\right) \\ \vdots \\ -\boldsymbol{e}_{q-1}\left(\boldsymbol{T}_{q-1}\boldsymbol{\theta}_{q-2} - \boldsymbol{\theta}_{q-1}\right) + \boldsymbol{T}_q^T \boldsymbol{e}_q\left(\boldsymbol{T}_q\boldsymbol{\theta}_{q-1} - \boldsymbol{\theta}_q\right) \end{bmatrix}, \end{aligned} \tag{16}$$

in which the sub-vector of the nonlinear elastic forces acting at the j^{th}-rotor is $-\boldsymbol{e}_{j-1}\left(\boldsymbol{T}_{j-1}\boldsymbol{\theta}_{j-2} - \boldsymbol{\theta}_{j-1}\right) + \boldsymbol{T}_j^T \boldsymbol{e}_j\left(\boldsymbol{T}_j\boldsymbol{\theta}_{j-1} - \boldsymbol{\theta}_j\right)$, involving the relative displacements between its neighborhoods and the transmission ratios. The nonlinear vector function $\boldsymbol{e}_j\left(\cdot\right)$ describes the elastic forces of the p-lumped elastic elements at the j^{th}-stage.

$\boldsymbol{\tau}$ is the generalized torque vector associated with the generalized coordinates. Referring to Fig. 1, it corresponds to the actual torque vector generated by the motors, $\boldsymbol{\tau}_m$, attached to the first stage. Therefore,

$$\boldsymbol{\tau} = \left[\; \boldsymbol{\tau}_m^T \quad \boldsymbol{0}^T \quad \cdots \quad \boldsymbol{0}^T \;\right]^T. \tag{17}$$

On the other end of the drivetrain, the actual output torques

$$\boldsymbol{\tau}_{dr} = \boldsymbol{e}_q\left(\boldsymbol{T}_q\boldsymbol{\theta}_{q-1} - \boldsymbol{\theta}_q\right), \tag{18}$$

are transmitted to the robot with the generalized velocity $\dot{\boldsymbol{\theta}}_q$ via the network of the elastic elements in the last stage.

It should be mentioned that if the elastic elements behave linearly, $\boldsymbol{e}_j\left(\cdot\right)$ may be written explicitly by the introduction of the stiffness matrix $\boldsymbol{K}_j$, i.e.

$$\boldsymbol{e}_j\left(\boldsymbol{T}_j\boldsymbol{\theta}_{j-1} - \boldsymbol{\theta}_j\right) = \boldsymbol{K}_j\left(\boldsymbol{T}_j\boldsymbol{\theta}_{j-1} - \boldsymbol{\theta}_j\right). \tag{19}$$

Also, since the drivetrain subsystem itself, i.e. excluding the actuators, is passive, the following constraint on the elastic force must hold;

$$\frac{\partial e_{ij}}{\partial \delta_{kj}} = \frac{\partial^2 V_{e,j}}{\partial \delta_{kj} \partial \delta_{ij}} = \frac{\partial^2 V_{e,j}}{\partial \delta_{ij} \partial \delta_{kj}} = \frac{\partial e_{kj}}{\partial \delta_{ij}}, \tag{20}$$

where δ_{kj} is the deformation of the k^{th}-elastic element in the j^{th}-stage. For the linear elastic elements, this implies the symmetric positive definiteness of $\boldsymbol{K}_j$.

2.3. Motor Model

Inclusion of the motor electrical dynamics in the controller design can increase the control performance at the cost of more complex model. For the series-wound DC motor, dynamical equation of the armature current may be derived readily by applying the Kirchhoff's voltage law to the circuit. From the principle, the equation describing the actual armature current dynamics $\boldsymbol{i}$ of the p-motors equipped to the transmission inport becomes

$$\boldsymbol{L}\dot{\boldsymbol{i}} + \boldsymbol{R}\boldsymbol{i} + \boldsymbol{K}_b\dot{\boldsymbol{\theta}}_0 = \boldsymbol{u}, \tag{21}$$

where $\boldsymbol{L}$, $\boldsymbol{R}$, and $\boldsymbol{K}_b$ are the diagonal matrix of lumped inductances, resistances, and the back-emf constants of the motors respectively. $\boldsymbol{u}$ is the control input vector of the motor voltages. Accordingly, the generated motor torques are governed by the torque constant matrix $\boldsymbol{K}_\tau$;

$$\boldsymbol{\tau}_m = \boldsymbol{K}_\tau \boldsymbol{i}. \tag{22}$$

If the SI standard unit system is adopted, $\boldsymbol{K}_\tau$ (in Nm/A) will have the same numerical values as $\boldsymbol{K}_b$ (in Vs). Note that the motor mechanical dynamics has already been treated by incorporating it into the drivetrain model.

In summary, the simplified model of the nonlinear flexible joint robot system according to the stated assumptions 2.1-2.4 is described by Eqs. 1, 13, 22, and 21. This reflects the physical cascaded connection of the three subsystems; namely the motor, the transmission, and the robot subsystems. The model will be used to develop the task space impedance controller in the next section.

3. Task Space Impedance Control

Appropriate impedance is an intrinsic key for the robot to perform the task successfully. In this work, the desirable impedance characteristics will be accomplished purely via the controller design. This method has the features of cheaper system, less developing time, and easier access to modification. Due to the artificial impedance modulation, however, it can bring the shortcomings of instability and hence unsafe system if not properly designed.

Several variations of the impedance controllers are proposed depending on the detailed specification of the physical systems and the control techniques used. For our system, the assumed rigid robot

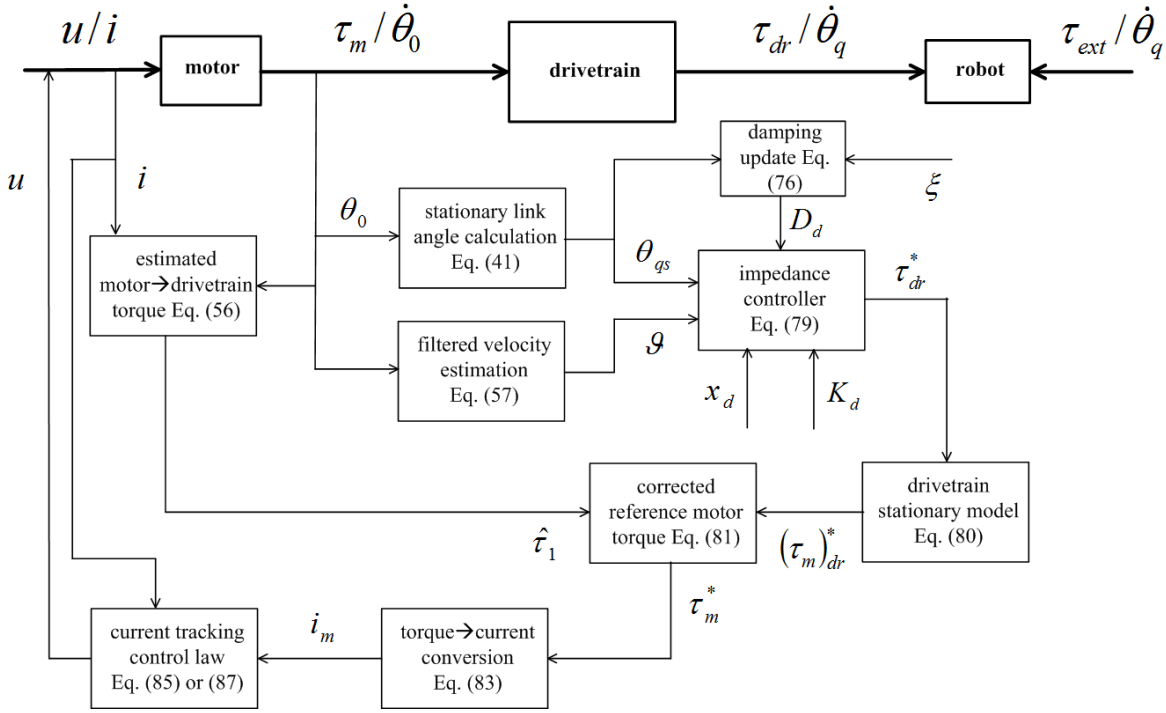

Figure 3: Overall diagram of the task space impedance controller.

is propelled by the motors through the flexible transmission subsystem of which the configurations match the developed model in section 2. Unfortunately, the available feedback signals are limited to the motor angles and currents only. This is indeed the most common case found in practice. Torque sensors, measuring the actual torque transmitted to the robot, and their electronics are uncommon for robotic system. End effector force sensor, which may induce undesirable dynamics especially for the lightweight robot, is expensive and found to be useless if the external forces are applied at unknown different locations from the sensor: a typical situation encountered when working in the unstructured environment. Worse yet, it may cause the system to become unstable if the feedback signal is not properly handled. The link angles can be measured by installing additional encoders except they will complicate the robot design. Moreover, for the robot employing some special joints, such as the compound pitch-roll differentials or the spherical joint, the link angles may not be measurable with ordinary encoders. Tachometer used to monitor the angular velocity signal is known to be noisy other than making the system be unwieldy.

Before presenting the task space impedance controller in details, a brief explanation of the control scheme will be given according to Fig. 3. At any instant, the motor angles $\boldsymbol{\theta}_0$ and currents $\boldsymbol{i}$ are read. Desired impedance behavior is specified by the task space constant stiffness matrix $\boldsymbol{K}_d$ according to the performed task. Based on this desired stiffness and the calculated stationary link angles $\boldsymbol{q}_s$, the suitable positive definite damping matrix $\boldsymbol{D}_d$ will be updated in the manner that the end effector oscillation is suppressed with the desired rate governed by the tunable damping ratio.

Set point of the end effector $\boldsymbol{x}_d$ is specified. Now the torque transmitted to the drivetrain unit is estimated that may be used to shape the motors' effective inertia. Following the modulated inertia, the impedance controller is designed using the stationary link angles $\boldsymbol{q}_s$ to accomplish the desired task space compliance. Damping force is added according to the computed task space damping matrix $\boldsymbol{D}_d$ making the system be asymptotically stable by which the nonmodel-based first order differentiation filter is employed to approximate the link joint velocity. Next, the required robot joint torque, $\boldsymbol{\tau}_{dr}^*$, is used to calculate the corresponding output motor torque, $(\boldsymbol{\tau}_m)_{dr}^*$. Finally, a feedback control law is designed to regulate the motor input voltage, $\boldsymbol{u}$, for supplying such output torque. Passivity and stability analysis of the closed loop system are demonstrated in the last subsection.

3.1. Drivetrain Stationary Model

A difficulty in controlling the flexible joint robot is that the system usually has less amount of the actuators than the total number of system's DOF. This kind of system is classified as the underactuated system [17] and the control problem is not straightforward due basically to indirect access to control the desired motion. Several control techniques are studied such as the singular perturbation analysis, the backstepping control design, or the partial feedback linearization technique. Recently there are interests in designing the controller from the energy consideration. Two equivalent methods of the interconnection and damping assignment passivity-based control (IDA-PBC) [18] and the method of controlled Lagrangian [19, 20] design the controllers such that, respectively, the closed loop system Hamiltonian and Lagrangian match the desired ones. Energy approach takes the physics of the system into account from the ground-up and hence has proven to provide a robust and stable control system.

To fully exploit the developed model in section 2 for the controller design, all system states such as the drivetrain's rotor angles or the link angles must be measurable. However, they are rarely available. Nevertheless, tandem structure of the system allows its states to be observable from its output measurement and the reference model. The control system may then be designed with regard to these observed states. Unfortunately, sensor placement at the output of some systems are not possible. This is the case of the compound joint robot, for example.

For such system, the energy cannot be completely shaped because the system states or their estimate are not available for inferring its present energy. An alleviation is to compute, in an open-loop fashion, certain states on the assumption of stationary motion. In other words, the robot operates smoothly at low enough speed that the motion-induced forces, i.e. the inertial and the Coriolis/centrifugal forces, may be omitted. With this assumption, velocity and acceleration terms in the equations of motion may be dropped, in which the remaining position-state terms can be solved algebraically. Stationary model of the transmission subsystem will be developed in this subsection while the one for the robot is deferred to the next subsection.

Full dynamics of the drivetrain is governed by Eq. 13. If the stationary motion assumption is

applied, the first two terms on the left of the equation can be dropped. Therefore, the reduced model may be written as

$$\boldsymbol{e}\left(\boldsymbol{\theta}_s\right) = \boldsymbol{\tau}, \tag{23}$$

where the subscripted s denotes the stationary value of the variable. Motor angles $\boldsymbol{\theta}_0$ can be read from their encoders. They may be used to solve for other generalized coordinates of the drivetrain subsystem successively towards the coordinates of the last q^{th}-stage and of the robot link angles, $\boldsymbol{\theta}_{(q-1)s}$ and $\boldsymbol{\theta}_{qs}$, if the supplied motor torques $\boldsymbol{\tau}_m$ are known. Nevertheless, the stationary relationship between them may be derived without the knowledge of motor torques. Consider the set of vector equations of the intermediate 2^{nd} to q^{th}-stages of the elastic model in Eq. 23. They can be expressed as

$$\begin{aligned}
\boldsymbol{e}_1\left(\boldsymbol{T}_1\boldsymbol{\theta}_0 - \boldsymbol{\theta}_{1s}\right) &= \boldsymbol{T}_2^T\boldsymbol{e}_2\left(\boldsymbol{T}_2\boldsymbol{\theta}_{1s} - \boldsymbol{\theta}_{2s}\right) \\
\boldsymbol{e}_2\left(\boldsymbol{T}_2\boldsymbol{\theta}_{1s} - \boldsymbol{\theta}_{2s}\right) &= \boldsymbol{T}_3^T\boldsymbol{e}_3\left(\boldsymbol{T}_3\boldsymbol{\theta}_{2s} - \boldsymbol{\theta}_{3s}\right) \\
&\vdots \\
\boldsymbol{e}_{q-1}\left(\boldsymbol{T}_{q-1}\boldsymbol{\theta}_{(q-2)s} - \boldsymbol{\theta}_{(q-1)s}\right) &= \boldsymbol{T}_q^T\boldsymbol{e}_q\left(\boldsymbol{T}_q\boldsymbol{\theta}_{(q-1)s} - \boldsymbol{\theta}_{qs}\right).
\end{aligned} \tag{24}$$

States of the transmission system may then be written explicitly for the purpose of derivation as

$$\begin{aligned}
\boldsymbol{\theta}_{1s} &= \boldsymbol{\theta}_{1s}\left(\boldsymbol{\theta}_0, \boldsymbol{\theta}_{2s}\right) \\
\boldsymbol{\theta}_{2s} &= \boldsymbol{\theta}_{2s}\left(\boldsymbol{\theta}_{1s}, \boldsymbol{\theta}_{3s}\right) \\
&\vdots \\
\boldsymbol{\theta}_{(q-1)s} &= \boldsymbol{\theta}_{(q-1)s}\left(\boldsymbol{\theta}_{(q-2)s}, \boldsymbol{\theta}_{qs}\right),
\end{aligned} \tag{25}$$

where the coordinates $\boldsymbol{\theta}_j$ are abusively used as the vector function name as well. Now $\boldsymbol{\theta}_{(q-1)s}$ may be expressed in terms of $\boldsymbol{\theta}_0$ (motor angles) and $\boldsymbol{\theta}_{qs}$ (robot link angles) explicitly. First, substituting the first vector equation of Eq. 25 into the second one. This will eliminate $\boldsymbol{\theta}_{1s}$ so the explicit relation of $\boldsymbol{\theta}_{2s}$ in terms of $\boldsymbol{\theta}_0$ and $\boldsymbol{\theta}_{3s}$

$$\boldsymbol{\theta}_{2s} = \boldsymbol{\theta}_{2s}\left(\boldsymbol{\theta}_0, \boldsymbol{\theta}_{3s}\right)$$

is obtained. This new vector equation is further substituted into the lower one; the third equation in this case. It then yields new expression for $\boldsymbol{\theta}_{3s}$:

$$\boldsymbol{\theta}_{3s} = \boldsymbol{\theta}_{3s}\left(\boldsymbol{\theta}_0, \boldsymbol{\theta}_{4s}\right).$$

Continue the substitution process for the rest, eventually the desired relation

$$\boldsymbol{\theta}_{(q-1)s} = \boldsymbol{\theta}_{(q-1)s}\left(\boldsymbol{\theta}_0, \boldsymbol{\theta}_{qs}\right) \tag{26}$$

is achieved. Therefore, stationary values of the position-states of the drivetrain may be inferred. It should be mentioned that numerical methods might be necessary to solve Eq. 24 and Eq. 31 (developed in subsection 3.2) for $\boldsymbol{\theta}_{js}$ with the nonlinear elastic force vector functions $\boldsymbol{e}_j\left(\cdot\right)$ in general.

Duality of the stationary motion is the stationary torque relationship between $\boldsymbol{\tau}_s$ and $(\boldsymbol{\tau}_{dr})_s$. With the drivetrain stationary model in Eq. 23, the corresponding $\boldsymbol{\tau}_s$ to $(\boldsymbol{\tau}_{dr})_s$ may be derived as follow. From the structure of $\boldsymbol{\tau}_{dr}$ in Eq. 18, output torque of the transmission subsystem is the elastic torque of the q^{th}-stage, $\boldsymbol{e}_q(\cdot)$. With the last vector equation in Eq. 24, the elastic torque of the $(q-1)^{\text{th}}$-stage, $\boldsymbol{e}_{(q-1)}(\cdot)$, may be evaluated readily. Substituting this result into its preceding equation, elastic torque of the previous stage may be determined. Continue the backward substitution process for the rest, the stationary output motor torque $(\boldsymbol{\tau}_m)_s$ may be solved from the equation of the 1^{st}-stage transmission in Eq. 23;

$$(\boldsymbol{\tau}_m)_s = \boldsymbol{T}_1^T \boldsymbol{e}_1 (\boldsymbol{T}_1 \boldsymbol{\theta}_0 - \boldsymbol{\theta}_{1s}), \tag{27}$$

indicating the equality of the supplied motor torque and the stepped elastic torque of the 1^{st}-stage. Combining these relevant equations altogether, the stationary relationship between the output torque of the drivetrain and the supplied motor torque becomes

$$\begin{aligned} (\boldsymbol{\tau}_m)_s &= \boldsymbol{T}_1^T \boldsymbol{T}_2^T \cdots \boldsymbol{T}_{q-1}^T \boldsymbol{T}_q^T \boldsymbol{e}_q \left(\boldsymbol{T}_q \boldsymbol{\theta}_{(q-1)s} - \boldsymbol{\theta}_{qs}\right) \\ &= \boldsymbol{T}_1^T \boldsymbol{T}_2^T \cdots \boldsymbol{T}_{q-1}^T \boldsymbol{T}_q^T (\boldsymbol{\tau}_{dr})_s . \end{aligned} \tag{28}$$

This equation will be useful in transforming the required robot stationary joint torque to the associated stationary output motor torque.

3.2. Stationary Link Angles

In subsection 3.1, the stationary model of the drivetrain is studied where the stationary relations between the drivetrain coordinates, the motor angles and the robot link angles have been developed. Nevertheless, there are not enough equations to fully solve for the system coordinates from the motor angles. In fact, additional p-scalar equations are required which can be obtained from the stationary model of the robot.

Equation 1 describes the full joint space dynamics of the rigid robot. If the robot is operating at low enough speed, its inertial and Coriolis/centrifugal forces may be neglected. Under this condition, the robot undergoes the stationary motion where the torques supplied by the transmission unit balance the gravity- and the external force-induced torques;

$$\boldsymbol{g}(\boldsymbol{\theta}_{qs}) = \boldsymbol{e}_q \left(\boldsymbol{T}_q \boldsymbol{\theta}_{(q-1)s} - \boldsymbol{\theta}_{qs}\right) + \boldsymbol{\tau}_{ext}. \tag{29}$$

In this stationary model, the robot generalized coordinates $\boldsymbol{q}$ are replaced with the outport coordinates $\boldsymbol{\theta}_q$ of the drivetrain unit.

Since the desired task space compliance $\boldsymbol{K}_d$ at the designated end effector set point $\boldsymbol{x}_d$ is to be achieved, the reflected torques caused by this behavior, under the stationary condition, will be

$$\boldsymbol{\tau}_{ext} = J(\boldsymbol{\theta}_{qs})^T \boldsymbol{F}_{ext} = J(\boldsymbol{\theta}_{qs})^T \boldsymbol{K}_d (\boldsymbol{f}(\boldsymbol{\theta}_{qs}) - \boldsymbol{x}_d), \tag{30}$$

where $\boldsymbol{f}(\cdot)$ is the forward kinematics mapping of the robot. Enforcing such compliance characteristics to the robot stationary model of Eq. 29, the vector equation

$$\boldsymbol{e}_q\left(\boldsymbol{T}_q\boldsymbol{\theta}_{(q-1)s}-\boldsymbol{\theta}_{qs}\right)=\boldsymbol{g}\left(\boldsymbol{\theta}_{qs}\right)-J\left(\boldsymbol{\theta}_{qs}\right)^T\boldsymbol{K}_d\left(\boldsymbol{f}\left(\boldsymbol{\theta}_{qs}\right)-\boldsymbol{x}_d\right)=\boldsymbol{h}\left(\boldsymbol{\theta}_{qs}\right) \tag{31}$$

displaying the stationary relationship between $\boldsymbol{\theta}_{(q-1)}$ and $\boldsymbol{\theta}_q$ may be formulated. Incorporating with the set of stationary equations in Eq. 24, calculation of the stationary drivetrain and robot link coordinates may be performed.

For the purpose of derivation, $\boldsymbol{\theta}_{qs}$ in Eq. 31 may be written explicitly as

$$\boldsymbol{\theta}_{qs}=\boldsymbol{\theta}_{qs}\left(\boldsymbol{\theta}_{(q-1)s}\right). \tag{32}$$

According to this result, explicit relationship between the stationary robot link angles and the motor angles may be derived by employing Eq. 26. After some algebraic manipulation, one would obtain

$$\boldsymbol{\theta}_{qs}=\boldsymbol{\theta}_{qs}\left(\boldsymbol{\theta}_0\right), \tag{33}$$

of which the stationary robot link angles can be determined directly.

Practically, $\boldsymbol{\theta}_{qs}$ may not be solved explicitly as shown in Eq. 32 due to the dependency of the Jacobian matrix on $\boldsymbol{\theta}_{qs}$. Still, Eq. 26 may be substituted into Eq. 31 and the link angles can be solved numerically. If the inverse of the elastic force vector function $\boldsymbol{e}_q(\cdot)$, denoted as $\boldsymbol{e}_q^{-1}(\cdot)$, can be determined analytically, the equation of $\boldsymbol{\theta}_{qs}$ may be expressed as

$$\begin{aligned}\boldsymbol{\theta}_{qs} &= \boldsymbol{T}_q\boldsymbol{\theta}_{(q-1)s}-\boldsymbol{e}_q^{-1}\left(\boldsymbol{h}\left(\boldsymbol{\theta}_{qs}\right)\right)\\ &= \boldsymbol{T}_q\boldsymbol{\theta}_{(q-1)s}\left(\boldsymbol{\theta}_0,\boldsymbol{\theta}_{qs}\right)-\boldsymbol{e}_q^{-1}\left(\boldsymbol{h}\left(\boldsymbol{\theta}_{qs}\right)\right),\end{aligned} \tag{34}$$

showing the robot link angles as the implicit function of the motor angles $\boldsymbol{\theta}_0$. With this arrangement, $\boldsymbol{\theta}_{qs}$ can now be solved by recursive evaluation.

Furthermore, if the elastic elements behaves linearly, the elastic force functions $\boldsymbol{e}_j(\cdot)$ can be simplified by using the stiffness matrix $\boldsymbol{K}_j$ instead. In that case, Eq. 26 may be written explicitly as follow. With the linear elasticity assumption and the stationary condition, Eq. 18 may be rewritten as

$$\boldsymbol{T}_q\boldsymbol{\theta}_{(q-1)s}-\boldsymbol{\theta}_{qs}=\boldsymbol{K}_q^{-1}\left(\boldsymbol{\tau}_{dr}\right)_s. \tag{35}$$

Next, consider the elastic forces in the preceding stages. Implicit equations of the drivetrain elastic model in Eq. 24 may be rewritten, in the reverse order, as

$$\begin{aligned}\boldsymbol{T}_{q-1}\boldsymbol{\theta}_{(q-2)s}-\boldsymbol{\theta}_{(q-1)s} &= \boldsymbol{K}_{q-1}^{-1}\boldsymbol{T}_q^T\left(\boldsymbol{\tau}_{dr}\right)_s\\ \boldsymbol{T}_{q-2}\boldsymbol{\theta}_{(q-3)s}-\boldsymbol{\theta}_{(q-2)s} &= \boldsymbol{K}_{q-2}^{-1}\boldsymbol{T}_{q-1}^T\boldsymbol{T}_q^T\left(\boldsymbol{\tau}_{dr}\right)_s\\ &\vdots\\ \boldsymbol{T}_2\boldsymbol{\theta}_{1s}-\boldsymbol{\theta}_{2s} &= \boldsymbol{K}_2^{-1}\boldsymbol{T}_3^T\boldsymbol{T}_4^T\cdots\boldsymbol{T}_{q-1}^T\boldsymbol{T}_q^T\left(\boldsymbol{\tau}_{dr}\right)_s\\ \boldsymbol{T}_1\boldsymbol{\theta}_0-\boldsymbol{\theta}_{1s} &= \boldsymbol{K}_1^{-1}\boldsymbol{T}_2^T\boldsymbol{T}_3^T\cdots\boldsymbol{T}_{q-1}^T\boldsymbol{T}_q^T\left(\boldsymbol{\tau}_{dr}\right)_s.\end{aligned} \tag{36}$$

To accomplish the direct relation between the stationary robot link angles and the motor angles, premultiply the previous equations with the appropriate compound transmission ratios such that the addition of these modified equations brings the ladder-cancellation of most of the terms on the left hand side except $\boldsymbol{\theta}_{qs}$ and $\boldsymbol{\theta}_0$. The resulting equation becomes

$$\begin{aligned}\boldsymbol{T}_q\boldsymbol{T}_{q-1}\cdots\boldsymbol{T}_1\boldsymbol{\theta}_0-\boldsymbol{\theta}_{qs} &= \Big[\left(\boldsymbol{T}_q\boldsymbol{T}_{q-1}\cdots\boldsymbol{T}_2\right)\boldsymbol{K}_1^{-1}\left(\boldsymbol{T}_q\boldsymbol{T}_{q-1}\cdots\boldsymbol{T}_2\right)^T \\ &\quad+\left(\boldsymbol{T}_q\boldsymbol{T}_{q-1}\cdots\boldsymbol{T}_3\right)\boldsymbol{K}_2^{-1}\left(\boldsymbol{T}_q\boldsymbol{T}_{q-1}\cdots\boldsymbol{T}_3\right)^T+\cdots \\ &\quad+\left(\boldsymbol{T}_q\boldsymbol{T}_{q-1}\right)\boldsymbol{K}_{q-2}^{-1}\left(\boldsymbol{T}_q\boldsymbol{T}_{q-1}\right)^T+\boldsymbol{T}_q\boldsymbol{K}_{q-1}^{-1}\boldsymbol{T}_q^T+\boldsymbol{K}_q^{-1}\Big]\left(\boldsymbol{\tau}_{dr}\right)_s.\end{aligned}$$

Let the compound transmission ratio from the j^{th}-stage to the q^{th}-stage, $\boldsymbol{T}_q\boldsymbol{T}_{q-1}\cdots\boldsymbol{T}_j$, be denoted as $\boldsymbol{T}_{qj}$. Then, the above equation may be written in a more clearly and concise manner as

$$\left(\boldsymbol{\tau}_{dr}\right)_s=\boldsymbol{K}_{1q}\left(\boldsymbol{T}_{q1}\boldsymbol{\theta}_0-\boldsymbol{\theta}_{qs}\right), \tag{37}$$

in which

$$\boldsymbol{K}_{1q}=\left[\boldsymbol{T}_{q2}\boldsymbol{K}_1^{-1}\boldsymbol{T}_{q2}^T+\boldsymbol{T}_{q3}\boldsymbol{K}_2^{-1}\boldsymbol{T}_{q3}^T+\cdots+\boldsymbol{T}_{q(q-1)}\boldsymbol{K}_{q-2}^{-1}\boldsymbol{T}_{q(q-1)}^T+\boldsymbol{T}_q\boldsymbol{K}_{q-1}^{-1}\boldsymbol{T}_q^T+\boldsymbol{K}_q^{-1}\right]^{-1} \tag{38}$$

is the overall effective stiffness of the transmission subsystem. The expression depicts the series connection of the elastic network of each stage. Note that the compound transmission ratios are necessary to reflect these stiffnesses to the last q^{th}-stage. Also, the stationary transmitted torque to the robot may be determined either from the stiffness of the last stage, Eq. 18, or from the overall effective stiffness, Eq. 37. Of course, the corresponding deformation would have been different.

Recalling Eq. 35, explicit expression of $\boldsymbol{\theta}_{(q-1)s}$ in Eq. 26 may now be obtained as

$$\boldsymbol{\theta}_{(q-1)s}=\boldsymbol{T}_q^{-1}\boldsymbol{K}_q^{-1}\left[\boldsymbol{K}_{1q}\boldsymbol{T}_{q1}\boldsymbol{\theta}_0+\left(\boldsymbol{K}_q-\boldsymbol{K}_{1q}\right)\boldsymbol{\theta}_{qs}\right], \tag{39}$$

where the stiffness $\left(\boldsymbol{K}_q-\boldsymbol{K}_{1q}\right)$ is symmetric positive definite due to the tandem structure of the drivetrain. Finally, substituting Eq. 39 into Eq. 34 and performing some reduction, recursive expression of $\boldsymbol{\theta}_{qs}$ may be written explicitly for the case of linear elastic elements as

$$\boldsymbol{\theta}_{qs}=\boldsymbol{T}_{q1}\boldsymbol{\theta}_0-\boldsymbol{K}_{1q}^{-1}\boldsymbol{h}\left(\boldsymbol{\theta}_{qs}\right). \tag{40}$$

This equation is the extension of the work in [9] to the multi-stage transmission system from the motors to the robot. Furthermore, if the elastic elements are nonlinear, the equation will be generalized to

$$\boldsymbol{\theta}_{qs}=\boldsymbol{T}_{q1}\boldsymbol{\theta}_0-\boldsymbol{e}_{1q}^{-1}\left(\boldsymbol{h}\left(\boldsymbol{\theta}_{qs}\right)\right), \tag{41}$$

where $\boldsymbol{e}_{1q}^{-1}\left(\cdot\right)$ is the overall effective nonlinear deformation function of the transmission subsystem. Figure 4 graphically illustrates the total compliance of the one-dimensional series-connected nonlinear springs with the identity transmission ratios.

A question of convergence arises in the numerical evaluation of Eq. 40 or 41. To answer whether the solution will converge or not, the contraction mapping theorem, which guarantees the existence and uniqueness of the fixed point, is employed.

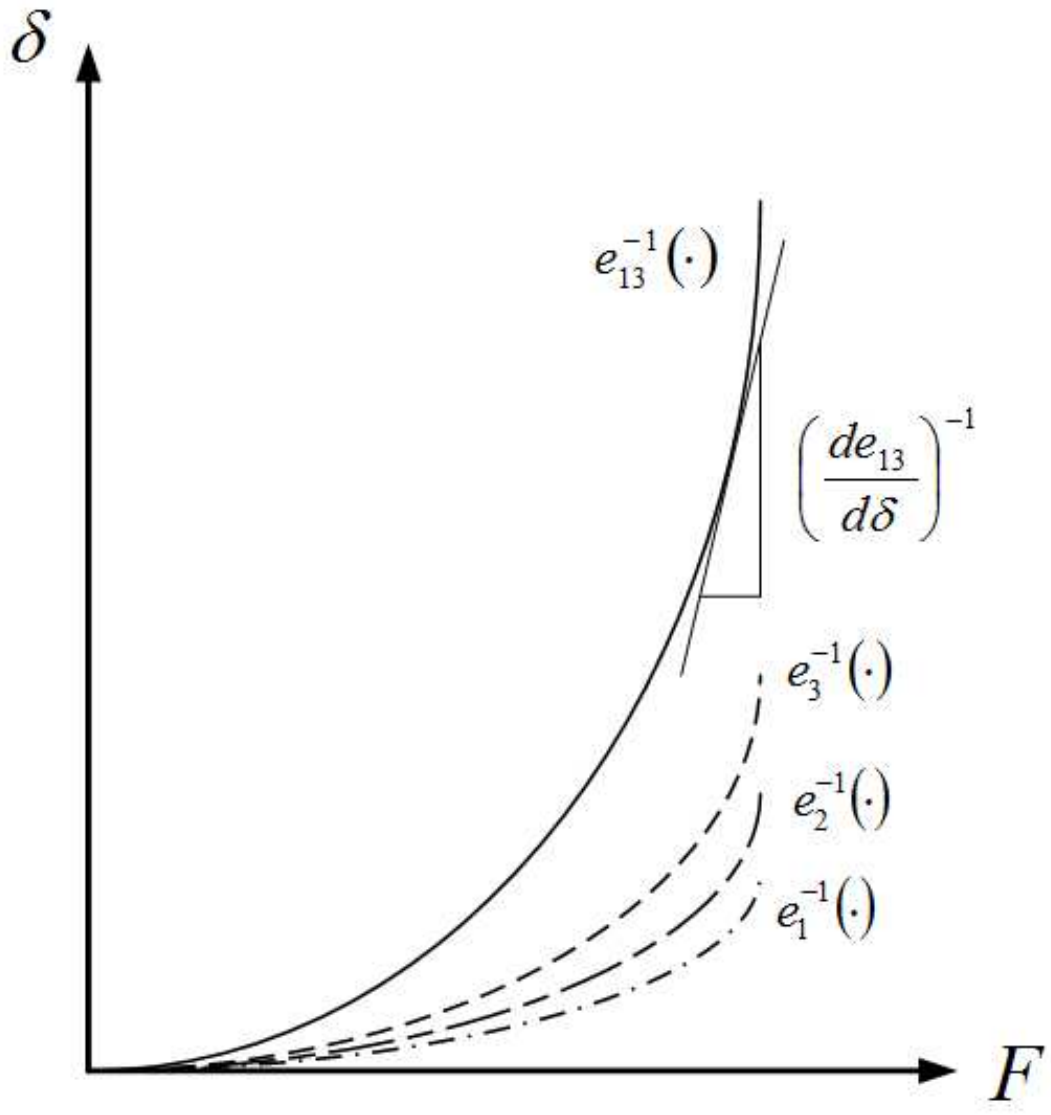

Figure 4: Total compliance may be determined graphically for the simple case of one-dimensional series-connected nonlinear springs.

Definition 1. CONTRACTION MAPPING: Let X be a metric space with $d(p,q)$ the distance between two points p and q. A map $P : X \to X$ is called a contraction mapping on X if there exists $\rho \in [0,1)$ such that

$$d(P(p), P(q)) \leq \rho d(p,q), \quad \forall p, q \in X.$$

Theorem 2. CONTRACTION MAPPING THEOREM: Let X be a non-empty complete metric space with $d(p,q)$ the distance between two points p and q. If $P : X \to X$ is a contraction mapping, then P admits a unique fixed point x^* in X, i.e.

$$P(x^*) = x^*.$$

Additionally, the fixed point x^* can be determined by starting with an arbitrary point $x_0 \in X$. The sequence $\{x_n\}$ where

$$x_n = P(x_{n-1})$$

brings about $x_n \to x^*$.

Therefore, to conclude that the recursive evaluation of Eq. 40 converges, it is sufficient to show that the mapping function

$$\boldsymbol{P}(\boldsymbol{q}) = \boldsymbol{T}_{q1}\boldsymbol{\theta}_0 - \boldsymbol{K}_{1q}^{-1}\boldsymbol{h}(\boldsymbol{q}) \tag{42}$$

is a contraction mapping. Nevertheless, the distance function must be defined first. If the coordinates in the vector $\boldsymbol{q}$ all have the same units, it is common to define the distance function with the help of the inner product or the Euclidean vector norm, i.e.

$$d(\boldsymbol{q}_1, \boldsymbol{q}_2) = \|\boldsymbol{q}_1 - \boldsymbol{q}_2\|_2 = \left[(\boldsymbol{q}_1 - \boldsymbol{q}_2)^T (\boldsymbol{q}_1 - \boldsymbol{q}_2)\right]^{1/2}.$$

However, for the general case where the robot possesses both the rotational and the prismatic joints, units of the coordinates in $\boldsymbol{q}$ are not consistent. Consequently, the above Euclidean distance function suffers from the coordinate distortion. A remedy to this problem is to define specific vector and matrix norms by scaling with the robot joint effective stiffness matrix, $\boldsymbol{K}_{1q}$. In effect, it will normalize the coordinate values to the same scale and unit so the standard Euclidean norm may again be used as the distance measure.

Arbitrary symmetric positive definite matrix $\boldsymbol{K}_{1q}$ may be decomposed into the product of a lower triangular matrix and its transpose. In other words,

$$\boldsymbol{K}_{1q} = \boldsymbol{U}^T\boldsymbol{U}, \tag{43}$$

in which $\boldsymbol{U}$ is an upper triangular matrix. This decomposition is known as the Cholesky decomposition. Accordingly, a new vector norm $\|\cdot\|_K : \mathbb{R}^p \to \mathbb{R}^+$ may be defined as

$$\|\boldsymbol{q}\|_K = \|\boldsymbol{U}\boldsymbol{q}\|_2 = \left[\boldsymbol{q}^T\boldsymbol{K}_{1q}\boldsymbol{q}\right]^{1/2}, \tag{44}$$

where $\boldsymbol{U}$ is used as the scaling matrix. In turn, the corresponding matrix norm $\|\cdot\|_K : \mathbb{R}^{p\times p} \to \mathbb{R}^+$ is defined via the spectral norm $\|\cdot\|_2$. For a matrix $\boldsymbol{A} \in \mathbb{R}^{p\times p}$, consider

$$\begin{aligned} \left|\boldsymbol{q}^T\boldsymbol{A}\boldsymbol{q}\right| &= \left|\boldsymbol{q}^T\boldsymbol{U}^T\boldsymbol{U}^{-T}\boldsymbol{A}\boldsymbol{U}^{-1}\boldsymbol{U}\boldsymbol{q}\right| \\ &\leq \left\|\boldsymbol{U}^{-T}\boldsymbol{A}\boldsymbol{U}^{-1}\right\|_2 \|\boldsymbol{U}\boldsymbol{q}\|_2^2 . \end{aligned}$$

According to the K-norm of the vector in Eq. 44, this motivates the corresponding matrix norm to be defined as

$$\|\boldsymbol{A}\|_K = \left\|\boldsymbol{U}^{-T}\boldsymbol{A}\boldsymbol{U}^{-1}\right\|_2 . \tag{45}$$

which is the largest singular value of the transformed matrix $\boldsymbol{U}^{-T}\boldsymbol{A}\boldsymbol{U}^{-1}$. With these new K-norms defined, the upper limit of the quadratic term $\boldsymbol{q}^T\boldsymbol{A}\boldsymbol{q}$ may be written as

$$\left|\boldsymbol{q}^T\boldsymbol{A}\boldsymbol{q}\right| \leq \|\boldsymbol{A}\|_K \|\boldsymbol{q}\|_K^2 .$$

Consequently, the new distance function, of which the coordinate scaling problem is taken into account, may be defined thanks to the vector K-norm as

$$\begin{aligned} d_K(\boldsymbol{q}_1, \boldsymbol{q}_2) &= \|\boldsymbol{q}_1 - \boldsymbol{q}_2\|_K \\ &= \|\boldsymbol{U}(\boldsymbol{q}_1 - \boldsymbol{q}_2)\|_2 = \left[(\boldsymbol{q}_1 - \boldsymbol{q}_2)^T \boldsymbol{K}_{1q} (\boldsymbol{q}_1 - \boldsymbol{q}_2)\right]^{1/2} . \end{aligned} \tag{46}$$

Now, requirements for the mapping function in Eq. 42 to be a contraction mapping will be determined. Applying definition 1 of the contraction mapping to Eq. 42,

$$\|\boldsymbol{P}(\boldsymbol{q}_2) - \boldsymbol{P}(\boldsymbol{q}_1)\|_K \leq \rho \|\boldsymbol{q}_2 - \boldsymbol{q}_1\|_K \tag{47}$$

must hold for any $\boldsymbol{q}_1$ and $\boldsymbol{q}_2$, with some $\rho \in [0, 1)$. Since the mapping $\boldsymbol{P}(\boldsymbol{q})$, for specific motor angles $\boldsymbol{\theta}_0$, at $\boldsymbol{q}_2$ is related to the value at $\boldsymbol{q}_1$ by

$$\begin{aligned} \boldsymbol{P}(\boldsymbol{q}_2) &= \boldsymbol{P}(\boldsymbol{q}_1) + \int_{\boldsymbol{q}_1}^{\boldsymbol{q}_2} \frac{\partial \boldsymbol{P}(\boldsymbol{q})}{\partial \boldsymbol{q}} d\boldsymbol{q} \\ &= \boldsymbol{P}(\boldsymbol{q}_1) - \int_{\boldsymbol{q}_1}^{\boldsymbol{q}_2} \boldsymbol{K}_{1q}^{-1} \frac{\partial \boldsymbol{h}(\boldsymbol{q})}{\partial \boldsymbol{q}} d\boldsymbol{q}. \end{aligned}$$

Manipulate the expression to suit Eq. 47 as

$$\begin{aligned} \boldsymbol{U}(\boldsymbol{P}(\boldsymbol{q}_2) - \boldsymbol{P}(\boldsymbol{q}_1)) &= -\int_{\boldsymbol{q}_1}^{\boldsymbol{q}_2} \boldsymbol{U}\boldsymbol{K}_{1q}^{-1} \frac{\partial \boldsymbol{h}(\boldsymbol{q})}{\partial \boldsymbol{q}} d\boldsymbol{q} \\ &= -\int_{\boldsymbol{q}_1}^{\boldsymbol{q}_2} \boldsymbol{U}^{-T} \frac{\partial \boldsymbol{h}(\boldsymbol{q})}{\partial \boldsymbol{q}} \boldsymbol{U}^{-1} d\boldsymbol{U}\boldsymbol{q}. \end{aligned}$$

One can thus conclude as follow about the K-norm of the mapping difference;

$$\begin{aligned} \|\boldsymbol{U}(\boldsymbol{P}(\boldsymbol{q}_2) - \boldsymbol{P}(\boldsymbol{q}_1))\|_2 &\leq \sup_{\forall \boldsymbol{q} \in \mathbb{R}^p} \left\|\boldsymbol{U}^{-T} \frac{\partial \boldsymbol{h}(\boldsymbol{q})}{\partial \boldsymbol{q}} \boldsymbol{U}^{-1}\right\|_2 \|\boldsymbol{U}(\boldsymbol{q}_2 - \boldsymbol{q}_1)\|_2 , \\ \|\boldsymbol{P}(\boldsymbol{q}_2) - \boldsymbol{P}(\boldsymbol{q}_1)\|_K &\leq \sup_{\forall \boldsymbol{q} \in \mathbb{R}^p} \left\|\frac{\partial \boldsymbol{h}(\boldsymbol{q})}{\partial \boldsymbol{q}}\right\|_K \|\boldsymbol{q}_2 - \boldsymbol{q}_1\|_K . \end{aligned} \tag{48}$$

Therefore, the mapping $\boldsymbol{P}(\boldsymbol{q})$ will be a contraction mapping if

$$\sup_{\forall \boldsymbol{q} \in \mathbb{R}^p} \left\| \frac{\partial \boldsymbol{h}(\boldsymbol{q})}{\partial \boldsymbol{q}} \right\|_K < \|\boldsymbol{K}_{1q}\|_K = 1. \tag{49}$$

Physically, it means the effective joint stiffness of the transmission must be larger than the joint stiffness induced by the gravity and the desired compliant forces. This implies the transmission stiffness is capable of preventing the robot 'after-the-joint' motion caused by its own weight and the position-mismatch induced compliant force. Consequently, the robot structure should be lightweight enough and the desired end effector stiffness should not be too high, otherwise the effective joint stiffness must be very stiff. With the condition of Eq. 49 and recalling Eq. 40, the computation converges to the stationary link angles for any starting iteration value.

The result may be generalized to the nonlinear stiffness case. It can be stated in a similar vein that the condition for the recursive evaluation of Eq. 41 to converge to the stationary link angles is

$$\sup_{\forall \boldsymbol{q} \in \mathbb{R}^p} \left\| \frac{\partial \boldsymbol{h}(\boldsymbol{q})}{\partial \boldsymbol{q}} \right\|_K < 1, \tag{50}$$

for which the vector norm and the matrix norm are defined as

$$\|\boldsymbol{q}\|_K = \|\boldsymbol{U}\boldsymbol{q}\|_2 \tag{51}$$

and

$$\|\boldsymbol{A}\|_K = \left\| \boldsymbol{U}^{-T} \boldsymbol{A} \boldsymbol{U}^{-1} \right\|_2. \tag{52}$$

Relevant scaling matrix $\boldsymbol{U}$ is chosen to satisfy

$$\boldsymbol{U}^T \boldsymbol{U} = \inf_{\forall \boldsymbol{\delta}_{1q} \in \mathbb{R}^p} \frac{\partial \boldsymbol{e}_{1q}(\boldsymbol{\delta}_{1q})}{\partial \boldsymbol{\delta}_{1q}}, \tag{53}$$

indicating the deformation-dependent nonlinear effective stiffness of the drivetrain.

3.3. Estimation of the Transmitted Torque

Desired task space impedance behavior has the mechanical analogy of a mass connected to a parallel spring/damper unit. This simple system is hardly achieved in practice because the unavoidable dynamics of the robot and the drivetrain intervene in the interaction of the, e.g. simple PD, controller and the end effector effective mass. Indeed, this is fundamental and any presented control scheme is devised to ultimately alleviate the problem. Even better, mechanical system should be designed, in the first place, to possess clean dynamics. Lightweight and stiff structural properties are some indications of such good system dynamics.

Motor inertia is a parameter that can deteriorate the desired impedance. It is especially important for the system that employs high transmission ratio since the effective motor inertia at the far end of the mechanism is the motor inertia amplified by square of the transmission ratio. [21] firstly showed that the implication of a force feedback controller is to reduce the effective mass of the system. [9]

applied this means by feeding back the joint torque to reduce the reflected motor inertia. Inertia reduction also has a merit of reducing the motor frictional torque.

The robot system in this work, and in general, is not equipped with the joint torque sensors or the accelerometers. Transmitted torques must therefore be estimated. They may be calculated based on its dynamical equation and the method of variational integrator [22]. In brief, this method numerically solves the system of differential equations with the principle of energy conservation enforced. The approach discretizes the system right at the beginning of formulating the Lagrangian and applying the variational principle, rather than at the system differential equations.

Consider the drivetrain dynamics in Eq. 13. Estimation of the transmitted torques at every stage, $\boldsymbol{e}(\boldsymbol{\theta})$ in Eq. 16, is of interest. Unfortunately, generalized coordinates of all rotor angles, not their stationary values developed in subsection 3.1 and 3.2, are not available for the integrator equations. Hence, it is not possible to estimate $\boldsymbol{e}(\boldsymbol{\theta})$ for multi-stage drivetrain system. Rather, let us consider the equations of the first stage of the transmission system which may be written as

$$\boldsymbol{B}_1\ddot{\boldsymbol{\theta}}_0 + \boldsymbol{C}_1\dot{\boldsymbol{\theta}}_0 + \boldsymbol{\tau}_1 = \boldsymbol{\tau}_m. \tag{54}$$

$\boldsymbol{\theta}_0$ is the vector of motor angles that are measurable. $\boldsymbol{B}_1$ is the diagonal matrix of the motors' inertia. Loss in a typical DC motor may be governed by a constant viscous damping coefficient depicted with the diagonal matrix $\boldsymbol{C}_1$. $\boldsymbol{\tau}_m$ is the actual torque generated from the electromagnetic induction force, of which the value can be deduced from the motor current by Eq. 22. The last term $\boldsymbol{\tau}_1$ represents the transmitted torque at the inport from the motor to the first stage of the transmission subsystem. Its value is governed by the elastic network at the first stage according to the first element of the elastic force vector function in Eq. 16. Here, $\boldsymbol{\tau}_1$ will be estimated for which it may then be used to modulate the motor inertia $\boldsymbol{B}_1$, as will be explained in subsection 3.5. Note again that knowledge of $\boldsymbol{e}(\boldsymbol{\theta})$ is necessary to modify the whole inertia matrix of the drivetrain, $\boldsymbol{B}$.

Discrete form of Eq. 54 may be obtained by considering the variation of the discrete integral of the Lagrangian over a time interval. If $\boldsymbol{\tau}_1$ is treated as the output torque, mechanical Lagrangian of the motor system will be due solely to the kinetic energy

$$\mathcal{L}\left(\boldsymbol{\theta}_0, \dot{\boldsymbol{\theta}}_0\right) = \frac{1}{2}\dot{\boldsymbol{\theta}}_0^T \boldsymbol{B}_1 \dot{\boldsymbol{\theta}}_0.$$

Integral of the Lagrangian during a sampling period h (called discrete Lagrangian in [22]) may be approximated as

$$\begin{aligned}\mathcal{L}_d\left(\boldsymbol{\theta}_{0k}, \boldsymbol{\theta}_{0(k+1)}, h\right) &= h\mathcal{L}\left(\frac{\boldsymbol{\theta}_{0k} + \boldsymbol{\theta}_{0(k+1)}}{2}, \frac{\boldsymbol{\theta}_{0(k+1)} - \boldsymbol{\theta}_{0k}}{h}\right) \\ &= \frac{1}{2h}\left(\boldsymbol{\theta}_{0(k+1)} - \boldsymbol{\theta}_{0k}\right)^T \boldsymbol{B}_1 \left(\boldsymbol{\theta}_{0(k+1)} - \boldsymbol{\theta}_{0k}\right)\end{aligned}$$

Conditions which nullify the variation of $\mathcal{L}_d(\cdot)$ leads to the equations of motion. In other words, equations of motion will minimize the integral action. It is shown in [22] that such conditions yield

the discrete Euler-Lagrange (DEL) formulation. However, the motor mechanical system according to Eq. 54 is the forced system. Therefore the original DEL formulation must be modified to cope with the approximated impulse at the k^{th}-sampling as

$$\boldsymbol{D}_1\mathcal{L}_d\left(\boldsymbol{\theta}_{0k},\boldsymbol{\theta}_{0(k+1)}\right)+\boldsymbol{D}_2\mathcal{L}_d\left(\boldsymbol{\theta}_{0(k-1)},\boldsymbol{\theta}_{0k}\right)+\boldsymbol{I}_d^+\left(\boldsymbol{\theta}_{0(k-1)},\boldsymbol{\theta}_{0k}\right)+\boldsymbol{I}_d^-\left(\boldsymbol{\theta}_{0k},\boldsymbol{\theta}_{0(k+1)}\right)=0. \tag{55}$$

In this formulation, $\boldsymbol{D}_1\mathcal{L}_d(\cdot)$ and $\boldsymbol{D}_2\mathcal{L}_d(\cdot)$ are the partial derivative of $\mathcal{L}_d$ with respect to the first and second argument, respectively. $\boldsymbol{I}_d^+(\cdot)+\boldsymbol{I}_d^-(\cdot)$ is a two-point quadrature that approximate the impulse of the external force $\boldsymbol{F}(t)$ at the k^{th}-sampling:

$$\boldsymbol{I}_d^+\left(\boldsymbol{\theta}_{0(k-1)},\boldsymbol{\theta}_{0k}\right)+\boldsymbol{I}_d^-\left(\boldsymbol{\theta}_{0k},\boldsymbol{\theta}_{0(k+1)}\right)\approx\int_{(t_{k-1}+t_k)/2}^{(t_k+t_{k+1})/2}\boldsymbol{F}(\xi)\,d\xi.$$

Specifically,

$$\boldsymbol{I}_d^+\left(\boldsymbol{\theta}_{0(k-1)},\boldsymbol{\theta}_{0k}\right)=\frac{h}{2}\boldsymbol{F}\left(\frac{\boldsymbol{\theta}_{0(k-1)}+\boldsymbol{\theta}_{0k}}{2}\right)$$

and

$$\boldsymbol{I}_d^-\left(\boldsymbol{\theta}_{0k},\boldsymbol{\theta}_{0(k+1)}\right)=\frac{h}{2}\boldsymbol{F}\left(\frac{\boldsymbol{\theta}_{0k}+\boldsymbol{\theta}_{0(k+1)}}{2}\right).$$

From Eq. 54, external force of the motor mechanical system is

$$\boldsymbol{F}(t)=\boldsymbol{\tau}_m-\boldsymbol{\tau}_1-\boldsymbol{C}_1\dot{\boldsymbol{\theta}}_0.$$

Its value at the inter-sampling point $\frac{\boldsymbol{\theta}_{0(k-1)}+\boldsymbol{\theta}_{0k}}{2}$ and $\frac{\boldsymbol{\theta}_{0k}+\boldsymbol{\theta}_{0(k+1)}}{2}$ may be expressed as

$$\boldsymbol{F}\left(\frac{\boldsymbol{\theta}_{0(k-1)}+\boldsymbol{\theta}_{0k}}{2}\right)=\boldsymbol{K}_\tau\left(\frac{\boldsymbol{i}_{k-1}+\boldsymbol{i}_k}{2}\right)-\boldsymbol{\tau}_{1k}-\boldsymbol{C}_1\left(\frac{\boldsymbol{\theta}_{0k}-\boldsymbol{\theta}_{0(k-1)}}{h}\right)$$

and

$$\boldsymbol{F}\left(\frac{\boldsymbol{\theta}_{0k}+\boldsymbol{\theta}_{0(k+1)}}{2}\right)=\boldsymbol{K}_\tau\left(\frac{\boldsymbol{i}_k+\boldsymbol{i}_{k+1}}{2}\right)-\boldsymbol{\tau}_{1(k+1)}-\boldsymbol{C}_1\left(\frac{\boldsymbol{\theta}_{0(k+1)}-\boldsymbol{\theta}_{0k}}{h}\right),$$

where the backward Euler integration method is employed. Evaluate each term in the forced-DEL formulation Eq. 55. After the substitution and simplification, the discretized version of Eq. 54,

$$\begin{aligned}\frac{1}{h}\boldsymbol{B}_1\left(\boldsymbol{\theta}_{0(k+1)}-2\boldsymbol{\theta}_{0k}+\boldsymbol{\theta}_{0(k-1)}\right)&\\ +\frac{1}{2}\boldsymbol{C}_1\left(\boldsymbol{\theta}_{0(k+1)}-\boldsymbol{\theta}_{0(k-1)}\right)+\frac{h}{2}\left(\boldsymbol{\tau}_{1k}+\boldsymbol{\tau}_{1(k+1)}\right)&=\frac{h}{4}\boldsymbol{K}_\tau\left(\boldsymbol{i}_{k-1}+2\boldsymbol{i}_k+\boldsymbol{i}_{k+1}\right),\end{aligned} \tag{56}$$

is obtained. Consequently, the up-to-date transmitted torque from the motor to the first stage of the drivetrain, $\boldsymbol{\tau}_{1(k+1)}$, may be estimated.

3.4. Estimation of the Link Joint Velocity

In subsection 3.5, energy dissipation is introduced in the impedance controller by the damping force which involves the velocity term that typically cannot be directly measured. Therefore, estimation of the link joint velocity must be utilized. Since the link angles are not avaiable, the observer for their

velocities cannot be formulated. Rather, the nonmodel-based first order differentiation filter will be employed to estimate the link joint velocity from the motor angles.

Concretely, for the set point impedance controller proposed in Eq. 79, the velocity related term $\boldsymbol{\vartheta}$ is the estimated link joint velocity scaled by the square root of the joint space symmetric damping matrix;

$$\boldsymbol{\vartheta} = s\boldsymbol{G}(s)\left[J(\boldsymbol{\theta}_{qs})^T \boldsymbol{D}_d(\boldsymbol{f}(\boldsymbol{\theta}_{qs}))J(\boldsymbol{\theta}_{qs})\right]^{1/2}\boldsymbol{T}_{q1}\boldsymbol{\theta}_0, \tag{57}$$

in which the estimated link angles are obtained from $\boldsymbol{T}_{q1}\boldsymbol{\theta}_0$ rather than $\boldsymbol{\theta}_{qs}$ to secure the stability of the system. s represents the complex argument of the Laplace transform. $\boldsymbol{G}(s)$ is a diagonal matrix of which its diagonal terms are identical and be a strictly proper and strictly positive real (SPR) filtering transfer function. The scaling matrix may be computed through the singular value decomposition (SVD). Namely, the joint space symmetric damping matrix (arguments omitted) may be expressed as

$$J^T\boldsymbol{D}_dJ = \boldsymbol{U}\boldsymbol{\Sigma}\boldsymbol{U}^T,$$

for some orthogonal matrix $\boldsymbol{U}$ and a diagonal matrix $\boldsymbol{\Sigma}$ containing the singular values of $J^T\boldsymbol{D}_dJ$. Then the square root of the joint space damping matrix can be computed as

$$\left[J^T\boldsymbol{D}_dJ\right]^{1/2} = \boldsymbol{U}\boldsymbol{\Sigma}^{1/2}\boldsymbol{U}^T, \tag{58}$$

where the elements in the diagonal matrix $\boldsymbol{\Sigma}^{1/2}$ are the square root of the paired values in $\boldsymbol{\Sigma}$. For convenience, this square root matrix will now be denoted as $\sqrt{\boldsymbol{K}_v}$. Note that Eq. 57 may be understood as a filtering of the time derivative of the estimated link angles, i.e.

$$\boldsymbol{\vartheta} = \boldsymbol{G}(s)\sqrt{\boldsymbol{K}_v}\boldsymbol{T}_{q1}\dot{\boldsymbol{\theta}}_0. \tag{59}$$

From the linear system theory, the above filtering system may be represented in either the input-output transfer function $\boldsymbol{G}(s)$ form or the minimal realization state space $\{\boldsymbol{A}, \boldsymbol{B}, \boldsymbol{C}\}$ form. Hence for this filtering, one may write

$$\begin{aligned}\dot{\boldsymbol{x}} &= \boldsymbol{A}\boldsymbol{x} + \boldsymbol{B}\sqrt{\boldsymbol{K}_v}\boldsymbol{T}_{q1}\dot{\boldsymbol{\theta}}_0 \\ \boldsymbol{\vartheta} &= \boldsymbol{C}\boldsymbol{x},\end{aligned} \tag{60}$$

where $\boldsymbol{G}(s) = \boldsymbol{C}(s\boldsymbol{I} - \boldsymbol{A})^{-1}\boldsymbol{B}$ and $\boldsymbol{x}$ is the filter states. Furthermore, by recognizing the Kalman-Yakubovich (KY) lemma [24], since $\boldsymbol{G}(s)$ is a strictly proper and SPR, there exists symmetric positive definite matrices $\boldsymbol{P}$ and $\boldsymbol{Q}$ such that

$$\boldsymbol{A}^T\boldsymbol{P} + \boldsymbol{P}\boldsymbol{A} = -\boldsymbol{Q} \tag{61}$$

$$\boldsymbol{B}^T\boldsymbol{P} = \boldsymbol{C}. \tag{62}$$

Because the specified constant Cartesian set point $\boldsymbol{x}_d$ is associated with the constant target motor angles $\boldsymbol{\theta}_{0d}$, Eq. 60 may be written as

$$\dot{\boldsymbol{x}} = \boldsymbol{A}\boldsymbol{x} + \boldsymbol{B}\sqrt{\boldsymbol{K}_v}\boldsymbol{T}_{q1}\dot{\tilde{\boldsymbol{\theta}}}_0, \tag{63}$$

where the error $\tilde{\boldsymbol{\theta}}_0 = \boldsymbol{\theta}_0 - \boldsymbol{\theta}_{0d}$ is defined. Moreover, let us define a new state vector $\boldsymbol{z}$ such that $\dot{\boldsymbol{z}} = \boldsymbol{x}$ holds. Explicitly,

$$\boldsymbol{z} = \boldsymbol{A}^{-1}\left(\boldsymbol{x} - \boldsymbol{B}\sqrt{\boldsymbol{K}_v}\boldsymbol{T}_{q1}\tilde{\boldsymbol{\theta}}_0\right). \tag{64}$$

As a result, the state space representation of the system in Eq. 57, of which the input is now the tracking error $\tilde{\boldsymbol{\theta}}_0$, may be written as

$$\begin{aligned} \dot{\boldsymbol{z}} &= \boldsymbol{A}\boldsymbol{z} + \boldsymbol{B}\sqrt{\boldsymbol{K}_v}\boldsymbol{T}_{q1}\tilde{\boldsymbol{\theta}}_0 \\ \boldsymbol{\vartheta} &= \boldsymbol{C}\boldsymbol{A}\boldsymbol{z} + \boldsymbol{C}\boldsymbol{B}\sqrt{\boldsymbol{K}_v}\boldsymbol{T}_{q1}\tilde{\boldsymbol{\theta}}_0. \end{aligned} \tag{65}$$

This form will be helpful in the stability analysis. At the moment, it is in doubt whether the usage of such velocity estimation in the impedance controller will lead to satisfactory result. Indeed, while $\boldsymbol{G}(s)$ is SPR, the positive real (PR) and hence the stability of $s\boldsymbol{G}(s)$ in general cannot be concluded. This issue is deferred to subsection 3.6 where the stability and passivity of the controlled system will be proven.

3.5. Impedance Controller

In this subsection, impedance controller for controlling the nonlinear flexible joint robot system using the computed stationary link angles and the estimation of the transmitted torques and link angular velocities, as described in the previous subsections, will be developed. It is assumed that the robot system is equipped with a higher-decision making unit which provides the end effector set point $\boldsymbol{x}_d$ and the task space symmetric positive definite constant stiffness matrix $\boldsymbol{K}_d$ appropriate for executing a task at hand.

Generally, mechanical impedance consists of three main parameters, i.e. the inertance, the resistance, and the compliance. The objective of the impedance controller is then to modulate the effective impedance parameters of the system to the desired values. However, it has been shown in [23], for example, that adjusting the inertance has a severe drawback of destroying the passivity of the controlled system. This is a sign indicating that the robot system may become unstable during the interaction with the passive environment. Consequently, the desired impedance dynamics subject to the external force applied at the robot end effector, $\boldsymbol{F}_{ext}$, is chosen as

$$\boldsymbol{\Lambda}(\boldsymbol{x})\ddot{\tilde{\boldsymbol{x}}} + (\boldsymbol{\mu}(\boldsymbol{x}, \dot{\boldsymbol{x}}) + \boldsymbol{D}_d)\dot{\tilde{\boldsymbol{x}}} + \boldsymbol{K}_d\tilde{\boldsymbol{x}} = \boldsymbol{F}_{ext}. \tag{66}$$

The equation is written in the task space coordinates $\boldsymbol{x}$, for which $\tilde{\boldsymbol{x}}$ denotes the coordinate errors of the end effector frame from the set point values, i.e. $\tilde{\boldsymbol{x}} = \boldsymbol{x} - \boldsymbol{x}_d$. $\boldsymbol{\Lambda}(\boldsymbol{x})$ and $\boldsymbol{\mu}(\boldsymbol{x}, \dot{\boldsymbol{x}})$ are the transformed inertia and Coriolis/centrifugal matrices in the task space coordinates. They are related to the parameters in joint space coordinates $\boldsymbol{q}$ by

$$\boldsymbol{\Lambda}(\boldsymbol{x}) = J(\boldsymbol{q})^{-T}\boldsymbol{M}(\boldsymbol{q})J(\boldsymbol{q})^{-1} \tag{67}$$

and

$$\boldsymbol{\mu}(\boldsymbol{x},\dot{\boldsymbol{x}}) = J(\boldsymbol{q})^{-T}\left(\boldsymbol{C}(\boldsymbol{q},\dot{\boldsymbol{q}}) - \boldsymbol{M}(\boldsymbol{q})J(\boldsymbol{q})^{-1}\dot{J}(\boldsymbol{q})\right)J(\boldsymbol{q})^{-1} \tag{68}$$

with $\boldsymbol{q} = \boldsymbol{f}^{-1}(\boldsymbol{x})$ and $\dot{\boldsymbol{q}} = J\left(\boldsymbol{f}^{-1}(\boldsymbol{x})\right)^{-1}\dot{\boldsymbol{x}}$ through the inverse kinematics mapping and its differential relationship. Note the existence of $\boldsymbol{\mu}(\boldsymbol{x},\dot{\boldsymbol{x}})$ in the desired impedance dynamics to preserve the passivity of the system. In essence, natural dynamics of the robot has been exploited.

$\boldsymbol{D}_d$ is the task space damping matrix that asymptotically stabilizes the system. Its value will be designed, according to the current values of $\boldsymbol{\Lambda}(\boldsymbol{x})$ and $\boldsymbol{K}_d$, to make the system response be appropriately damped with the specified damping ratio. To accomplish this, first, Eq. 66 is approximated by

$$\boldsymbol{\Lambda}(\boldsymbol{x})\ddot{\tilde{\boldsymbol{x}}} + \boldsymbol{D}_d(\boldsymbol{x})\dot{\tilde{\boldsymbol{x}}} + \boldsymbol{K}_d\tilde{\boldsymbol{x}} = \boldsymbol{F}_{ext}, \tag{69}$$

where the Coriolis/centrifugal matrix is neglected. Introduce the following linear transformation of the coordinate errors;

$$\boldsymbol{z} = \boldsymbol{Q}(\boldsymbol{x})^{-1}\tilde{\boldsymbol{x}}. \tag{70}$$

The transformation matrix $\boldsymbol{Q}(\boldsymbol{x})$, treated constant for a particular stationary point, is the matrix where its columns are the eigenvectors $\boldsymbol{u}_i$ of the generalized eigenproblem

$$\left(\boldsymbol{K}_d - \omega_{ni}^2\boldsymbol{\Lambda}(\boldsymbol{x})\right)\boldsymbol{u}_i = 0, \tag{71}$$

where both $\boldsymbol{\Lambda}(\boldsymbol{x})$ and $\boldsymbol{K}_d$ are symmetric positive definite matrices. Premultiplying Eq. 69 with $\boldsymbol{Q}(\boldsymbol{x})^T$ and writing the equation in the new transformed coordinates lead to

$$\boldsymbol{Q}(\boldsymbol{x})^T\boldsymbol{\Lambda}(\boldsymbol{x})\boldsymbol{Q}(\boldsymbol{x})\ddot{\boldsymbol{z}} + \boldsymbol{Q}(\boldsymbol{x})^T\boldsymbol{D}_d(\boldsymbol{x})\boldsymbol{Q}(\boldsymbol{x})\dot{\boldsymbol{z}} + \boldsymbol{Q}(\boldsymbol{x})^T\boldsymbol{K}_d\boldsymbol{Q}(\boldsymbol{x})\boldsymbol{z} = \boldsymbol{Q}(\boldsymbol{x})^T\boldsymbol{F}_{ext}. \tag{72}$$

The eigenvectors in $\boldsymbol{Q}(\boldsymbol{x})$ may be normalized such that

$$\boldsymbol{Q}(\boldsymbol{x})^T\boldsymbol{\Lambda}(\boldsymbol{x})\boldsymbol{Q}(\boldsymbol{x}) = \boldsymbol{I} \tag{73}$$

holds. Consequently, the transformed stiffness matrix will become

$$\boldsymbol{Q}(\boldsymbol{x})^T\boldsymbol{K}_d\boldsymbol{Q}(\boldsymbol{x}) = \boldsymbol{\Sigma}(\boldsymbol{x}). \tag{74}$$

Diagonoal matrix $\boldsymbol{\Sigma}(\boldsymbol{x})$ is known in vibration terminology [27] as the spectral matrix containing the square of the natural frequencies ω_{ni}^2, or the generalized eigenvalues of $\boldsymbol{K}_d$ with respect to $\boldsymbol{\Lambda}(\boldsymbol{x})$ of the generalized eigenproblem Eq. 71. The transformed equation may thus be written as

$$\ddot{\boldsymbol{z}} + \boldsymbol{Q}(\boldsymbol{x})^T\boldsymbol{D}_d(\boldsymbol{x})\boldsymbol{Q}(\boldsymbol{x})\dot{\boldsymbol{z}} + \boldsymbol{\Sigma}(\boldsymbol{x})\boldsymbol{z} = \boldsymbol{Q}(\boldsymbol{x})^T\boldsymbol{F}_{ext}. \tag{75}$$

If the damping matrix is designed to be

$$\boldsymbol{D}_d(\boldsymbol{x}) = 2\boldsymbol{Q}(\boldsymbol{x})^{-T}\boldsymbol{\xi}\boldsymbol{\Sigma}(\boldsymbol{x})^{1/2}\boldsymbol{Q}(\boldsymbol{x})^{-1}, \tag{76}$$

where $\boldsymbol{\Sigma}(\boldsymbol{x})^{1/2}$ denotes the diagonal matrix of which its diagonal elements are the square root of the paired values in $\boldsymbol{\Sigma}(\boldsymbol{x})$. The diagonal damping ratio matrix $\boldsymbol{\xi}$ is used to adjust the oscillatory behavior of the response. Through this choice of damping matrix, the transformed equation may finally be written as

$$\ddot{\boldsymbol{z}} + 2\boldsymbol{\xi}\boldsymbol{\Sigma}(\boldsymbol{x})^{1/2}\dot{\boldsymbol{z}} + \boldsymbol{\Sigma}(\boldsymbol{x})\boldsymbol{z} = \boldsymbol{Q}(\boldsymbol{x})^T \boldsymbol{F}_{ext} \tag{77}$$

as a set of p-decoupled second order linear time invariant differential equations. It is evident that the response of each decoupled coordinate z_i is described by the damping factor ξ_i and the natural frequency ω_{ni} of the i^{th}-element of $\boldsymbol{\Sigma}(\boldsymbol{x})^{1/2}$.

In this work, the impedance control problem is constrained to only the constant set point case. This implies $\dot{\boldsymbol{x}}_d = \boldsymbol{0}$ and $\ddot{\boldsymbol{x}}_d = \boldsymbol{0}$. According to the robot dynamics Eq. 1, the desired impedance dynamics may be achieved with the control law

$$\boldsymbol{\tau}^*_{dr} = \boldsymbol{g}(\boldsymbol{q}) - J(\boldsymbol{q})^T \left(\boldsymbol{K}_d\tilde{\boldsymbol{x}} + \boldsymbol{D}_d\dot{\boldsymbol{x}}\right), \tag{78}$$

where the star-mark is used here to denote the desired torque transmitted to the robot. The actual one deviates from the desired value due to the uncompensated motor and drivetrain dynamics. Unfortunately, the link angles and the end effector coordinates are not measurable directly. Intuitively, their estimated values shall be used. This results in the modified control law

$$\begin{aligned}\boldsymbol{\tau}^*_{dr} &= \boldsymbol{g}(\boldsymbol{\theta}_{qs}) - J(\boldsymbol{\theta}_{qs})^T \boldsymbol{K}_d\left(\boldsymbol{f}(\boldsymbol{\theta}_{qs}) - \boldsymbol{x}_d\right) - \left[J(\boldsymbol{\theta}_{qs})^T \boldsymbol{D}_d\left(\boldsymbol{f}(\boldsymbol{\theta}_{qs})\right) J(\boldsymbol{\theta}_{qs})\right]^{1/2}\boldsymbol{\vartheta} \\ &= \boldsymbol{h}(\boldsymbol{\theta}_{qs}) - \left[J(\boldsymbol{\theta}_{qs})^T \boldsymbol{D}_d\left(\boldsymbol{f}(\boldsymbol{\theta}_{qs})\right) J(\boldsymbol{\theta}_{qs})\right]^{1/2}\boldsymbol{\vartheta},\end{aligned} \tag{79}$$

where the stationary link angle and the velocity term from Eqs. 41 and 57 are employed. Passivity and stability of the proposed controller will be given in the next subsection.

Since the robot is actuated indirectly by the motor torques through the flexible transmission subsystem, desirable torques applied at the robot joints according to Eq. 79 must be mapped to the space of the motor torques. Due to the lack of the complete system states information, as a result, degenerated stationary model of the drivetrain system shall be used to compute such motor torques. In particular, as demonstrated in Eq. 28,

$$(\boldsymbol{\tau}_m)^*_{dr} = \boldsymbol{T}_1^T\boldsymbol{T}_2^T\cdots\boldsymbol{T}_{q-1}^T\boldsymbol{T}_q^T\boldsymbol{\tau}^*_{dr}. \tag{80}$$

As described in subsection 3.3, transmitted torque may be used to improve the system dynamics so the response from applying the simple control law, which neglects the transmission dynamics, of Eqs. 79 and 80 to the actual system will be closer to the one with ideal transmission. Specifically, negative feedback of the estimated transmitted torque $\hat{\boldsymbol{\tau}}_1$ from Eq. 56 may be used to reduce the motors' inertia from $\boldsymbol{B}_1$ to $\boldsymbol{B}_{1r}$ by correcting the reference motor torque $(\boldsymbol{\tau}_m)^*_{dr}$ to

$$\boldsymbol{\tau}^*_m = \boldsymbol{B}_1\boldsymbol{B}_{1r}^{-1}(\boldsymbol{\tau}_m)^*_{dr} + \left(\boldsymbol{I} - \boldsymbol{B}_1\boldsymbol{B}_{1r}^{-1}\right)\hat{\boldsymbol{\tau}}_1. \tag{81}$$

The resulting system dynamics of the first stage of the drivetrain becomes

$$\boldsymbol{B}_{1r}\ddot{\boldsymbol{\theta}}_0 + \boldsymbol{B}_{1r}\boldsymbol{B}_1^{-1}\boldsymbol{C}_1\dot{\boldsymbol{\theta}}_0 + \boldsymbol{\tau}_1 = (\boldsymbol{\tau}_m)_{dr}^*\,, \tag{82}$$

if the transmitted torque estimation is exact. Effectively, feeding back the transmitted torque will try to equalize it to the reference motor torque; thus making the motor closer to an ideal torque source. This will be advantageous to the current controlled motor. In practice, motor inertia cannot be reduced arbitrarily. Saturation of the motor torque, amplification of the noise, and quantization errors restrict the lower bound of $\boldsymbol{B}_{1r}$.

Lastly, the reference motor torque in Eq. 81 may be attained through the motor torque constant via the current control mode as in Eq. 22 by which the motor, as a whole, is assumed an ideal effort source. Hence one may command the motor current directly. However, this may not be realistic because the motor torque also depends on its velocity as well. Indeed, Eq. 22 holds for the stall torque only. Moreover, this simple linear relationship does not take the current dynamics of Eq. 21 into consideration. Although the time constant of the electrical system is faster than the coupled-mechanical one, its dynamics is still be significant if the high performance motion system is the goal.

Regarding with the reference motor torque, reference value of the motor current can be calculated from

$$\boldsymbol{i}_m = \boldsymbol{K}_\tau^{-1}\boldsymbol{\tau}_m^*. \tag{83}$$

For the voltage control mode, the actual motor current $\boldsymbol{i}$ is controlled to track the reference value indirectly via the motor voltage. According to Eq. 21, one may choose the dynamical behavior of the current tracking error, $\boldsymbol{e}_i = \boldsymbol{i} - \boldsymbol{i}_m$, to be

$$\boldsymbol{L}\dot{\boldsymbol{e}}_i + \boldsymbol{K}_c\boldsymbol{e}_i = \boldsymbol{0} \tag{84}$$

where $\boldsymbol{K}_c$ is the tunable constant diagonal matrix of the positive gains for the tracking responsiveness. To this end, the control input vector of the motor voltages must be

$$\boldsymbol{u} = \boldsymbol{L}\dot{\boldsymbol{i}}_m + \boldsymbol{R}\boldsymbol{i} + \boldsymbol{K}_b\dot{\boldsymbol{\theta}}_0 - \boldsymbol{K}_c\,(\boldsymbol{i} - \boldsymbol{i}_m) \tag{85}$$

that relies on the exact cancellation of the motor current and angular velocity terms. If this is not realizable, the following current tracking second-order error dynamics

$$\boldsymbol{L}\ddot{\boldsymbol{e}}_i + \boldsymbol{K}_c\dot{\boldsymbol{e}}_i + \boldsymbol{K}_b\boldsymbol{B}_1^{-1}\boldsymbol{K}_b\boldsymbol{e}_i = \boldsymbol{0}, \tag{86}$$

may be chosen instead. Here, $\boldsymbol{K}_c$ is the constant diagonal matrix of the positive gains to regulate the damping characteristics and $\boldsymbol{K}_b$ is the diagonal matrix of the back-emf constants of the motors, as before. It can be shown that the following control input vector

$$\boldsymbol{u} = \boldsymbol{L}\dot{\boldsymbol{i}}_m + \boldsymbol{R}\boldsymbol{i} + \boldsymbol{K}_b\boldsymbol{B}_1^{-1}\int_{t_i}^{t}(\boldsymbol{K}_b\boldsymbol{i}_m - \hat{\boldsymbol{\tau}}_{1cs})\,dt - \boldsymbol{K}_c\,(\boldsymbol{i} - \boldsymbol{i}_m) \tag{87}$$

shapes the closed loop dynamics to Eq. 86. In the equation, $\hat{\boldsymbol{\tau}}_{1cs}$ is the estimated value of $\boldsymbol{C}_1\dot{\boldsymbol{\theta}}_0 + \boldsymbol{\tau}_1$ in Eq. 54. It is determined by solving for $\boldsymbol{\tau}_{1cs(k+1)}$ in the following equation:

$$\frac{1}{h}\boldsymbol{B}_1\left(\boldsymbol{\theta}_{0(k+1)} - 2\boldsymbol{\theta}_{0k} + \boldsymbol{\theta}_{0(k-1)}\right) + \frac{h}{2}\left(\boldsymbol{\tau}_{1csk} + \boldsymbol{\tau}_{1cs(k+1)}\right) = \frac{h}{4}\boldsymbol{K}_\tau\left(\boldsymbol{i}_{k-1} + 2\boldsymbol{i}_k + \boldsymbol{i}_{k+1}\right). \tag{88}$$

In summary, captured in Fig. 3, task space impedance controller of a nonlinear flexible-joint robot system, Eq. 79, is proposed based on the stationary link angles and the velocity term according to Eq. 41 and Eq. 57, respectively. The controller allows the user to specify the desired compliance and dissipation characteristics at a set point. Then the appropriate task space damping matrix is computed by means of the matrix factorization as shown in Eq. 76. From the control law of Eq. 79, the required motor torque corresponding to the desirable robot joint torque is calculated via Eq. 80. Additionally, feedback of the estimated transmitted torque from Eq. 56 is employed to relieve the effect of the unmodeled motor inertia. This results in the corrected reference motor torque of Eq. 81. Motor current which yields such torque may be calculated from the simple relationship of Eq. 83 if it is reasonable to model the motor as an ideal torque source. Otherwise, the motor should be controlled at the voltage level where Eq. 85 provides the voltage control law. If the motor angular velocity is not available, Eq. 87 should be applied instead.

3.6. Passivity and Stability Analysis

Stability and passivity of the proposed task space impedance control scheme to the nonlinear flexible-joint robot system will now be analyzed. For this purpose, it is worthy to put an effort on investigating the underlying energy related to the desirable robot joint torque Eq. 79. From the observation, the positional dependent function $\boldsymbol{h}\left(\boldsymbol{\theta}_{qs}\right)$ is the torque component responsible for counterbalancing the robot gravity torque and supplying the desired compliance force, through the network of the flexible transmission elements, under the stationary condition. Therefore, the term $\boldsymbol{h}\left(\boldsymbol{\theta}_{qs}\right)$ must be the differential of some potential energy $V_{\bar{h}}\left(\boldsymbol{\theta}_{qs}\right)$ that is related to the gravitational potential energy of the passive robot and elastic potential energy of the transmission subsystems. Such potential function will be determined.

Note that the function $\boldsymbol{h}\left(\boldsymbol{q}\right)$, where the outport generalized coordinates $\boldsymbol{\theta}_q$ or the robot generalized coordinates $\boldsymbol{q}$ are the function arguments, is the differential of the potential energy

$$V_h\left(\boldsymbol{q}\right) = V_g\left(\boldsymbol{q}\right) - \frac{1}{2}\left(\boldsymbol{x}\left(\boldsymbol{q}\right) - \boldsymbol{x}_d\right)^T \boldsymbol{K}_d\left(\boldsymbol{x}\left(\boldsymbol{q}\right) - \boldsymbol{x}_d\right). \tag{89}$$

Nevertheless, it will be shown that the function $\boldsymbol{h}\left(\boldsymbol{\theta}_{qs}\right)$ is the differential of a different potential energy function, not $V_h\left(\boldsymbol{\theta}_{qs}\right)$, which shall be denoted as $V_{\bar{h}}\left(\boldsymbol{\theta}_{qs}\right)$. Recall the recusive equation 41 used to determine the stationary robot link angles from the motor angles. It may be rewritten as

$$\boldsymbol{T}_{q1}\boldsymbol{\theta}_0 = \boldsymbol{\theta}_{qs} + \boldsymbol{e}_{1q}^{-1}\left(\boldsymbol{h}\left(\boldsymbol{\theta}_{qs}\right)\right) = \boldsymbol{l}_1\left(\boldsymbol{\theta}_{qs}\right). \tag{90}$$

Consider $\boldsymbol{h}(\boldsymbol{\theta}_{qs})$ as the composite function of $\boldsymbol{T}_{q1}\boldsymbol{\theta}_0$ and acknowledge the differential of the potential energy. One then can write

$$\boldsymbol{h}\left(\boldsymbol{l}_1^{-1}\left(\boldsymbol{T}_{q1}\boldsymbol{\theta}_0\right)\right)^T = \frac{\partial V_{\bar{h}}\left(\boldsymbol{T}_{q1}\boldsymbol{\theta}_0\right)}{\partial\left(\boldsymbol{T}_{q1}\boldsymbol{\theta}_0\right)} = \left.\frac{\partial V_{\bar{h}}\left(\boldsymbol{\theta}_{qs}\right)}{\partial\boldsymbol{\theta}_{qs}}\right|_{\boldsymbol{\theta}_{qs}=\boldsymbol{\theta}_{qs}\left(\boldsymbol{T}_{q1}\boldsymbol{\theta}_0\right)} \times \frac{\partial\boldsymbol{\theta}_{qs}\left(\boldsymbol{T}_{q1}\boldsymbol{\theta}_0\right)}{\partial\left(\boldsymbol{T}_{q1}\boldsymbol{\theta}_0\right)}. \tag{91}$$

In the following, $\frac{\partial\boldsymbol{\theta}_{qs}\left(\boldsymbol{T}_{q1}\boldsymbol{\theta}_0\right)}{\partial\left(\boldsymbol{T}_{q1}\boldsymbol{\theta}_0\right)}$ will be determined first. Differentiate Eq. 90 with respect to $\boldsymbol{\theta}_{qs}$, one get

$$\frac{\partial\boldsymbol{l}_1\left(\boldsymbol{\theta}_{qs}\right)}{\partial\boldsymbol{\theta}_{qs}} = \boldsymbol{I} + \left.\frac{\partial\boldsymbol{e}_{1q}^{-1}\left(\boldsymbol{h}\right)}{\partial\boldsymbol{h}}\right|_{\boldsymbol{h}=\boldsymbol{h}\left(\boldsymbol{\theta}_{qs}\right)} \times \frac{\partial\boldsymbol{h}\left(\boldsymbol{\theta}_{qs}\right)}{\partial\boldsymbol{\theta}_{qs}}. \tag{92}$$

Since $\boldsymbol{l}_1\left(\boldsymbol{\theta}_{qs}\left(\boldsymbol{T}_{q1}\boldsymbol{\theta}_0\right)\right) = \boldsymbol{l}_1\left(\boldsymbol{l}_1^{-1}\left(\boldsymbol{T}_{q1}\boldsymbol{\theta}_0\right)\right) = \boldsymbol{T}_{q1}\boldsymbol{\theta}_0$,

$$\frac{\partial\boldsymbol{l}_1\left(\boldsymbol{\theta}_{qs}\left(\boldsymbol{T}_{q1}\boldsymbol{\theta}_0\right)\right)}{\partial\left(\boldsymbol{T}_{q1}\boldsymbol{\theta}_0\right)} = \boldsymbol{I} = \frac{\partial\boldsymbol{l}_1\left(\boldsymbol{\theta}_{qs}\right)}{\partial\boldsymbol{\theta}_{qs}} \times \frac{\partial\boldsymbol{\theta}_{qs}\left(\boldsymbol{T}_{q1}\boldsymbol{\theta}_0\right)}{\partial\left(\boldsymbol{T}_{q1}\boldsymbol{\theta}_0\right)}.$$

Hence,

$$\frac{\partial\boldsymbol{\theta}_{qs}\left(\boldsymbol{T}_{q1}\boldsymbol{\theta}_0\right)}{\partial\left(\boldsymbol{T}_{q1}\boldsymbol{\theta}_0\right)} = \left.\left[\boldsymbol{I} + \left.\frac{\partial\boldsymbol{e}_{1q}^{-1}\left(\boldsymbol{h}\right)}{\partial\boldsymbol{h}}\right|_{\boldsymbol{h}=\boldsymbol{h}\left(\boldsymbol{\theta}_{qs}\right)} \times \frac{\partial\boldsymbol{h}\left(\boldsymbol{\theta}_{qs}\right)}{\partial\boldsymbol{\theta}_{qs}}\right]^{-1}\right|_{\boldsymbol{\theta}_{qs}=\boldsymbol{\theta}_{qs}\left(\boldsymbol{T}_{q1}\boldsymbol{\theta}_0\right)}. \tag{93}$$

Substituting this expression into Eq. 91, differential of $V_{\bar{h}}\left(\boldsymbol{\theta}_{qs}\right)$ may then be determined as

$$\frac{\partial V_{\bar{h}}\left(\boldsymbol{\theta}_{qs}\right)}{\partial\boldsymbol{\theta}_{qs}} = \boldsymbol{h}\left(\boldsymbol{\theta}_{qs}\right)^T \left[\boldsymbol{I} + \left.\frac{\partial\boldsymbol{e}_{1q}^{-1}\left(\boldsymbol{h}\right)}{\partial\boldsymbol{h}}\right|_{\boldsymbol{h}=\boldsymbol{h}\left(\boldsymbol{\theta}_{qs}\right)} \times \frac{\partial\boldsymbol{h}\left(\boldsymbol{\theta}_{qs}\right)}{\partial\boldsymbol{\theta}_{qs}}\right]. \tag{94}$$

It will be integrated to finally obtain $V_{\bar{h}}\left(\boldsymbol{\theta}_{qs}\right)$. To meet this goal, consider the following differentiation;

$$\begin{aligned}\frac{\partial}{\partial\boldsymbol{\theta}_{qs}}\left[\frac{1}{2}\boldsymbol{h}\left(\boldsymbol{\theta}_{qs}\right)^T\boldsymbol{e}_{1q}^{-1}\left(\boldsymbol{h}\left(\boldsymbol{\theta}_{qs}\right)\right)\right] &= \frac{1}{2}\boldsymbol{e}_{1q}^{-1}\left(\boldsymbol{h}\left(\boldsymbol{\theta}_{qs}\right)\right)^T\frac{\partial\boldsymbol{h}\left(\boldsymbol{\theta}_{qs}\right)}{\partial\boldsymbol{\theta}_{qs}} \\ &\quad + \frac{1}{2}\boldsymbol{h}\left(\boldsymbol{\theta}_{qs}\right)^T\left.\frac{\partial\boldsymbol{e}_{1q}^{-1}\left(\boldsymbol{h}\right)}{\partial\boldsymbol{h}}\right|_{\boldsymbol{h}=\boldsymbol{h}\left(\boldsymbol{\theta}_{qs}\right)} \times \frac{\partial\boldsymbol{h}\left(\boldsymbol{\theta}_{qs}\right)}{\partial\boldsymbol{\theta}_{qs}}.\end{aligned}$$

Performing the inner product with the differential of $\boldsymbol{\theta}_{qs}$ and integrating the result yield a scalar equality of

$$\begin{aligned}&\int_{\left(\boldsymbol{\theta}_{qs}\right)_i}^{\boldsymbol{\theta}_{qs}} \boldsymbol{h}\left(\boldsymbol{\phi}\right)^T\left.\frac{\partial\boldsymbol{e}_{1q}^{-1}\left(\boldsymbol{h}\right)}{\partial\boldsymbol{h}}\right|_{\boldsymbol{h}=\boldsymbol{h}\left(\boldsymbol{\phi}\right)} \times \frac{\partial\boldsymbol{h}\left(\boldsymbol{\phi}\right)}{\partial\boldsymbol{\phi}}\cdot d\boldsymbol{\phi} \\ &= \boldsymbol{h}\left(\boldsymbol{\theta}_{qs}\right)^T\boldsymbol{e}_{1q}^{-1}\left(\boldsymbol{h}\left(\boldsymbol{\theta}_{qs}\right)\right) - \int_{\left(\boldsymbol{\theta}_{qs}\right)_i}^{\boldsymbol{\theta}_{qs}} \boldsymbol{e}_{1q}^{-1}\left(\boldsymbol{h}\left(\boldsymbol{\phi}\right)\right)^T\frac{\partial\boldsymbol{h}\left(\boldsymbol{\phi}\right)}{\partial\boldsymbol{\phi}}\cdot d\boldsymbol{\phi},\end{aligned} \tag{95}$$

where $\left(\boldsymbol{\theta}_{qs}\right)_i$ is the stationary link angles that makes $\boldsymbol{h}\left(\cdot\right)^T\boldsymbol{e}_{1q}^{-1}\left(\boldsymbol{h}\left(\cdot\right)\right) = 0$. Physically, they correspond to the robot posture which causes no overall effective deformation of the drivetrain. This may happen during the operation when the compensating gravity torque vector matches the desired compliant contact force.

Equation 95 indeed relates the stationary potential energy (leftmost term) of the network of the elastic transmission elements to its co-potential energy (rightmost term) through the well-known Legendre transformation. The equation is written with the stationary link angles $\boldsymbol{\theta}_{qs}$ as the coordinates

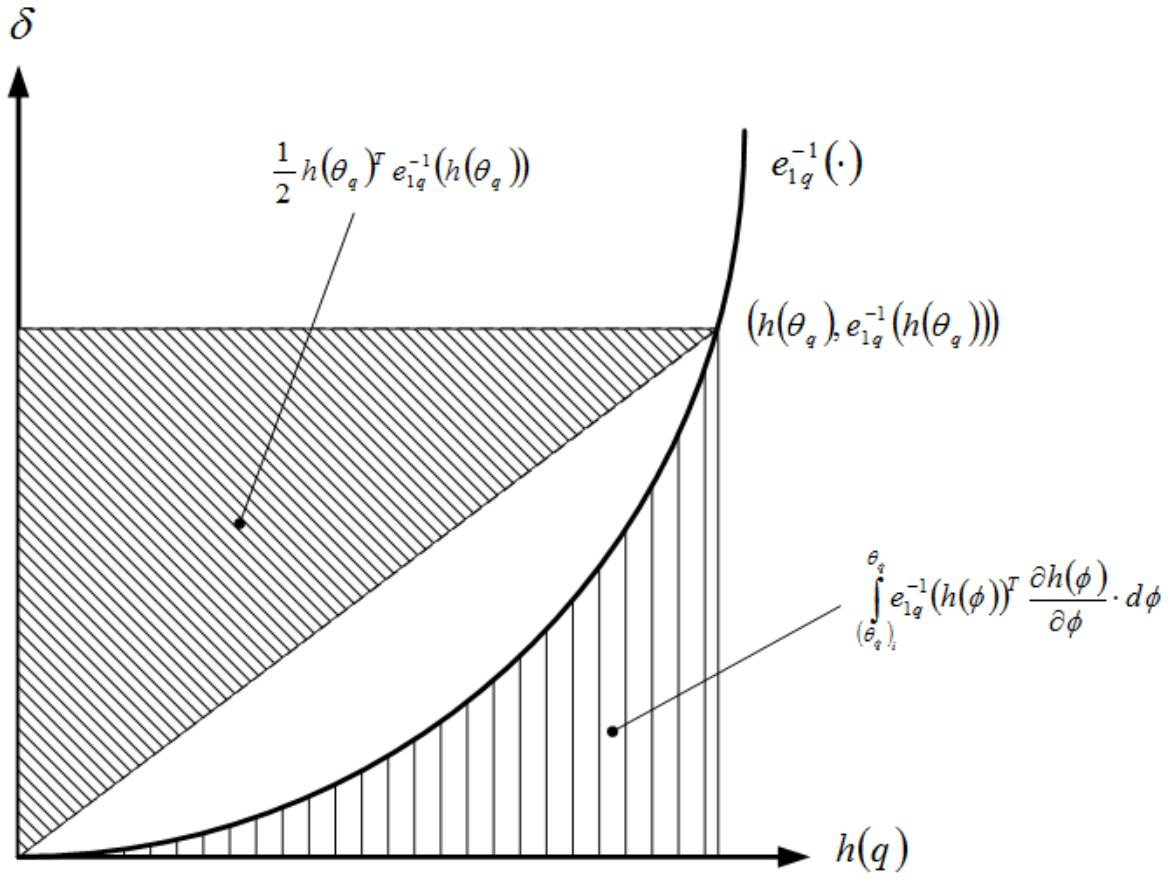

Figure 5: Compliance characteristics of a nonlinear spring displaying the related elastic potential/co-potential energy. The softening spring can store and restore more potential energy than the linear spring.

that can be replaced with true link angles $\boldsymbol{q}$ for the elastic potential energy of the physical drivetrain system. Graphical illustration for the case of one-dimensional nonlinear spring is depicted in Fig. 5. For the softening nonlinear spring characteristics, such as the behavior of the cable-pulley driven transmission system, it can be further stated that

$$\int_{(\boldsymbol{\theta}_{qs})_i}^{\boldsymbol{\theta}_{qs}} \boldsymbol{h}(\boldsymbol{\phi})^T \left.\frac{\partial \boldsymbol{e}_{1q}^{-1}(\boldsymbol{h})}{\partial \boldsymbol{h}}\right|_{\boldsymbol{h}=\boldsymbol{h}(\boldsymbol{\phi})} \times \frac{\partial \boldsymbol{h}(\boldsymbol{\phi})}{\partial \boldsymbol{\phi}} \cdot d\boldsymbol{\phi} > \frac{1}{2}\boldsymbol{h}(\boldsymbol{\theta}_{qs})^T \boldsymbol{e}_{1q}^{-1}(\boldsymbol{h}(\boldsymbol{\theta}_{qs})) \tag{96}$$

as it can store and restore more energy than the linear spring.

Integrating Eq. 94 and making use of Eq. 95 leads to

$$V_{\bar{h}}(\boldsymbol{\theta}_{qs}) = V_h(\boldsymbol{\theta}_{qs}) + \boldsymbol{e}_{1q}(\boldsymbol{T}_{q1}\boldsymbol{\theta}_0 - \boldsymbol{\theta}_{qs})^T(\boldsymbol{T}_{q1}\boldsymbol{\theta}_0 - \boldsymbol{\theta}_{qs}) - \int_{(\boldsymbol{\theta}_{qs})_i}^{\boldsymbol{\theta}_{qs}} \boldsymbol{e}_{1q}^{-1}(\boldsymbol{h}(\boldsymbol{\phi}))^T \frac{\partial \boldsymbol{h}(\boldsymbol{\phi})}{\partial \boldsymbol{\phi}} \cdot d\boldsymbol{\phi}, \tag{97}$$

in which the function $\boldsymbol{h}(\cdot)$ is recognized as the differential of the potential function $V_h(\cdot)$ and the relation in Eq. 41 is substituted. Recalling Eq. 89, $V_{\bar{h}}(\boldsymbol{\theta}_{qs})$ of Eq. 97 may thus be interpreted as the difference of the gravitational plus elastic potential energy of the passive robot/transmission subsystems and the elastic potential energy of the desired task space compliance, all at the stationary link angles $\boldsymbol{\theta}_{qs}$. The controller of Eq. 79 will inject negative of this potential energy into the (closed loop) system via the negative feedback on the attempt to cancel the original system potential energy and then shape to the one according to the desired compliance. Alternatively, Eq. 97 may be expressed in terms of $\boldsymbol{T}_{q1}\boldsymbol{\theta}_0$ from which $\boldsymbol{\theta}_{qs}$ is determined. This representation is useful in the stability analysis as $\boldsymbol{T}_{q1}\boldsymbol{\theta}_0$, not $\boldsymbol{\theta}_{qs}$, are the system state variables.

3.6.1. Proof of Stability

Model of the nonlinear flexible joint robot system is described by Eqs. 1, 13, 22, and 21. Its controller is governed by Eqs. 79, 80, 81, 83, 85, and 87. Additionally, the robot link joint velocity estimator, Eq. 57, is included. To prove the stability of the closed loop system, consider the following function;

$$\begin{aligned} V\left(\boldsymbol{q}, \dot{\boldsymbol{q}}, \boldsymbol{\theta}, \dot{\boldsymbol{\theta}}, \boldsymbol{e}_i, \dot{\boldsymbol{z}}\right) &= \frac{1}{2}\dot{\boldsymbol{q}}^T\boldsymbol{M}(\boldsymbol{q})\dot{\boldsymbol{q}} + V_g(\boldsymbol{q}) + \frac{1}{2}\dot{\boldsymbol{\theta}}^T\boldsymbol{B}_r\dot{\boldsymbol{\theta}} + V_e(\boldsymbol{q}, \boldsymbol{T}_{q1}\boldsymbol{\theta}_0) \\ &\quad + \frac{1}{2}\boldsymbol{e}_i^T\boldsymbol{L}\boldsymbol{e}_i - V_{\bar{h}}(\boldsymbol{T}_{q1}\boldsymbol{\theta}_0) + \frac{1}{2}\dot{\boldsymbol{z}}^T\boldsymbol{P}\dot{\boldsymbol{z}} \end{aligned} \tag{98}$$

consisting of the kinetic and potential energies of the robot, modified drivetrain, motor, and the negative feedback controller.

$$V_e(\boldsymbol{q}, \boldsymbol{T}_{q1}\boldsymbol{\theta}_0) = \boldsymbol{e}_{1q}(\boldsymbol{T}_{q1}\boldsymbol{\theta}_0 - \boldsymbol{q})^T(\boldsymbol{T}_{q1}\boldsymbol{\theta}_0 - \boldsymbol{q}) - \int_{\boldsymbol{q}_i}^{\boldsymbol{q}} \boldsymbol{e}_{1q}^{-1}(\boldsymbol{h}(\boldsymbol{\phi}))^T \frac{\partial \boldsymbol{h}(\boldsymbol{\phi})}{\partial \boldsymbol{\phi}} \cdot d\boldsymbol{\phi} \tag{99}$$

is the elastic potential energy of the drivetrain subsystem and $V_{\bar{h}}(\boldsymbol{T}_{q1}\boldsymbol{\theta}_0)$ is the (potential) energy of the controller Eq. 97 but expressed in terms of $\boldsymbol{T}_{q1}\boldsymbol{\theta}_0$. The last term represents the state kinetic

energy-like function of the velocity estimator unit. $\boldsymbol{P}$ is a symmetric positive definite matrix as described in subsection 3.4.

It should be mentioned that the potential energy of the drivetrain in Eq. 10 is the same as the one of Eq. 99. The difference is that the previous is expressed based on the elastic behavior of each flexible element through the deformation caused by the generalized coordinates of the drivetrain, $\boldsymbol{\theta}$, and the robot generalized coordinates, $\boldsymbol{q}$. On the other hand, the potential energy in Eq. 99 is stated based on the elastic behavior of the overall unit, $\boldsymbol{e}_{1q}(\cdot)$, via the effective deformation caused by the transformed coordinates of the motor angles, $\boldsymbol{T}_{q1}\boldsymbol{\theta}_0$, and $\boldsymbol{q}$. With this comprehension, the following expression

$$\frac{\partial V_e(\boldsymbol{q},\boldsymbol{\theta})}{\partial \boldsymbol{q}}\dot{\boldsymbol{q}} + \frac{\partial V_e(\boldsymbol{q},\boldsymbol{\theta})}{\partial \boldsymbol{\theta}}\dot{\boldsymbol{\theta}} = \frac{\partial V_e(\boldsymbol{q},\boldsymbol{T}_{q1}\boldsymbol{\theta}_0)}{\partial \boldsymbol{q}}\dot{\boldsymbol{q}} + \frac{\partial V_e(\boldsymbol{q},\boldsymbol{T}_{q1}\boldsymbol{\theta}_0)}{\partial(\boldsymbol{T}_{q1}\boldsymbol{\theta}_0)}\boldsymbol{T}_{q1}\dot{\boldsymbol{\theta}}_0$$

holds. This implies

$$\frac{\partial V_e(\boldsymbol{q},\boldsymbol{\theta})}{\partial \boldsymbol{\theta}}\dot{\boldsymbol{\theta}} = \frac{\partial V_e(\boldsymbol{q},\boldsymbol{T}_{q1}\boldsymbol{\theta}_0)}{\partial(\boldsymbol{T}_{q1}\boldsymbol{\theta}_0)}\boldsymbol{T}_{q1}\dot{\boldsymbol{\theta}}_0 \tag{100}$$

and

$$\frac{\partial V_e(\boldsymbol{q},\boldsymbol{\theta})}{\partial \boldsymbol{q}} = \frac{\partial V_e(\boldsymbol{q},\boldsymbol{T}_{q1}\boldsymbol{\theta}_0)}{\partial \boldsymbol{q}}. \tag{101}$$

Explicitly,

$$\begin{aligned}
&\boldsymbol{e}_1(\boldsymbol{T}_1\boldsymbol{\theta}_0-\boldsymbol{\theta}_1)^T\left(\boldsymbol{T}_1\dot{\boldsymbol{\theta}}_0-\dot{\boldsymbol{\theta}}_1\right)+\boldsymbol{e}_2(\boldsymbol{T}_2\boldsymbol{\theta}_1-\boldsymbol{\theta}_2)^T\left(\boldsymbol{T}_2\dot{\boldsymbol{\theta}}_1-\dot{\boldsymbol{\theta}}_2\right)+\cdots\\
&+\boldsymbol{e}_{q-1}(\boldsymbol{T}_{q-1}\boldsymbol{\theta}_{q-2}-\boldsymbol{\theta}_{q-1})^T\left(\boldsymbol{T}_{q-1}\dot{\boldsymbol{\theta}}_{q-2}-\dot{\boldsymbol{\theta}}_{q-1}\right)+\boldsymbol{e}_q(\boldsymbol{T}_q\boldsymbol{\theta}_{q-1}-\boldsymbol{q})^T\boldsymbol{T}_q\dot{\boldsymbol{\theta}}_{q-1} \quad =\\
&\boldsymbol{e}_{1q}(\boldsymbol{T}_{q1}\boldsymbol{\theta}_0-\boldsymbol{q})^T\boldsymbol{T}_{q1}\dot{\boldsymbol{\theta}}_0+(\boldsymbol{T}_{q1}\boldsymbol{\theta}_0-\boldsymbol{q})^T\left.\frac{\partial \boldsymbol{e}_{1q}(\boldsymbol{\delta})}{\partial\boldsymbol{\delta}}\right|_{\boldsymbol{\delta}=\boldsymbol{T}_{q1}\boldsymbol{\theta}_0-\boldsymbol{q}}\boldsymbol{T}_{q1}\dot{\boldsymbol{\theta}}_0
\end{aligned} \tag{102}$$

and

$$\boldsymbol{e}_q(\boldsymbol{T}_q\boldsymbol{\theta}_{q-1}-\boldsymbol{q}) = \boldsymbol{e}_{1q}(\boldsymbol{T}_{q1}\boldsymbol{\theta}_0-\boldsymbol{q}) \tag{103}$$

after the simplification.

The function $V(\cdot)$ is a Lyapunov function candidate, i.e. it is a positive definite function and continuously differentiable in a neighborhood of a particular point. According to Eq. 98, that point corresponds to the equilibrium point having a specific value of $\boldsymbol{q}$ and $\boldsymbol{\theta}$ but with $\dot{\boldsymbol{q}}=\boldsymbol{0}$, $\dot{\boldsymbol{\theta}}=\boldsymbol{0}$, $\boldsymbol{e_i}=\boldsymbol{0}$, and $\dot{\boldsymbol{z}}=\boldsymbol{0}$. The function value will be zero, while at other points the value will be positive. To verify that $V(\cdot)$ is indeed a Lyapunov function candidate, first, employ Eq. 89 and 97, and rearrange the expression of Eq. 98 as

$$\begin{aligned}
V(\cdot) \quad = \quad & \frac{1}{2}\dot{\boldsymbol{q}}^T\boldsymbol{M}(\boldsymbol{q})\dot{\boldsymbol{q}}+\frac{1}{2}\dot{\boldsymbol{\theta}}^T\boldsymbol{B}_r\dot{\boldsymbol{\theta}}+\frac{1}{2}\boldsymbol{e}_i^T\boldsymbol{L}\boldsymbol{e}_i+\frac{1}{2}\dot{\boldsymbol{z}}^T\boldsymbol{P}\dot{\boldsymbol{z}}+V_h(\boldsymbol{q})+\frac{1}{2}(\boldsymbol{x}(\boldsymbol{q})-\boldsymbol{x}_d)^T\boldsymbol{K}_d(\boldsymbol{x}(\boldsymbol{q})-\boldsymbol{x}_d)\\
&+\boldsymbol{e}_{1q}(\boldsymbol{T}_{q1}\boldsymbol{\theta}_0-\boldsymbol{\theta}_{qs}+\boldsymbol{\theta}_{qs}-\boldsymbol{q})^T(\boldsymbol{T}_{q1}\boldsymbol{\theta}_0-\boldsymbol{\theta}_{qs}+\boldsymbol{\theta}_{qs}-\boldsymbol{q})-\int_{\boldsymbol{\phi}_i}^{\boldsymbol{q}}\boldsymbol{e}_{1q}^{-1}(\boldsymbol{h}(\boldsymbol{\phi}))^T\frac{\partial\boldsymbol{h}(\boldsymbol{\phi})}{\partial\boldsymbol{\phi}}\cdot d\boldsymbol{\phi}\\
&-V_h(\boldsymbol{\theta}_{qs})-\boldsymbol{e}_{1q}(\boldsymbol{T}_{q1}\boldsymbol{\theta}_0-\boldsymbol{\theta}_{qs})^T(\boldsymbol{T}_{q1}\boldsymbol{\theta}_0-\boldsymbol{\theta}_{qs})+\int_{\boldsymbol{\phi}_i}^{\boldsymbol{\theta}_{qs}}\boldsymbol{e}_{1q}^{-1}(\boldsymbol{h}(\boldsymbol{\phi}))^T\frac{\partial\boldsymbol{h}(\boldsymbol{\phi})}{\partial\boldsymbol{\phi}}\cdot d\boldsymbol{\phi},
\end{aligned} \tag{104}$$

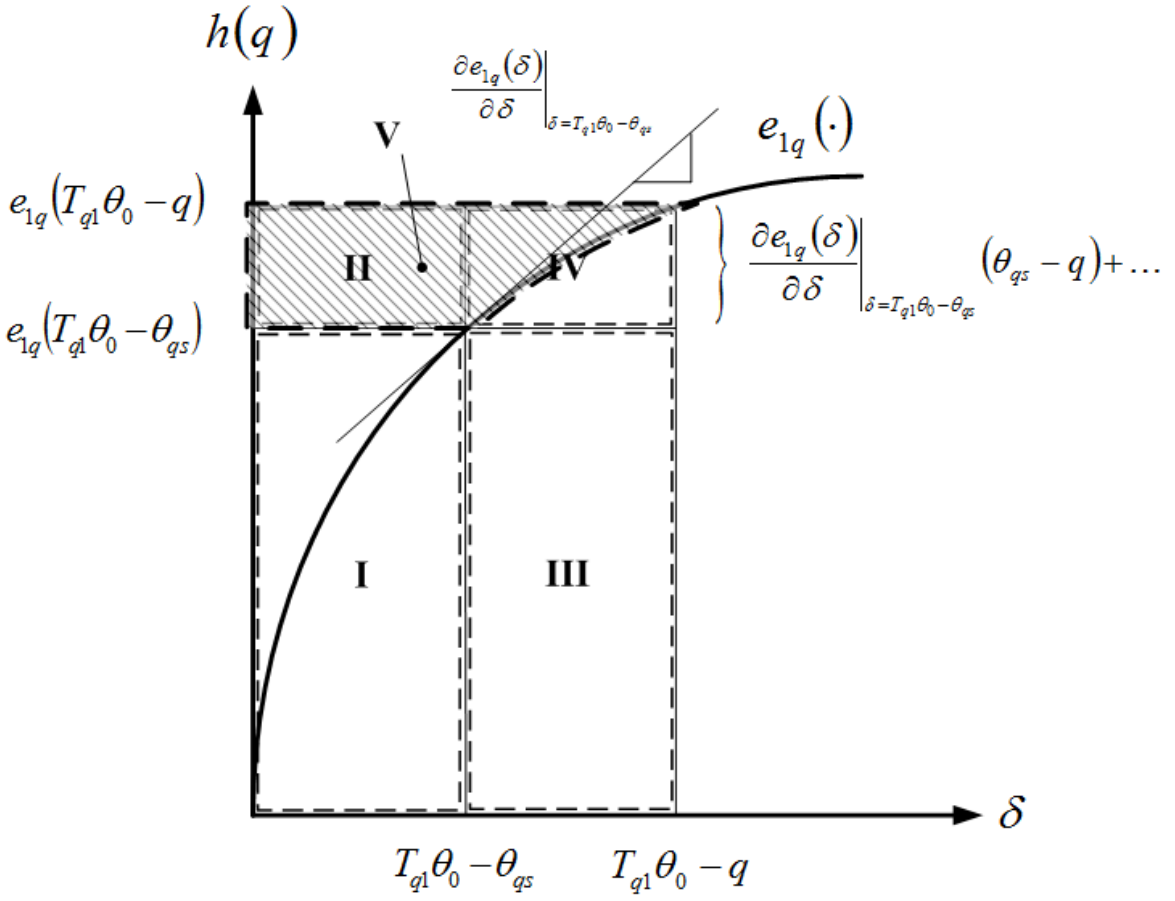

Figure 6: Interpretation of various expressions as the sub-areas of the elastic potential/co-potential energy.

where $\boldsymbol{\theta}_{qs} = \boldsymbol{\theta}_{qs}(\boldsymbol{T}_{q1}\boldsymbol{\theta}_0)$ is implied and the angle $\boldsymbol{\phi}_i$ be the link angles that cause no overall effective deformation of the drivetrain.

Using Taylor's series, the term $\boldsymbol{e}_{1q}(\boldsymbol{T}_{q1}\boldsymbol{\theta}_0 - \boldsymbol{\theta}_{qs} + \boldsymbol{\theta}_{qs} - \boldsymbol{q})$ may be expanded as

$$\boldsymbol{e}_{1q}(\boldsymbol{T}_{q1}\boldsymbol{\theta}_0 - \boldsymbol{\theta}_{qs} + \boldsymbol{\theta}_{qs} - \boldsymbol{q}) = \boldsymbol{e}_{1q}(\boldsymbol{T}_{q1}\boldsymbol{\theta}_0 - \boldsymbol{\theta}_{qs}) + \left.\frac{\partial \boldsymbol{e}_{1q}(\boldsymbol{\delta})}{\partial \boldsymbol{\delta}}\right|_{\boldsymbol{\delta}=\boldsymbol{T}_{q1}\boldsymbol{\theta}_0-\boldsymbol{\theta}_{qs}} (\boldsymbol{\theta}_{qs} - \boldsymbol{q}) + \dots$$

Hence,

$$\begin{aligned}
&\boldsymbol{e}_{1q}(\boldsymbol{T}_{q1}\boldsymbol{\theta}_0 - \boldsymbol{\theta}_{qs} + \boldsymbol{\theta}_{qs} - \boldsymbol{q})^T(\boldsymbol{T}_{q1}\boldsymbol{\theta}_0 - \boldsymbol{\theta}_{qs} + \boldsymbol{\theta}_{qs} - \boldsymbol{q}) = \\
&\boldsymbol{e}_{1q}(\boldsymbol{T}_{q1}\boldsymbol{\theta}_0 - \boldsymbol{\theta}_{qs})^T(\boldsymbol{T}_{q1}\boldsymbol{\theta}_0 - \boldsymbol{\theta}_{qs}) + (\boldsymbol{\theta}_{qs} - \boldsymbol{q})^T \left.\frac{\partial \boldsymbol{e}_{1q}(\boldsymbol{\delta})}{\partial \boldsymbol{\delta}}\right|_{\boldsymbol{\delta}=\boldsymbol{T}_{q1}\boldsymbol{\theta}_0-\boldsymbol{\theta}_{qs}} (\boldsymbol{T}_{q1}\boldsymbol{\theta}_0 - \boldsymbol{\theta}_{qs}) + \dots \\
&+\boldsymbol{e}_{1q}(\boldsymbol{T}_{q1}\boldsymbol{\theta}_0 - \boldsymbol{\theta}_{qs})^T(\boldsymbol{\theta}_{qs} - \boldsymbol{q}) + (\boldsymbol{\theta}_{qs} - \boldsymbol{q})^T \left.\frac{\partial \boldsymbol{e}_{1q}(\boldsymbol{\delta})}{\partial \boldsymbol{\delta}}\right|_{\boldsymbol{\delta}=\boldsymbol{T}_{q1}\boldsymbol{\theta}_0-\boldsymbol{\theta}_{qs}} (\boldsymbol{\theta}_{qs} - \boldsymbol{q}) + \dots \qquad (105)
\end{aligned}$$

This equation has the graphical interpretation of the sum of the total elastic potential and co-potential energy of the transmission system. For one-dimensional nonlinear spring, it can be depicted in Fig. 6 as the area of the imposed rectangle on the force/deformation curve plotting of $e_{1q}(\cdot)$ with the corner points of $(0,0)$ representing the undeformed state and $(T_{q1}\theta_0 - q, e_{1q}(T_{q1}\theta_0 - q))$ for the present state with the deformation $T_{q1}\theta_0 - q$. Considering the terms on the right hand side, the first term depicts

the sum of the potential and co-potential energy when the robot link angle is at the stationary value θ_{qs} (area I in Fig. 6). The third term represent area III. Recalling the Taylor's series expansion, the second term and its residue is the area II, while the fourth and its residue is the area IV.

Back to Eq. 104, two integral terms can be summed to

$$-\int_{\boldsymbol{\phi}_i}^{\boldsymbol{q}} \boldsymbol{e}_{1q}^{-1}\left(\boldsymbol{h}\left(\boldsymbol{\phi}\right)\right)^T \frac{\partial \boldsymbol{h}\left(\boldsymbol{\phi}\right)}{\partial \boldsymbol{\phi}} \cdot d\boldsymbol{\phi} + \int_{\boldsymbol{\phi}_i}^{\boldsymbol{\theta}_{qs}} \boldsymbol{e}_{1q}^{-1}\left(\boldsymbol{h}\left(\boldsymbol{\phi}\right)\right)^T \frac{\partial \boldsymbol{h}\left(\boldsymbol{\phi}\right)}{\partial \boldsymbol{\phi}} \cdot d\boldsymbol{\phi} = \int_{\boldsymbol{q}}^{\boldsymbol{\theta}_{qs}} \boldsymbol{e}_{1q}^{-1}\left(\boldsymbol{h}\left(\boldsymbol{\phi}\right)\right)^T \frac{\partial \boldsymbol{h}\left(\boldsymbol{\phi}\right)}{\partial \boldsymbol{\phi}} \cdot d\boldsymbol{\phi}.$$

Since $\boldsymbol{h}\left(\boldsymbol{\phi}\right) = \boldsymbol{e}_{1q}\left(\boldsymbol{T}_{q1}\boldsymbol{\theta}_0 - \boldsymbol{\phi}\right)$,

$$\frac{\partial \boldsymbol{h}\left(\boldsymbol{\phi}\right)}{\partial \boldsymbol{\phi}} = \left.\frac{\partial \boldsymbol{e}_{1q}\left(\boldsymbol{\delta}\right)}{\partial \boldsymbol{\delta}}\right|_{\boldsymbol{\delta}=\boldsymbol{T}_{q1}\boldsymbol{\theta}_0-\boldsymbol{\phi}} \frac{\partial\left(\boldsymbol{T}_{q1}\boldsymbol{\theta}_0 - \boldsymbol{\phi}\right)}{\partial \boldsymbol{\phi}} = -\left.\frac{\partial \boldsymbol{e}_{1q}\left(\boldsymbol{\delta}\right)}{\partial \boldsymbol{\delta}}\right|_{\boldsymbol{\delta}=\boldsymbol{T}_{q1}\boldsymbol{\theta}_0-\boldsymbol{\phi}}$$

and

$$\boldsymbol{e}_{1q}^{-1}\left(\boldsymbol{h}\left(\boldsymbol{\phi}\right)\right) = \boldsymbol{T}_{q1}\boldsymbol{\theta}_0 - \boldsymbol{\phi} = \boldsymbol{\delta},$$

one may write the above integral as the function of the deformation variable $\boldsymbol{\delta}$;

$$\int_{\boldsymbol{q}}^{\boldsymbol{\theta}_{qs}} \boldsymbol{e}_{1q}^{-1}\left(\boldsymbol{h}\left(\boldsymbol{\phi}\right)\right)^T \frac{\partial \boldsymbol{h}\left(\boldsymbol{\phi}\right)}{\partial \boldsymbol{\phi}} \cdot d\boldsymbol{\phi} = \int_{\boldsymbol{T}_{q1}\boldsymbol{\theta}_0-\boldsymbol{q}}^{\boldsymbol{T}_{q1}\boldsymbol{\theta}_0-\boldsymbol{\theta}_{qs}} \boldsymbol{\delta}^T \frac{\partial \boldsymbol{e}_{1q}\left(\boldsymbol{\delta}\right)}{\partial \boldsymbol{\delta}} \cdot d\boldsymbol{\delta}. \tag{106}$$

This is the co-potential energy stored in changing from the state $\boldsymbol{T}_{q1}\boldsymbol{\theta}_0 - \boldsymbol{q}$ to the state $\boldsymbol{T}_{q1}\boldsymbol{\theta}_0 - \boldsymbol{\theta}_{qs}$. It corresponds to the negative of the area V for the case of one-dimensional nonlinear spring as shown in Fig. 6.

Arming with such understanding, the Lyapunov function candidate in Eq. 104 may be simplified to

$$\begin{aligned} V\left(\cdot\right) \;=\; & \frac{1}{2}\dot{\boldsymbol{q}}^T\boldsymbol{M}\left(\boldsymbol{q}\right)\dot{\boldsymbol{q}} + \frac{1}{2}\dot{\boldsymbol{\theta}}^T\boldsymbol{B}_r\dot{\boldsymbol{\theta}} + \frac{1}{2}\boldsymbol{e}_i^T\boldsymbol{L}\boldsymbol{e}_i + \frac{1}{2}\dot{\boldsymbol{z}}^T\boldsymbol{P}\dot{\boldsymbol{z}} + \frac{1}{2}\left(\boldsymbol{x}\left(\boldsymbol{q}\right) - \boldsymbol{x}_d\right)^T\boldsymbol{K}_d\left(\boldsymbol{x}\left(\boldsymbol{q}\right) - \boldsymbol{x}_d\right) \\ & + V_h\left(\boldsymbol{q}\right) - V_h\left(\boldsymbol{\theta}_{qs}\right) + \int_{\boldsymbol{T}_{q1}\boldsymbol{\theta}_0-\boldsymbol{\theta}_{qs}}^{\boldsymbol{T}_{q1}\boldsymbol{\theta}_0-\boldsymbol{q}} \boldsymbol{e}_{1q}\left(\boldsymbol{\delta}\right)^T \cdot d\boldsymbol{\delta}. \end{aligned} \tag{107}$$

The last term on the right hand side represents the incremental potential energy from the state $\boldsymbol{T}_{q1}\boldsymbol{\theta}_0 - \boldsymbol{\theta}_{qs}$ to the state $\boldsymbol{T}_{q1}\boldsymbol{\theta}_0 - \boldsymbol{q}$. This apparently agrees, in the one-dimensional case, with the remaining area of the big rectangle (I+II+III+IV) after subtracting off the area of the small rectangle (I) and the incremental co-potential energy (V).

For the system of which the elastic elements possess the softening spring characteristics, Eq. 107 may further be written as

$$\begin{aligned} V\left(\cdot\right) \;\geq\; & \frac{1}{2}\dot{\boldsymbol{q}}^T\boldsymbol{M}\left(\boldsymbol{q}\right)\dot{\boldsymbol{q}} + \frac{1}{2}\dot{\boldsymbol{\theta}}^T\boldsymbol{B}_r\dot{\boldsymbol{\theta}} + \frac{1}{2}\boldsymbol{e}_i^T\boldsymbol{L}\boldsymbol{e}_i + \frac{1}{2}\dot{\boldsymbol{z}}^T\boldsymbol{P}\dot{\boldsymbol{z}} \\ & + \frac{1}{2}\left(\boldsymbol{x}\left(\boldsymbol{q}\right) - \boldsymbol{x}_d\right)^T\boldsymbol{K}_d\left(\boldsymbol{x}\left(\boldsymbol{q}\right) - \boldsymbol{x}_d\right) + \frac{1}{2}\left(\boldsymbol{\theta}_{qs} - \boldsymbol{q}\right)^T \left.\frac{\partial \boldsymbol{e}_{1q}\left(\boldsymbol{\delta}\right)}{\partial \boldsymbol{\delta}}\right|_{\boldsymbol{\delta}^*} \left(\boldsymbol{\theta}_{qs} - \boldsymbol{q}\right) \\ & + V_h\left(\boldsymbol{q}\right) - V_h\left(\boldsymbol{\theta}_{qs}\right) + \boldsymbol{h}\left(\boldsymbol{\theta}_{qs}\right)^T\left(\boldsymbol{\theta}_{qs} - \boldsymbol{q}\right), \end{aligned} \tag{108}$$

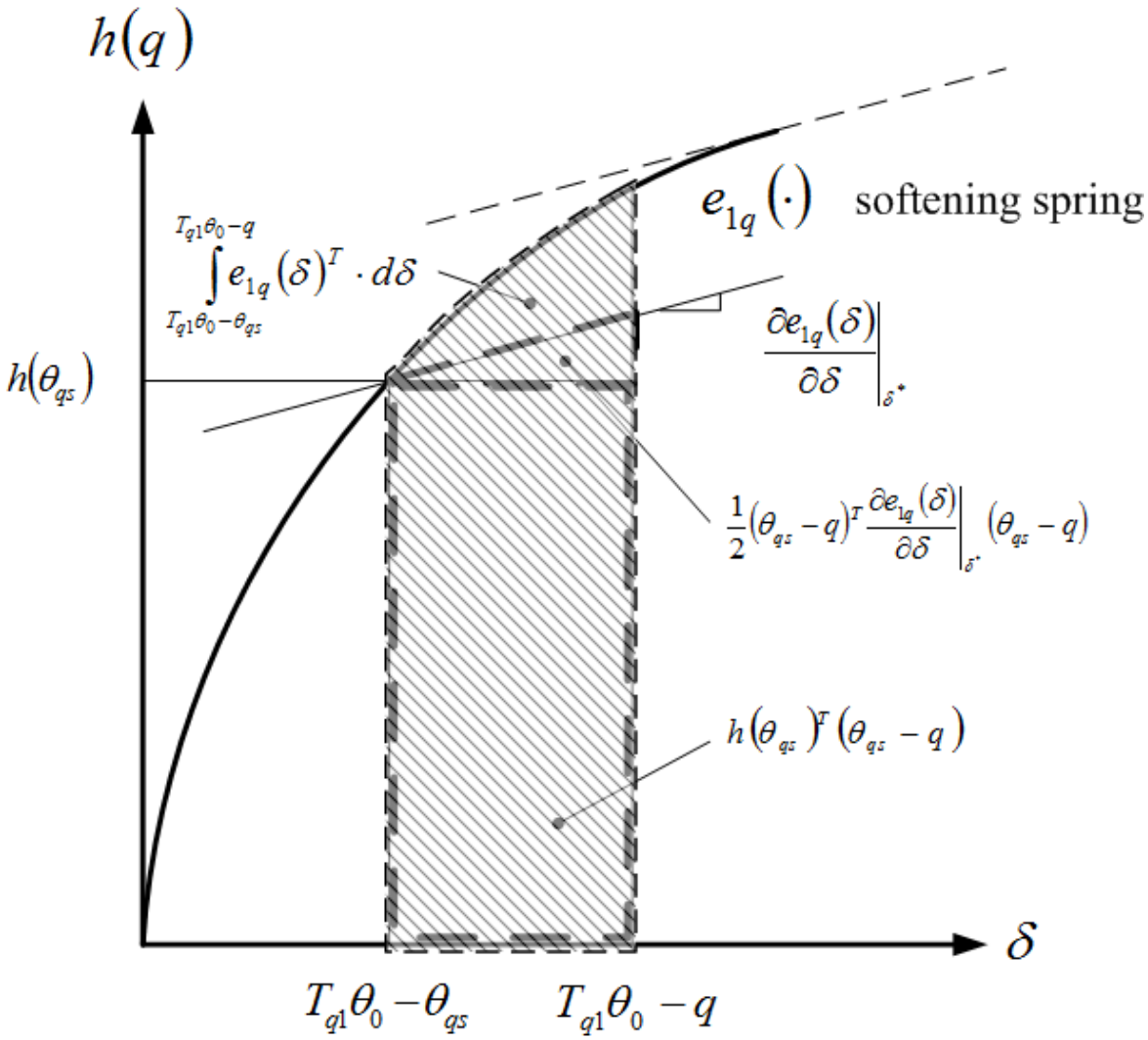

Figure 7: Graphical interpretation of the incremental potential energy and its inequality expression used in Eq. 108. This fact leads to the positive definiteness of $V(\cdot)$.

in which

$$\left.\frac{\partial \boldsymbol{e}_{1q}(\boldsymbol{\delta})}{\partial \boldsymbol{\delta}}\right|_{\boldsymbol{\delta}^*} = \inf_{\forall \boldsymbol{\delta} \in \mathbb{R}^p} \frac{\partial \boldsymbol{e}_{1q}(\boldsymbol{\delta})}{\partial \boldsymbol{\delta}} \leq \left.\frac{\partial \boldsymbol{e}_{1q}(\boldsymbol{\delta})}{\partial \boldsymbol{\delta}}\right|_{\boldsymbol{\delta}=\boldsymbol{T}_{q1}\boldsymbol{\theta}_0-\boldsymbol{q}} \leq \left.\frac{\partial \boldsymbol{e}_{1q}(\boldsymbol{\delta})}{\partial \boldsymbol{\delta}}\right|_{\boldsymbol{\delta}=\boldsymbol{T}_{q1}\boldsymbol{\theta}_0-\boldsymbol{\theta}_{qs}}.$$

Graphical interpretation of the above inequality caused by the integral term in Eq. 107 is illustrated in Fig. 7 for the case of one-dimensional effective spring. To show that $V(\cdot)$ is a positive definite function, the following assumption is necessary.

Assumption 3.1 The Hessian $\boldsymbol{H}_h(\boldsymbol{q}) = \frac{\partial \boldsymbol{h}(\boldsymbol{q})}{\partial \boldsymbol{q}} = \frac{\partial^2 V_h(\boldsymbol{q})}{\partial \boldsymbol{q}^2}$ of the potential function $V_h(\boldsymbol{q})$ satisfies the condition

$$\alpha_h \equiv \sup_{\forall \boldsymbol{q} \in \mathbb{R}^p} \|\boldsymbol{H}_h(\boldsymbol{q})\|_K < 1, \tag{109}$$

where the matrix K-norm is as defined in subsection 3.2.

This practical assumption is exactly the condition for the recursive evaluation of Eq. 41 to converge to the stationary link angles. An important consequence of assumption 3.1 is the following property.

Property 3.2 Let α_h be the upper bound for the Hessian of $V_h(\boldsymbol{q})$ as defined in assumption 3.1. Then the inequality

$$\left|V_h(\boldsymbol{q}_2) - V_h(\boldsymbol{q}_1) + h(\boldsymbol{q}_1)^T(\boldsymbol{q}_1 - \boldsymbol{q}_2)\right| \leq \frac{1}{2}\alpha_h \|\boldsymbol{q}_1 - \boldsymbol{q}_2\|_K^2 \tag{110}$$

holds for all $\boldsymbol{q}_1, \boldsymbol{q}_2 \in \mathbb{R}^p$. See [9] for the proof.

Applying property 3.2 to Eq. 108, one would further obtain

$$\begin{aligned} V(\cdot) \geq\ & \frac{1}{2}\dot{\boldsymbol{q}}^T\boldsymbol{M}(\boldsymbol{q})\dot{\boldsymbol{q}} + \frac{1}{2}\dot{\boldsymbol{\theta}}^T\boldsymbol{B}_r\dot{\boldsymbol{\theta}} + \frac{1}{2}\boldsymbol{e}_i^T\boldsymbol{L}\boldsymbol{e}_i + \frac{1}{2}\dot{\boldsymbol{z}}^T\boldsymbol{P}\dot{\boldsymbol{z}} + \frac{1}{2}(\boldsymbol{x}(\boldsymbol{q}) - \boldsymbol{x}_d)^T\boldsymbol{K}_d(\boldsymbol{x}(\boldsymbol{q}) - \boldsymbol{x}_d) \\ & + \frac{1}{2}(\boldsymbol{\theta}_{qs} - \boldsymbol{q})^T \left.\frac{\partial \boldsymbol{e}_{1q}(\boldsymbol{\delta})}{\partial \boldsymbol{\delta}}\right|_{\boldsymbol{\delta}^*} (\boldsymbol{\theta}_{qs} - \boldsymbol{q}) - \frac{1}{2}\alpha_h \|\boldsymbol{\theta}_{qs} - \boldsymbol{q}\|_K^2. \end{aligned}$$

From the definition of the matrix K-norm in Eq. 52-53,

$$\left\| \left.\frac{\partial \boldsymbol{e}_{1q}(\boldsymbol{\delta})}{\partial \boldsymbol{\delta}}\right|_{\boldsymbol{\delta}^*} \right\|_K = 1.$$

Hence, the inequality may finally be written as

$$\begin{aligned} V(\cdot) \geq\ & \frac{1}{2}\dot{\boldsymbol{q}}^T\boldsymbol{M}(\boldsymbol{q})\dot{\boldsymbol{q}} + \frac{1}{2}\dot{\boldsymbol{\theta}}^T\boldsymbol{B}_r\dot{\boldsymbol{\theta}} + \frac{1}{2}\boldsymbol{e}_i^T\boldsymbol{L}\boldsymbol{e}_i + \frac{1}{2}\dot{\boldsymbol{z}}^T\boldsymbol{P}\dot{\boldsymbol{z}} \\ & + \frac{1}{2}(\boldsymbol{x}(\boldsymbol{q}) - \boldsymbol{x}_d)^T\boldsymbol{K}_d(\boldsymbol{x}(\boldsymbol{q}) - \boldsymbol{x}_d) + \frac{1}{2}(1 - \alpha_h)\|\boldsymbol{\theta}_{qs} - \boldsymbol{q}\|_K^2. \end{aligned}$$

Recalling assumption 3.1 and recognizing all quadratic terms in the above inequality, it can be concluded that $V(\cdot) \geq 0$.

To determine the equilibrium point where $V(\cdot) \equiv 0$, it is evident from the quadratic terms on the right hand side of Eq. 98 that $\dot{\boldsymbol{q}} = \boldsymbol{0}$, $\dot{\boldsymbol{\theta}} = \boldsymbol{0}$, $\boldsymbol{e}_i = \boldsymbol{0}$, and $\dot{\boldsymbol{z}} = \boldsymbol{0}$ for each of them to be zero. Referring

to Eq. 65, $\dot{\boldsymbol{z}} = \mathbf{0}$ yields zero velocity related term $\boldsymbol{\vartheta} = \mathbf{0}$. The remaining terms may be rearranged using Eq. 89 as

$$\begin{aligned} V_g(\boldsymbol{q}) + V_e(\boldsymbol{q}, \boldsymbol{T}_{q1}\boldsymbol{\theta}_0) - V_{\bar{h}}(\boldsymbol{T}_{q1}\boldsymbol{\theta}_0) &= V_h(\boldsymbol{q}) + V_e(\boldsymbol{q}, \boldsymbol{T}_{q1}\boldsymbol{\theta}_0) - V_{\bar{h}}(\boldsymbol{T}_{q1}\boldsymbol{\theta}_0) \\ &\quad + \frac{1}{2}(\boldsymbol{x}(\boldsymbol{q}) - \boldsymbol{x}_d)^T \boldsymbol{K}_d(\boldsymbol{x}(\boldsymbol{q}) - \boldsymbol{x}_d). \end{aligned}$$

Referring to Eq. 97, the first three terms on the right hand side will add up to zero if the robot link angles $\boldsymbol{q}$ are equal to the stationary link angles $\boldsymbol{\theta}_{qs}$. The last term is a quadratic function which will be zero only when $\boldsymbol{x}(\boldsymbol{q}) = \boldsymbol{x}_d$. This requires

$$\boldsymbol{q} = \boldsymbol{q}_s = \boldsymbol{f}^{-1}(\boldsymbol{x}_d). \tag{111}$$

Consequently, $\boldsymbol{\theta}_{qs} = \boldsymbol{f}^{-1}(\boldsymbol{x}_d)$. Since $\boldsymbol{\theta}_{qs}$ is the function of $\boldsymbol{\theta}_{0s}$ via Eq. 41, the motor angles at the equilibrium point may be determined explicitly as

$$\boldsymbol{\theta}_{0s} = \boldsymbol{T}_{q1}^{-1}\left[\boldsymbol{\theta}_{qs} + \boldsymbol{e}_{1q}^{-1}(\boldsymbol{h}(\boldsymbol{\theta}_{qs}))\right] = \boldsymbol{T}_{q1}^{-1}\boldsymbol{l}_1(\boldsymbol{\theta}_{qs}) = \boldsymbol{T}_{q1}^{-1}\boldsymbol{l}_1\left(\boldsymbol{f}^{-1}(\boldsymbol{x}_d)\right).$$

Likewise, the equilibrium rotor angles of the drivetrain at the i^{th}-stage are

$$\boldsymbol{\theta}_{(i-1)s} = \boldsymbol{T}_{qi}^{-1}\left[\boldsymbol{\theta}_{qs} + \boldsymbol{e}_{iq}^{-1}(\boldsymbol{h}(\boldsymbol{\theta}_{qs}))\right] = \boldsymbol{T}_{qi}^{-1}\boldsymbol{l}_i(\boldsymbol{\theta}_{qs}) = \boldsymbol{T}_{qi}^{-1}\boldsymbol{l}_i\left(\boldsymbol{f}^{-1}(\boldsymbol{x}_d)\right), \tag{112}$$

where $\boldsymbol{T}_{qi} = \boldsymbol{T}_q\boldsymbol{T}_{q-1}\cdots\boldsymbol{T}_i$ and $\boldsymbol{e}_{iq}^{-1}(\cdot)$ is the effective nonlinear deformation function of the transmission subsystem from the i^{th}-stage to the last q^{th}-stage. If the elastic elements behave linearly, $\boldsymbol{e}_{iq}^{-1}(\boldsymbol{h}(\boldsymbol{\theta}_{qs}))$ may be calculated explicitly as the matrix multiplication $\boldsymbol{K}_{iq}^{-1}\boldsymbol{h}(\boldsymbol{\theta}_{qs})$ using the corresponding effective stiffness matrix;

$$\begin{aligned} \boldsymbol{K}_{iq} &= \Big[\boldsymbol{T}_{q(i+1)}\boldsymbol{K}_i^{-1}\boldsymbol{T}_{q(i+1)}^T + \boldsymbol{T}_{q(i+2)}\boldsymbol{K}_{i+1}^{-1}\boldsymbol{T}_{q(i+2)}^T + \cdots \\ &\quad + \boldsymbol{T}_{q(q-1)}\boldsymbol{K}_{q-2}^{-1}\boldsymbol{T}_{q(q-1)}^T + \boldsymbol{T}_q\boldsymbol{K}_{q-1}^{-1}\boldsymbol{T}_q^T + \boldsymbol{K}_q^{-1}\Big]^{-1}. \end{aligned} \tag{113}$$

Function $\boldsymbol{l}_i(\cdot)$, denoting the stationary rotor angles at the i^{th}-stage reflected to the robot link angles, is introduced merely for convenience. Note that the equilibrium rotor angles at the last stage may be evaluated by

$$\boldsymbol{\theta}_{(q-1)s} = \boldsymbol{T}_q^{-1}\left[\boldsymbol{\theta}_{qs} + \boldsymbol{e}_q^{-1}(\boldsymbol{h}(\boldsymbol{\theta}_{qs}))\right] = \boldsymbol{T}_q^{-1}\boldsymbol{l}_q(\boldsymbol{\theta}_{qs}) = \boldsymbol{T}_q^{-1}\boldsymbol{l}_q\left(\boldsymbol{f}^{-1}(\boldsymbol{x}_d)\right).$$

In the following, it will be shown by the Lyapunov stability theorem and the Lasalle's invariance principle [24] that the system equilibrium point $\left(\boldsymbol{q}, \dot{\boldsymbol{q}}, \boldsymbol{\theta}, \dot{\boldsymbol{\theta}}, \boldsymbol{e}_i, \dot{\boldsymbol{z}}\right) = (\boldsymbol{q}_s, \mathbf{0}, \boldsymbol{\theta}_s, \mathbf{0}, \mathbf{0}, \mathbf{0})$, where $\boldsymbol{q}_s$ and $\boldsymbol{\theta}_s$ are according to Eqs. 111 and 112, is (locally) asymptotically stable. Differentiating the Lyapunov function candidate Eq. 98 with respect to time results in

$$\begin{aligned} \dot{V}(\cdot) &= \frac{1}{2}\dot{\boldsymbol{q}}^T\dot{\boldsymbol{M}}(\boldsymbol{q})\dot{\boldsymbol{q}} + \dot{\boldsymbol{q}}^T\boldsymbol{M}(\boldsymbol{q})\ddot{\boldsymbol{q}} + \dot{\boldsymbol{\theta}}^T\boldsymbol{B}_r\ddot{\boldsymbol{\theta}} + \boldsymbol{e}_i^T\boldsymbol{L}\dot{\boldsymbol{e}}_i + \frac{1}{2}\ddot{\boldsymbol{z}}^T\boldsymbol{P}\dot{\boldsymbol{z}} + \frac{1}{2}\dot{\boldsymbol{z}}^T\boldsymbol{P}\ddot{\boldsymbol{z}} \\ &\quad + \boldsymbol{g}(\boldsymbol{q})^T\dot{\boldsymbol{q}} + \frac{\partial V_e(\boldsymbol{q}, \boldsymbol{T}_{q1}\boldsymbol{\theta}_0)}{\partial \boldsymbol{q}}\dot{\boldsymbol{q}} + \frac{\partial V_e(\boldsymbol{q}, \boldsymbol{T}_{q1}\boldsymbol{\theta}_0)}{\partial(\boldsymbol{T}_{q1}\boldsymbol{\theta}_0)}\boldsymbol{T}_{q1}\dot{\boldsymbol{\theta}}_0 - \frac{\partial V_{\bar{h}}(\boldsymbol{T}_{q1}\boldsymbol{\theta}_0)}{\partial(\boldsymbol{T}_{q1}\boldsymbol{\theta}_0)}\boldsymbol{T}_{q1}\dot{\boldsymbol{\theta}}_0. \end{aligned}$$

Along the trajectory of the closed loop system, the derivative may be written as

$$\begin{aligned}\dot{V}(\cdot) &= \frac{1}{2}\dot{\boldsymbol{q}}^T\dot{\boldsymbol{M}}(\boldsymbol{q})\dot{\boldsymbol{q}} + \dot{\boldsymbol{q}}^T\left(\boldsymbol{\tau}_{dr} + \boldsymbol{\tau}_{ext} - \boldsymbol{C}(\boldsymbol{q},\dot{\boldsymbol{q}})\dot{\boldsymbol{q}} - \boldsymbol{g}(\boldsymbol{q})\right) + \dot{\boldsymbol{\theta}}^T\left(\boldsymbol{\tau}_r - \boldsymbol{c}_r\left(\dot{\boldsymbol{\theta}}\right) - \boldsymbol{e}(\boldsymbol{\theta})\right)\\ &+\boldsymbol{e}_i^T\left(-\boldsymbol{K}_c\boldsymbol{e}_i\right) + \frac{1}{2}\left(\boldsymbol{A}\dot{\boldsymbol{z}} + \boldsymbol{B}\sqrt{\boldsymbol{K}_v}\boldsymbol{T}_{q1}\dot{\boldsymbol{\theta}}_0\right)^T\boldsymbol{P}\dot{\boldsymbol{z}} + \frac{1}{2}\dot{\boldsymbol{z}}^T\boldsymbol{P}\left(\boldsymbol{A}\dot{\boldsymbol{z}} + \boldsymbol{B}\sqrt{\boldsymbol{K}_v}\boldsymbol{T}_{q1}\dot{\boldsymbol{\theta}}_0\right)\\ &+\boldsymbol{g}(\boldsymbol{q})^T\dot{\boldsymbol{q}} + \frac{\partial V_e(\boldsymbol{q},\boldsymbol{T}_{q1}\boldsymbol{\theta}_0)}{\partial\boldsymbol{q}}\dot{\boldsymbol{q}} + \frac{\partial V_e(\boldsymbol{q},\boldsymbol{T}_{q1}\boldsymbol{\theta}_0)}{\partial(\boldsymbol{T}_{q1}\boldsymbol{\theta}_0)}\boldsymbol{T}_{q1}\dot{\boldsymbol{\theta}}_0 - \boldsymbol{h}(\boldsymbol{\theta}_{qs})^T\boldsymbol{T}_{q1}\dot{\boldsymbol{\theta}}_0,\end{aligned}$$

where

$$\boldsymbol{\tau}_r = \begin{bmatrix} (\boldsymbol{\tau}_m)_{dr}^T & \boldsymbol{0}^T & \cdots & \boldsymbol{0}^T \end{bmatrix}^T$$

and $\boldsymbol{c}_r(\cdot)$ are the modified generalized torque vector and the modified dissipative function of the drivetrain subsystem according to Eq. 82.

Applying the passivity property of the robot [26] and substituting the elastic force/transmitted torque relationship of Eq. 18, the equation may be simplified to

$$\begin{aligned}\dot{V}(\cdot) &= \dot{\boldsymbol{\theta}}_0^T(\boldsymbol{\tau}_m)_{dr} + \dot{\boldsymbol{\theta}}^T\left(-\boldsymbol{c}_r\left(\dot{\boldsymbol{\theta}}\right) - \left(\frac{\partial V_e(\boldsymbol{q},\boldsymbol{\theta})}{\partial\boldsymbol{\theta}}\right)^T\right)\\ &+\dot{\boldsymbol{q}}^T\left(\boldsymbol{e}_q\left(\boldsymbol{T}_q\boldsymbol{\theta}_{q-1} - \boldsymbol{q}\right) + \boldsymbol{\tau}_{ext}\right) - \boldsymbol{e}_i^T\boldsymbol{K}_c\boldsymbol{e}_i + \frac{1}{2}\dot{\boldsymbol{z}}^T\left(\boldsymbol{A}^T\boldsymbol{P} + \boldsymbol{P}\boldsymbol{A}\right)\dot{\boldsymbol{z}}\\ &+\dot{\boldsymbol{\theta}}_0^T\boldsymbol{T}_{q1}^T\sqrt{\boldsymbol{K}_v}\boldsymbol{B}^T\boldsymbol{P}\dot{\boldsymbol{z}} + \frac{\partial V_e(\boldsymbol{q},\boldsymbol{T}_{q1}\boldsymbol{\theta}_0)}{\partial\boldsymbol{q}}\dot{\boldsymbol{q}} + \frac{\partial V_e(\boldsymbol{q},\boldsymbol{T}_{q1}\boldsymbol{\theta}_0)}{\partial(\boldsymbol{T}_{q1}\boldsymbol{\theta}_0)}\boldsymbol{T}_{q1}\dot{\boldsymbol{\theta}}_0 - \boldsymbol{h}(\boldsymbol{\theta}_{qs})^T\boldsymbol{T}_{q1}\dot{\boldsymbol{\theta}}_0.\end{aligned}$$

Since

$$\boldsymbol{e}_i = \boldsymbol{i}_r - \boldsymbol{i}_{mr} = \boldsymbol{K}_\tau^{-1}\left[(\boldsymbol{\tau}_m)_{dr} - (\boldsymbol{\tau}_m)_{dr}^*\right],$$

where $\boldsymbol{i}_r$ and $\boldsymbol{i}_{mr}$ are the actual and reference motor current according to the modulated inertia $\boldsymbol{B}_{1r}$, the actual motor torque is related to the desired one by

$$\begin{aligned}(\boldsymbol{\tau}_m)_{dr} &= (\boldsymbol{\tau}_m)_{dr}^* + \boldsymbol{K}_\tau\boldsymbol{e}_i\\ &= \boldsymbol{T}_{q1}^T\left(\boldsymbol{h}(\boldsymbol{\theta}_{qs}) - \sqrt{\boldsymbol{K}_v}\boldsymbol{\vartheta}\right) + \boldsymbol{K}_\tau\boldsymbol{e}_i,\end{aligned}$$

in which the impedance control law Eqs. 79 and 80 are substituted. Hence the derivative becomes

$$\begin{aligned}\dot{V}(\cdot) &= \dot{\boldsymbol{\theta}}_0^T\boldsymbol{T}_{q1}^T\left(\boldsymbol{h}(\boldsymbol{\theta}_{qs}) - \sqrt{\boldsymbol{K}_v}\boldsymbol{\vartheta}\right) + \dot{\boldsymbol{\theta}}_0^T\boldsymbol{K}_\tau\boldsymbol{e}_i + \dot{\boldsymbol{\theta}}^T\left(-\boldsymbol{c}_r\left(\dot{\boldsymbol{\theta}}\right) - \left(\frac{\partial V_e(\boldsymbol{q},\boldsymbol{\theta})}{\partial\boldsymbol{\theta}}\right)^T\right)\\ &+\dot{\boldsymbol{q}}^T\left(\boldsymbol{e}_{1q}\left(\boldsymbol{T}_{q1}\boldsymbol{\theta}_0 - \boldsymbol{q}\right) + \boldsymbol{\tau}_{ext}\right) - \boldsymbol{e}_i^T\boldsymbol{K}_c\boldsymbol{e}_i + \frac{1}{2}\dot{\boldsymbol{z}}^T\left(\boldsymbol{A}^T\boldsymbol{P} + \boldsymbol{P}\boldsymbol{A}\right)\dot{\boldsymbol{z}}\\ &+\dot{\boldsymbol{\theta}}_0^T\boldsymbol{T}_{q1}^T\sqrt{\boldsymbol{K}_v}\boldsymbol{B}^T\boldsymbol{P}\dot{\boldsymbol{z}} + \frac{\partial V_e(\boldsymbol{q},\boldsymbol{T}_{q1}\boldsymbol{\theta}_0)}{\partial\boldsymbol{q}}\dot{\boldsymbol{q}} + \frac{\partial V_e(\boldsymbol{q},\boldsymbol{T}_{q1}\boldsymbol{\theta}_0)}{\partial(\boldsymbol{T}_{q1}\boldsymbol{\theta}_0)}\boldsymbol{T}_{q1}\dot{\boldsymbol{\theta}}_0 - \boldsymbol{h}(\boldsymbol{\theta}_{qs})^T\boldsymbol{T}_{q1}\dot{\boldsymbol{\theta}}_0.\end{aligned}$$

Further, by recalling Eqs. 100, 101, the KY lemma Eqs. 61, 62, and noticing some cancellation, the equation results in

$$\dot{V}(\cdot) = -\dot{\boldsymbol{\theta}}^T\boldsymbol{c}_r\left(\dot{\boldsymbol{\theta}}\right) + \dot{\boldsymbol{q}}^T\boldsymbol{\tau}_{ext} - \boldsymbol{e}_i^T\boldsymbol{K}_c\boldsymbol{e}_i - \frac{1}{2}\dot{\boldsymbol{z}}^T\boldsymbol{Q}\dot{\boldsymbol{z}} + \dot{\boldsymbol{\theta}}_0^T\boldsymbol{K}_\tau\boldsymbol{e}_i. \tag{114}$$

Since the last term may be written as

$$\dot{\boldsymbol{\theta}}_0^T\boldsymbol{K}_\tau\boldsymbol{e}_i = -\frac{1}{2}\left(\dot{\boldsymbol{\theta}}_0 - \boldsymbol{e}_i\right)^T\boldsymbol{K}_\tau\left(\dot{\boldsymbol{\theta}}_0 - \boldsymbol{e}_i\right) + \frac{1}{2}\dot{\boldsymbol{\theta}}_0^T\boldsymbol{K}_\tau\dot{\boldsymbol{\theta}}_0 + \frac{1}{2}\boldsymbol{e}_i^T\boldsymbol{K}_\tau\boldsymbol{e}_i, \tag{115}$$

the derivative of the Lyapunov function may be rearranged;

$$\begin{aligned}\dot{V}(\cdot) &= \dot{\boldsymbol{q}}^T\boldsymbol{\tau}_{ext} - \frac{1}{2}\dot{\boldsymbol{z}}^T\boldsymbol{Q}\dot{\boldsymbol{z}} - \frac{1}{2}\left(\dot{\boldsymbol{\theta}}_0 - \boldsymbol{e}_i\right)^T\boldsymbol{K}_\tau\left(\dot{\boldsymbol{\theta}}_0 - \boldsymbol{e}_i\right) - \sum_{k=2}^{q}\dot{\boldsymbol{\theta}}_{k-1}^T\boldsymbol{c}_{rk}\left(\dot{\boldsymbol{\theta}}_{k-1}\right) \\ &\quad -\frac{1}{2}\boldsymbol{e}_i^T\left(2\boldsymbol{K}_c - \boldsymbol{K}_\tau\right)\boldsymbol{e}_i - \frac{1}{2}\dot{\boldsymbol{\theta}}_0^T\left(2\boldsymbol{c}_{r1}\left(\dot{\boldsymbol{\theta}}_0\right) - \boldsymbol{K}_\tau\dot{\boldsymbol{\theta}}_0\right). \end{aligned} \tag{116}$$

The expression explicitly shows the transmission damping forces of each stage. For the case of free motion, $\boldsymbol{\tau}_{ext} = \boldsymbol{0}$. Assume that the dissipative function $\boldsymbol{c}_r\left(\dot{\boldsymbol{\theta}}\right)$ satisfies

$$\dot{\boldsymbol{\theta}}^T\boldsymbol{c}_r\left(\dot{\boldsymbol{\theta}}\right) \geq \sum_{i=1}^{pq}\alpha_i\dot{\theta}_i^2, \qquad \alpha_i > 0 \quad \forall i$$

and

$$\boldsymbol{c}_r(\boldsymbol{0}) = \boldsymbol{0},$$

or the transmission subsystem is fully damped. If the diagonal matrix current gain $\boldsymbol{K}_c$ is designed for the fast enough current tracking such that

$$\boldsymbol{K}_c > \frac{1}{2}\boldsymbol{K}_\tau, \tag{117}$$

and the 1st-stage (the motors) has been damped enough that

$$\dot{\boldsymbol{\theta}}_0^T\left(2\boldsymbol{c}_{r1}\left(\dot{\boldsymbol{\theta}}_0\right) - \boldsymbol{K}_\tau\dot{\boldsymbol{\theta}}_0\right) > 0, \tag{118}$$

or for the linear damped motors,

$$\boldsymbol{C}_{r1} > \frac{1}{2}\boldsymbol{K}_\tau,$$

where $\boldsymbol{C}_{r1}$ be the motor constant damping matrix, then it can be concluded that

$$\dot{V}\left(\boldsymbol{q}, \dot{\boldsymbol{q}}, \boldsymbol{\theta}, \dot{\boldsymbol{\theta}}, \boldsymbol{e}_i, \dot{\boldsymbol{z}}\right) \leq 0.$$

Therefore, Eq. 98 is a Lyapunov function. Applying the Lyapunov stability theorem, the closed loop system is stable. The stability is generally, however, local due to the local invertibility of the forward kinematics mapping. Asymptotic stability of the system may be stated through the help of the Lasalle's invariance principle. Essentially, if the equilibrium is the only point (in the invariant set) which makes $\dot{V}(\cdot) \equiv 0$, the system is asymptotically stable to the equilibrium point.

Consider Eq. 116. For the time derivative of the Lyapunov function to vanish identically, it is required that $\dot{\boldsymbol{\theta}} \equiv \boldsymbol{0}$, $\dot{\boldsymbol{z}} \equiv \boldsymbol{0}$, and $\boldsymbol{e}_i \equiv \boldsymbol{0}$. $\dot{\boldsymbol{\theta}} \equiv \boldsymbol{0}$ and $\dot{\boldsymbol{z}} \equiv \boldsymbol{0}$ imply $\ddot{\boldsymbol{\theta}} = \boldsymbol{0}$ and $\boldsymbol{\vartheta} \equiv \boldsymbol{0}$, respectively. With these conditions, closed loop dynamics of the drivetrain unit in Eq. 13 degenerates to

$$\begin{bmatrix} \boldsymbol{T}_1^T\boldsymbol{e}_1\left(\boldsymbol{T}_1\boldsymbol{\theta}_0 - \boldsymbol{\theta}_1\right) \\ -\boldsymbol{e}_1\left(\boldsymbol{T}_1\boldsymbol{\theta}_0 - \boldsymbol{\theta}_1\right) + \boldsymbol{T}_2^T\boldsymbol{e}_2\left(\boldsymbol{T}_2\boldsymbol{\theta}_1 - \boldsymbol{\theta}_2\right) \\ \vdots \\ -\boldsymbol{e}_{q-1}\left(\boldsymbol{T}_{q-1}\boldsymbol{\theta}_{q-2} - \boldsymbol{\theta}_{q-1}\right) + \boldsymbol{T}_q^T\boldsymbol{e}_q\left(\boldsymbol{T}_q\boldsymbol{\theta}_{q-1} - \boldsymbol{q}\right) \end{bmatrix} = \begin{bmatrix} \boldsymbol{T}_{q1}^T\boldsymbol{h}\left(\boldsymbol{\theta}_{qs}\right) \\ \boldsymbol{0} \\ \vdots \\ \boldsymbol{0} \end{bmatrix}. \tag{119}$$

Substituting

$$\boldsymbol{h}\left(\boldsymbol{\theta}_{qs}\right)=\boldsymbol{e}_{q}\left(\boldsymbol{T}_{q}\boldsymbol{\theta}_{(q-1)s}-\boldsymbol{\theta}_{qs}\right)$$

into the above equation and manipulating the expressions, one may deduce $\boldsymbol{q}=\boldsymbol{\theta}_{qs}$ and $\boldsymbol{\theta}_{q-1}=\boldsymbol{\theta}_{(q-1)s}$. Moreover, since $\dot{\boldsymbol{\theta}}\equiv\mathbf{0}$ and $\ddot{\boldsymbol{\theta}}=\mathbf{0}$, the drivetrain stationary model may be recalled. Comparing Eq. 24 and Eq. 119, the rotor angles subject to $\dot{V}\left(\cdot\right)\equiv 0$ must be such that $\boldsymbol{\theta}=\boldsymbol{\theta}_{s}$.

With the above findings, one may rewrite the equations in Eq. 119 pertaining to the first stage of the drivetrain as

$$\boldsymbol{T}_{1}^{T}\boldsymbol{e}_{1}\left(\boldsymbol{T}_{1}\boldsymbol{\theta}_{0s}-\boldsymbol{\theta}_{1s}\right)=\boldsymbol{T}_{q1}^{T}\boldsymbol{e}_{q}\left(\boldsymbol{T}_{q}\boldsymbol{\theta}_{(q-1)s}-\boldsymbol{\theta}_{qs}\right).$$

Under the condition $\dot{V}\left(\cdot\right)\equiv 0$, $\dot{\boldsymbol{\theta}}\equiv\mathbf{0}$ implies the values of $\boldsymbol{\theta}_{0s}$, $\boldsymbol{\theta}_{1s}$, and $\boldsymbol{\theta}_{(q-1)s}$ are unchanged. Consequently, $\boldsymbol{\theta}_{qs}$ will be constant, which means the unique values of the link angles $\boldsymbol{q}$ and hence $\dot{\boldsymbol{q}}\equiv\mathbf{0}$ and $\ddot{\boldsymbol{q}}=\mathbf{0}$. Closed loop dynamics of the robot in Eq. 1 thus becomes

$$\boldsymbol{g}\left(\boldsymbol{q}\right)=\boldsymbol{h}\left(\boldsymbol{\theta}_{qs}\right)=\boldsymbol{g}\left(\boldsymbol{\theta}_{qs}\right)-J\left(\boldsymbol{\theta}_{qs}\right)^{T}\boldsymbol{K}_{d}\left(\boldsymbol{f}\left(\boldsymbol{\theta}_{qs}\right)-\boldsymbol{x}_{d}\right).$$

This equation requires, in general, $\boldsymbol{q}=\boldsymbol{\theta}_{qs}$ and $\boldsymbol{f}\left(\boldsymbol{\theta}_{qs}\right)=\boldsymbol{x}_{d}$, or $\boldsymbol{\theta}_{qs}=\boldsymbol{f}^{-1}\left(\boldsymbol{x}_{d}\right)$. In other words, $\boldsymbol{q}=\boldsymbol{f}^{-1}\left(\boldsymbol{x}_{d}\right)$. Furthermore, the rotor angles of the drivetrain at the i^{th}-stage are determined by Eq. 112 regarding to the equilibrium condition $\dot{\boldsymbol{\theta}}\equiv\mathbf{0}$.

In summary, the system states corresponding to $\dot{V}\left(\cdot\right)\equiv 0$ are the coordinates of the (locally) unique equilibrium point. Applying the Lassalle's invariance principle, the closed loop system is (locally) asymptotically stable to the equilibrium point $\left(\boldsymbol{q},\dot{\boldsymbol{q}},\boldsymbol{\theta},\dot{\boldsymbol{\theta}},\boldsymbol{e}_{i},\dot{\boldsymbol{z}}\right)=\left(\boldsymbol{q}_{s},\mathbf{0},\boldsymbol{\theta}_{s},\mathbf{0},\mathbf{0},\mathbf{0}\right)$, where $\boldsymbol{q}_{s}$ and $\boldsymbol{\theta}_{s}$ are determined by Eqs. 111 and 112. Note that the motor current will converge to the reference value $\boldsymbol{i}_{m}$ of Eq. 83 and the estimated velocity related term $\boldsymbol{\vartheta}$ will finally be vanished identically. If the motor back-emf force cannot be precisely cancelled, the system stability will be indeterminate.

3.6.2. Proof of Passivity

Passivity is an important property for the robot system to perform interaction tasks successfully since the passive system will respond to the incoming input energy in a stable manner according to the underlying principle of energy conservation. As a result, the system will be robust to the disturbance and interact safely with the passive environment.

Definition 3. PASSIVE SYSTEM: [25] The system

$$\begin{aligned}\dot{\boldsymbol{x}} &= \boldsymbol{f}\left(\boldsymbol{x},\boldsymbol{u}\right)\\ \boldsymbol{y} &= \boldsymbol{h}\left(\boldsymbol{x},\boldsymbol{u}\right)\end{aligned}$$

is said to be passive if there exists a continuously differentiable lower bounded function $S\left(\boldsymbol{x}\right)$, called the storage function, such that

$$\boldsymbol{u}^{T}\boldsymbol{y}\geq\dot{S}\left(\boldsymbol{x}\right)+\epsilon\left\|\boldsymbol{u}\right\|^{2}+\delta\left\|\boldsymbol{y}\right\|^{2}+\rho\psi\left(\boldsymbol{x}\right).$$

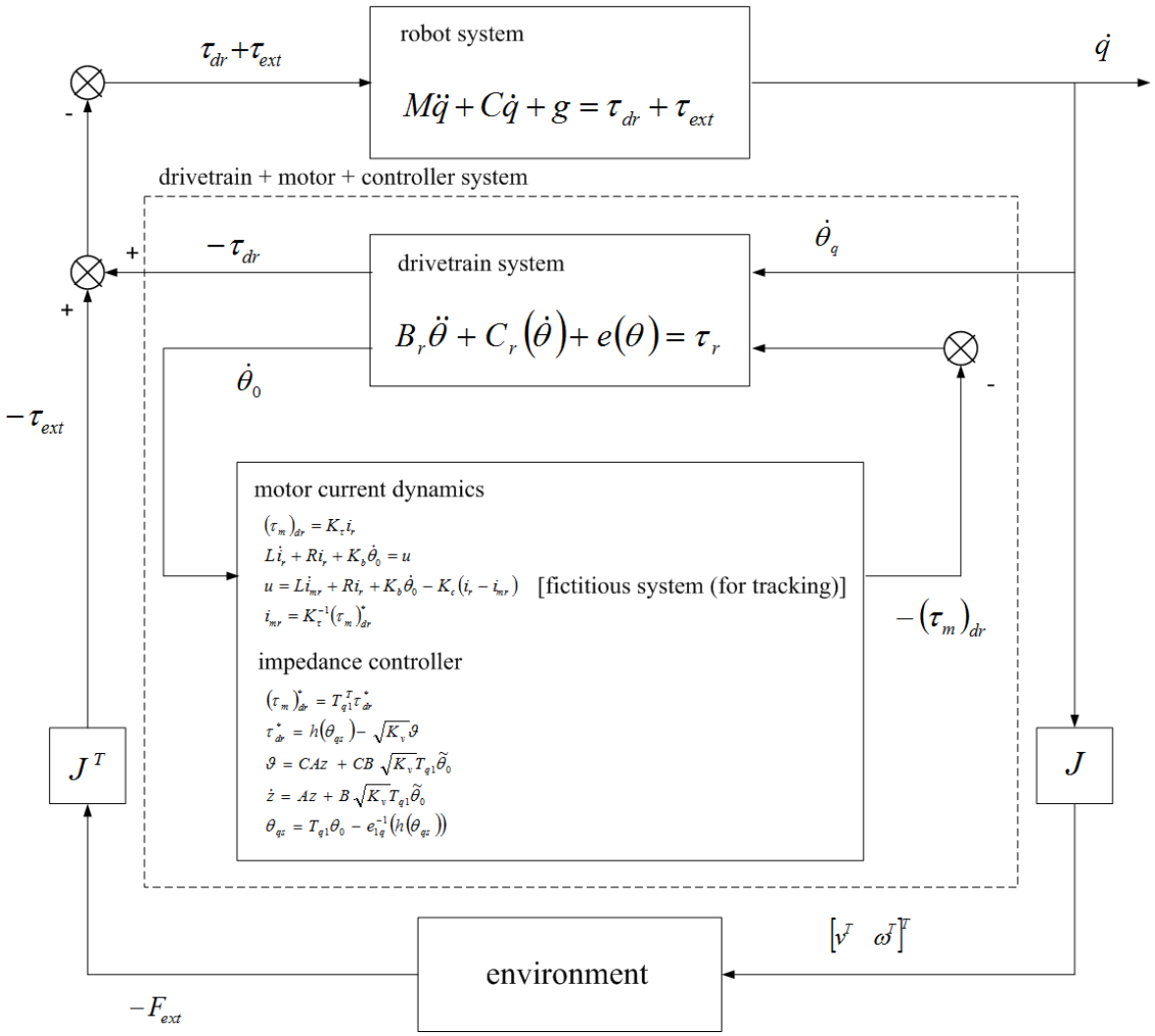

Figure 8: Feedback interconnection of three subsystems of the nonlinear flexible-joint robot controlled system interacting with the passive environment. The system as a whole is passive.

ϵ, δ, and ρ are nonnegative constants and $\psi(\boldsymbol{x}) : \mathbb{R}^m \rightarrow \mathbb{R}$ is a positive definite function of $\boldsymbol{x}$. The term $\rho\psi(\boldsymbol{x})$ is called the state dissipation rate. Furthermore, the system is said to be: *lossless* if $\boldsymbol{u}^T\boldsymbol{y} = \dot{S}(\boldsymbol{x})$; *input strictly passive* if $\boldsymbol{u}^T\boldsymbol{y} \geq \dot{S}(\boldsymbol{x}) + \epsilon\|\boldsymbol{u}\|^2$, $\exists\epsilon > 0$; *output strictly passive* if $\boldsymbol{u}^T\boldsymbol{y} \geq \dot{S}(\boldsymbol{x}) + \delta\|\boldsymbol{y}\|^2$, $\exists\delta > 0$; *state strictly passive* if $\boldsymbol{u}^T\boldsymbol{y} \geq \dot{S}(\boldsymbol{x}) + \rho\psi(\boldsymbol{x})$, $\exists\rho > 0$.

Figure 8 depicts the block diagram of the nonlinear flexible-joint robot controlled system. The system may be decomposed into three units representing the robot, the drivetrain, and the motor plus the controller subsystems. They are interconnecting in tandem feedback topology. The whole system is then coupled to the passive environment which maps the velocity flow $\dot{\boldsymbol{x}}$ to the effort torque $-\boldsymbol{F}_{ext}$. These quantities in the task space are transformed to the joint space as $\dot{\boldsymbol{q}}$ and $-\boldsymbol{\tau}_{ext}$ by the Jacobian matrix. Since the robot moves with the same velocity, the torque acting onto the robot will then be the reaction torque $\boldsymbol{\tau}_{ext}$.

Passivity of the robot subsystem Eq. 1 can be shown readily by the storage function

$$S_r\left(\boldsymbol{q},\dot{\boldsymbol{q}}\right)=\frac{1}{2}\dot{\boldsymbol{q}}^T\boldsymbol{M}\left(\boldsymbol{q}\right)\dot{\boldsymbol{q}}+V_g\left(\boldsymbol{q}\right), \tag{120}$$

with $V_g\left(\boldsymbol{q}\right)$ the gravitational potential function such that $\left|V_g\left(\boldsymbol{q}\right)\right|<\beta$, for some $\beta>0$. Hence, S_r is guaranteed to be bounded from below. Its time derivative along the trajectory of the robot dynamics is

$$\begin{aligned}\dot{S}_r &= \frac{1}{2}\dot{\boldsymbol{q}}^T\dot{\boldsymbol{M}}\left(\boldsymbol{q}\right)\dot{\boldsymbol{q}}+\dot{\boldsymbol{q}}^T\boldsymbol{M}\left(\boldsymbol{q}\right)\ddot{\boldsymbol{q}}+\boldsymbol{g}\left(\boldsymbol{q}\right)^T\dot{\boldsymbol{q}}\\ &= \dot{\boldsymbol{q}}^T\left(\boldsymbol{\tau}_{dr}+\boldsymbol{\tau}_{ext}\right).\end{aligned} \tag{121}$$

Note that the skew symmetry property of the matrix $\dot{\boldsymbol{M}}\left(\boldsymbol{q}\right)-2\boldsymbol{C}\left(\boldsymbol{q},\dot{\boldsymbol{q}}\right)$ is used. From definition 3, the robot subsystem is hence the lossless system mapping $\left(\boldsymbol{\tau}_{dr}+\boldsymbol{\tau}_{ext}\right)\mapsto\dot{\boldsymbol{q}}$.

Passivity of the modified drivetrain subsystem Eqs. 13 and 82 may be analyzed with the storage function

$$S_{dr}\left(\boldsymbol{q},\boldsymbol{\theta},\dot{\boldsymbol{\theta}}\right)=\frac{1}{2}\dot{\boldsymbol{\theta}}^T\boldsymbol{B}_r\dot{\boldsymbol{\theta}}+V_e\left(\boldsymbol{q},\boldsymbol{\theta}\right), \tag{122}$$

of which its derivative along the trajectory of the drivetrain dynamics is

$$\begin{aligned}\dot{S}_{dr} &= \dot{\boldsymbol{\theta}}^T\boldsymbol{B}_r\ddot{\boldsymbol{\theta}}+\frac{\partial V_e\left(\boldsymbol{q},\boldsymbol{\theta}\right)}{\partial\boldsymbol{q}}\dot{\boldsymbol{q}}+\frac{\partial V_e\left(\boldsymbol{q},\boldsymbol{\theta}\right)}{\partial\boldsymbol{\theta}}\dot{\boldsymbol{\theta}}\\ &= \dot{\boldsymbol{\theta}}_0^T\left(\boldsymbol{\tau}_m\right)_{dr}-\dot{\boldsymbol{q}}^T\boldsymbol{\tau}_{dr}-\dot{\boldsymbol{\theta}}^T\boldsymbol{c}_r\left(\dot{\boldsymbol{\theta}}\right).\end{aligned} \tag{123}$$

Equations 16, 18, 102, and 103 have been used to achieve the above expression. Therefore, if the transmission subsystem is fully damped, it will be the state strictly passive system mapping $\dot{\boldsymbol{q}}\mapsto-\boldsymbol{\tau}_{dr}$ at the port connecting the drivetrain to the robot, and $\left(\boldsymbol{\tau}_m\right)_{dr}\mapsto\dot{\boldsymbol{\theta}}_0$ at the port connecting to the motor electrical dynamics and the controller.

The last unit, which combines the motor current dynamics plus the controller, is characterized by the following set of equations:

$$\begin{aligned}\left(\boldsymbol{\tau}_m\right)_{dr} &= \boldsymbol{K}_\tau\boldsymbol{i}_r\\ \boldsymbol{L}\dot{\boldsymbol{i}}_r+\boldsymbol{R}\boldsymbol{i}_r+\boldsymbol{K}_b\dot{\boldsymbol{\theta}}_0 &= \boldsymbol{u}\\ \boldsymbol{u} &= \boldsymbol{L}\dot{\boldsymbol{i}}_{mr}+\boldsymbol{R}\boldsymbol{i}_r+\boldsymbol{K}_b\dot{\boldsymbol{\theta}}_0-\boldsymbol{K}_c\left(\boldsymbol{i}_r-\boldsymbol{i}_{mr}\right)\\ \boldsymbol{i}_{mr} &= \boldsymbol{K}_\tau^{-1}\left(\boldsymbol{\tau}_m\right)_{dr}^*\\ \left(\boldsymbol{\tau}_m\right)_{dr}^* &= \boldsymbol{T}_{q1}^T\boldsymbol{\tau}_{dr}^*\\ \boldsymbol{\tau}_{dr}^* &= \boldsymbol{h}\left(\boldsymbol{\theta}_{qs}\right)-\sqrt{\boldsymbol{K}_v}\boldsymbol{\vartheta}\\ \boldsymbol{\vartheta} &= \boldsymbol{C}\boldsymbol{A}\boldsymbol{z}+\boldsymbol{C}\boldsymbol{B}\sqrt{\boldsymbol{K}_v}\boldsymbol{T}_{q1}\tilde{\boldsymbol{\theta}}_0\\ \dot{\boldsymbol{z}} &= \boldsymbol{A}\boldsymbol{z}+\boldsymbol{B}\sqrt{\boldsymbol{K}_v}\boldsymbol{T}_{q1}\tilde{\boldsymbol{\theta}}_0\\ \boldsymbol{\theta}_{qs} &= \boldsymbol{T}_{q1}\boldsymbol{\theta}_0-\boldsymbol{e}_{1q}^{-1}\left(\boldsymbol{h}\left(\boldsymbol{\theta}_{qs}\right)\right),\end{aligned} \tag{124}$$

for the voltage mode controlled motors. It is assumed that the cancellation of the motor current/angular velocity terms in motor dynamics and the estimation of the transmitted torque are perfect. Thus, passivity of this unit may be assured by the storage function

$$S_{mc}\left(\boldsymbol{e}_i, \dot{\boldsymbol{z}}, \boldsymbol{\theta}_0\right) = \frac{1}{2}\boldsymbol{e}_i^T \boldsymbol{L}\boldsymbol{e}_i + \frac{1}{2}\dot{\boldsymbol{z}}^T \boldsymbol{P}\dot{\boldsymbol{z}} - V_{\bar{h}}\left(\boldsymbol{T}_{q1}\boldsymbol{\theta}_0\right). \tag{125}$$

The first two terms show the state kinetic energy-like functions of the current tracking controller and the velocity estimator unit. The last term is the negative of the potential energy, Eq. 97, of the proposed impedance control law, $\boldsymbol{\tau}_{dr}^*$, for the negative feedback configuration. Time derivative along the trajectory of the current tracking and velocity estimator dynamics is thus

$$\begin{aligned}
\dot{S}_{mc} &= \boldsymbol{e}_i^T \boldsymbol{L}\dot{\boldsymbol{e}}_i + \frac{1}{2}\ddot{\boldsymbol{z}}^T \boldsymbol{P}\dot{\boldsymbol{z}} + \frac{1}{2}\dot{\boldsymbol{z}}^T \boldsymbol{P}\ddot{\boldsymbol{z}} - \frac{\partial V_{\bar{h}}\left(\boldsymbol{T}_{q1}\boldsymbol{\theta}_0\right)}{\partial\left(\boldsymbol{T}_{q1}\boldsymbol{\theta}_0\right)}\boldsymbol{T}_{q1}\dot{\boldsymbol{\theta}}_0 \\
&= -\boldsymbol{e}_i^T \boldsymbol{K}_c\boldsymbol{e}_i - \frac{1}{2}\dot{\boldsymbol{z}}^T \boldsymbol{Q}\dot{\boldsymbol{z}} - \dot{\boldsymbol{\theta}}_0^T \boldsymbol{T}_{q1}^T\left(\boldsymbol{h}\left(\boldsymbol{\theta}_{qs}\right) - \sqrt{\boldsymbol{K}_v}\boldsymbol{\vartheta}\right) \\
&= -\boldsymbol{e}_i^T \boldsymbol{K}_c\boldsymbol{e}_i - \frac{1}{2}\dot{\boldsymbol{z}}^T \boldsymbol{Q}\dot{\boldsymbol{z}} - \dot{\boldsymbol{\theta}}_0^T\left(\boldsymbol{\tau}_m\right)_{dr}^*,
\end{aligned}$$

using the current tracking error dynamics Eq. 84, the KY lemma Eqs. 61-62, and recognizing the stationary cancellation of the gravity torque and generation of the desired compliance as the negative of the differential of $V_{\bar{h}}\left(\boldsymbol{T}_{q1}\boldsymbol{\theta}_0\right)$. Furthermore, since

$$\left(\boldsymbol{\tau}_m\right)_{dr} = \left(\boldsymbol{\tau}_m\right)_{dr}^* + \boldsymbol{K}_\tau \boldsymbol{e}_i,$$

the time rate of change of the storage function $S_{mc}\left(\cdot\right)$ may be written as

$$\dot{S}_{mc} = -\dot{\boldsymbol{\theta}}_0^T\left(\boldsymbol{\tau}_m\right)_{dr} - \boldsymbol{e}_i^T \boldsymbol{K}_c\boldsymbol{e}_i - \frac{1}{2}\dot{\boldsymbol{z}}^T \boldsymbol{Q}\dot{\boldsymbol{z}} + \dot{\boldsymbol{\theta}}_0^T \boldsymbol{K}_\tau \boldsymbol{e}_i.$$

Employing the decomposition of the cross term in Eq. 115, the equation becomes

$$\dot{S}_{mc} = -\dot{\boldsymbol{\theta}}_0^T\left(\boldsymbol{\tau}_m\right)_{dr} - \boldsymbol{e}_i^T \boldsymbol{K}_c\boldsymbol{e}_i - \frac{1}{2}\dot{\boldsymbol{z}}^T \boldsymbol{Q}\dot{\boldsymbol{z}} - \frac{1}{2}\left(\dot{\boldsymbol{\theta}}_0 - \boldsymbol{e}_i\right)^T \boldsymbol{K}_\tau\left(\dot{\boldsymbol{\theta}}_0 - \boldsymbol{e}_i\right) + \frac{1}{2}\dot{\boldsymbol{\theta}}_0^T \boldsymbol{K}_\tau \dot{\boldsymbol{\theta}}_0 + \frac{1}{2}\boldsymbol{e}_i^T \boldsymbol{K}_\tau \boldsymbol{e}_i. \tag{126}$$

Because the last two terms are always non-negative, passivity and passive mapping $\dot{\boldsymbol{\theta}}_0 \mapsto -\left(\boldsymbol{\tau}_m\right)_{dr}$ of this subsystem solely cannot be concluded. This is due to the current tracking error dynamics. On the other hand, it implies that the third subsystem will be state strictly passive if the motors are current-controlled.

Nevertheless, one may combine the drivetrain, motor, and controller subsystems (second and third units) altogether. Consequently, the storage function of this integral unit may be proposed as the sum of the storage functions of the subsystems;

$$S_{dr,mc}\left(\boldsymbol{q}, \boldsymbol{\theta}, \dot{\boldsymbol{\theta}}, \boldsymbol{e}_i, \dot{\boldsymbol{z}}\right) = S_{dr}\left(\cdot\right) + S_{mc}\left(\cdot\right). \tag{127}$$

Hence it is obvious that the time derivative will merely be the sum of the derivative of these subsystem storage functions;

$$\dot{S}_{dr,mc}\left(\cdot\right) = \dot{S}_{dr}\left(\cdot\right) + \dot{S}_{mc}\left(\cdot\right)$$

$$= -\dot{\boldsymbol{q}}^T\boldsymbol{\tau}_{dr} - \dot{\boldsymbol{\theta}}^T\boldsymbol{c}_r\left(\dot{\boldsymbol{\theta}}\right) - \boldsymbol{e}_i^T\boldsymbol{K}_c\boldsymbol{e}_i - \frac{1}{2}\dot{\boldsymbol{z}}^T\boldsymbol{Q}\dot{\boldsymbol{z}}$$
$$-\frac{1}{2}\left(\dot{\boldsymbol{\theta}}_0 - \boldsymbol{e}_i\right)^T\boldsymbol{K}_\tau\left(\dot{\boldsymbol{\theta}}_0 - \boldsymbol{e}_i\right) + \frac{1}{2}\dot{\boldsymbol{\theta}}_0^T\boldsymbol{K}_\tau\dot{\boldsymbol{\theta}}_0 + \frac{1}{2}\boldsymbol{e}_i^T\boldsymbol{K}_\tau\boldsymbol{e}_i. \quad (128)$$

Under the conditions of Eqs. 117-118 and if the transmission is fully damped, Eq. 128 may be rearranged as

$$\dot{S}_{dr,mc}(\cdot) = -\dot{\boldsymbol{q}}^T\boldsymbol{\tau}_{dr} - \frac{1}{2}\dot{\boldsymbol{z}}^T\boldsymbol{Q}\dot{\boldsymbol{z}} - \frac{1}{2}\left(\dot{\boldsymbol{\theta}}_0 - \boldsymbol{e}_i\right)^T\boldsymbol{K}_\tau\left(\dot{\boldsymbol{\theta}}_0 - \boldsymbol{e}_i\right) - \sum_{k=2}^{q}\dot{\boldsymbol{\theta}}_{k-1}^T\boldsymbol{c}_{rk}\left(\dot{\boldsymbol{\theta}}_{k-1}\right)$$
$$-\frac{1}{2}\boldsymbol{e}_i^T\left(2\boldsymbol{K}_c - \boldsymbol{K}_\tau\right)\boldsymbol{e}_i - \frac{1}{2}\dot{\boldsymbol{\theta}}_0^T\left(2\boldsymbol{c}_{r1}\left(\dot{\boldsymbol{\theta}}_0\right) - \boldsymbol{K}_\tau\dot{\boldsymbol{\theta}}_0\right). \quad (129)$$

Consequently, the state strictly passive mapping $\dot{\boldsymbol{q}} \mapsto -\boldsymbol{\tau}_{dr}$ at the port connecting to the robot of the integrated drivetrain, motor, and controller subsystems is ensured. As a result, Fig. 8 may be view as the negative feedback interconnection of two passive systems. Further, it is possible that the robot is coupled to the passive environment.

Theorem 4. FEEDBACK INTERCONNECTION OF THE SYSTEMS: [25] The negative feedback interconnection of two passive systems is passive.

Applying the stated theorem 4, proof of the passivity of the nonlinear flexible-joint robot controlled system interacting with the passive environment is thus completed.

4. Simulation and Discussions

In this section, a two DOF cable-pulley driven flexible joint robot with the proposed task space impedance control law in section 3 is studied and simulated. This robot, shown in Fig. 9, is intended to be a prototype supporting the fundamental study of the cable driven robot which will further be useful in developing the whole arm of the ongoing service robot project. The prototype is capable of providing the output motion at the end of the shoulder link in the pitch and yaw directions that emulates the principal motion performed by the human shoulder. Natural coordinates describing the position are thus the pitch and yaw angles, denoted as θ_p and θ_y in turn.

Fig. 10 depicts the winches and pulleys arrangement of the flexible joint robot. Starting from the input side, the motor axle is coupled to winch#1, which then drives winch#2 through the wrapped cables. Winch#2 in turn drives pulley#1 (for right winch) and pulley#2 (for left winch). Together with pulley#3, these pulleys form the differential mechanism which produces the rotational motion of the output shoulder link about two mutually perpendicular axes. For the specific pose of the shoulder compound joint mechanism, the axes of rotation causes the motion of the shoulder link end tip in the pitch and yaw directions. Note that the differential mechanism in this work is implemented through the cables and stepped pulleys. Also, the additional pulley#4 is not attached with any cable. Its purposes are to counter pulley#3 and to strengthen the structure.

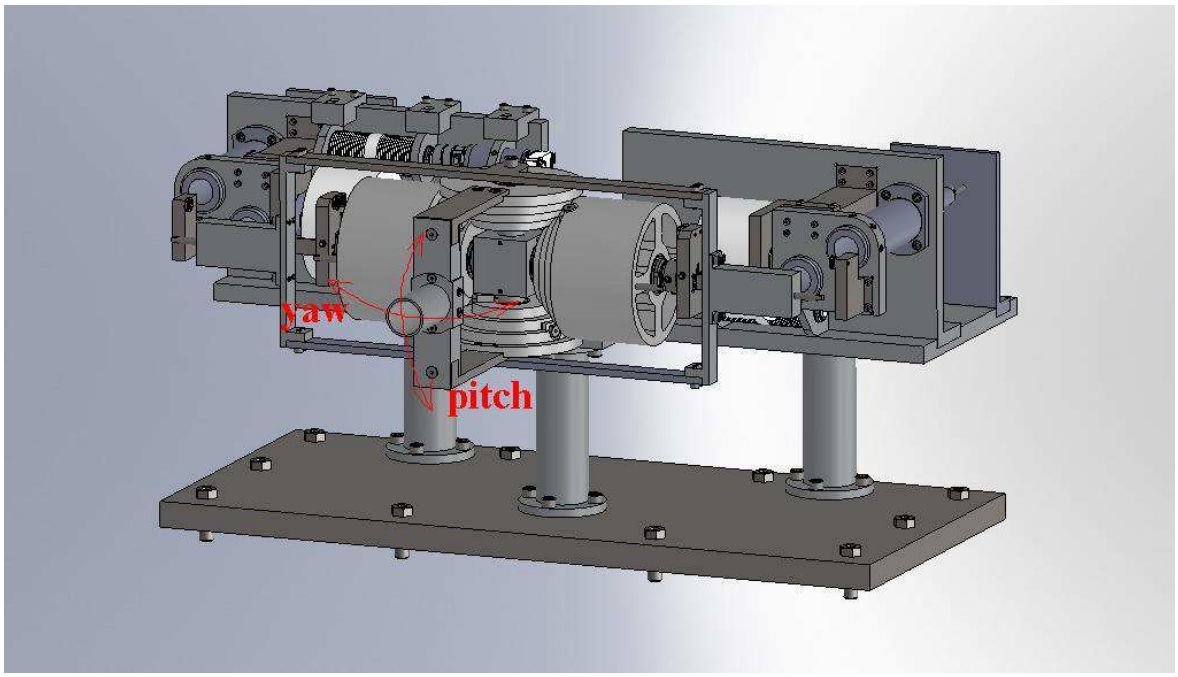

Figure 9: CAD drawing of the prototypical two DOF cable-pulley driven flexible joint robot.

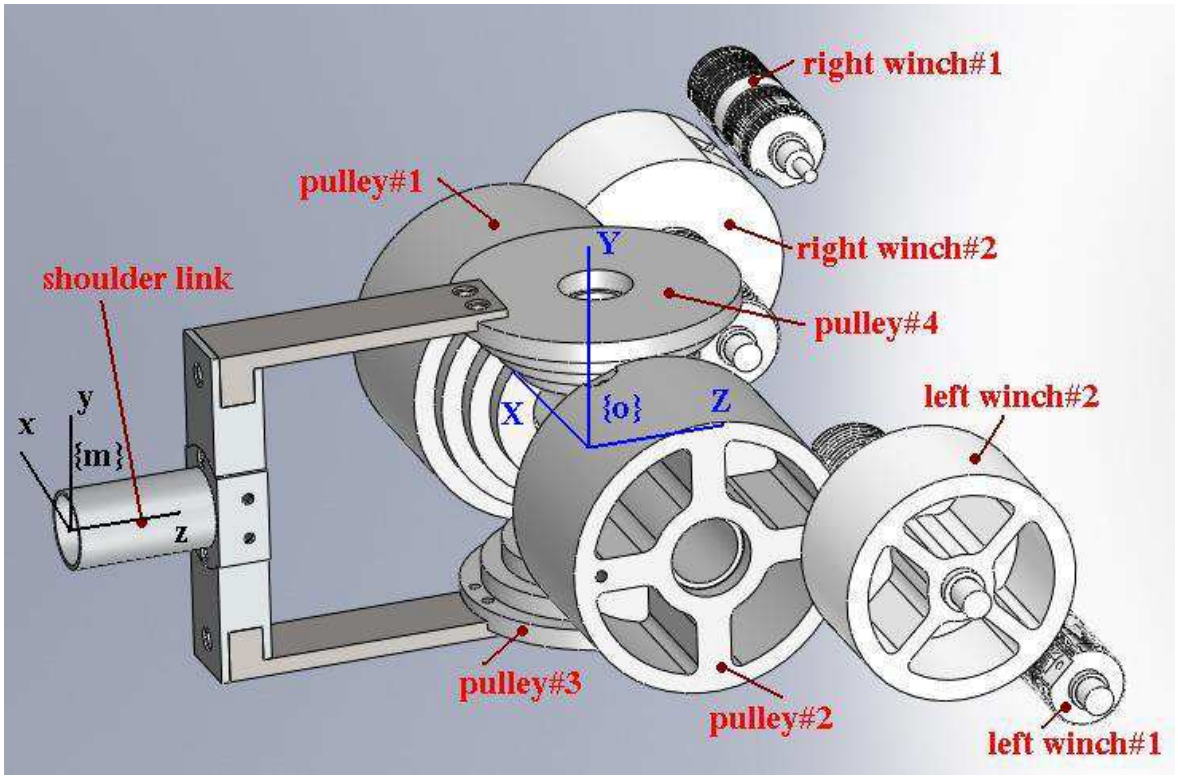

Figure 10: Winches and pulleys arrangement in the drivetrain unit of the flexible joint robot.

Furthermore, the robot is equipped with the patented pending counterbalancing mechanism [30] invented to reduce the amount of torque commonly required from the motors to sustain the weight and hence to improve the safety of the robot. Basically, motion of pulley#1 and pulley#2 are transmitted via the cable routing to elongate a set of springs. With the appropriate spring stiffness used, the generated torque can match with the configuration dependent gravitational torque. The consideration may also be acquired from the viewpoint of maintaining the total potential energy of the system.

4.1. Modeling of the Robot and Its Drivetrain

Developed framework of the robot and its drivetrain modeling in section 2 is applicable to this prototype. Furthermore, the technique of bond graph modeling shall be employed in order to promote more systematic modeling and to gain deeper understanding of the system physics.

4.1.1. Kinematics

Modeling analysis begins with the kinematics of the system. Referring to the pulleys and winches arrangement of the flexible transmission in Fig. 10, let θ_m, θ_w, θ_1, θ_2, θ_p, and θ_y be the angular position of the motor, winch, pulley#1, pulley#2, and the pitch and yaw angles of the shoulder link, respectively. Positive direction of the rotations are defined to be along $+X$, $-X$, and $+X$-axis for winch#1, winch#2, and pulley#1 and pulley#2. Positive pitch and yaw angles happen along $+x$ and $+y$-axis, respectively. Positive direction of each motor, however, depends on the manufacturer as well as the orientation of the installed axis. For this system, positive turn of the left and right motors occur about $+X$ and $-X$-axis. Interconnection between these parts by the cables and structures poses the following kinematical constraints:

$$\begin{aligned} \dot{\theta}_{w1r} &= -\dot{\theta}_{mr} & \dot{\theta}_{w1l} &= \dot{\theta}_{ml} \\ \dot{\theta}_{w2r} &= n_{2r}\dot{\theta}_{w1r} & \dot{\theta}_{w2l} &= n_{2l}\dot{\theta}_{w1l} \\ \dot{\theta}_1 &= n_{3r}\dot{\theta}_{w2r} & \dot{\theta}_2 &= n_{3l}\dot{\theta}_{w2l} \\ \dot{\theta}_p &= \frac{1}{2}\left(\dot{\theta}_1 + \dot{\theta}_2\right) & \dot{\theta}_y &= \frac{1}{2}\left(\dot{\theta}_1 - \dot{\theta}_2\right). \end{aligned} \tag{130}$$

This particular system is designed such that the transmission ratio at the 2$^{\text{nd}}$ and the 3$^{\text{rd}}$-stage are all be $\frac{1}{3}$. According to the notations introduced in subsection 2.2,

$$\boldsymbol{T}_1 = \begin{bmatrix} -1 & 0 \\ 0 & 1 \end{bmatrix} \qquad \boldsymbol{T}_2 = \begin{bmatrix} \frac{1}{3} & 0 \\ 0 & \frac{1}{3} \end{bmatrix} \qquad \boldsymbol{T}_3 = \begin{bmatrix} \frac{1}{3} & 0 \\ 0 & \frac{1}{3} \end{bmatrix} \qquad \boldsymbol{T}_q = \boldsymbol{T}_4 = \begin{bmatrix} \frac{1}{2} & \frac{1}{2} \\ \frac{1}{2} & -\frac{1}{2} \end{bmatrix}, \tag{131}$$

where

$$\dot{\boldsymbol{\theta}}_0 = \begin{bmatrix} \dot{\theta}_{mr} & \dot{\theta}_{ml} \end{bmatrix}^T \qquad \dot{\boldsymbol{\theta}}_{w1} = \dot{\boldsymbol{\theta}}_1 = \begin{bmatrix} \dot{\theta}_{w1r} & \dot{\theta}_{w1l} \end{bmatrix}^T \qquad \dot{\boldsymbol{\theta}}_{w2} = \dot{\boldsymbol{\theta}}_2 = \begin{bmatrix} \dot{\theta}_{w2r} & \dot{\theta}_{w2l} \end{bmatrix}^T$$
$$\dot{\boldsymbol{\theta}}_d = \dot{\boldsymbol{\theta}}_3 = \begin{bmatrix} \dot{\theta}_1 & \dot{\theta}_2 \end{bmatrix}^T \qquad \dot{\boldsymbol{\theta}}_q = \begin{bmatrix} \dot{\theta}_p & \dot{\theta}_y \end{bmatrix}^T.$$

Kinematics of the robot may be analyzed using the rotation matrix. Referring to Fig. 10, position vector of the shoulder link end point relative to the origin of $\{XYZ\}$ described in $\{xyz\}$ is

$$^{\{xyz\}}\boldsymbol{x} = \begin{bmatrix} 0 & 0 & -l_o \end{bmatrix}^T$$

for which $l_o = 315$ mm is the shoulder link length from the center of rotation. Besides, the relative rotation between $\{xyz\}$ and $\{XYZ\}$ is described by the rotation matrix

$$^{\{XYZ\}}R_{\{xyz\}} = R_{x,\theta_p}R_{y,\theta_y} = \begin{bmatrix} c_y & 0 & s_y \\ s_p s_y & c_p & -s_p c_y \\ -c_p s_y & s_p & c_p c_y \end{bmatrix}. \tag{132}$$

Therefore, position vector $\boldsymbol{x}$ described in the reference frame $\{XYZ\}$ is

$$\begin{aligned} ^{\{XYZ\}}\boldsymbol{x} &= {}^{\{XYZ\}}R_{\{xyz\}}{}^{\{xyz\}}\boldsymbol{x} \\ &= \begin{bmatrix} -l_o s_y & l_o s_p c_y & -l_o c_p c_y \end{bmatrix}^T. \end{aligned} \tag{133}$$

Velocity of the end point may be determined simply from the fact that its motion is the pure rotation about the origin of the fixed frame $\{XYZ\}$. If $\boldsymbol{\omega}$ is the link angular velocity, the end point velocity expressed in the moving frame $\{xyz\}$ is

$$^{\{xyz\}}\boldsymbol{v}_e = \boldsymbol{\omega} \times \boldsymbol{x} = \begin{bmatrix} -l_o\dot{\theta}_y & l_o\dot{\theta}_p c_y & 0 \end{bmatrix}^T. \tag{134}$$

Consequently, the Jacobian matrix represented in $\{xyz\}$ becomes

$$^{\{xyz\}}J = \begin{bmatrix} 0 & -l_o \\ l_o c_y & 0 \\ 0 & 0 \end{bmatrix}. \tag{135}$$

In addition, the Jacobian matrix expressed in $\{XYZ\}$ may then be determined as

$$\begin{aligned} ^{\{XYZ\}}J &= {}^{\{XYZ\}}R_{\{xyz\}}{}^{\{xyz\}}J \\ &= \begin{bmatrix} 0 & -l_o c_y \\ l_o c_p c_y & -l_o s_p s_y \\ l_o s_p c_y & l_o c_p s_y \end{bmatrix}. \end{aligned} \tag{136}$$

4.1.2. Compliance

After the kinematical analysis, dynamics of the system will then be considered. Since the practical robot system is too complicated for anyone to comprehend the complete dynamics in a whole single step, dynamics of each subsystem shall be analyzed separately first. This subsection concentrates on the compliance behavior of the transmission unit. At the 1st-stage, power from the motor is delivered to winch#1 via the disk coupling. Thus, the transmission compliance is simply the inverse of the coupling stiffness. Its stiffness constant of 5700 [N/m] is taken from the data sheet. For the 2nd

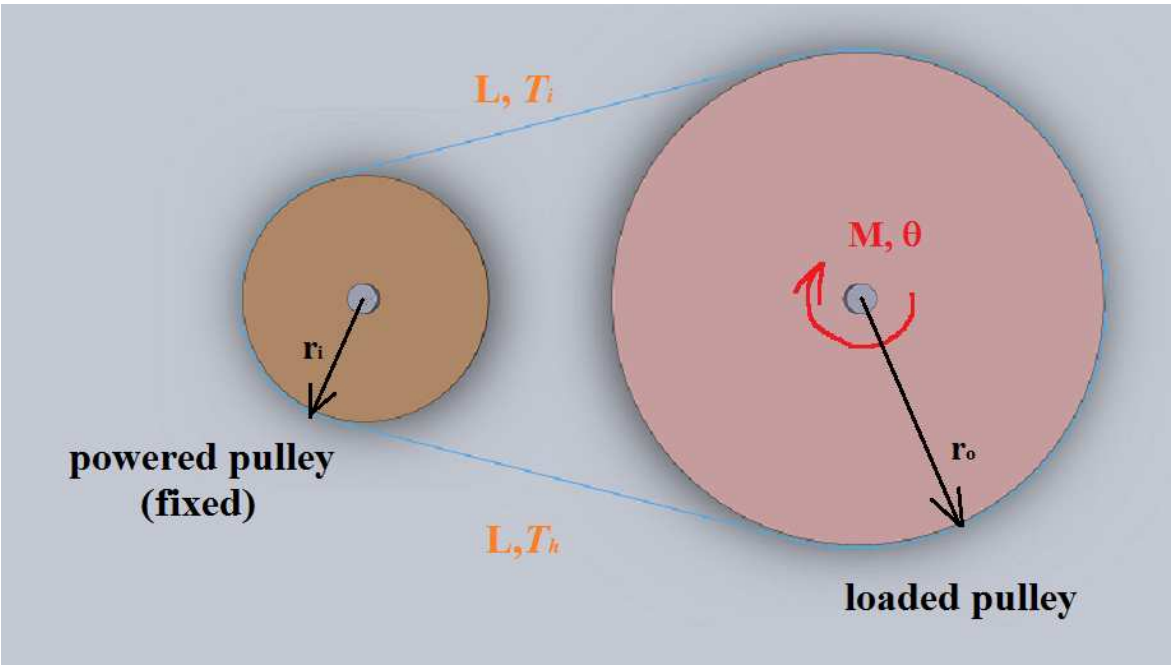

Figure 11: Simple drive unit and the parameters related to its transmission compliance.

and the 3rd-stage, cable and pulley mechanisms are the root of the flexibilty. The transmission here is constructed from winding the cable between the powered and the loaded pulleys as schematically drawn in Fig. 11. This is called the simple drive unit.

Based on the assumption that the cables have been securely wrapped around the pulleys with proper pretension so the total slippage between the cable and the pulley groove over the circuit is negligible, the explicit torque-angle deflection equation may be determined [28] as

$$\theta = \frac{T_o}{EA\mu_{\text{eff}}}\left[\left(\frac{me^m}{e^m-1}-1\right)(1+GF)-\log\frac{me^m}{e^m-1}\right]. \tag{137}$$

This constitutive equation involves several parameters. The cable circuit, with the properties E and A for the Young modulus and the effective cross-sectional area, has been pretensioned to T_o. m is the dimensionless torque of the loaded torque M applied at the loaded pulley of radius r_o. It is calculated by

$$m = \frac{M}{r_o T_o}. \tag{138}$$

μ_{eff} is the effective coefficient of friction determined by

$$\mu_{\text{eff}} = \left(\frac{1}{\mu_{r_o}} + \frac{r_i}{r_o}\frac{1}{\mu_{r_i}}\right)^{-1}, \tag{139}$$

where the coefficients of friction between the powered/loaded pulleys (radius r_i and r_o, respectively) and the cables are μ_{r_i} and μ_{r_o}. Finally, the symbol GF stands for the geometric friction number

$$GF = \frac{L\mu_{\text{eff}}}{r}, \tag{140}$$

Table 1: Numerical values of the parameters for the flexible cable-pulley driven drivetrain

Parameters	2^{nd}-stage	3^{rd}-stage	4^{th}-stage
pretension, T_o	74 [N]	185 [N]	238 [N]
Young modulus, E	200 [GPa]	200 [GPa]	200 [GPa]
cable cross sectional area, A	1.767 [mm^2]	3.534 [mm^2]	7.069 [mm^2]
effective coeff. friction, μ_{eff}	0.1	0.1	0.1
effective output pulley radius, r	67.5 [mm]	81.0 [mm]	63 [mm]
geometric friction number, GF	45×10^{-3}	41×10^{-3}	0

where L is the cable length of the unwrapped portion on each side. This term characterizes the deflection response of the system to the applied torque. Intuitively from Eq. 137, high value of GF yields a drive with low and nearly linear stiffness. On the other hand, low GF value will be found in the transmission system that possesses high stiffness but softening spring characteristics.

Equation 137, expressing the deflected angle θ as an explicit nonlinear function of the loaded torque M, is indeed the inverse function of the nonlinear elastic force function $e(\cdot) = M(\theta)$ for the flexible joint constructed from the cable-pulley mechanism. Unfortunately, it is not possible to determine the closed form of $M(\theta)$ from the deflection equation. Nevertheless, this is not necessary for the proposed control scheme. It should be mentioned that Eq. 137 is derived with an assumption of $GF \approx 0$, which is valid for the simulated system. Numerical values of the pertinent parameters from the design are tabulated in Table 1.

Nevertheless, the dimensionless stiffness may be determined from Eq. 137 by evaluating the derivative of θ with respect to m and resolving for its inverse:

$$k(m) = \frac{dm}{d\theta} = \left(\frac{d\theta}{dm}\right)^{-1} = \frac{EA\mu_{\text{eff}}}{T_o}\left(\frac{(e^m-1)^2}{e^m(e^m-m-1)}\right)\left(1+GF-\frac{e^m-1}{me^m}\right)^{-1}. \tag{141}$$

The stiffness of this simple drive unit, as a function of the applied torque though, is thus

$$K(m) = \frac{dM}{d\theta} = \frac{dM}{dm}\frac{dm}{d\theta} = EA\mu_{\text{eff}}r_o\left(\frac{(e^m-1)^2}{e^m(e^m-m-1)}\right)\left(1+GF-\frac{e^m-1}{me^m}\right)^{-1}. \tag{142}$$

As M approaches zero, the stiffness value converges to

$$K|_{M\to 0} = \lim_{M\to 0} K = \frac{2EAr_o^2}{L}. \tag{143}$$

Analysis for the simple drive unit can be extended to the case of the differential drive unit that is employed in the 4^{th}-stage of the drivetrain. As a result, the torque-angle deflection equation along the pitch DOF may be written as

$$\theta_p = \frac{T_o}{EA\mu_{\text{eff}}}\left[\left(\frac{m_p e^{m_p/2}}{2\left(e^{m_p/2}-1\right)}-1\right)(1+GF)-\log\frac{m_p e^{m_p/2}}{2\left(e^{m_p/2}-1\right)}\right]. \tag{144}$$

In this case, m_p is the dimensionless torque of the loaded torque M_p applied along the pitch direction, which would induce the counter-tension force in the cable circuit having the effective moment arm of the pulley radius r about the pitch axis. It is calculated by

$$m_p = \frac{M_p}{rT_o}. \tag{145}$$

Since the pulleys of the differential drive unit are assembled in a manner that the axes of the input and output pulleys be perpendicular and their edges are in contact with each other, effectively $GF = 0$. In a similar manner, the torque-angle deflection equation along the yaw DOF may be derived as

$$\theta_y = \frac{T_o}{EA\mu_{\text{eff}}}\left[\left(\frac{m_y e^{m_y/2}}{2\left(e^{m_y/2}-1\right)}-1\right)(1+GF) - \log\frac{m_y e^{m_y/2}}{2\left(e^{m_y/2}-1\right)}\right], \tag{146}$$

for the dimensionless torque m_y from the loaded torque M_y applied along the yaw direction calculated by

$$m_y = \frac{M_y}{rT_o}. \tag{147}$$

Likewise, the stiffness along the pitch and yaw directions may be determined from the above deflection equations. The results are

$$K_p\left(m_p\right) = \frac{dM_p}{d\theta_p} = 2EA\mu_{\text{eff}} r\left(\frac{\left(e^{m_p/2}-1\right)^2}{e^{m_p/2}\left(e^{m_p/2}-\frac{m_p}{2}-1\right)}\right)\left(1+GF-\frac{2\left(e^{m_p/2}-1\right)}{m_p e^{m_p/2}}\right)^{-1} \tag{148}$$

and

$$K_y\left(m_y\right) = \frac{dM_y}{d\theta_y} = 2EA\mu_{\text{eff}} r\left(\frac{\left(e^{m_y/2}-1\right)^2}{e^{m_y/2}\left(e^{m_y/2}-\frac{m_y}{2}-1\right)}\right)\left(1+GF-\frac{2\left(e^{m_y/2}-1\right)}{m_y e^{m_y/2}}\right)^{-1}. \tag{149}$$

Stiffnesses are maximized when the drive unit bears no load, of which their values are

$$K_p|_{M_p\to 0} = \lim_{M_p\to 0} K_p = \frac{4EAr^2}{L} \tag{150}$$

and

$$K_y|_{M_y\to 0} = \lim_{M_y\to 0} K_y = \frac{4EAr^2}{L}. \tag{151}$$

Because the unwrapped segment of the cables for the differential drive is nearly zero, the stiffness at this stage can be very high.

The above deformation functions of various elastic elements in the transmission stages may be grouped into vector functions corresponding to the notations in subsection 2.2 to assist the development of the control law. They are

$$\begin{aligned}
\boldsymbol{e}_{w1}^{-1}\left(\boldsymbol{\tau}_{w1}\right) = \boldsymbol{e}_1^{-1}\left(\boldsymbol{\tau}_{w1}\right) &= \begin{bmatrix} 175.44\times 10^{-6}\tau_{w1r} \\ 175.44\times 10^{-6}\tau_{w1l} \end{bmatrix} \\
\boldsymbol{e}_{w2}^{-1}\left(\boldsymbol{\tau}_{w2}\right) = \boldsymbol{e}_2^{-1}\left(\boldsymbol{\tau}_{w2}\right) &= \begin{bmatrix} \frac{T_o}{EA\mu_{\text{eff}}}\left[\left(\frac{m_{w2r}e^{m_{w2r}}}{e^{m_{w2r}}-1}-1\right)(1+GF)-\log\frac{m_{w2r}e^{m_{w2r}}}{e^{m_{w2r}}-1}\right] \\ \frac{T_o}{EA\mu_{\text{eff}}}\left[\left(\frac{m_{w2l}e^{m_{w2l}}}{e^{m_{w2l}}-1}-1\right)(1+GF)-\log\frac{m_{w2l}e^{m_{w2l}}}{e^{m_{w2l}}-1}\right] \end{bmatrix}
\end{aligned}$$

$$\begin{aligned} \boldsymbol{e}_d^{-1}(\boldsymbol{\tau}_d) = \boldsymbol{e}_3^{-1}(\boldsymbol{\tau}_d) &= \begin{bmatrix} \frac{T_o}{EA\mu_{\text{eff}}}\left[\left(\frac{m_1 e^{m_1}}{e^{m_1}-1}-1\right)(1+GF)-\log\frac{m_1 e^{m_1}}{e^{m_1}-1}\right] \\ \frac{T_o}{EA\mu_{\text{eff}}}\left[\left(\frac{m_2 e^{m_2}}{e^{m_2}-1}-1\right)(1+GF)-\log\frac{m_2 e^{m_2}}{e^{m_2}-1}\right] \end{bmatrix} \\ \boldsymbol{e}_q^{-1}(\boldsymbol{\tau}_{dr}) &= \begin{bmatrix} \frac{T_o}{EA\mu_{\text{eff}}}\left[\left(\frac{m_p e^{m_p/2}}{2\left(e^{m_p/2}-1\right)}-1\right)(1+GF)-\log\frac{m_p e^{m_p/2}}{2\left(e^{m_p/2}-1\right)}\right] \\ \frac{T_o}{EA\mu_{\text{eff}}}\left[\left(\frac{m_y e^{m_y/2}}{2\left(e^{m_y/2}-1\right)}-1\right)(1+GF)-\log\frac{m_y e^{m_y/2}}{2\left(e^{m_y/2}-1\right)}\right] \end{bmatrix}, \end{aligned} \tag{152}$$

where

$$\boldsymbol{\tau}_{w1} = \begin{bmatrix} \tau_{w1r} & \tau_{w1l} \end{bmatrix}^T \qquad \boldsymbol{\tau}_{w2} = \begin{bmatrix} \tau_{w2r} & \tau_{w2l} \end{bmatrix}^T$$
$$\boldsymbol{\tau}_d = \begin{bmatrix} \tau_1 & \tau_2 \end{bmatrix}^T \qquad \boldsymbol{\tau}_{dr} = \begin{bmatrix} \tau_p & \tau_y \end{bmatrix}^T$$

are the torque vectors transmitted over the elastic couplings and cable-pulley mechanisms to winch#1, winch#2, pulley#1, pulley#2, and the pitch and yaw joints of the robot. Also,

$$m_{w2r} = \tfrac{\tau_{w2r}}{r_o T_o} \qquad m_{w2l} = \tfrac{\tau_{w2l}}{r_o T_o}$$
$$m_1 = \tfrac{\tau_1}{r_o T_o} \qquad m_2 = \tfrac{\tau_2}{r_o T_o}$$
$$m_p = \tfrac{\tau_p}{r T_o} \qquad m_y = \tfrac{\tau_y}{r T_o}$$

are their dimensionless values.

4.1.3. Losses

Loss plays an important role in dynamics response by retarding the output motion, which degrades the efficiency of the system to a certain extent. On the other hand, it may be a boon to the system stability. Major losses in this system are found at the cable-pulley matings and at the bearing units. For the cable-pulley mechanism, variation of the cable tension along the length causes the segments to undergo elongation and contraction in a cyclic manner. When the pulleys are rotating, cable slippage will occur at the grooves of the wrapped pulleys. Developing friction will then do the resistive work, resulting in the lost power. This friction loss may be modeled indirectly through the efficiency of the power transmission, where the result does not meet the form in Eq. 15. Yet it provides an additional channel to dissipate the energy, making the system be more strictly passive.

The transmission efficiency may be determined by acknowledging the fact that the power the powered pulley delivers to the cables must be equal to the power the loaded pulley takes from the cables. Infinitesimal power dissipation is integrated for the entire wrapping angles to obtain the power loss at the powered and loaded pulleys. After the evaluation and manipulation, the transmission efficiency η may be written as [28]

$$\eta = \frac{P_{\text{out}}}{P_{\text{in}}} = 1 - \frac{M}{rEA}, \tag{153}$$

for the simple drive unit at the 2$^{\text{nd}}$ and the 3$^{\text{rd}}$-stage of the drivetrain. Derivation is extended to the case of differential drive unit. With pulley#1 and pulley#2 as the input pulleys and pulley#3 as the

Table 2: Transmission efficiency of the flexible cable-pulley driven drivetrain under the working condition 10 kg rated load of the robot.

Parameters	2^{nd}-stage	3^{rd}-stage	4^{th}-stage
rated loaded torque, M	10 [Nm]	30 [Nm]	60 [Nm]
loaded pulley radius, r	67.5 [mm]	81 [mm]	45 [mm]
cable diameter, d	1.5 [mm]	1.5 [mm] (double cables)	3 [mm]
transmission efficiency, η	0.99958	0.99948	0.99976

output pulley depicted in Fig. 10, the efficiency may be derived as

$$\eta = \frac{P_{\text{out}}}{P_{\text{in}}} = 1 - \frac{M}{2rEA}, \tag{154}$$

where M is the torque transmitted to the load. Note that these equations are determined on the assumption that the difference of the cable tension forces at both sides of the loaded pulley (low and high tension) are not significant. This is valid when the load is small.

Assume the robot can bear the rated load of 10 kg. The corresponding rated loaded torque at each stage may then be calculated using the transpose of the transmission ratio matrices. They are summarized in Table 2 along with their minimum pulley radius and cable diameters. Hence the numerical values of the transmission efficiency at each stage may be evaluated, which are tabulated in the same table. It is observed that the efficiency is very good, which agrees with the well-known adoption of the cable-pulley mechanism in many high performance motion control systems [1, 31]. Therefore, loss in the cable-pulley mechanism may be safely ignored.

Friction loss at the bearing is typically more significant than the dissipation at the cable-pulley transmission depending on the quality of the machining and assembly product. Natural complexity of the friction at the bearing support prevents one to develop purely theoretical equations that are realistic. Consequently, the proposed friction model used in this simulation will be the combination of the simple Coulomb's friction torque when the relative velocity of the mating surfaces is virtually zero, and the empirical formulation of the frictional torque for the standard sealed deep-grooved ball bearing [29] when the relative motion occurs. Mathematically,

$$M_f = \begin{cases} M_{\text{in}}, & \omega = 0 \text{ and } M_{\min} \le M_{\text{in}} \le M_{\max} \\ 35812.5\frac{Hd}{nr}, & \omega \neq 0, \end{cases} \tag{155}$$

where M_{in} [Nmm] and H [kW] are the transmitted torque and the transmitted power through the cable-pulley mechanism, M_f [Nmm] the developed frictional torque, d [mm] and r [mm] the shaft diameter and the pulley radius, and n [rpm] the angular velocity of the pulley. $M_{\min}$ and $M_{\max}$ limit the maximum amount of power loss that can occur at the bearing. Their typical values, experimentally chosen, are $M_{\min} = -10$ [Nmm] and $M_{\max} = 10$ [Nmm].

According to the design, locations of the bearing support are determined and the appropriate parameter values are substituted into Eq 155. See the bond graph diagram of the system in Fig. 12.

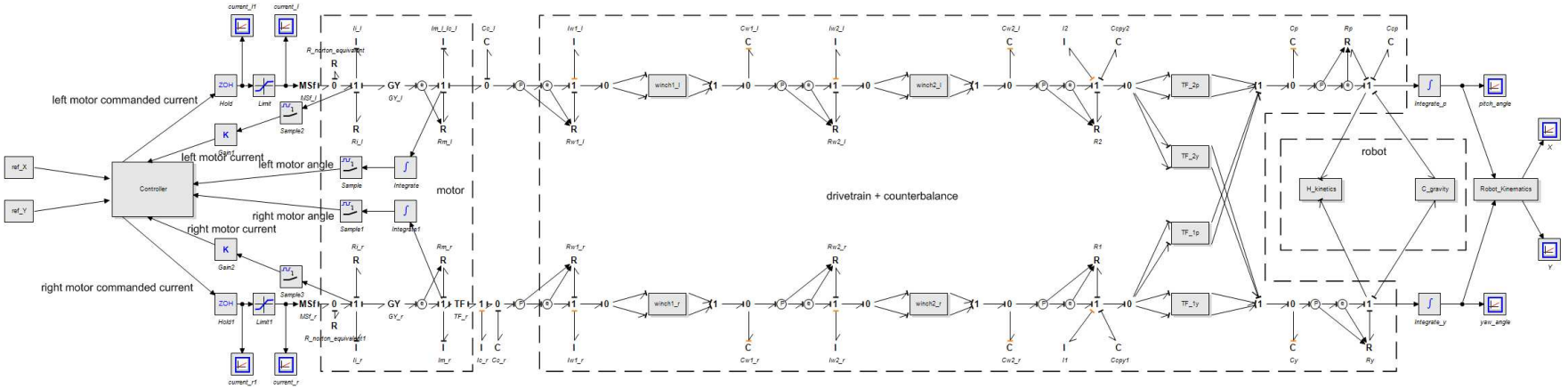

Figure 12: Detailed bond graph diagram of the two-DOF cable-pulley driven flexible joint robot controlled system. The diagram displays the interconnection of the controller, motor, drivetrain, counterbalance, and robot units. In addition, physical system-like couplings of the lumped model of the system components ease the understanding of the overall dynamics.

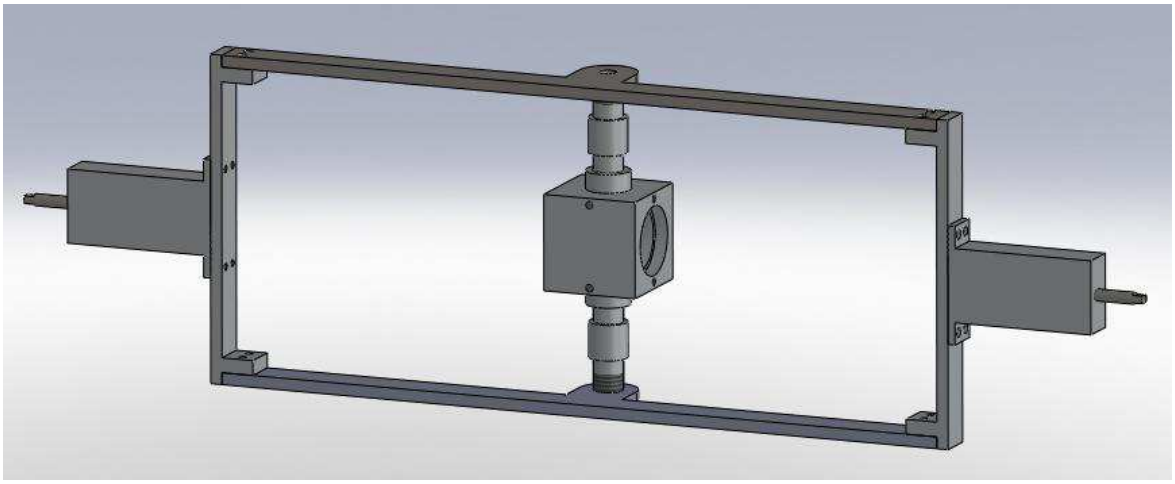

Figure 13: Collection of mechanical parts undergoing the pitching motion.

They all can be arranged into the implicit dissipative vector function $\boldsymbol{c}\left(\dot{\boldsymbol{\theta}}\right)$ of Eq. 15 where the details shall be omitted here.

4.1.4. Robot Dynamics

Referring to the Fig. 9 and 10, main parts of the two DOF (pitch and yaw) robot are pulley#3, pulley#4, and the output shoulder link. As a matter of convenience, the rectangle frame of the counterbalancing mechanism subject to the pitch motion will be included as well. These components have compound motion formed by the primitive pitch and yaw motion. Direct application of the Lagrangian formulation will be performed to derive the robot equations of motion.

Mechanical parts of the robot may be grouped into two collections: one undergoing the pitching motion solely and the other undergoing the composite pitching and yawing motion. CAD drawings of these two collections are depicted in Fig. 13 and 14. Their related parameters will thus be subscripted as 'p' and 'py', respectively. The reference and moving coordinate frames employed are the same one as shown in Fig. 10.

For the first collection undergoing the pitch motion, its compound center of gravity (C.G.) may be approximated to be at

$$^{\{xyz\}}\left(\boldsymbol{r}_G\right)_p = \begin{bmatrix} 0 & 0 & r_{z_p} \end{bmatrix}^T$$

relative to the origin of $\{XYZ\}$, for $r_{z_p} = -28.8$ [mm]. Because its motion is the rotation about the fixed pitch axis with the angular velocity

$$^{\{xyz\}}\boldsymbol{\omega}_p = \begin{bmatrix} \dot{\theta}_p & 0 & 0 \end{bmatrix}^T,$$

the associated kinetic energy may be determined as

$$T_p = \frac{1}{2}\boldsymbol{\omega}_p^T \boldsymbol{I}_{o_p} \boldsymbol{\omega}_p = \frac{1}{2} I_{xx_p} \dot{\theta}_p^2, \tag{156}$$

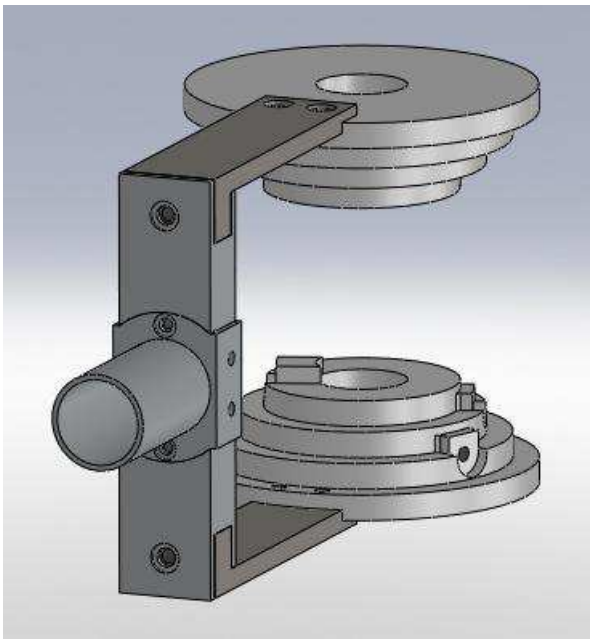

Figure 14: Collection of mechanical parts undergoing the pitching and yawing motion.

where $\boldsymbol{I}_{o_p}$ is the pitch-collection inertia matrix of which its inertia about x-x axis is $I_{xx_p} = 276.0$ [kg $\cdot$ cm^2] from the CAD program evaluation. The potential energy may be derived simply as

$$V_p = -m_p \boldsymbol{g} \cdot (\boldsymbol{r}_G)_p = -m_p g r_{z_p} s_p, \tag{157}$$

for which $m_p = 3.55$ [kg] is the mass of this collection and $\boldsymbol{g}$ the vector of gravitational acceleration.

Similarly, the kinetic and potential energy of the pitch/yaw-collection may be derived as follow. From the geometry, the compound C.G. location may be approximated as

$${}^{\{xyz\}}(\boldsymbol{r}_G)_{py} = \begin{bmatrix} 0 & 0 & r_{z_{py}} \end{bmatrix}^T,$$

where $r_{z_{py}} = -120.2$ [mm]. However, its angular velocity are due to both the pitch and yaw motion. In the body fixed frame, it may thus be written as

$${}^{\{xyz\}}\boldsymbol{\omega}_{py} = \begin{bmatrix} \dot{\theta}_p c_y & \dot{\theta}_y & \dot{\theta}_p s_y \end{bmatrix}^T.$$

Therefore the kinetic energy expression after some simplification may be expressed as

$$\begin{aligned} T_{py} &= \frac{1}{2}\boldsymbol{\omega}_{py}^T \boldsymbol{I}_{o_{py}} \boldsymbol{\omega}_{py} \\ &= \frac{1}{2}\Big[\left(I_{xx_{py}} c_y^2 + I_{zz_{py}} s_y^2 + 2 I_{xz_{py}} s_y c_y\right)\dot{\theta}_p^2 \\ &\quad + 2\left(I_{xy_{py}} c_y + I_{yz_{py}} s_y\right)\dot{\theta}_p \dot{\theta}_y + I_{yy_{py}} \dot{\theta}_y^2\Big], \end{aligned} \tag{158}$$

for which

$$\boldsymbol{I}_{o_{py}} = \begin{bmatrix} I_{xx_{py}} & I_{xy_{py}} & I_{xz_{py}} \\ I_{xy_{py}} & I_{yy_{py}} & I_{yz_{py}} \\ I_{xz_{py}} & I_{yz_{py}} & I_{zz_{py}} \end{bmatrix}$$

is the inertia matrix of the pitch/yaw-collection. Careful decision on the shape of the parts is made during the robot design, resulting in the simplified inertia property where the off-diagonal elements may be neglected. See Fig. 14. Particularly, $I_{xx_{py}} = 932.0$ [kg $\cdot$ cm^2], $I_{yy_{py}} = 761.5$ [kg $\cdot$ cm^2], $I_{zz_{py}} = 205.2$ [kg $\cdot$ cm^2], and $I_{xy_{py}} = I_{xz_{py}} = I_{yz_{py}} = 0$ [kg $\cdot$ cm^2]. The potential energy may be calculated as

$$V_{py} = -m_{py}\boldsymbol{g} \cdot (\boldsymbol{r}_G)_{py} = -m_{py} g r_{z_{py}} s_p c_y, \tag{159}$$

with $m_{py} = 3.07$ [kg] be the mass of this collection.

Furthermore, the counterbalancing mechanism contributes to the robot dynamics by shaping the robot potential energy with the storing and restoring spring potential energy. The mechanism may be divided into two components. One is to counter the gravitational potential energy of the pitch-collection. The other, more complicated, is for accounting that of the pitch/yaw-collection. Conceptually, the mechanism is designed so the sum of the gravitational and the spring potential energy yields a constant value. Unfortunately, actual implementation of this idea makes the cancellation be imperfect due mainly to the nonzero initial tension of the spring, the cable routing over non-zero radius idlers, and the traveling limitation hit of the mechanism.

Spring potential energy of the counterbalance may be determined from the area under the force-deformation curve. Geometric constraint of the mechanism enforces the elongated length of the springs to be related to the robot configuration through its generalized coordinates θ_p and θ_y. Details shall be omitted and only the results are provided. Potential energy of the counterbalance for the pitch-collection is

$$V_{C_p} = 2k_p h_p^2 \left[1 - \sin\left(\theta_p + \frac{25\pi}{180}\right)\right] + 2h_p T_{i_p} \sqrt{2\left[1 - \sin\left(\theta_p + \frac{25\pi}{180}\right)\right]}, \tag{160}$$

where the spring stiffness and the mounting distance of the cable-spring at the rectangle frame from the X-X axis, $k_p = 311.88$ [N/m] and $h_p = 40$ [mm], are designed based on the perfect gravitational torque cancellation of the ideal counterbalancing mechanism according to the following relation;

$$k_p h_p^2 = \frac{m_p g \left| r_{z_p} \right|}{2}. \tag{161}$$

According to the data sheet of the selected spring, initial tension T_{i_p} is 5.10 [N]. The constant angle of $\frac{25\pi}{180}$ [rad] reflects the safety limit of the mechanism at 65°.

Analogously, potential energy of the counterbalance for the pitch/yaw-collection may be expressed as

$$\begin{aligned} V_{C_{py}} &= k_{py} h_{py}^2 (2 - s_1 - s_2) + h_{py} T_{i_{py}} \left[\sqrt{2(1 - s_1)} + \sqrt{2(1 - s_2)}\right] \\ &= 2k_{py} h_{py}^2 (1 - s_p c_y) \\ &\quad + h_{py} T_{i_{py}} \left[\sqrt{2\left[1 - s(\theta_p + \theta_y)\right]} + \sqrt{2\left[1 - s(\theta_p - \theta_y)\right]}\right], \end{aligned} \tag{162}$$

where the spring stiffness and the mounting distance of the cable-spring at pulley#1 and pulley#2 from the X-X axis are designed to have the values of $k_{py} = 426.9$ [N/m] and $h_{py} = 60$ [mm], respectively, based upon the relation

$$k_{py} h_{py}^2 = \frac{m_{py} g \left| r_{z_{py}} \right|}{2}. \tag{163}$$

Initial tension for this set of springs is $T_{i_{py}} = 7.94$ [N].

One important practical issue is the tension spring and the cable cannot bear the compression load. In other words, the spring cannot store the energy beyond its unstretched length. Physically, the spring and the cable get slack and the spring force becomes zero. According to the mechanism design, it happens at $\theta_p \geq 65^\circ$ for the counterbalance of the pitch-collection as it hits the hard limit, and at $\theta_1 = 90^\circ / \theta_2 = 90^\circ$ for the counterbalancing springs connected to pulley#1/pulley#2 of the pitch/yaw-collection as they are at their nominal lengths.

Additionally, the friction force F_f developed at the linear bushing, which bears and provides the way for the stroke of the spring, should be taken into account. It is modeled simply by a nonlinear switching function

$$F_f = \begin{cases} -\text{sgn}\,(v)\, F_m, & v \neq 0 \\ 0 & v = 0, \end{cases} \tag{164}$$

where v is the signed velocity of the slider and the constant friction limit value F_m is selected to be 0.5×10^{-2} [N]. In this regard, the friction force is comparable to an extra initial dynamic tension force of the spring.

According to the above analysis, Lagrangian of the robot plus its counterbalances may be determined as

$$L\left(\boldsymbol{\theta}_q, \dot{\boldsymbol{\theta}}_q\right) = T_p + T_{py} - V_p - V_{py} - V_{C_p} - V_{C_{py}}.$$

Applying the Lagrangian formulation along the system generalized coordinates θ_p and θ_y, one would have

$$\begin{aligned} \frac{d}{dt}\left(\frac{\partial L}{\partial \dot{\theta}_p}\right) - \frac{\partial L}{\partial \theta_p} &= \tau_p \\ \frac{d}{dt}\left(\frac{\partial L}{\partial \dot{\theta}_y}\right) - \frac{\partial L}{\partial \theta_y} &= \tau_y, \end{aligned}$$

where τ_p and τ_y are the corresponding generalized torques. Evaluating the above formulation with the system Lagrangian, the robot dynamics model may be manipulated into the modified standard form of Eq. 1 that includes the frictional torque $\boldsymbol{f}$;

$$\boldsymbol{M}(\boldsymbol{q})\,\ddot{\boldsymbol{q}} + \boldsymbol{C}(\boldsymbol{q}, \dot{\boldsymbol{q}})\,\dot{\boldsymbol{q}} + \boldsymbol{f} + \boldsymbol{g}(\boldsymbol{q}) = \boldsymbol{\tau}_{dr} + \boldsymbol{\tau}_{ext}, \tag{165}$$

with

$$\boldsymbol{M}(\boldsymbol{q}) = \begin{bmatrix} I_{xx_{py}} c_y^2 + I_{zz_{py}} s_y^2 + I_{xx_p} & 0 \\ 0 & I_{yy_{py}} \end{bmatrix}$$

$$
\begin{aligned}
\boldsymbol{C}\left(\boldsymbol{q},\dot{\boldsymbol{q}}\right) &= \begin{bmatrix} \left(I_{zz_{py}}-I_{xx_{py}}\right)s_y c_y\dot{\theta}_y & \left(I_{zz_{py}}-I_{xx_{py}}\right)s_y c_y\dot{\theta}_p \\ \left(I_{xx_{py}}-I_{zz_{py}}\right)s_y c_y\dot{\theta}_p & 0 \end{bmatrix} \\
\boldsymbol{f} &= \begin{bmatrix} \frac{2h_p\mathrm{sgn}\left(\dot{\theta}_p\right)F_m\cos\left(\theta_p+\frac{25\pi}{180}\right)}{\sqrt{2\left[1-\sin\left(\theta_p+\frac{25\pi}{180}\right)\right]}}+\frac{h_{py}\mathrm{sgn}\left(\dot{\theta}_1\right)F_m c_1}{\sqrt{2(1-s_1)}}+\frac{h_{py}\mathrm{sgn}\left(\dot{\theta}_2\right)F_m c_2}{\sqrt{2(1-s_2)}} \\ \frac{h_{py}\mathrm{sgn}\left(\dot{\theta}_1\right)F_m c_1}{\sqrt{2(1-s_1)}}-\frac{h_{py}\mathrm{sgn}\left(\dot{\theta}_2\right)F_m c_2}{\sqrt{2(1-s_2)}} \end{bmatrix} \\
&= \begin{bmatrix} \frac{2h_p\mathrm{sgn}\left(\dot{\theta}_p\right)F_m\cos\left(\theta_p+\frac{25\pi}{180}\right)}{\sqrt{2\left[1-\sin\left(\theta_p+\frac{25\pi}{180}\right)\right]}}+\frac{h_{py}\mathrm{sgn}\left(\dot{\theta}_p+\dot{\theta}_y\right)F_m c(\theta_p+\theta_y)}{\sqrt{2[1-s(\theta_p+\theta_y)]}}+\frac{h_{py}\mathrm{sgn}\left(\dot{\theta}_p-\dot{\theta}_y\right)F_m c(\theta_p-\theta_y)}{\sqrt{2[1-s(\theta_p-\theta_y)]}} \\ \frac{h_{py}\mathrm{sgn}\left(\dot{\theta}_p+\dot{\theta}_y\right)F_m c(\theta_p+\theta_y)}{\sqrt{2[1-s(\theta_p+\theta_y)]}}-\frac{h_{py}\mathrm{sgn}\left(\dot{\theta}_p-\dot{\theta}_y\right)F_m c(\theta_p-\theta_y)}{\sqrt{2[1-s(\theta_p-\theta_y)]}} \end{bmatrix} \\
\boldsymbol{g}\left(\boldsymbol{q}\right) &= \begin{bmatrix} g_p\left(\theta_p,\theta_y\right) \\ g_y\left(\theta_p,\theta_y\right) \end{bmatrix}. \qquad (166)
\end{aligned}
$$

In this equation, $\boldsymbol{g}\left(\boldsymbol{q}\right)$ is the resulting torque vector of the robot gravity torque compensated by the counterbalancing spring torque. Their components along θ_p and θ_y generalized coordinates are

$$
\begin{aligned}
g_p\left(\theta_p,\theta_y\right) &= -m_p g r_{z_p} c_p - 2k_p h_p^2\cos\left(\frac{25\pi}{180}\right)c_p + 2k_p h_p^2\sin\left(\frac{25\pi}{180}\right)s_p - \frac{2h_p T_{i_p}\cos\left(\theta_p+\frac{25\pi}{180}\right)}{\sqrt{2\left[1-\sin\left(\theta_p+\frac{25\pi}{180}\right)\right]}} \\
&\quad -m_{py} g r_{z_{py}} c_p c_y - 2k_{py} h_{py}^2 c_p c_y - \frac{h_{py} T_{i_{py}} c\left(\theta_p+\theta_y\right)}{\sqrt{2\left[1-s\left(\theta_p+\theta_y\right)\right]}} - \frac{h_{py} T_{i_{py}} c\left(\theta_p-\theta_y\right)}{\sqrt{2\left[1-s\left(\theta_p-\theta_y\right)\right]}} \qquad (167) \\
g_y\left(\theta_p,\theta_y\right) &= m_{py} g r_{z_{py}} s_p s_y + 2k_{py} h_{py}^2 s_p s_y - \frac{h_{py} T_{i_{py}} c\left(\theta_p+\theta_y\right)}{\sqrt{2\left[1-s\left(\theta_p+\theta_y\right)\right]}} + \frac{h_{py} T_{i_{py}} c\left(\theta_p-\theta_y\right)}{\sqrt{2\left[1-s\left(\theta_p-\theta_y\right)\right]}}. \qquad (168)
\end{aligned}
$$

External force $\boldsymbol{F}_{ext}$, caused by the robot interaction with the environment at the end of the shoulder link, may naturally be described in the task space frame $\{xyz\}$. Therefore the reflected torque vector $\boldsymbol{\tau}_{ext}$ at the robot joints is determined by

$$
\boldsymbol{\tau}_{ext} = {}^{\{xyz\}}J^{T\{xyz\}}\boldsymbol{F}_{ext} = \begin{bmatrix} F_y l_o c_y \\ -F_x l_o \end{bmatrix}, \qquad (169)
$$

as can be verified by inspecting the robot geometry directly as well.

4.1.5. Transmission System Dynamics

To complete the dynamics of the drivetrain unit, inertia and dissipation properties must be considered. As depicted in Fig. 10, rotors of the drivetrain subsystem consist of the motor rotor, winch#1, winch#2, pulley#1, and pulley#2. Their inertia about the fixed rotating axes are evaluated by the CAD program and tabulated in Table 3. Note that the inertia of pulley#3 and pulley#4 are already included into the inertia of the pitch/yaw-collection of the robot.

Recalling the dissipation of the drivetrain at the bearing units discussed in subsection 4.1.3, represented by Eq. 15and 155, and the elastic force acting at each rotor of the cable-pulley power transmission subsystem explained in subsection 4.1.2, governed by Eq. 16 and 152, dynamics of the drivetrain subsystem may thus be determined from Eq. 13.

For this particular system, explicit form of the equations is hardly achieved due to the inversion problem of the complicated nonlinear deformation function. This, however, does not affect the im-

Table 3: Rotor inertias in the drivetrain subsystem about their own rotating axis

Rotor	Inertia [$g \cdot cm^2$]
motor	248
winch#1	344.6
winch#2	16728
pulley#1	48436
pulley#2	48440

Table 4: Some electrical parameters of the DC brushed MAXON®motor model #148877

Parameter	Value
inductance	0.33 [mH]
resistance	1.16 Ω
back emf const.	60.3 [mV-s]
torque const.	60.3 [mNm/A]

plementation of the presented control law. Besides, the simulation program adopted is 20-sim [32]. It is based on the bond graph modeling language which does not require explicit formulation of the system differential equations. Therefore, this problem does not affect the simulation process either.

4.1.6. Electrical Dynamics of the Motor

The motors employed in this system are two DC brushed motors of MAXON®model #148877 of which its electrical parameters read off from the data sheet are depicted in Table 4. Accordingly, electrical dynamics of the motor dictating the relationship between the voltage/armature current and the torque/angular velocity may be acquired by substituting the parameter values into Eq. 21 and 22.

4.1.7. Complete Model

At this point, dynamics analysis of each subsystem has been completed. Theoretically, a set of lengthy differential equations describing the change of system states may be formulated. Nevertheless for some practical system, e.g. this two DOF cable-pulley driven flexible joint robot, the behavior of some components is governed by a set of complex nonlinear equations. This prevents one to determine for their inverse functions needed in formulating the equations of motion explicitly. As a result, a set of implicit differential-algebraic equations (i-DAE) may be formulated. Unfortunately, solving a system of i-DAE is not so straightforward compared to a typical system of ordinary differential equations (ODE).

Bond graph technique [16] is an approach in modeling the system. The modeler focuses on describing the behavior of each subsystem and/or subcomponent first. The complete system is then

constructed by interconnecting them through the effort and flow constraints corresponding to the physical connection of the actual components. Thus by this modeling approach, it is not necessary to know the explicit differential equations of the whole system since the simulation will proceed from one basic element to the nearby element according to the assigned causality.

In brief, all important dynamical equations of every subsystem as explained in the preceding subsections are placed into the bond graph basic elements of the power transformation (TF, GY), the inertance (I), the linear/nonlinear compliance (C), and the nonlinear resistance (R). Dynamics of the two DOF robot and its gravity are modeled by the customized nonlinear two-port inertance and compliance elements. Additional work is necessary to rewrite the robot dynamics in the Hamiltonian framework by which the bond graph modeling language employs. This can be achieved with the help of the Legendre transformation. Details fall beyond the scope of this paper. Finally, the subsystems are altogether combined through the power bonds and the effort (0) and flow (1) ports. Complete bond graph digram drawn by 20-sim, a modeling and simulation program [32] from Controllab Products B.V., of the two DOF cable-pulley driven flexible joint robot system is shown in Fig. 12.

4.2. Task Space Impedance Control

The proposed task space impedance control law in subsection 3.5 will now be designed for the two DOF cable-pulley driven flexible joint robot. At any instant, the reachable end effector set point $\boldsymbol{x}_d$ and the task space constant stiffness matrix $\boldsymbol{K}_d$ are assigned. The following natural form of the stiffness matrix

$$ {}^{\{xyz\}}\boldsymbol{K}_d = \begin{bmatrix} k_{dx} & 0 \\ 0 & k_{dy} \end{bmatrix} \tag{170} $$

expressed in the end tip body-fixed frame may be used. k_{dx} and k_{dy} are the desired stiffnesses along the x and y-direction. Note the dimension of $\boldsymbol{K}_d$ is 2×2 because the robot has two DOF, which physically allows the end point to move only in the plane tangent to the hemispherical surface of the workspace at the current location.

Desired position $\boldsymbol{x}_d$ is commonly described with respect to a reference frame. Consequently, to determine the virtual spring force when the stiffness parameters are expressed in the body-fixed frame, description of the coordinate error $\tilde{\boldsymbol{x}}$ must be changed from the fixed to the moving frame by

$$ {}^{\{xyz\}}\tilde{\boldsymbol{x}} \quad = \quad {}^{\{XYZ\}}R^T_{\{xyz\}} \left({}^{\{XYZ\}}\boldsymbol{x} - {}^{\{XYZ\}}\boldsymbol{x}_d \right). \tag{171} $$

Since the workspace of this robot forms a hemispherical surface of radius l_o, reachable end effector set point ${}^{\{XYZ\}}\boldsymbol{x}_d = \begin{bmatrix} x_d & y_d & z_d \end{bmatrix}^T$ must satisfied the constraint

$$ x_d^2 + y_d^2 + z_d^2 = l_o^2. \tag{172} $$

With respect to the reference frame orientation in Fig. 10, the z-coordinate must be

$$ z_d = -\sqrt{l_o^2 - x_d^2 - y_d^2}. \tag{173} $$

Recalling the robot kinematics analyzed in subsection 4.1.1 and substituting these terms into Eq. 171, the coordinate error may be written as

$$ {}^{\{xyz\}}\tilde{\boldsymbol{x}} = \begin{bmatrix} -x_d c_y - y_d s_p s_y - \sqrt{l_o^2 - x_d^2 - y_d^2}\, c_p s_y \\ -y_d c_p + \sqrt{l_o^2 - x_d^2 - y_d^2}\, s_p \\ -l_o - x_d s_y + y_d s_p c_y + \sqrt{l_o^2 - x_d^2 - y_d^2}\, c_p c_y \end{bmatrix}. \tag{174} $$

Only its x and y-components are needed since the end effector motion is constrained to lie in the tangent plane.

At each control sampling, the task space damping matrix $\boldsymbol{D}_d(\boldsymbol{x})$ will be updated. For this purpose, the generalized eigenproblem of $\boldsymbol{K}_d$ and $\boldsymbol{\Lambda}(\boldsymbol{x})$ must be solved first. With this particular two DOF problem, it is possible to solve analytically for the closed form expressions. Firstly, the task space inertia matrix may be determined from Eq. 67 and 166 as

$$ \begin{aligned} \boldsymbol{\Lambda}(\boldsymbol{x}) &= J(\boldsymbol{q})^{-T} \boldsymbol{M}(\boldsymbol{q}) J(\boldsymbol{q})^{-1} \\ &= \begin{bmatrix} 0 & -\frac{1}{l_o} \\ \frac{1}{l_o c_y} & 0 \end{bmatrix} \begin{bmatrix} I_{xx_{py}} c_y^2 + I_{zz_{py}} s_y^2 + I_{xx_p} & 0 \\ 0 & I_{yy_{py}} \end{bmatrix} \begin{bmatrix} 0 & \frac{1}{l_o c_y} \\ -\frac{1}{l_o} & 0 \end{bmatrix} \\ &= \begin{bmatrix} \frac{I_{yy_{py}}}{l_o^2} & 0 \\ 0 & \frac{1}{l_o^2 c_y^2}\left(I_{xx_{py}} c_y^2 + I_{zz_{py}} s_y^2 + I_{xx_p}\right) \end{bmatrix}. \end{aligned} \tag{175} $$

According to Eq. 71, the generalized eigenproblem is then to solve

$$ \begin{bmatrix} k_{dx} - \omega_{ni}^2 \frac{I_{yy_{py}}}{l_o^2} & 0 \\ 0 & k_{dy} - \frac{\omega_{ni}^2}{l_o^2 c_y^2}\left(I_{xx_{py}} c_y^2 + I_{zz_{py}} s_y^2 + I_{xx_p}\right) \end{bmatrix} \boldsymbol{u}_i = 0 $$

for the eigenvalues ω_n and the corresponding eigenvectors $\boldsymbol{u}$. The eigenvalues may be simply determined and arranged as the spectral matrix:

$$ \boldsymbol{\Sigma}(\boldsymbol{x}) = \begin{bmatrix} \frac{k_{dx} l_o^2}{I_{yy_{py}}} & 0 \\ 0 & \frac{k_{dy} l_o^2 c_y^2}{I_{xx_{py}} c_y^2 + I_{zz_{py}} s_y^2 + I_{xx_p}} \end{bmatrix}. \tag{176} $$

Associated normalized eigenvectors satisfying Eq. 73 may thus be written as the columns of the transformation matrix $\boldsymbol{Q}(\boldsymbol{x})$;

$$ \boldsymbol{Q}(\boldsymbol{x}) = \begin{bmatrix} \frac{l_o}{\sqrt{I_{yy_{py}}}} & 0 \\ 0 & \frac{l_o c_y}{\sqrt{I_{xx_{py}} c_y^2 + I_{zz_{py}} s_y^2 + I_{xx_p}}} \end{bmatrix}. \tag{177} $$

As a result, the task space damping matrix may be designed according to Eq. 76 as

$$ \begin{aligned} \boldsymbol{D}_d(\boldsymbol{x}) &= 2\boldsymbol{Q}(\boldsymbol{x})^{-T} \boldsymbol{\xi} \boldsymbol{\Sigma}(\boldsymbol{x})^{1/2} \boldsymbol{Q}(\boldsymbol{x})^{-1} \\ &= \begin{bmatrix} \frac{2\xi\sqrt{k_{dx} I_{yy_{py}}}}{l_o} & 0 \\ 0 & \frac{2\xi\sqrt{k_{dy}\left(I_{xx_{py}} c_y^2 + I_{zz_{py}} s_y^2 + I_{xx_p}\right)}}{l_o c_y} \end{bmatrix}. \end{aligned} \tag{178} $$

The matrix is positive definite since θ_y lies in the range $\left[-\frac{\pi}{2}, \frac{\pi}{2}\right]$ for the robot workspace of the hemispherical surface.

Stationary link angles are used as the estimation for the actual link angles in the task space impedance control law. They are recursively computed from the measured motor angles and the elastic model of the transmission subsystem as summarized in Eq. 41. To achieve this, necessary compound transmission ratios may first be computed as follow;

$$\begin{aligned} \boldsymbol{T}_q &= \begin{bmatrix} \frac{1}{2} & \frac{1}{2} \\ \frac{1}{2} & -\frac{1}{2} \end{bmatrix} \qquad \boldsymbol{T}_{q3} = \begin{bmatrix} \frac{1}{6} & \frac{1}{6} \\ \frac{1}{6} & -\frac{1}{6} \end{bmatrix} \\ \boldsymbol{T}_{q2} &= \begin{bmatrix} \frac{1}{18} & \frac{1}{18} \\ \frac{1}{18} & -\frac{1}{18} \end{bmatrix} \qquad \boldsymbol{T}_{q1} = \begin{bmatrix} -\frac{1}{18} & \frac{1}{18} \\ -\frac{1}{18} & -\frac{1}{18} \end{bmatrix}. \end{aligned} \tag{179}$$

The overall effective nonlinear deformation function of the drivetrain may then be determined from the generalization of Eq. 38 as

$$\begin{aligned} \boldsymbol{e}_{1q}^{-1}\left(\boldsymbol{h}\left(\boldsymbol{\theta}_{qs}\right)\right) &= \boldsymbol{T}_{q2}\boldsymbol{e}_1^{-1}\left(\boldsymbol{T}_{q2}^T\boldsymbol{h}\left(\boldsymbol{\theta}_{qs}\right)\right) + \boldsymbol{T}_{q3}\boldsymbol{e}_2^{-1}\left(\boldsymbol{T}_{q3}^T\boldsymbol{h}\left(\boldsymbol{\theta}_{qs}\right)\right) \\ &\quad + \boldsymbol{T}_q\boldsymbol{e}_3^{-1}\left(\boldsymbol{T}_q^T\boldsymbol{h}\left(\boldsymbol{\theta}_{qs}\right)\right) + \boldsymbol{e}_q^{-1}\left(\boldsymbol{h}\left(\boldsymbol{\theta}_{qs}\right)\right). \end{aligned} \tag{180}$$

Effectively, the stationary torque transmitted to the robot at the last q^{th}-stage $\boldsymbol{h}\left(\boldsymbol{\theta}_{qs}\right)$ is scaled by the appropriate transmission ratios and substituted into the corresponding deformation vector function of the elastic network at each stage. Individual deformation according to Eq. 152 is then scaled to the equivalent motion at the last q^{th}-stage and sum to obtain the total deformation. Finally, subtracting the total deformation from the rigid motion of the links caused purely by the transmission kinematics, $\boldsymbol{T}_{q1}\boldsymbol{\theta}_0$, one would obtain the stationary link angles.

According to the preceding derivations, the expression for the required stationary torque from the transmission unit which counterbalances the remaining gravity torque and supplies the desired compliance force may be written as

$$\begin{aligned} \boldsymbol{h}\left(\boldsymbol{\theta}_{qs}\right) &= \boldsymbol{g}\left(\boldsymbol{\theta}_{qs}\right) - J\left(\boldsymbol{\theta}_{qs}\right)^T \boldsymbol{K}_d\left(\boldsymbol{f}\left(\boldsymbol{\theta}_{qs}\right) - \boldsymbol{x}_d\right) \\ &= \begin{bmatrix} g_p\left(\theta_{ps}, \theta_{ys}\right) \\ g_y\left(\theta_{ps}, \theta_{ys}\right) \end{bmatrix} \\ &\quad - \begin{bmatrix} 0 & l_o c_{ys} \\ -l_o & 0 \end{bmatrix} \begin{bmatrix} k_{dx} & 0 \\ 0 & k_{dy} \end{bmatrix} \begin{bmatrix} -x_d c_{ys} - y_d s_{ps} s_{ys} - \sqrt{l_o^2 - x_d^2 - y_d^2}\, c_{ps} s_{ys} \\ -y_d c_{ps} + \sqrt{l_o^2 - x_d^2 - y_d^2}\, s_{ps} \end{bmatrix} \\ &= \begin{bmatrix} g_p\left(\theta_{ps}, \theta_{ys}\right) \\ g_y\left(\theta_{ps}, \theta_{ys}\right) \end{bmatrix} - \begin{bmatrix} k_{dy} l_o \left(\sqrt{l_o^2 - x_d^2 - y_d^2}\, s_{ps} c_{ys} - y_d c_{ps} c_{ys}\right) \\ k_{dx} l_o \left(x_d c_{ys} + y_d s_{ps} s_{ys} + \sqrt{l_o^2 - x_d^2 - y_d^2}\, c_{ps} s_{ys}\right) \end{bmatrix}, \end{aligned} \tag{181}$$

where the subscript 'ps' and 'ys' denote the stationary angle of θ_p and θ_y, respectively. Equations 167 and 168 display the vector $\boldsymbol{g}\left(\boldsymbol{\theta}_{qs}\right)$ explicitly. Thus, $\boldsymbol{h}\left(\boldsymbol{\theta}_{qs}\right)$ may be computed by evaluating Eq. 181 with the updated values of θ_{ps} and θ_{ys} at each iteration.

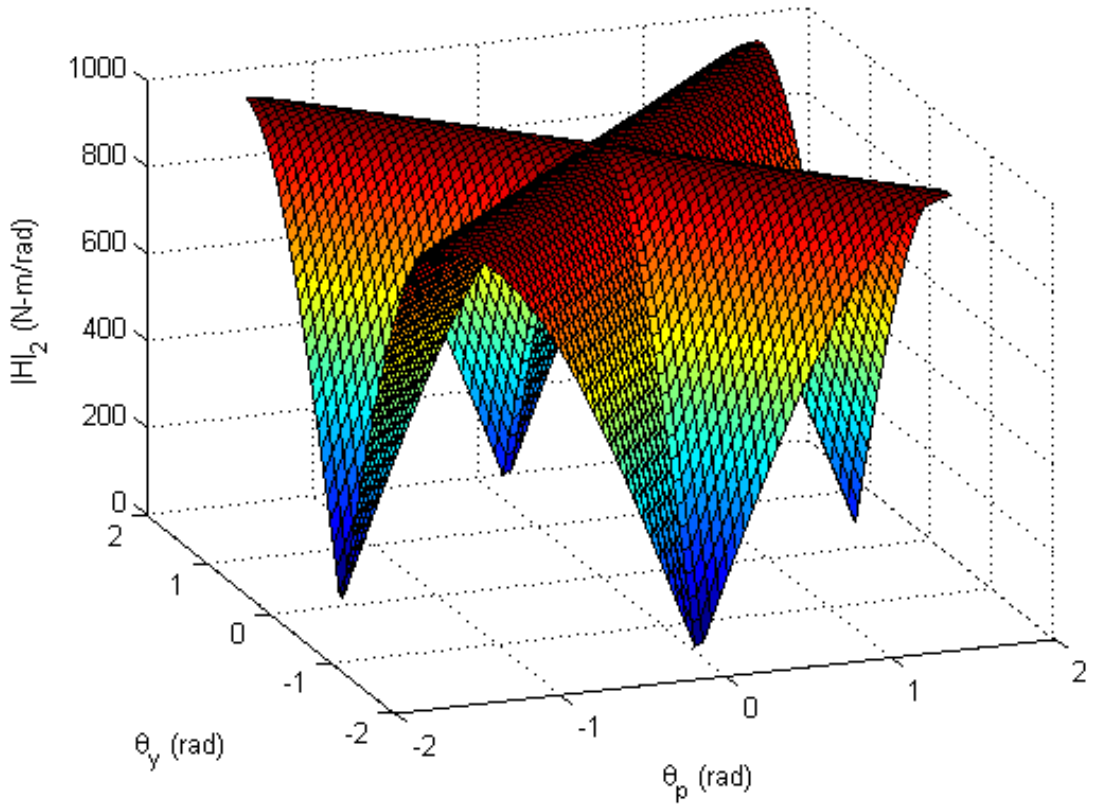

Figure 15: Surface plot of the 2-norm of the Hessian matrix of $V_h(\boldsymbol{q})$ over the robot workspace when $x_d = y_d = 0$ m and $k_{dx} = k_{dy} = 1 \times 10^4$ N/m.

It can be shown numerically that the supremum of $\left\| \frac{\partial \boldsymbol{h}(\boldsymbol{q})}{\partial \boldsymbol{q}} \right\|_K$ over the workspace satisfies Eq. 50. Particularly, from Eq. 181 where $\boldsymbol{h}(\boldsymbol{q}) = \begin{bmatrix} h_p(\boldsymbol{q}) & h_y(\boldsymbol{q}) \end{bmatrix}^T$, the Hessian matrix of $V_h(\boldsymbol{q})$ depicting the ideal controller joint stiffness is

$$\boldsymbol{H}_h(\boldsymbol{q}) = \frac{\partial \boldsymbol{h}(\boldsymbol{q})}{\partial \boldsymbol{q}} = \begin{bmatrix} \frac{\partial h_p}{\partial \theta_p}(\boldsymbol{q}) & \frac{\partial h_p}{\partial \theta_y}(\boldsymbol{q}) \\ \frac{\partial h_y}{\partial \theta_p}(\boldsymbol{q}) & \frac{\partial h_y}{\partial \theta_y}(\boldsymbol{q}) \end{bmatrix}.$$

Its 2-norm is evaluated numerically of which the value over the hemispherical workspace is depicted in Fig. 15 when the desired set point at the center of the workspace and the nominal stiffness of $k_{dx} = k_{dy} = 10 \times 10^3$ N/m are chosen. From the surface plot, the minimum norm is 20.65 N-m/rad which occurs when $\theta_p = \pm\pi/2$ and $\theta_y = 0$ rad or $\theta_p = 0$ and $\theta_y = \pm\pi/2$ rad, while the maximum norm is 992.65 N-m/rad occuring when $\theta_p = \pm\theta_y$.

As discussed earlier, analytical expression for the nonlinear effective stiffness of the drivetrain of this robot is not possible. Nevertheless, its infimum may be approximated by half of the stiffness at no load. Stiffness of the elastic transmission at the 1st-stage is the stiffness of the coupling between the motor and winch#1:

$$\boldsymbol{K}_1 = \begin{bmatrix} 5.7 \times 10^3 & 0 \\ 0 & 5.7 \times 10^3 \end{bmatrix} \quad \text{N} \cdot \text{m/rad}.$$

Minimum stiffness at the 2nd and the 3rd-stage is estimated by half of the stiffness at no load of Eq. 143, considering from the worst case loading that makes one side of the cable circuit go slack:

$$\begin{aligned} \boldsymbol{K}_2 &= \begin{bmatrix} \frac{EAr_o^2}{L} & 0 \\ 0 & \frac{EAr_o^2}{L} \end{bmatrix} = \begin{bmatrix} 52.97 \times 10^3 & 0 \\ 0 & 52.97 \times 10^3 \end{bmatrix} \quad \text{N} \cdot \text{m/rad}, \\ \boldsymbol{K}_3 &= \begin{bmatrix} \frac{EAr_o^2}{L} & 0 \\ 0 & \frac{EAr_o^2}{L} \end{bmatrix} = \begin{bmatrix} 139.52 \times 10^3 & 0 \\ 0 & 139.52 \times 10^3 \end{bmatrix} \quad \text{N} \cdot \text{m/rad}. \end{aligned}$$

Similarly, at the last stage of the differential drive, the minimum stiffness is estimated by half of the stiffness at no load of Eqs. 150 and 151:

$$\boldsymbol{K}_q = \begin{bmatrix} \frac{2EAr^2}{L} & 0 \\ 0 & \frac{2EAr^2}{L} \end{bmatrix} = \begin{bmatrix} 1122.2 \times 10^3 & 0 \\ 0 & 1122.2 \times 10^3 \end{bmatrix} \quad \text{N} \cdot \text{m/rad}.$$

Consequently, the infimum of the effective stiffness of the transmission system reflected to the last stage may be determined from Eq. 38 as

$$\begin{aligned} \boldsymbol{K}_{1q} &= \left(\boldsymbol{T}_{q2} \boldsymbol{K}_1^{-1} \boldsymbol{T}_{q2}^T + \boldsymbol{T}_{q3} \boldsymbol{K}_2^{-1} \boldsymbol{T}_{q3}^T + \boldsymbol{T}_q \boldsymbol{K}_3^{-1} \boldsymbol{T}_q^T + \boldsymbol{K}_q^{-1} \right)^{-1} \\ &= \begin{bmatrix} 151.36 \times 10^3 & 0 \\ 0 & 151.36 \times 10^3 \end{bmatrix} \quad \text{N} \cdot \text{m/rad}. \end{aligned}$$

From the above calculation, it can be concluded that the supremum of the virtual stiffness generated by the ideal controller (0.99×10^3 N-m/rad) is less than the infimum of the effective stiffness of the

transmission (151.36×10^3 N-m/rad) by about 150 times. This is due to the high joint stiffness characteristics of the cable-pulley transmission mechanism. Thus the flexible joint stiffness is large enough to withstand the robot 'after-the-joint' motion caused by its own weight and the position-mismatch compliant force. Furthermore, according to the condition of Eq. 50, iterative calculation of the stationary link angles is guaranteed to converge to the actual values. Additionally, stability of the task space impedance control of this system is ensured by the same condition. Note from the Hessian matrix expression and the convergence condition that the stationary link angle calculation algorithm still works if the task space stiffness value is set below 1500×10^3 N/m.

Moreover, a separate experiment was conducted to study the convergence rate of stationary link angles. According to the present system parameters, the determination converges to the stationary values, under the criteria that the relative error be less than 5×10^{-5} radian, within 5 iterations independent of whether the robot is subject to external force or not. Therefore, recursive evaluation of Eq. 41 converges to the actual stationary link angles as desired within a rapid finite time and so it may be used in the real-time implementation of the controller.

The task space damping term $\boldsymbol{D}_d\dot{\boldsymbol{x}}$ is implemented through the joint space damping matrix and the filtering of the estimated link joint velocity as described in subsection 3.4 and 3.5. For this system, the stationary joint space symmetric damping matrix is a diagonal matrix. Thus the square root of the damping matrix can be computed without using SVD as

$$\left[J\left(\boldsymbol{\theta}_{qs}\right)^T \boldsymbol{D}_d\left(\boldsymbol{f}\left(\boldsymbol{\theta}_{qs}\right)\right) J\left(\boldsymbol{\theta}_{qs}\right)\right]^{1/2} = \begin{bmatrix} \left[2\xi l_o c_{ys}\sqrt{k_{dy}\left(I_{xx_{py}}c_{ys}^2 + I_{zz_{py}}s_{ys}^2 + I_{xx_p}\right)}\right]^{1/2} & 0 \\ 0 & \left[2\xi l_o\sqrt{k_{dx}I_{yy_{py}}}\right]^{1/2} \end{bmatrix}. \tag{182}$$

A strictly proper and SPR filtering transfer function matrix

$$\boldsymbol{G}(s) = \begin{bmatrix} \frac{\lambda}{s+\lambda} & 0 \\ 0 & \frac{\lambda}{s+\lambda} \end{bmatrix} \tag{183}$$

employing a simple first order low-pass filter is chosen. Its cutoff frequency is selected to be $\lambda = 500$ rad/s, which is roughly about five times larger than the desired system natural frequency determined by Eq. 176 with the nominal stiffness value of 10×10^3 N/m. Hence, the estimate of the scaled link joint velocity $\boldsymbol{\vartheta}$, Eq. 57, may be obtained, which further will be used to calculate the required torque $\boldsymbol{\tau}_{dr}^*$ applied at the robot joints according to Eq. 79.

Since the controller is implemented digitally, the continuous filtering transfer function is discretized via the Tustin approximation with prewarping (at its cutoff) method. Particularly, at the cutoff frequency of 500 rad/s and the sampling time of 1 ms, the emulated discrete-time filtered velocity transfer function is identified as

$$sG(s)\big|_{s=\frac{\omega_c}{\tan(\omega_c T_s/2)}\frac{z-1}{z+1}} = \frac{398.3\,(z-1)}{z-0.5932}. \tag{184}$$

The corresponding reference motor torque which ideally provides such joint torque may be determined using Eqs. 80, 81, and 56. With the system parameter values mentioned earlier, the associated motor torque is determined by

$$\begin{aligned}
\boldsymbol{\tau}_m^* &= \begin{bmatrix} 2.48\times10^{-5} & 0 \\ 0 & 2.48\times10^{-5} \end{bmatrix} \begin{bmatrix} b_{1r}^{-1} & 0 \\ 0 & b_{1r}^{-1} \end{bmatrix} \begin{bmatrix} -\frac{1}{18} & \frac{1}{18} \\ -\frac{1}{18} & -\frac{1}{18} \end{bmatrix}^T \boldsymbol{\tau}_{dr}^* \\
&\quad + \left(\begin{bmatrix} 1 & 0 \\ 0 & 1 \end{bmatrix} - \begin{bmatrix} 2.48\times10^{-5} & 0 \\ 0 & 2.48\times10^{-5} \end{bmatrix} \begin{bmatrix} b_{1r}^{-1} & 0 \\ 0 & b_{1r}^{-1} \end{bmatrix} \right) \hat{\boldsymbol{\tau}}_1 \\
&= \frac{1}{b_{1r}} \begin{bmatrix} -1.378\times10^{-6} & -1.378\times10^{-6} \\ 1.378\times10^{-6} & -1.378\times10^{-6} \end{bmatrix} \boldsymbol{\tau}_{dr}^* \\
&\quad + \begin{bmatrix} 1-\frac{2.48\times10^{-5}}{b_{1r}} & 0 \\ 0 & 1-\frac{2.48\times10^{-5}}{b_{1r}} \end{bmatrix} \hat{\boldsymbol{\tau}}_1, \qquad (185)
\end{aligned}$$

where b_{1r} is the reduced motor's inertia and $\hat{\boldsymbol{\tau}}_1$ is the estimated transmitted torque obtained from Eq. 56. Specifically, the estimated torque at the k^{th}-sampling (1 kHz) may be calculated as

$$\begin{aligned}
\hat{\boldsymbol{\tau}}_{1k} &= -\hat{\boldsymbol{\tau}}_{1(k-1)} - 49.6\left(\boldsymbol{\theta}_{0k} - 2\boldsymbol{\theta}_{0(k-1)} + \boldsymbol{\theta}_{0(k-2)}\right) \\
&\quad -0.0022\,\mathrm{sgn}\left(\frac{\boldsymbol{\theta}_{0k} - \boldsymbol{\theta}_{0(k-2)}}{2h}\right) + 0.0302\left(\boldsymbol{i}_k + 2\boldsymbol{i}_{k-1} + \boldsymbol{i}_{k-2}\right). \qquad (186)
\end{aligned}$$

The amplifier [33] which regulates the DC brushed MAXON® motor provides two major modes of operations, i.e. the speed and torque control. For the torque control mode, the user can specify set value that is proportional to the armature current supplied to the motor and thus the torque generated by the motor. With the typical operating condition at very low speed in the interacting robotics application, the reference motor torque Eq. 185 may be reasonably acquired through the current control directly simply by Eq. 83 with the torque constant $K_\tau = 60.3\times10^{-3}$ Nm/A.

To summarize, the controller is implemented in the 20-sim simulation program at the frequency of 1 kHz according to the typical sampling rate of the acquisition card. At each sampling, the stationary link angles are determined recursively by Eq. 41 with $\boldsymbol{h}\left(\boldsymbol{\theta}_{qs}\right)$ and $\boldsymbol{e}_{1q}^{-1}\left(\boldsymbol{h}\left(\boldsymbol{\theta}_{qs}\right)\right)$ computed from Eq. 181 and 180. Required torque at the robot joints is calculated using Eq. 79 with the damping matrix computed from Eq. 178 and the approximated velocity term by Eqs. 182, 184, and 57. Accordingly, the corresponding motor torque and the commanded current are determined from Eqs. 185, 186, and 83. Zero-order-hold (ZOH) and the current limiter of ±10 A are implemented in the simulator to reflect the finite power supply behavior of the actual motor.

4.3. Simulation

Task space impedance controller designed in the previous subsection is integrated with the developed model of the two DOF cable-pulley driven flexible joint robot. Figure 12 depicts the signal interconnection between the system and the controller where the motor current and angle are fed

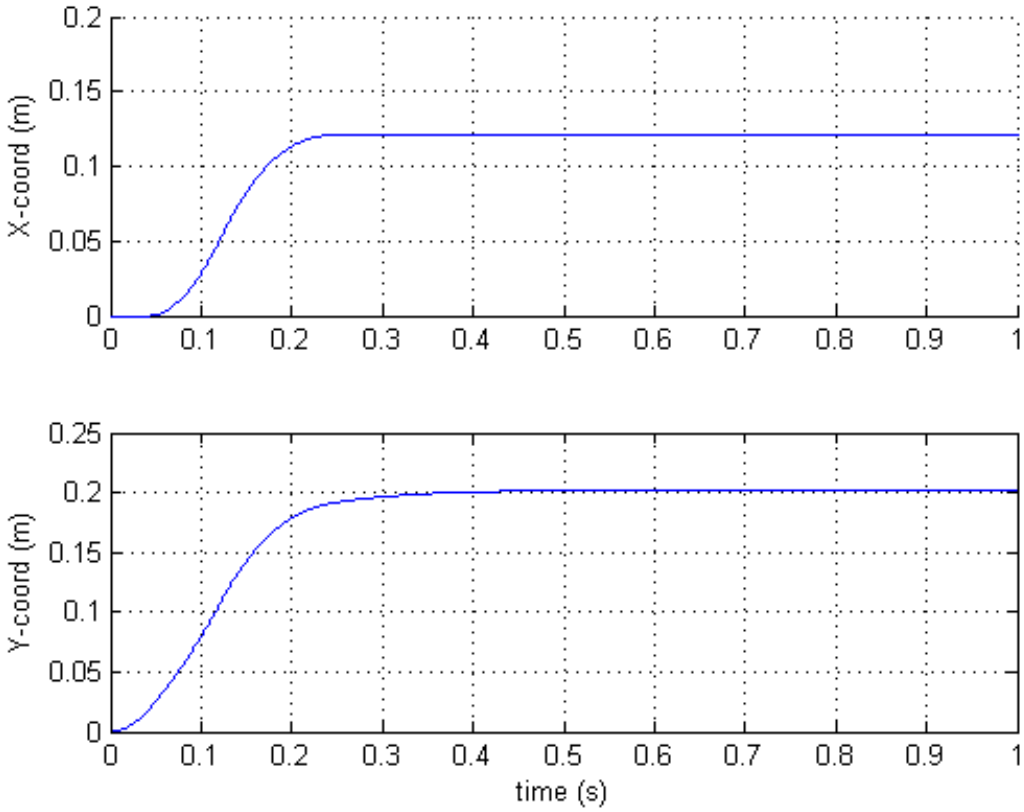

Figure 16: Motion response of the end point X/Y-coordinates for a constant set point ${}^{\{XYZ\}}\boldsymbol{x}_d = \begin{bmatrix} 0.1207 & 0.2025 & -0.2090 \end{bmatrix}^T$ m.

back to the controller for processing the commanded current. In the following, various simulations are performed to investigate the effect of several control parameters on the system response and to illustrate the effectiveness of the control law. Since the system is rather stiff, backward differentiation formula integration method with the step size of 1 ms is used in all simulations.

4.3.1. Constant Set Point

Let the initial position of the robot end point be at the center of its hemispherical workspace, i.e. ${}^{\{XYZ\}}\boldsymbol{x}(0) = \begin{bmatrix} 0 & 0 & -0.315 \end{bmatrix}^T$ m. This corresponds to $\theta_p = 0°$ and $\theta_y = 0°$. Desired position is set to be at ${}^{\{XYZ\}}\boldsymbol{x}_d = \begin{bmatrix} 0.1207 & 0.2025 & -0.2090 \end{bmatrix}^T$ m by rotating the shoulder link from the initial posture for 40° about X-axis followed by $-30°$ about Y-axis. This desired set point corresponds to $\theta_p = 0.7696$ rad $= 44.095°$ and $\theta_y = -0.3931$ rad $= -22.521°$.

The task space stiffness matrix, the damping ratio, and the desired motor inertia for this simulation are selected to be

$$ {}^{\{xyz\}}\boldsymbol{K}_d = \begin{bmatrix} 10 \times 10^3 & 0 \\ 0 & 10 \times 10^3 \end{bmatrix} \text{ N/m}, $$

$$\begin{aligned} \xi &= 4.0 \\ b_{1r} &= 200 \quad \mathrm{g \cdot cm^2}. \end{aligned} \tag{187}$$

Figure 16 shows the graph of the measured X/Y-coordinates of the end point. The response reaches the desired position $\boldsymbol{x}_d$ in 0.5 seconds with no overshoot. Hence with the proposed controller, step response of the flexible joint robot is reasonably fast yet has no overshoot thanks to a large damping ratio. It should be noted that the controlled system is not destabilized despite a large magnitude of the step input (26.63 cm of path distance); only the current is saturated in the transient phase.

4.3.2. Trajectory Tracking

A circular trajectory is generated for the tracking experiment. The starting point is at the rightmost, ${}^{\{XYZ\}}\boldsymbol{x}_d(0) = \begin{bmatrix} 0.2025 & 0 & -0.2413 \end{bmatrix}^T$ m, caused by rotating the shoulder link in the yaw direction for $-40°$. Then the trajectory is made by rotating the link around the Z-axis for a complete round in 6 seconds with a moderate constant speed of 21.2 cm/s. After that, the desired position is held constant at the starting point for the next 0.5 second. Initial position of the robot end point is intentionally placed at the center of the workspace to create a large position mismatch (22 cm of path distance) at the beginning. The controller and its parameters are the same as used in the constant set point case.

Figure 17 displays the trajectory tracking of the robot along with the reference trajectory. It is seen that the proposed controller, which is designed for the regulation objective, may be used in the tracking task that can tolerate with a moderate speed and accuracy. The initial mismatch does not tamper the tracking performance or destabilize the system. It merely causes the motor current saturation during large position error. Once the end tip enters its track, the current consumption is quite low (0.45 A average) thanks to the energy restoration from the augmented counterbalancing mechanism.

4.3.3. Motor Inertia Reduction

Reduced motor inertia has been adjusted from its nominal value of $200\,\mathrm{g \cdot cm^2}$ to investigate its effect to the controlled system. Figure 18 displays the current consumption for regulating the robot end tip at its initial position using three different values of the effective motor inertia. When the $150\,\mathrm{g \cdot cm^2}$ effective motor inertia (40% reduction) is tuned, the motor current exponentially oscillates during the transient before settling down to a constant value of 0.381 A. On the other hand, if the $248\,\mathrm{g \cdot cm^2}$ or the original motor inertia value is used, the current shows a sudden dropping pulse of 0.060 A due to immediate exposition of the gravity force to the robot. Then, the pulse disappears and the drawn current bounces back to the constant value of 0.345 A with no oscillation. From the plot, the choice of unmodified inertia yields the cleanest current response.

However, difference of the motion responses of these three cases is imperceptible due to small motor inertia portion compared to the inertia of the whole drivetrain. Specifically, $\|\boldsymbol{B}_1\| / \|\boldsymbol{B}\| = 0.088$. It

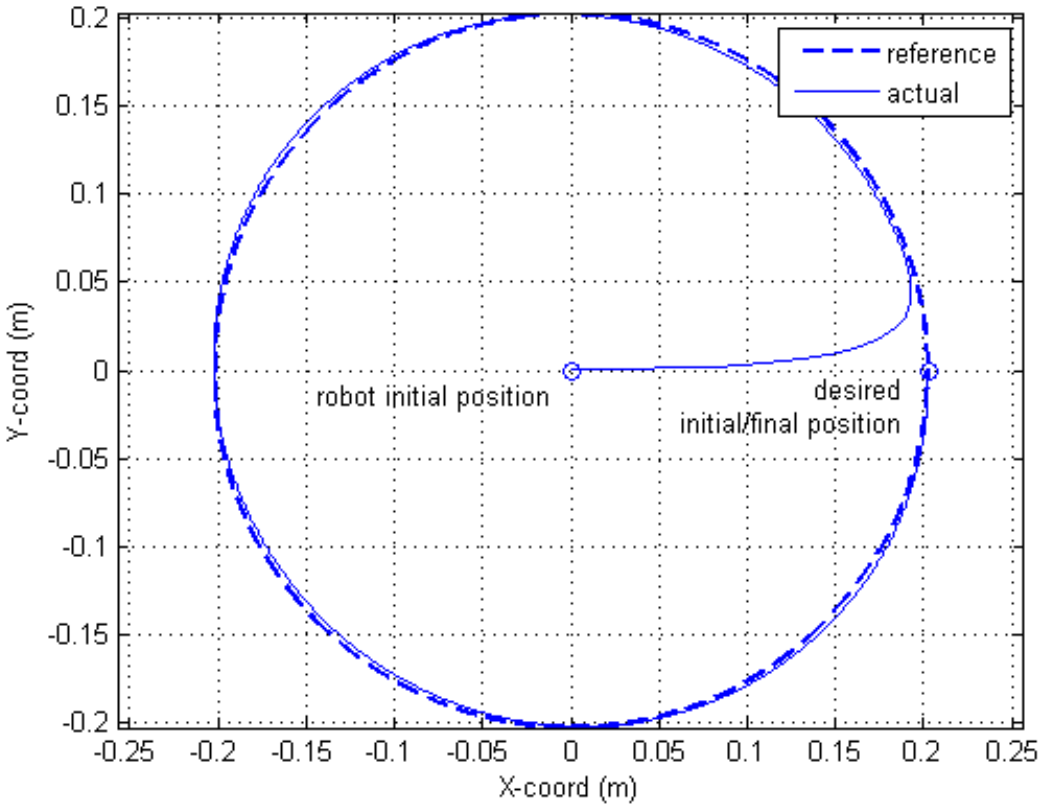

Figure 17: Trajectory tracking of the robot with initial posiiton mismatch.

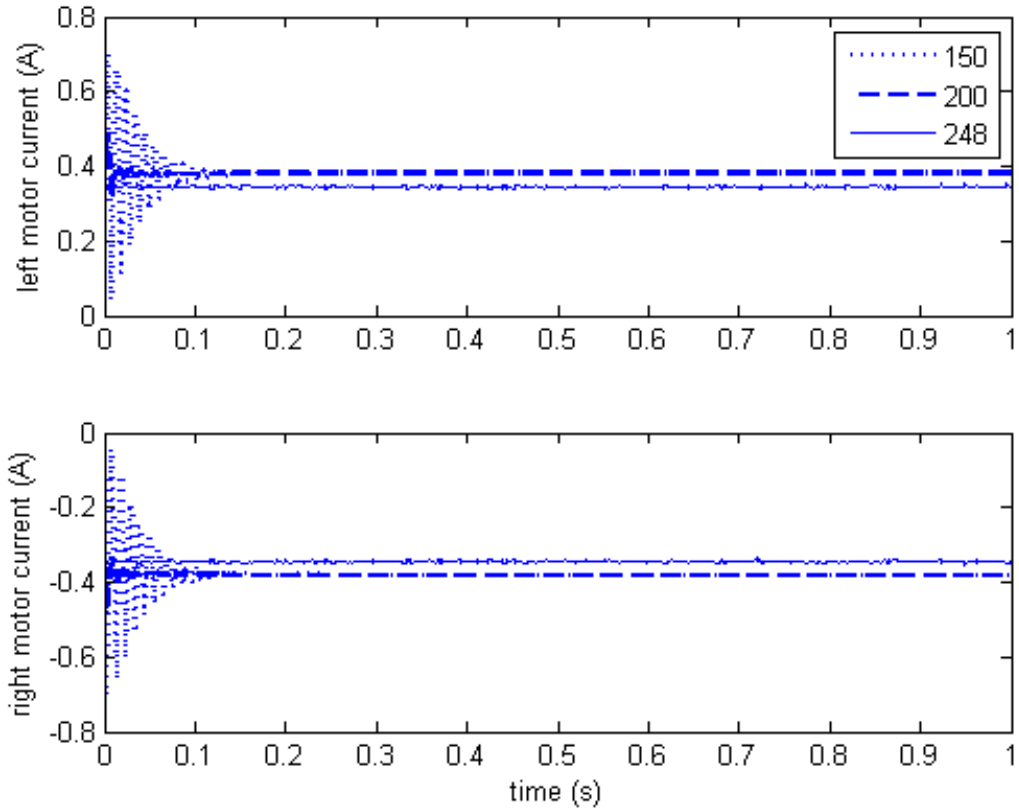

Figure 18: Current consumption of the regulation task under three different values of the effective motor inertia (150, 200, and 248 $g \cdot cm^2$).

may be concluded that the reduction of a small motor inertia in a small gear ratio system does not improve the dynamics meaningfully. If the inertia is reduced further, the current will be saturated, hitting its limits in a bang-bang manner. In turn, the end point motion starts to exhibit the oscillatory drift from the set value.

Same modulation of the motor inertia is performed when the robot end tip tracks the circular trajectory in subsection 4.3.2. Comparison of the current consumption for different effective motor inertia is depicted in Fig. 19. In the tracking case, the lowest value that can be selected is increased to 170 $g \cdot cm^2$ (30% reduction) which would induce moderate oscillation when motion discontinuity occurs. Percentage of admissible inertia reduction is decreased because larger current is involved in the tracking motion. Essentially the inertia reduction is equivalent to the increase in control loop gain. Therefore, too large inertia reduction makes the system become unstable. If the physical motor inertia value is retained (no inertia reduction), there will be no feedback of the transmitted torque. Implicitly, natural dynamics of the drivetrain is employed. The original system will draw less energy and be more stable than the modulated one, on the price of contaminated desired dynamics.

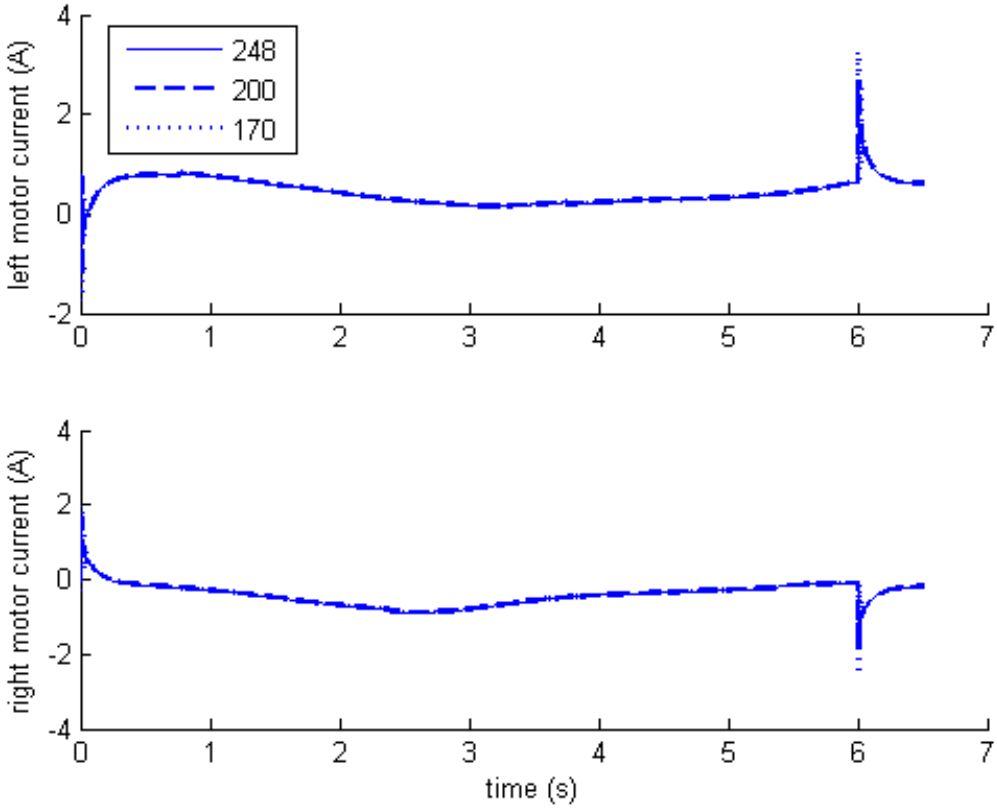

Figure 19: Current consumption of the circular tracking task under three different values of the effective motor inertia (170, 200, and 248 $g \cdot cm^2$).

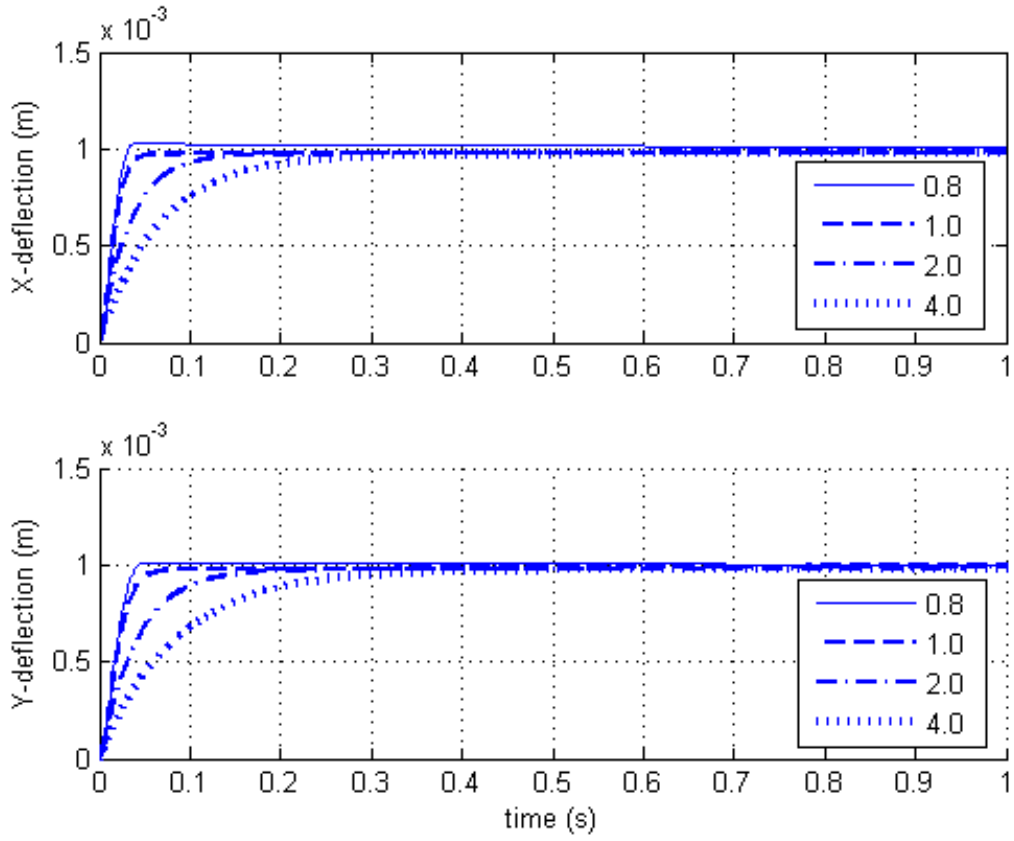

Figure 20: End tip deflection of the flexible robot with the nominal stiffness value of 10×10^3 N/m and the external force of 10 N for a set of damping ratios.

4.3.4. Task Space Stiffness and Damping

To verify that the desired task space stiffness is actually achieved, the robot is set at the center of the workspace and the external force of 10 N is applied in the x and y-direction, respectively. With the nominal stiffness value of 10×10^3 N/m, the end tip deflection responses are shown in Fig. 20 for a set of damping ratio of 0.8, 1.0, 2.0, and 4.0. It is observed that in practice larger damping makes the motion be more sluggish, while the current drawn (not shown) becomes more responsive. Together with larger stiffness (order of 10^5 N/m), this can drive the system unstable. In any case of Fig. 20, eventually the end tip reaches the point corresponding to the deflection of about 1 mm that agrees with the desired stiffness and the applied force.

Figure 21 and 22 are the deflection plots for the stiffness value of 1×10^3 and 100×10^3 N/m. Lower stiffness with high damping makes the end tip to deflect slowly and prevents it from reaching the expected deviation. Subsequently, the environment will feel the robot be stiffer than its actual value. Deflection of the system with high stiffness and light damping will largely oscillate around the steady value long before it dies out. On the other hand, if too high damping ratio is selected, responsive motor current will suppress the deflection aggressively such that the undershoot may be

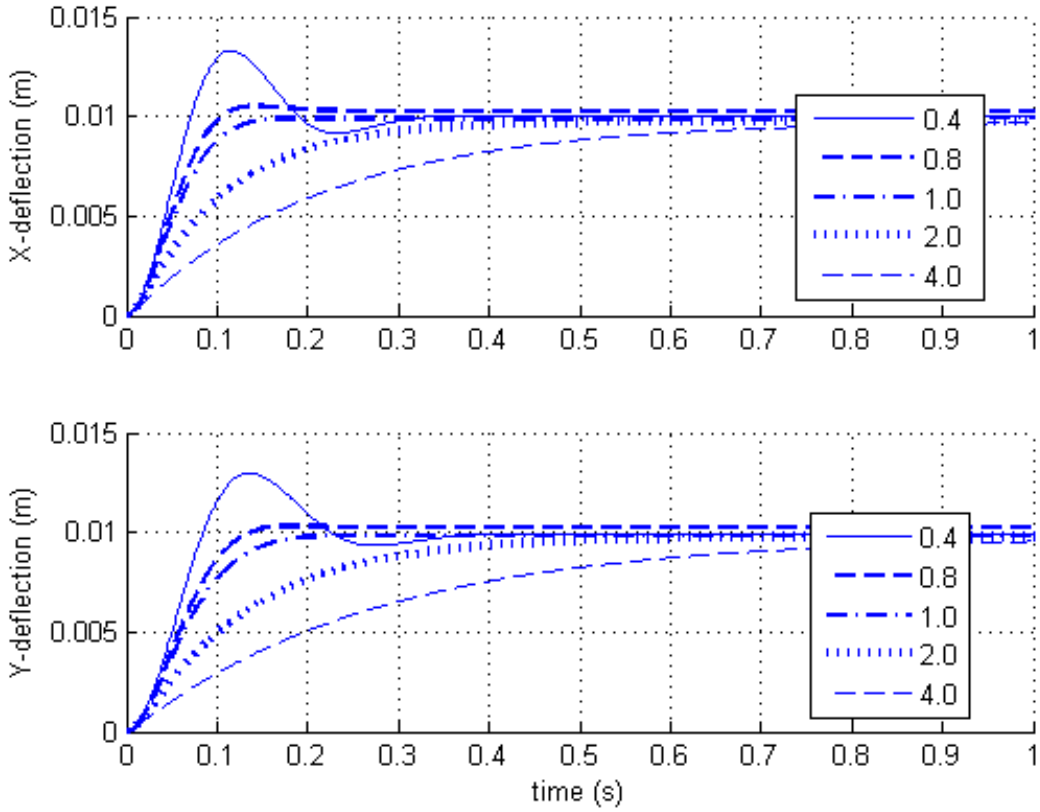

Figure 21: End tip deflection of the flexible robot with the stiffness value of 1×10^3 N/m and the external force of 10 N for a set of damping ratios.

detected. If the damping is further increased, it can cause the system to go unstable. With the stiffness value of 100×10^3 N/m selected, this system will become unstable when the damping ratio value of 4.0 or higher is used (its response not shown).

It should be mentioned that motor inertia reduction would increase the effective stiffness since it has the effect of modifying the control torque Eqs. 79 and 80 to the new one of Eq. 81. Its consequence is the increase of the control loop gain and thus the resultant stiffness becomes larger than the desired value. Therefore, motor inertia reduction is not implemented if the exact desired stiffness is of concern.

4.3.5. Application of the External Force

For the last experiment, the external force is applied to the end point while the robot is tracking the circular trajectory in subsection 4.3.2. Task space stiffness and damping ratio are set to their nominal values used in subsection 4.3.1. Figure 23 and 24 display the tracking result when the robot is subject to the 10 N force acting in the X and Y-direction throughout the path, respectively. It is observed that the end tip follows the reference trajectory closely because of the high stiffness value and the small magnitude of the applied force. As depicted in the figures, finally the end point deviates

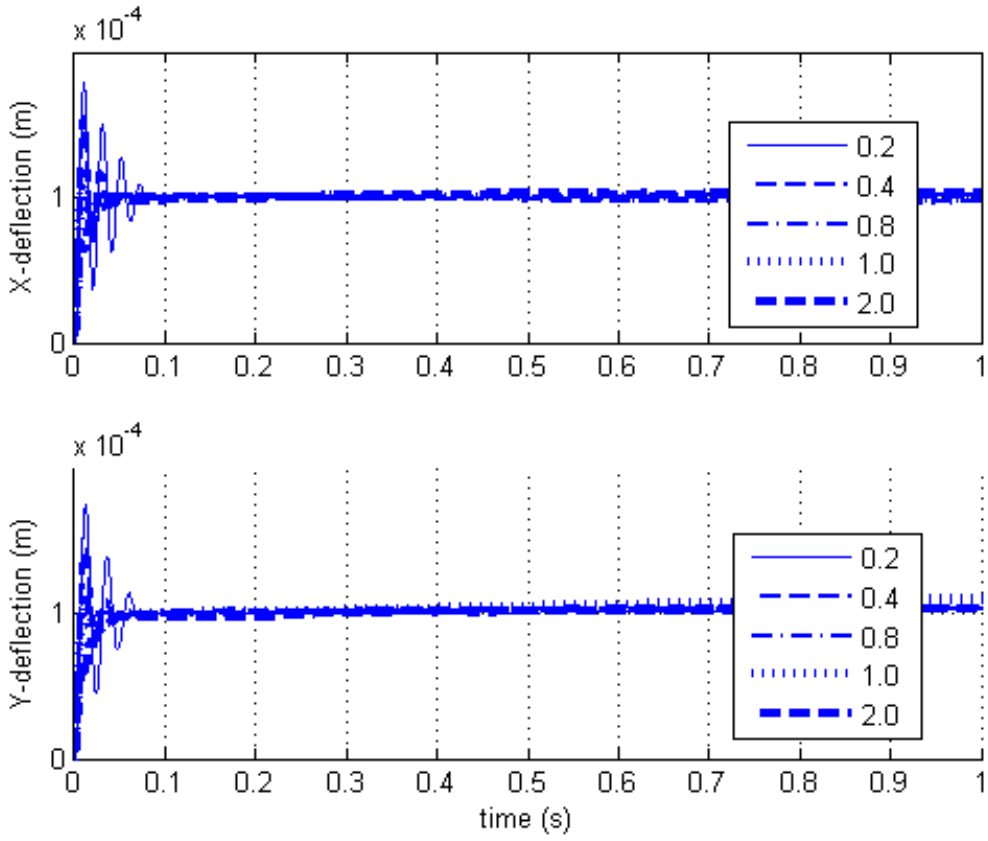

Figure 22: End tip deflection of the flexible robot with the stiffness value of 100×10^3 N/m and the external force of 10 N for a set of damping ratios. The system will be unstable if the ratio value of 4.0 or higher is used.

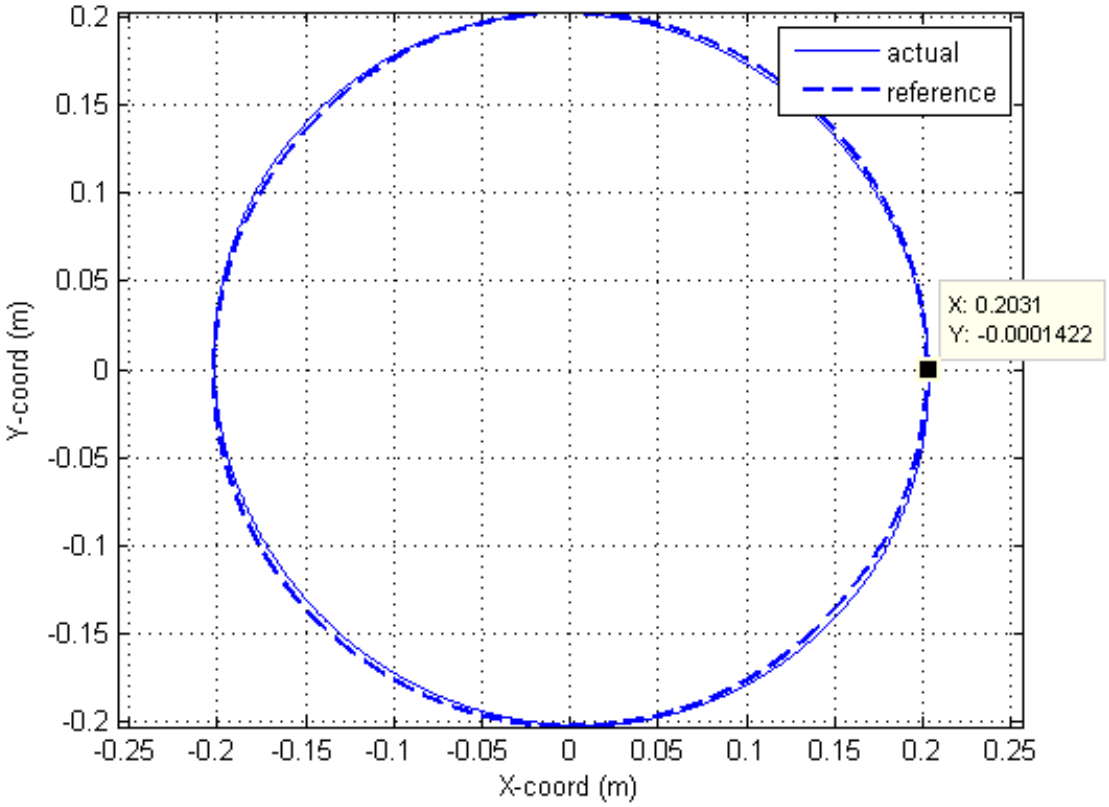

Figure 23: Trajectory tracking with nominal stiffness subject to the 10 N force applied in X-direction.

from the desired location by 0.6 and 0.86 mm in X and Y-direction respectively.

When the end point is at its final position, nominal task space stiffness matrix expressed in the local frame parallel to the reference frame $\{XYZ\}$ is determined by [34]

$$
\begin{aligned}
{}^{\{XYZ\}}\boldsymbol{K}_d &= {}^{\{xyz\}}R^T_{\{XYZ\}}\,{}^{\{xyz\}}\boldsymbol{K}_d\,{}^{\{xyz\}}R_{\{XYZ\}} \\
&= \begin{bmatrix}
k_{dx}c_y^2 + k_{dz}s_y^2 & s_p s_y c_y\left(k_{dx} - k_{dz}\right) & -c_p s_y c_y\left(k_{dx} - k_{dz}\right) \\
s_p s_y c_y\left(k_{dx} - k_{dz}\right) & k_{dx}s_p^2 s_y^2 + k_{dy}c_p^2 + k_{dz}s_p^2 c_y^2 & s_p c_p\left(-k_{dx}s_y^2 + k_{dy} - k_{dz}c_y^2\right) \\
-c_p s_y c_y\left(k_{dx} - k_{dz}\right) & s_p c_p\left(-k_{dx}s_y^2 + k_{dy} - k_{dz}c_y^2\right) & k_{dx}c_p^2 s_y^2 + k_{dy}s_p^2 + k_{dz}c_p^2 c_y^2
\end{bmatrix},
\end{aligned}
\tag{188}
$$

where the numerical value of k_{dz} is selected to be 1000×10^3 N/m as the robot cannot move along the z-direction. For the external force acting along the X and Y-direction, the pitch and yaw angles corresponding to the final end point position are $\begin{bmatrix} \theta_p & \theta_y \end{bmatrix}^T = \begin{bmatrix} -0.00059 & -0.70053 \end{bmatrix}^T$ and $\begin{bmatrix} 0.00357 & -0.69809 \end{bmatrix}^T$ rad, respectively. Substituting these values into Eq. 188, the stiffness matrix represented in $\{XYZ\}$ are

$$
{}^{\{XYZ\}}\boldsymbol{K}_d = \begin{bmatrix}
4.2138 \times 10^5 & -0.0029 \times 10^5 & -4.8789 \times 10^5 \\
-0.0029 \times 10^5 & 0.1 \times 10^5 & 0.0034 \times 10^5 \\
-4.8789 \times 10^5 & 0.0034 \times 10^5 & 5.8862 \times 10^5
\end{bmatrix}
$$

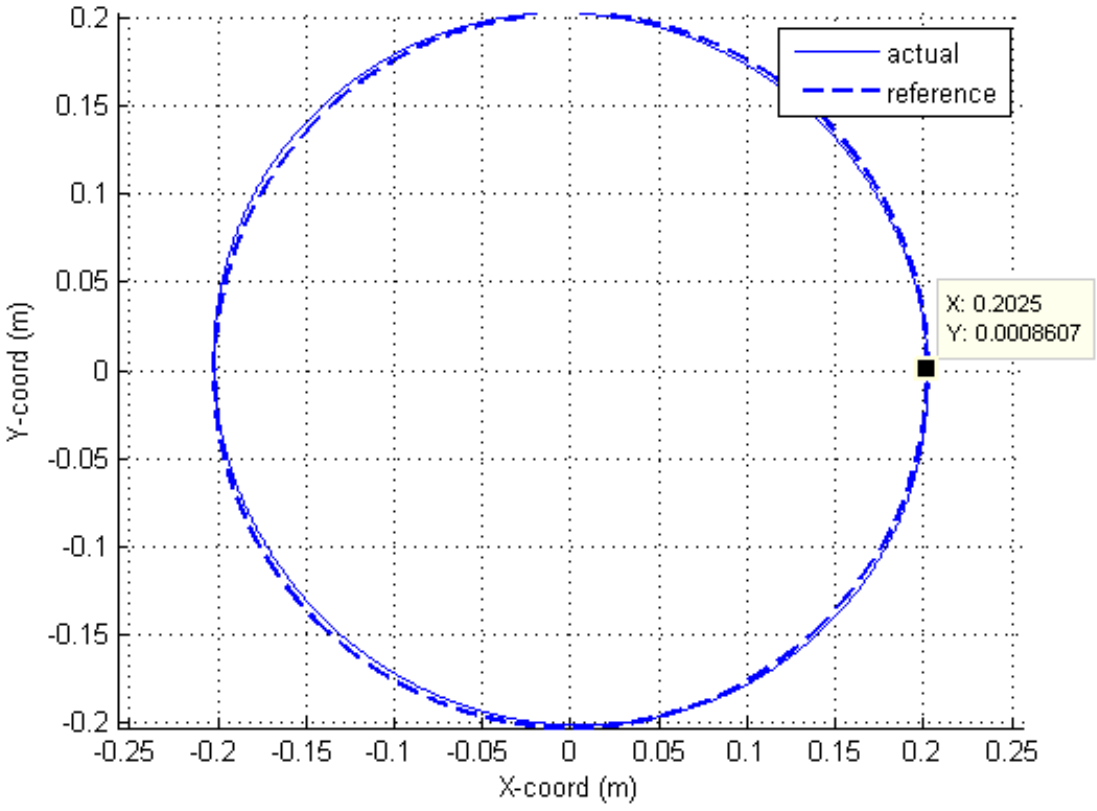

Figure 24: Trajectory tracking with nominal stiffness subject to the 10 N force applied in Y-direction.

for the first case, and

$$ {}^{\{XYZ\}}\boldsymbol{K}_d = \begin{bmatrix} 4.1900 \times 10^5 & 0.0174 \times 10^5 & -4.8747 \times 10^5 \\ 0.0174 \times 10^5 & 0.1001 \times 10^5 & -0.0207 \times 10^5 \\ -4.8747 \times 10^5 & -0.0207 \times 10^5 & 5.9099 \times 10^5 \end{bmatrix} $$

for the latter case.

Thus the associated deflections, determined from

$$ {}^{\{XYZ\}}\boldsymbol{\delta} = {}^{\{XYZ\}}\boldsymbol{K}_d^{-1}\, {}^{\{XYZ\}}\boldsymbol{F}, \tag{189} $$

along the direction of the applied force will be 0.59 and 1.0 mm for each case in order. Hence, actual deviations agree with the theoretical values. Indeed their values will match if the final constant period of 0.5 second is prolonged. Additionally, it should be noted that large application of the external force requires large current to keep the robot end tip in the track. If such current cannot be supplied, the tracking will fail and the motion will be unstable. For this flexible robot system, the external force of 40 N or more will drive the system unstable.

5. Conclusions

This work presents a task space impedance control of the manipulator driven through the nonlinear flexible transmission unit. The proposed controller regulates the stiffness and damping of the end effector at the specified position to the desired values based on the only available feedback signal information of the motor current and angle. To derive such controller, at first, a mathematical model of the transmission or drivetrain system built from the multi-stage network of nonlinear elastic mechanisms is developed. Together with the standard model of the manipulator and the DC motor, the complete model of the nonlinear flexible-joint manipulator is attained.

Since the feedback of the motor current and angle cannot be used to estimate the remaining system unobservable states, the traditional impedance control law is modified so that it uses the open-loop state estimation of the robot link angle and joint velocity as a substitute. They are computed from the motor angle recursively using the simplified stationary model of the drivetrain and robot system on the assumption that the robot operates smoothly at low enough speed. It is shown that the torque from the control law constitutes the potential energy equal to the difference of the gravitational plus elastic potential energy of the passive robot/transmission subsystems and the elastic potential energy of the desired task space compliance, all at the stationary link angles. This fact is used to prove the stability and passivity of the system.

Additionally, the motor current is used to infer the updated transmitted torque to the drivetrain from the motor. This is achieved with the discretized mechanical model of the motor derived from the discrete Euler-Lagrange formulation. The estimated transmitted torque then is employed in the impedance control law to reduce the motor inertia. As a result, the motor dynamics which distorts

the desired transmitted torque will be attenuated. Effectively the modulated motor behaves closer to an ideal torque source, and so does the actual robot characteristics to the ideal target impedance. Implementation of the control law via the current or the voltage control mode of the motor system is discussed.

An example system of a two DOF cable-pulley driven flexible joint robot is designed and controlled with the proposed task space impedance controller. The controller exhibits satisfactory results in standard tasks such as regulation or trajectory tracking with and without the external force applied. Additional simulation is performed to verify that the specified task space stiffness is indeed achieved. Effects of the damping ratio value on the motion response is studied. Overly high stiffness and light damping makes the robot oscillate for a long period before settling down. On the other hand, the robot moves sluggishly if too low stiffness and high damping are selected. The robot might even be unable to reach the desired position. Worse yet, excessively large stiffness and damping implemented digitally causes the system to go unstable.

Experimenting with several reduced motor inertia values to improve the dynamical response indicates that the lightweight mechanical system design at the beginning yields better response than using the torque or current feedback in shaping the inertia to the desired value later. From the investigation, it is clear that the proposed controller is capable of regulating the task space impedance of the practical nonlinear flexible-joint manipulators, which will be of great benefit for accomplishing the challenging missions.

References

[1] Guthart, G. S. and Salisbury, J. K., "The Intuitive® Telesurgery System: Overview and Application," *Proc. of the IEEE International Conference on Robotics and Automation*, pp. 618-621, 2000.

[2] Wyrobek, K. A., et al., "Towards a Personal Robotics Development Platform: Rationale and Design of an Intrinsically Safe Personal Robot," *Proc. of the IEEE International Conference on Robotics and Automation*, pp. 2165-2170, 2008.

[3] Hogan, N., "Impedance Control: An Approach to Manipulation," *Trans. of the ASME Journal of Dynamic Systems, Measurement, and Control*, Vol. 107, No. 1, pp. 1-24, 1985.

[4] Chiaverini, S., et al., "A Survey of Robot Interaction Control Schemes with Experimental Comparison," *IEEE/ASME Trans. on Mechatronics*, Vol. 4, No. 3, pp. 273-285, 1999.

[5] Spong, M., "Modeling and Control of Elastic Joint Robots," *Trans. of the ASME Journal of Dynamic Systems, Measurement, and Control*, Vol. 109, No. 4, pp. 310-319, 1987.

[6] Zollo, L., et al., "Compliance Control for an Anthropomorphic Robot with Elastic Joints: Theory and Experiments," *Trans. of the ASME Journal of Dynamic Systems, Measurement, and Control*, Vol. 127, No. 3, pp. 321-328, 2005.

[7] Tomei, P., "A Simple PD Controller for Robots with Elastic Joints," *IEEE Trans. on Automatic Control*, Vol. 36, No. 10, pp. 1208-1213, 1991.

[8] Albu-Schaffer, A., et al., "Cartesian Impedance Control of Redundant Robots: Recent Results with the DLR-Light-Weight-Arms," *Proc. of the IEEE International Conference on Robotics and Automation*, pp. 3704-3709, 2003.

[9] Ott, C., et al., "On the Passivity-Based Impedance Control of Flexible Joint Robots," *IEEE Trans. on Robotics*, Vol. 24, No. 2, pp. 416-429, 2008.

[10] Chien, M. C. and Huang, A. C., "Adaptive Impedance Controller Design for Flexible-Joint Electrically-Driven Robots without Computation of the Regressor Matrix," *Robotica*, Vol. 30, No. 1, pp. 133-144, 2012.

[11] Pratt, G. and Williamson, M., "Series Elastic Actuators," *Proc. of the IEEE/RSJ International Conference on Intelligent Robots and Systems*, pp. 399-406, 1995.

[12] Zinn, M., et al., "A New Actuation Approach for Human Friendly Robot Design," *International Journal of Robotics Research*, Vol. 23, No. 4-5, pp. 379-398, 2004.

[13] Wolf, S. and Hirzinger, G., "A New Variable Stiffness Design: Matching Requirements of the Next Robot Generation," *Proc. of the IEEE International Conference on Robotics and Automation*, pp. 1741-1746, 2008.

[14] Grebenstein, M., et al., "The DLR Hand Arm System," *Proc. of the IEEE International Conference on Robotics and Automation*, pp. 3175-3182, 2011.

[15] Spong, M. W., et al., "Robot Modeling and Control," *John Wiley & Sons*, New York, 2006.

[16] Karnopp, D. C., et al., "System Dynamics: Modeling and Simulation of Mechatronic Systems," *John Wiley & Sons*, New York, 2006.

[17] Spong, M. W., "Underactuated Mechanical Systems," in *Control Problems in Robotics and Automation, Springer-Verlag*, London, 1997.

[18] Ortega, R., et al., "Interconnection and Damping Assignment Passivity-Based Control of Port-Controlled Hamiltonian Systems," *Automatica*, Vol. 38, No. 4, pp. 585-596, 2002.

[19] Bloch, A. M., et al., "Controlled Lagrangian and the Stabilization of Mechanical Systems I: The First Matching Theorem," *IEEE Trans. on Automatic Control*, Vol. 45, No. 12, pp. 2253-2270, 2000.

[20] Bloch, A. M., et al., "Controlled Lagrangian and the Stabilization of Mechanical Systems II: Potential Shaping," *IEEE Trans. on Automatic Control*, Vol. 46, No. 10, pp. 1556-1571, 2001.

[21] Colgate, J. E., "The Control of Dynamically Interacting Systems," Ph.D. thesis, M.I.T., 1988.

[22] Marsden, J. E. and West, M., "Discrete Mechanics and Variational Integrators," *Acta Numerica*, Vol. 10, pp. 357-514, 2001.

[23] Anderson, R. J., "Passive Computed Torque Algorithms for Robots," *Proc. of the IEEE Conference on Decison and Control*, pp. 1638-1644, 1989.

[24] Slotine, J-J. E. and Li, W., "Applied Nonlinear Control," *Prentice-Hall*, New Jersey, 1991.

[25] Khalil, H. K., "Nonlinear Systems," Third edition, *Prentice-Hall*, New Jersey, 2001.

[26] Koditschek, D., "Natural Motion for Robot Arms," *Proc. of the IEEE Conference on Decision and Control*, pp. 733-735, 1984.

[27] Meirovitch, L., "Fundamentals of Vibrations," *McGraw-Hill*, New York, 2001.

[28] Snow, E. R., "The Load/Deflection Behavior of Pretensioned Cable/Pulley Transmission Mechanisms," S.M. thesis, M.I.T., 1993.

[29] Nippon System Kaihatsu, "NSK Rolling Bearing Catalog," CAT. No. E1102e, 2007.

[30] Pitakwatchara, P., "Spring-Cable Counter-Balancing System for Pitch-Yaw Compound Joint Mechanism," *Thailand Patent Office*, Patent Pending Application #1201002792, filed on June 12, 2012.

[31] Townsend, W., "The Effect of Transmission Design on Force-Controlled Manipulator Performance," Ph.D. thesis, M.I.T., 1988.

[32] 20-sim simulation program, URL: http://www.20sim.com, Controllab Products B.V., the Netherlands, access on Jul., 5$^{\text{th}}$, 2013.

[33] MAXON® motor 4-Q-DC Servoamplifier operating instructions, model no. ADS 50/10, #201583, July 2009 edition, URL: http://www.maxonmotor.com, maxon motor ag, access on Jul., 15$^{\text{th}}$, 2013.

[34] Loncaric, J., "Normal Forms of Stiffness and Compliance Matrices," *IEEE J. of Robotics and Automation*, Vol. 3, No. 6, pp. 567-572, 1987.

ผลผลิตที่ได้จากโครงการ

1. Phongsaen Pitakwatchara. “Task Space Impedance Control of the Manipulator Driven Through the Multistage Nonlinear Flexible Transmission.” Transactions of the ASME Journal of Dynamic Systems, Measurement, and Control 137, 2 (2015): 1-17. (ISI/SCOPUS)
2. Phongsaen Pitakwatchara. “Modelling and Control of the Multi-stage Cable Pulley-driven Flexible-joint Robot.” International Journal of Advanced Robotic Systems 11, 1 (2014): 1-16. (ISI/SCOPUS)
3. ผู้ช่วยศาสตราจารย์ ดร.พงศ์แสน พิทักษ์วัชระ และ นายฉัตรชัยวัฒน์ โลวะกิจ. “อนุสิทธิบัตร: กลไกปรับแรงตึงในลวดสลิง.” กรมทรัพย์สินทางปัญญา เลขที่อนุสิทธิบัตร 9201 ออกให้ ณ วันที่ 8 ตุลาคม 2557.
4. ชุดหุ่นยนต์ต้นแบบที่ข้อต่อมีความยืดหยุ่น เพื่อการศึกษาการควบคุมแบบอันตรกิริยา
5. Phongsaen Pitakwatchara. “Task Space Impedance Control of the Multi-Stage Cable-Pulley Driven Flexible Joint Robot System.” The 5th TSME International Conference on Mechanical Engineering, Chiang Mai (2014).
6. Chatchaiwat Lowakij and Phongsaen Pitakwatchara. “Kinematical Design of a General-Purpose Service Robot Arm Based on the Mobility Consideration.” The 4th TSME International Conference on Mechanical Engineering, Chon-Buri (2013).
7. Phongsaen Pitakwatchara. “Control of a Two-Degree of Freedom Cable Driven Compound Joint System: Preliminary Results.” The 3rd TSME International Conference on Mechanical Engineering, Chiang Rai (2012).

Task Space Impedance Control of the Manipulator Driven Through the Multistage Nonlinear Flexible Transmission

Phongsaen Pitakwatchara
Assistant Professor
Department of Mechanical Engineering,
Faculty of Engineering,
Chulalongkorn University,
Bangkok 10330, Thailand
e-mail: phongsaen.p@chula.ac.th

This paper addresses the task space impedance control of a robot driven through the multistage nonlinear flexible transmission. The proposed controller uses limited information of the angle and the current of the motors to regulate the end point compliance at the specified set point. In particular, motor angle is employed to estimate the stationary robot link angle and joint velocity in real time. They are then used to constitute the stationary force on the attempt to cancel the robot gravity force and to form the task space interacting force according to the desired impedance characteristics. Motor current is used to infer the transmitted torque to the robot. This torque is fed back to mitigate the effect of the motor inertia from deteriorating the desired impedance. Asymptotic stability of this controller with the flexible joint robot is guaranteed with additional damping. Passivity of the system is also investigated. Simulation and experiments of the proposed control scheme on a two degrees-of-freedom (DOF) cable-pulley driven flexible joint robot model are examined. [DOI: 10.1115/1.4028252]

1 Introduction

Current robotic systems are extending their capability to work in more unstructured and complex environment, e.g., a laparoscopic surgical robotic system [1] or a service robot system [2] among others. To successfully implement such challenging tasks, the robot must be controlled to exhibit appropriate impedance behavior [3]. Many control laws are devised to achieve the desired impedance behavior especially for the rigid robots [4]. Later, the controllers have been modified to cope with flexible robots where their elastic behavior is typically viewed as undesirable dynamics that complicates the control problem. Only few works attempted on controlling the impedance of the flexible joint robots compared to the regulation and tracking control. According to the simplified model of the flexible joint robot [5], compliance control with online gravity compensation based on the measurable motor angles and their derivatives, and the desired robot link angles is applied to a cable-actuated robot [6]. The proposed control law resembles the proportional-derivative regulation control with constant gravity compensation [7].

Improvement of the response may be achieved by feeding back additional (noncollocated) signals, e.g., link angles or joint torques. Applying the singular perturbation analysis to the flexible robot model, the simplified tracking impedance controller using the measured joint torques and their derivatives, the robot link angles and their derivatives, and the desired end effector trajectory is implemented on the Deutsches Zentrum für Luft-und Raumfahrt (DLR)-II arm [8]. Passivity approach has also been used in designing the highly robust and stable impedance controller with the feedback signals of the joint torques and their derivatives as well as the motor angles and their derivatives for the desired robot end effector posture [9]. Sophisticated adaptive impedance controller based on the function approximation technique, where the transmission and actuator dynamics are taken into account, is proposed [10]. Note that this controller requires the measurement of the robot link angles and their derivatives, the joint torques, the motor currents, and the external force, which is presumed to act precisely at the robot end effector. Since extra feedback information has been exploited, the system response using these controllers will be improved in various aspects.

Novel manipulators treat their inherent flexibility as a boon, particularly to the tasks involving uncertainties and shock loads as frequently encountered in general service operation, where the interaction with the environment is inevitable. Physical spring is intentionally introduced [11] as the interface between the actuator and the equipped joint of the legged robot, for the main purpose of temporarily storing and restoring the impact energy from walking and running. An important consequence is the lower effective impedance. Reference [12] proposed the micro–macro actuation scheme for driving the robot. With this actuation approach, the safety and the performance of the robot may be attained simultaneously. In recent work, physically controllable compliance elements such as the variable stiffness actuators [13], where a redundant actuator is employed to adjust the effective stiffness of the actuator through some mechanisms, are designed and applied to the robots. The DLR hand-arm manipulator [14] uses these advanced actuators and the embedded joint torque sensors, making it capable of adjusting the stiffness in a passive manner and reacting to the collision force safely. In MEMS research, it is common to employ the inherently flexible piezo-electric microgripper in assembling the microparts. Appropriate impedance characteristics of this microrobot may be regulated through the control system based on the position feedback of the gripper manipulating point [15].

This research extends the previous work of passive impedance control [9] to the robot system driven through the multistage nonlinear flexible transmission whereby only the motor angle and current measurement are available. The proposed controller resembles that of Ref. [6] in the way that they regulate the task space stiffness and damping of the end effector without any noncollocated signal feeding back. In Ref. [6], the robot link angles are estimated from the motor angles through the joint stiffness/gravity equilibrium torque. For the proposed controller, however, they are estimated from the motor angles using the quasi-static torque balancing between the gravity and the joint stiffness plus the desired task space compliance. This ensures the correct

Contributed by the Dynamic Systems Division of ASME for publication in the Journal of Dynamic Systems, Measurement, and Control. Manuscript received September 20, 2013; final manuscript received August 4, 2014; published online September 10, 2014. Assoc. Editor: Yongchun Fang.

estimation of the link angles even the robot is interacting with the environment. Also, the controller does not require the motor velocity measurement. Rather, the related damping force is estimated from the motor angle via the nonmodel-based first-order differentiation filter. Additionally, the motor current is fed back to suppress the intervening dynamics of the transmission system. Therefore, the proposed controller is superior to Ref. [6].

The controller of Ref. [8] makes use of the actual robot link angles and their derivatives to shape the slow dynamics of the rigid robot, as well as the real transmitted joint torques and their derivatives to improve the fast dynamics of the flexible joint, rather than using the quasi-static estimation values as in the proposed controller. In addition, the controller structure of Ref. [8] is designed for tracking the reference trajectory, not merely for regulating around the set point. Therefore, the tracking performance with the desired end effector compliance should be better. However, the stability of the system in Ref. [8] cannot be concluded because the underlying Tychonov stability theorem requires exponential stability of both the boundary layer and the quasi steady state systems. Consequently, the use of this singular perturbation based controller with moderately or highly flexible joint manipulator system may be unacceptable.

The work of Ref. [9] addresses the problem of harmonic gear driven flexible joint robot in which its drivetrain may be viewed as a single-stage linear flexible transmission unit. In this paper, the proposed controller has been generalized to support the case where the manipulator is driven through the multistage nonlinear compliant transmission system. Furthermore, realizing the limited availability of the joint torque sensor in standard manipulators, this work employs the motor current in estimating the transmitted torque instead. In both works, the torque feedback is used to reduce the effective motor inertia thus enhancing the transmission dynamics. However, Ref. [9] also uses the derivative of torque feedback that helps attenuating the fluctuating response. Therefore, the controller of Ref. [9] should yield better result than the proposed controller on the price of extra torque feedback signal and its derivative.

The controller in Ref. [10] is designed using the backstepping technique for the cascaded plants of the robot, the transmission, and the actuator systems. Similar to Ref. [9], the development is based on the simplified single-stage linear flexible transmission unit. However, this impedance controller is much more involved than others since it takes into account full system dynamics and adaptively handles the time-varying uncertainties and disturbances. As a result, it requires several feedback signals including the robot joint torque and the interaction force where the practicality issue needs to be concerned. Nevertheless, Ref. [10] shows a promising tracking result in the presence of the constraint wall that is expected to outperform other controllers. To summarize, the proposed controller is capable of displaying the desired task space stiffness and damping for the manipulator driven through the multistage nonlinear flexible transmission system. Since it uses only the minimal feedback signals of the motor angle and current, and the controller formulation does not address the system robustness, the performance will be degraded for the demanding tasks such as trajectory tracking with high-speed. Nevertheless, the closed-loop stability and passivity are guaranteed throughout the operations.

The outline of this paper is as follow: In Sec. 2, the system model consisting of the rigid robot and the multistage transmission is derived. Based on this model and the widely available motor angle and current feedback, task space impedance control yielding the desired viscoelastic behavior at the specified set point is developed in Sec. 3. Proof of the system passivity and stability are provided. A prototypical 2DOF cable-pulley driven flexible joint robot with the proposed control law is simulated in Sec. 4 to study the motion response subject to the external force and the effect of the motor inertia reduction. Initial experiments on the actual apparatus are also performed. Section 5 concludes the study.

2 Modeling of the Robot System Driven Through the Multistage Flexible Transmission Unit

Very few manipulators are driven by the actuators directly. Typically, some mechanisms must be employed to transmit and modulate the power, motion, and force, from the actuators to the input joints of the robot. The transmission mechanism possessing certain degrees of complex dynamics may have to be inevitably devised due to some design requirements. Particularly, the multistage flexible drivetrain unit are widely adopted in order to fulfill the space constraint of the speed reducer and to provide suitable inherent compliance to the advanced manipulator. In the following, a simplified model of the robot system driven through the multistage nonlinear flexible transmission is derived. Since the majority of the system flexibility is concentrated in the transmission unit and at the joints connecting the drivetrain to the rigid robot, the modeling may be performed through separate analysis of each subsystem.

2.1 Rigid Robot Model. Joint space model of the rigid robot is well studied and hence it will just be mentioned here

$$\boldsymbol{M}(\boldsymbol{q})\ddot{\boldsymbol{q}} + \boldsymbol{C}(\boldsymbol{q},\dot{\boldsymbol{q}})\dot{\boldsymbol{q}} + \boldsymbol{g}(\boldsymbol{q}) = \boldsymbol{\tau}_{\mathrm{dr}} + \boldsymbol{\tau}_{\mathrm{ext}} \tag{1}$$

where $\boldsymbol{M}(\boldsymbol{q})$ is the joint inertia matrix, $\boldsymbol{C}(\boldsymbol{q},\dot{\boldsymbol{q}})$ is the Coriolis/centrifugal matrix, and $\boldsymbol{g}(\boldsymbol{q})$ is the gravitational torque vector. In most cases, the translational kinetic energy of the rotors in the transmission unit may be incorporated with that of the manipulator. Therefore, the joint inertia matrix $\boldsymbol{M}(\boldsymbol{q})$ is determined by

$$\boldsymbol{M}(\boldsymbol{q}) = \sum_{i=1}^{n} \boldsymbol{J}_{\mathrm{l},i}^{\mathrm{b}}(\boldsymbol{q})^{\mathrm{T}} \mathcal{M}_{\mathrm{l},i} \boldsymbol{J}_{\mathrm{l},i}^{\mathrm{b}}(\boldsymbol{q}) + \sum_{j=1}^{m} m_{\mathrm{r},j} \boldsymbol{J}_{\mathrm{vr},j}^{\mathrm{b}}(\boldsymbol{q})^{\mathrm{T}} \boldsymbol{J}_{\mathrm{vr},j}^{\mathrm{b}}(\boldsymbol{q}) \tag{2}$$

addressing the robot link inertia, $\mathcal{M}_{\mathrm{l},i}$, and the rotor mass, $m_{\mathrm{r},j}$. $\boldsymbol{J}_{\mathrm{l},i}^{\mathrm{b}}(\boldsymbol{q})$ and $\boldsymbol{J}_{\mathrm{vr},j}^{\mathrm{b}}(\boldsymbol{q})$ are the body-fixed geometric Jacobian matrices of the link and the rotor, respectively.

$\boldsymbol{C}(\boldsymbol{q},\dot{\boldsymbol{q}})$ is known as the Coriolis/centrifugal matrix where its elements may be calculated directly from $\boldsymbol{M}(\boldsymbol{q})$ using the Christoffel symbol of the first kind. The gravity torque vector $\boldsymbol{g}(\boldsymbol{q})$ is governed by the gravitational potential energy (PE) of the link and the rotor masses $V_g(\boldsymbol{q})$, i.e., $\boldsymbol{g}(\boldsymbol{q}) = \left(\partial V_g(\boldsymbol{q})/\partial \boldsymbol{q}\right)^{\mathrm{T}}$. On the right-hand side, the vector $\boldsymbol{\tau}_{\mathrm{dr}}$ is the actual torque applied at the robot joint by the transmission unit and the vector $\boldsymbol{\tau}_{\mathrm{ext}}$ is the reflected torque at the robot joint caused by the external force $\boldsymbol{F}_{\mathrm{ext}}$, i.e., $\boldsymbol{\tau}_{\mathrm{ext}} = \boldsymbol{J}(\boldsymbol{q})^{\mathrm{T}} \boldsymbol{F}_{\mathrm{ext}}$ through the linear mapping of its analytical Jacobian matrix $\boldsymbol{J}(\boldsymbol{q})$ of the frame attached to the point of application of the external force.

2.2 Multistage Flexible Transmission Model. The drivetrain or the transmission system is the mechanism that transmits the power from the input power source to the remote system which receives its output power. For the robotic system, the drivetrain typically comprises several parts as linkages, gears, belts, etc., in delivering the power. While the power is being transmitted through the mechanism, the power variables are often being modulated to amplify the output torque or to reduce the output velocity. Ideal transmission would preserve the power flow at any instant. Nonetheless, the actual system deviates from this ideal line due to the underlying dynamics and impedance properties of the parts and matings. Therefore, it is important to understand the dynamics of this subsystem in order to improve the validity of the system model for the design of the controller.

Complicated structure of the drivetrain mechanism may in general be divided into multiple stages of the subtransmission connecting in tandem. Each stage has the submechanism to transmit the power to the next stage. The submechanism itself may be constructed from a multitude of mechanical elements. However, from the modeling viewpoint, they can be modeled using only three elemental behaviors of the inertance, the compliance, and the

resistance, in conjunction with the zero (0) and one (1) nodes and the transformers. Bond graph technique [16] may be useful in the modeling process.

The ideal subtransmission at each stage can be modeled as the network of the transformers (the reducers) connecting the inport to the outport. To make the model be more realistic, lumped compliance elements should be included to capture the compliant characteristics of the mechanism, as depicted in Fig. 1. At the inport and the outport of each stage, lumped inertance elements may be connected where the resistance may be introduced as well.

For a large class of the transmission systems where the key elements are the rotors, such as the gear-train or the cable-pulley circuit, the mechanical advantage or the transmission ratio of the mechanism in each stage is constant. Hence, the modulated velocity vector $\dot{\boldsymbol{\theta}}_{\mathrm{m},j}$ after the jth-stage reducer would be $\dot{\boldsymbol{\theta}}_{\mathrm{m},j} = \boldsymbol{T}_j \dot{\boldsymbol{\theta}}_{j-1}$, where $\dot{\boldsymbol{\theta}}_{j-1}$ is the p-dimensional outport velocity vector from the previous stage and $\boldsymbol{T}_j$ is the $p \times p$ jth-stage constant transmission ratio matrix. Referring to the lumped elastic elements of the jth-stage in Figs. 1 and 2, the elastic PE of the ith-elastic element may be written as

$$V_{e,ij}(\boldsymbol{\theta}_{j-1}, \boldsymbol{\theta}_j) = \int_0^{\delta} e_{ij}(\boldsymbol{\theta}_{\mathrm{m},j} - \boldsymbol{\theta}_j) d(\boldsymbol{\theta}_{\mathrm{m},j} - \boldsymbol{\theta}_j) = \int_0^{\delta} e_{ij}(\boldsymbol{T}_j \boldsymbol{\theta}_{j-1} - \boldsymbol{\theta}_j) d(\boldsymbol{T}_j \boldsymbol{\theta}_{j-1} - \boldsymbol{\theta}_j) \tag{3}$$

where $e_{ij}(\boldsymbol{T}_j \boldsymbol{\theta}_{j-1} - \boldsymbol{\theta}_j)$ is the nonlinear elastic force of the ith-elastic element in the jth-stage, which depends on the generalized coordinates $\boldsymbol{\theta}_{j-1}$ and $\boldsymbol{\theta}_j$. Hence, the total elastic PE of the transmission unit is merely the sum of the PE of every elastic elements, i.e.,

$$V_e(\boldsymbol{q}, \boldsymbol{\theta}) = \sum_{j=1}^{q} V_{e,j} = \sum_{j=1}^{q} \sum_{i=1}^{p} V_{e,ij} \tag{4}$$

Note that the total number of stages of the transmission system is q and the configuration of the jth-stage may be described by the p-generalized coordinates $\boldsymbol{\theta}_{j-1}$. In turn, the total number of DOF of the transmission system is pq, including the actuator generalized coordinates $\boldsymbol{\theta}_0$ at the transmission inport. They are lumped into the vector $\boldsymbol{\theta} = \begin{bmatrix} \boldsymbol{\theta}_0^{\mathrm{T}} & \boldsymbol{\theta}_1^{\mathrm{T}} & \cdots & \boldsymbol{\theta}_{q-1}^{\mathrm{T}} \end{bmatrix}^{\mathrm{T}}$. It should be mentioned that the outport generalized coordinates, $\boldsymbol{\theta}_q$, are the generalized coordinates of the robot, $\boldsymbol{q}$, corresponding to the generalized torque $\boldsymbol{\tau}_{\mathrm{dr}}$ applied at the robot joints.

Gravitational PE of the rotor drivetrain system is independent of its own generalized coordinates $\boldsymbol{\theta}$ if the rotors are geometrically symmetric about their rotating axes where the center of masses are located. It has already been taken care of within the rigid robot model by $V_g(\boldsymbol{q})$. With the same assumption, the translational kinetic energy of the drivetrain due mainly to the rotor masses is not relevant to $\boldsymbol{\theta}$ and $\dot{\boldsymbol{\theta}}$, and it has been accounted with the kinetic energy of the rigid robot. Hence only the rotational kinetic energy T_{r} of the drivetrain is left. Usually, the rotors in the drivetrain system rotate at much higher speed than the robot angular velocity.

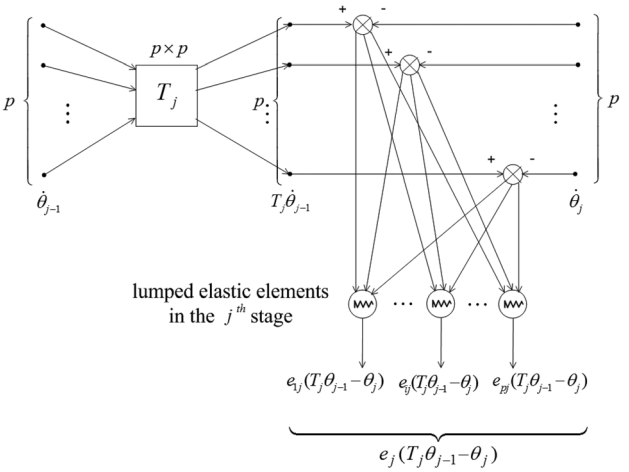

Fig. 2 Signal flow diagram illustrating the network of the elastic elements and the subscript notations of the *j*th-stage transmission system

Therefore, the kinetic energy of the specific rotor drivetrain may be simplified to

$$T_{\mathrm{r}} = \sum_{k=1}^{pq} T_{\mathrm{r},k} = \sum_{k=1}^{pq} \frac{1}{2} b_k \dot{\theta}_k^2 \tag{5}$$

in which b_k is the kth-rotor inertia about its rotational axis and $\dot{\theta}_k$ is its spinning angular velocity. The rotors of the motors are counted in here as well.

Lagrangian formulation is applied to derive the drivetrain model. Equations of motion for the drivetrain subsystem expressed in its generalized coordinates $\boldsymbol{\theta}$ may be determined as

$$\boldsymbol{B}\ddot{\boldsymbol{\theta}} + \boldsymbol{c}(\dot{\boldsymbol{\theta}}) + \boldsymbol{e}(\boldsymbol{\theta}) = \boldsymbol{\tau} \tag{6}$$

where $\boldsymbol{B}$ is the diagonal matrix containing the rotor inertias about their axes of rotation associated with the generalized coordinates. $\boldsymbol{c}(\dot{\boldsymbol{\theta}})$ is the nonlinear vector function expressing the major loss at the rotor bearings, which might be modeled as the switching between the Coulomb's and the empirical viscous friction models.

$\boldsymbol{e}(\boldsymbol{\theta})$ is the nonlinear vector function of the elastic forces according to the elastic PE in Eq. (4).

$$\boldsymbol{e}(\boldsymbol{\theta}) = \left(\frac{\partial V_e(\boldsymbol{q}, \boldsymbol{\theta})}{\partial \boldsymbol{\theta}} \right)^{\mathrm{T}} = \begin{bmatrix} \boldsymbol{T}_1^{\mathrm{T}} \boldsymbol{e}_1(\boldsymbol{T}_1 \boldsymbol{\theta}_0 - \boldsymbol{\theta}_1) \\ -\boldsymbol{e}_1(\boldsymbol{T}_1 \boldsymbol{\theta}_0 - \boldsymbol{\theta}_1) + \boldsymbol{T}_2^{\mathrm{T}} \boldsymbol{e}_2(\boldsymbol{T}_2 \boldsymbol{\theta}_1 - \boldsymbol{\theta}_2) \\ \vdots \\ -\boldsymbol{e}_{q-1}(\boldsymbol{T}_{q-1} \boldsymbol{\theta}_{q-2} - \boldsymbol{\theta}_{q-1}) + \boldsymbol{T}_q^{\mathrm{T}} \boldsymbol{e}_q(\boldsymbol{T}_q \boldsymbol{\theta}_{q-1} - \boldsymbol{\theta}_q) \end{bmatrix} \tag{7}$$

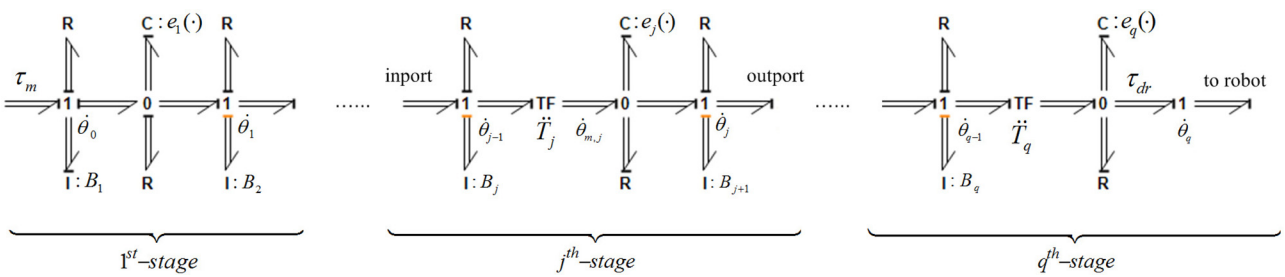

Fig. 1 Multidimensional bond graph diagram of the transmission system displaying the interconnection of the lumped elements along the cascading stages. Causality assignments conform to the cable-pulley transmission elastic model $e_j^{-1}(\cdot)$.

in which the subvector of the nonlinear elastic forces acting at the jth-rotor is $-\boldsymbol{e}_{j-1}(\boldsymbol{T}_{j-1}\boldsymbol{\theta}_{j-2}-\boldsymbol{\theta}_{j-1})+\boldsymbol{T}_j^{\mathrm{T}}\boldsymbol{e}_j(\boldsymbol{T}_j\boldsymbol{\theta}_{j-1}-\boldsymbol{\theta}_j)$, involving the relative displacements between its neighborhoods and the transmission ratios. The nonlinear vector function $\boldsymbol{e}_j(\cdot)$ describes the elastic forces of the p-lumped elastic elements at the jth-stage. If the elastic elements behave linearly, $\boldsymbol{e}_j(\cdot)$ may be written explicitly by the introduction of the stiffness matrix $\boldsymbol{K}_j$, i.e., $\boldsymbol{e}_j(\boldsymbol{T}_j\boldsymbol{\theta}_{j-1}-\boldsymbol{\theta}_j)=\boldsymbol{K}_j(\boldsymbol{T}_j\boldsymbol{\theta}_{j-1}-\boldsymbol{\theta}_j)$.

$\boldsymbol{\tau}$ is the generalized torque vector of the drivetrain associated with the generalized coordinates. Referring to Fig. 1, it corresponds to the actual torque vector generated by the motors, $\boldsymbol{\tau}_{\mathrm{m}}$, attached to the first stage. Therefore, $\boldsymbol{\tau}=\begin{bmatrix}\boldsymbol{\tau}_{\mathrm{m}}^{\mathrm{T}} & \boldsymbol{0}^{\mathrm{T}} & \cdots & \boldsymbol{0}^{\mathrm{T}}\end{bmatrix}^{\mathrm{T}}$. On the other end of the drive train, the actual output torques $\boldsymbol{\tau}_{\mathrm{dr}}=\boldsymbol{e}_q(\boldsymbol{T}_q\boldsymbol{\theta}_{q-1}-\boldsymbol{\theta}_q)$ are transmitted to the robot with the generalized velocity $\dot{\boldsymbol{\theta}}_q$ via the network of the elastic elements in the last stage. In summary, the simplified model of the nonlinear flexible joint robot system is described by Eqs. (1) and (6). The model will be used to develop the task space impedance controller in Sec. 3.

3 Task Space Impedance Control

Appropriate impedance is an intrinsic key for the robot to perform the task successfully. In this work, the desirable impedance characteristics will be accomplished purely via the controller design. For our system, the assumed rigid robot is propelled by the motors through the multistage flexible transmission unit of which the configurations match the model in Sec. 2. The system is an underactuated system [17] and the control problem is not straightforward due basically to indirect actuation. Worse yet, the available feedback signals are limited to the motor angles and currents only. This is indeed the most common case found in practice. In many systems, sensor placement at the output may not be possible and the output measurement is not available. Therefore, the system states cannot be reconstructed and the dynamic model cannot be fully exploited.

3.1 Stationary Model. An alleviation to this problem is to compute the system states in an open-loop fashion on the assumption of stationary motion. In other words, the system operates smoothly at low enough speed that the motion-induced forces, i.e., the inertial and the Coriolis/centrifugal forces, may be omitted. Hence, the velocity and acceleration terms in the equations of motion may be dropped, in which the remaining position dependent terms can be solved algebraically.

For the drivetrain, the reduced model may be written as

$$\boldsymbol{e}(\boldsymbol{\theta}_s)=\boldsymbol{\tau}_s \tag{8}$$

where the subscript s denotes the stationary value of the variable. Recalling Eq. (7), the equation may be expanded to

$$\begin{aligned}\boldsymbol{e}_1(\boldsymbol{T}_1\boldsymbol{\theta}_0-\boldsymbol{\theta}_{1s})&=\boldsymbol{T}_2^{\mathrm{T}}\boldsymbol{e}_2(\boldsymbol{T}_2\boldsymbol{\theta}_{1s}-\boldsymbol{\theta}_{2s})\\ \boldsymbol{e}_2(\boldsymbol{T}_2\boldsymbol{\theta}_{1s}-\boldsymbol{\theta}_{2s})&=\boldsymbol{T}_3^{\mathrm{T}}\boldsymbol{e}_3(\boldsymbol{T}_3\boldsymbol{\theta}_{2s}-\boldsymbol{\theta}_{3s})\\ &\vdots\\ \boldsymbol{e}_{q-1}(\boldsymbol{T}_{q-1}\boldsymbol{\theta}_{(q-2)s}-\boldsymbol{\theta}_{(q-1)s})&=\boldsymbol{T}_q^{\mathrm{T}}\boldsymbol{e}_q(\boldsymbol{T}_q\boldsymbol{\theta}_{(q-1)s}-\boldsymbol{\theta}_{qs})\end{aligned} \tag{9}$$

For the robot, the torque supplied by the transmission unit balance the gravity and the external forces in its stationary model, i.e.,

$$\boldsymbol{g}(\boldsymbol{\theta}_{qs})=\boldsymbol{e}_q(\boldsymbol{T}_q\boldsymbol{\theta}_{(q-1)s}-\boldsymbol{\theta}_{qs})+\boldsymbol{\tau}_{\mathrm{ext}} \tag{10}$$

where the robot generalized coordinates $\boldsymbol{q}$ are replaced with the outport coordinates $\boldsymbol{\theta}_q$ of the drivetrain unit. Since the desired task space compliance $\boldsymbol{K}_{\mathrm{d}}$ at the designated end effector set point $\boldsymbol{x}_{\mathrm{d}}$ is to be achieved, the reflected torques caused by this behavior, under the stationary condition, will be

$$\boldsymbol{\tau}_{\mathrm{ext}}=\boldsymbol{J}(\boldsymbol{\theta}_{qs})^{\mathrm{T}}\boldsymbol{F}_{\mathrm{ext}}=\boldsymbol{J}(\boldsymbol{\theta}_{qs})^{\mathrm{T}}\boldsymbol{K}_{\mathrm{d}}(\boldsymbol{f}(\boldsymbol{\theta}_{qs})-\boldsymbol{x}_{\mathrm{d}}) \tag{11}$$

where $\boldsymbol{f}(\cdot)$ is the forward kinematics mapping of the robot. Therefore, the stationary model of the compliance controlled robot becomes

$$\boldsymbol{e}_q(\boldsymbol{T}_q\boldsymbol{\theta}_{(q-1)s}-\boldsymbol{\theta}_{qs})=\boldsymbol{g}(\boldsymbol{\theta}_{qs})-\boldsymbol{J}(\boldsymbol{\theta}_{qs})^{\mathrm{T}}\boldsymbol{K}_{\mathrm{d}}(\boldsymbol{f}(\boldsymbol{\theta}_{qs})-\boldsymbol{x}_{\mathrm{d}})=\boldsymbol{h}(\boldsymbol{\theta}_{qs}) \tag{12}$$

displaying the stationary relationship between $\boldsymbol{\theta}_{(q-1)}$ and $\boldsymbol{\theta}_q$.

Stationary robot link angles and multistage drivetrain rotor angles may be determined from Eqs. (9) and (12) with the known motor angles, although the numerical evaluation is mandatory in general. If the inverse of the elastic force vector function $\boldsymbol{e}_j(\cdot)$, or the deformation function denoted as $\boldsymbol{e}_j^{-1}(\cdot)$, can be determined analytically, Eqs. (9) and (12) may be rewritten as

$$\begin{aligned}\boldsymbol{T}_q\boldsymbol{\theta}_{(q-1)s}-\boldsymbol{\theta}_{qs}&=\boldsymbol{e}_q^{-1}(\boldsymbol{h}(\boldsymbol{\theta}_{qs}))\\ \boldsymbol{T}_{q-1}\boldsymbol{\theta}_{(q-2)s}-\boldsymbol{\theta}_{(q-1)s}&=\boldsymbol{e}_{q-1}^{-1}\left(\boldsymbol{T}_q^{\mathrm{T}}\boldsymbol{h}(\boldsymbol{\theta}_{qs})\right)\\ \boldsymbol{T}_{q-2}\boldsymbol{\theta}_{(q-3)s}-\boldsymbol{\theta}_{(q-2)s}&=\boldsymbol{e}_{q-2}^{-1}\left(\boldsymbol{T}_{q-1}^{\mathrm{T}}\boldsymbol{T}_q^{\mathrm{T}}\boldsymbol{h}(\boldsymbol{\theta}_{qs})\right)\\ &\vdots\\ \boldsymbol{T}_2\boldsymbol{\theta}_{1s}-\boldsymbol{\theta}_{2s}&=\boldsymbol{e}_2^{-1}\left(\boldsymbol{T}_3^{\mathrm{T}}\boldsymbol{T}_4^{\mathrm{T}}\cdots\boldsymbol{T}_{q-1}^{\mathrm{T}}\boldsymbol{T}_q^{\mathrm{T}}\boldsymbol{h}(\boldsymbol{\theta}_{qs})\right)\\ \boldsymbol{T}_1\boldsymbol{\theta}_0-\boldsymbol{\theta}_{1s}&=\boldsymbol{e}_1^{-1}\left(\boldsymbol{T}_2^{\mathrm{T}}\boldsymbol{T}_3^{\mathrm{T}}\cdots\boldsymbol{T}_{q-1}^{\mathrm{T}}\boldsymbol{T}_q^{\mathrm{T}}\boldsymbol{h}(\boldsymbol{\theta}_{qs})\right)\end{aligned} \tag{13}$$

Direct relationship between the stationary robot link angles and the motor angles may thus be achieved by premultiplying the above equations with the suitable compound transmission ratios such that the addition of these modified equations brings about the ladder-cancellation of most of the terms on the left-hand side except $\boldsymbol{\theta}_{qs}$ and $\boldsymbol{\theta}_0$. The resulting equation may be written compactly as

$$\boldsymbol{\theta}_{qs}=\boldsymbol{T}_{q1}\boldsymbol{\theta}_0-\boldsymbol{e}_{1q}^{-1}(\boldsymbol{h}(\boldsymbol{\theta}_{qs})) \tag{14}$$

in which $\boldsymbol{T}_{qj}=\boldsymbol{T}_q\boldsymbol{T}_{q-1}\cdots\boldsymbol{T}_j$ denotes the compound transmission ratio from the jth-stage to the qth-stage and

$$\begin{aligned}\boldsymbol{e}_{1q}^{-1}(\boldsymbol{h}(\boldsymbol{\theta}_{qs}))=\boldsymbol{T}_{q2}\boldsymbol{e}_1^{-1}\left(\boldsymbol{T}_{q2}^{\mathrm{T}}\boldsymbol{h}(\boldsymbol{\theta}_{qs})\right)+\boldsymbol{T}_{q3}\boldsymbol{e}_2^{-1}\left(\boldsymbol{T}_{q3}^{\mathrm{T}}\boldsymbol{h}(\boldsymbol{\theta}_{qs})\right)\\ +\cdots+\boldsymbol{T}_{q(q-1)}\boldsymbol{e}_{q-2}^{-1}\left(\boldsymbol{T}_{q(q-1)}^{\mathrm{T}}\boldsymbol{h}(\boldsymbol{\theta}_{qs})\right)\\ +\boldsymbol{T}_q\boldsymbol{e}_{q-1}^{-1}\left(\boldsymbol{T}_q^{\mathrm{T}}\boldsymbol{h}(\boldsymbol{\theta}_{qs})\right)+\boldsymbol{e}_q^{-1}(\boldsymbol{h}(\boldsymbol{\theta}_{qs}))\end{aligned} \tag{15}$$

is the overall effective nonlinear deformation of the multistage drivetrain unit, here subject to the stationary gravity and compliance forces according to Eq. (12). Therefore, the stationary link angles may be determined directly by the recursive evaluation of Eq. (14), of which the convergence issue is discussed in the Appendix.

Note that duality of the stationary motion is the stationary torque relationship between the motor input torque and the drivetrain output torque transmitted to the robot. It may be derived readily from Eq. (9) and adjunct relations of $(\boldsymbol{\tau}_{\mathrm{m}})_s=\boldsymbol{T}_1^{\mathrm{T}}\boldsymbol{e}_1(\boldsymbol{T}_1\boldsymbol{\theta}_0-\boldsymbol{\theta}_{1s})$ and $(\boldsymbol{\tau}_{\mathrm{dr}})_s=\boldsymbol{e}_q(\boldsymbol{T}_q\boldsymbol{\theta}_{(q-1)s}-\boldsymbol{\theta}_{qs})$. The result is

$$(\boldsymbol{\tau}_{\mathrm{m}})_s=\boldsymbol{T}_{q1}^{\mathrm{T}}(\boldsymbol{\tau}_{\mathrm{dr}})_s \tag{16}$$

which will be useful in mapping the robot stationary joint torque to the associated stationary torque of the motor.

3.2 Impedance Controller. An impedance control law of the robot driven through the multistage nonlinear flexible transmission using the computed stationary robot link angle, link joint velocity, and transmitted torque (to be discussed along with) will now be developed. It is assumed that the robot system is equipped with a higher-decision making unit which determines the end effector set point $\boldsymbol{x}_{\mathrm{d}}$ and the task space symmetric positive definite constant stiffness matrix $\boldsymbol{K}_{\mathrm{d}}$ appropriate for executing a task at hand.

The objective of the impedance controller is to modulate the effective impedance parameters, i.e., the inertance, the resistance, and the compliance, of the system to the desired values. Nevertheless, it has been shown in Ref. [18] that adjusting the inertance has a severe drawback of destroying the passivity of the controlled system. This is a sign indicating that the robot system might become unstable during the interaction with passive environment. Therefore, the following target impedance dynamics subject to the external force, $\boldsymbol{F}_{\mathrm{ext}}$, applied at the end effector is selected:

$$\boldsymbol{\Lambda}(\boldsymbol{x})\ddot{\tilde{\boldsymbol{x}}} + (\boldsymbol{\mu}(\boldsymbol{x},\dot{\boldsymbol{x}}) + \boldsymbol{D}_{\mathrm{d}})\dot{\tilde{\boldsymbol{x}}} + \boldsymbol{K}_{\mathrm{d}}\tilde{\boldsymbol{x}} = \boldsymbol{F}_{\mathrm{ext}} \tag{17}$$

The equation is written in the task space coordinates $\boldsymbol{x}$, for which $\tilde{\boldsymbol{x}}$ indicates the coordinate errors of $\boldsymbol{x}$ from the set point values $\boldsymbol{x}_{\mathrm{d}}$. $\boldsymbol{\Lambda}(\boldsymbol{x})$ and $\boldsymbol{\mu}(\boldsymbol{x},\dot{\boldsymbol{x}})$ are the transformed inertia and Coriolis/centrifugal matrices in the task space coordinates. They are related to the parameters in joint space coordinates $\boldsymbol{q}$ by

$$\boldsymbol{\Lambda}(\boldsymbol{x}) = \boldsymbol{J}(\boldsymbol{q})^{-T}\boldsymbol{M}(\boldsymbol{q})\boldsymbol{J}(\boldsymbol{q})^{-1} \tag{18}$$

and

$$\boldsymbol{\mu}(\boldsymbol{x},\dot{\boldsymbol{x}}) = \boldsymbol{J}(\boldsymbol{q})^{-T}\left(\boldsymbol{C}(\boldsymbol{q},\dot{\boldsymbol{q}}) - \boldsymbol{M}(\boldsymbol{q})\boldsymbol{J}(\boldsymbol{q})^{-1}\dot{\boldsymbol{J}}(\boldsymbol{q})\right)\boldsymbol{J}(\boldsymbol{q})^{-1} \tag{19}$$

with $\boldsymbol{q} = \boldsymbol{f}^{-1}(\boldsymbol{x})$ and $\dot{\boldsymbol{q}} = \boldsymbol{J}\left(\boldsymbol{f}^{-1}(\boldsymbol{x})\right)^{-1}\dot{\boldsymbol{x}}$ through the inverse kinematics mapping and its differential relationship. Note the existence of $\boldsymbol{\mu}(\boldsymbol{x},\dot{\boldsymbol{x}})$ in the desired impedance dynamics to preserve the passivity of the system. In essence, natural dynamics of the robot has been exploited.

$\boldsymbol{D}_{\mathrm{d}}$ is the task space damping matrix that asymptotically stabilizes the system. Its value will be designed, according to the current values of $\boldsymbol{\Lambda}(\boldsymbol{x})$ and $\boldsymbol{K}_{\mathrm{d}}$, to make the system response be appropriately damped with the specified damping ratio. To accomplish this, first, Eq. (17) is approximated by

$$\boldsymbol{\Lambda}(\boldsymbol{x})\ddot{\tilde{\boldsymbol{x}}} + \boldsymbol{D}_{\mathrm{d}}(\boldsymbol{x})\dot{\tilde{\boldsymbol{x}}} + \boldsymbol{K}_{\mathrm{d}}\tilde{\boldsymbol{x}} = \boldsymbol{F}_{\mathrm{ext}} \tag{20}$$

where the Coriolis/centrifugal matrix is neglected. Introduce the linear transformation of the coordinate errors $\boldsymbol{z} = \boldsymbol{Q}(\boldsymbol{x})^{-1}\tilde{\boldsymbol{x}}$. The transformation matrix $\boldsymbol{Q}(\boldsymbol{x})$, treated constant for a particular stationary point, is the matrix of which its columns are the eigenvectors $\boldsymbol{u}_i$ of the generalized eigenproblem

$$\left(\boldsymbol{K}_{\mathrm{d}} - \omega_{ni}^2\boldsymbol{\Lambda}(\boldsymbol{x})\right)\boldsymbol{u}_i = \boldsymbol{0} \tag{21}$$

Premultiplying Eq. (20) with $\boldsymbol{Q}(\boldsymbol{x})^{\mathrm{T}}$ and writing the equation in the new transformed coordinates lead to

$$\begin{aligned}\boldsymbol{Q}(\boldsymbol{x})^{\mathrm{T}}\boldsymbol{\Lambda}(\boldsymbol{x})\boldsymbol{Q}(\boldsymbol{x})\ddot{\boldsymbol{z}} + \boldsymbol{Q}(\boldsymbol{x})^{\mathrm{T}}\boldsymbol{D}_{\mathrm{d}}(\boldsymbol{x})\boldsymbol{Q}(\boldsymbol{x})\dot{\boldsymbol{z}} + \boldsymbol{Q}(\boldsymbol{x})^{\mathrm{T}}\boldsymbol{K}_{\mathrm{d}}\boldsymbol{Q}(\boldsymbol{x})\boldsymbol{z} \\ = \boldsymbol{Q}(\boldsymbol{x})^{\mathrm{T}}\boldsymbol{F}_{\mathrm{ext}}\end{aligned} \tag{22}$$

The eigenvectors in $\boldsymbol{Q}(\boldsymbol{x})$ may be normalized such that $\boldsymbol{Q}(\boldsymbol{x})^{\mathrm{T}}\boldsymbol{\Lambda}(\boldsymbol{x})\boldsymbol{Q}(\boldsymbol{x}) = \boldsymbol{I}$ holds. Consequently, the transformed stiffness matrix will become $\boldsymbol{Q}(\boldsymbol{x})^{\mathrm{T}}\boldsymbol{K}_{\mathrm{d}}\boldsymbol{Q}(\boldsymbol{x}) = \boldsymbol{\Sigma}(\boldsymbol{x})$, in which the diagonal matrix $\boldsymbol{\Sigma}(\boldsymbol{x})$ is known in vibration terminology [19] as the spectral matrix containing the square of the natural frequencies ω_{ni}^2, or the generalized eigenvalues of $\boldsymbol{K}_{\mathrm{d}}$ with respect to $\boldsymbol{\Lambda}(\boldsymbol{x})$. The transformed equation may thus be written as

$$\ddot{\boldsymbol{z}} + \boldsymbol{Q}(\boldsymbol{x})^{\mathrm{T}}\boldsymbol{D}_{\mathrm{d}}(\boldsymbol{x})\boldsymbol{Q}(\boldsymbol{x})\dot{\boldsymbol{z}} + \boldsymbol{\Sigma}(\boldsymbol{x})\boldsymbol{z} = \boldsymbol{Q}(\boldsymbol{x})^{\mathrm{T}}\boldsymbol{F}_{\mathrm{ext}} \tag{23}$$

Hence, the damping matrix may be designed to be

$$\boldsymbol{D}_d(\boldsymbol{x}) = 2\boldsymbol{Q}(\boldsymbol{x})^{-T}\boldsymbol{\xi}\boldsymbol{\Sigma}(\boldsymbol{x})^{1/2}\boldsymbol{Q}(\boldsymbol{x})^{-1} \tag{24}$$

where $\boldsymbol{\Sigma}(\boldsymbol{x})^{1/2}$ denotes the diagonal matrix of which its diagonal elements are the square root of the paired values in $\boldsymbol{\Sigma}(\boldsymbol{x})$. The diagonal damping ratio matrix $\boldsymbol{\xi}$ is used to adjust the oscillatory behavior of the response. Through this choice of the damping matrix, the transformed equation may finally be written

$$\ddot{\boldsymbol{z}} + 2\boldsymbol{\xi}\boldsymbol{\Sigma}(\boldsymbol{x})^{1/2}\dot{\boldsymbol{z}} + \boldsymbol{\Sigma}(\boldsymbol{x})\boldsymbol{z} = \boldsymbol{Q}(\boldsymbol{x})^{\mathrm{T}}\boldsymbol{F}_{\mathrm{ext}} \tag{25}$$

as a set of decoupled second-order linear time invariant differential equations.

In this work, the impedance control problem is constrained to only the constant set point case which implies $\dot{\boldsymbol{x}}_{\mathrm{d}} = \boldsymbol{0}$ and $\ddot{\boldsymbol{x}}_{\mathrm{d}} = \boldsymbol{0}$. According to the robot dynamics Eq. (1), the desired impedance dynamics may be achieved with the control law

$$\boldsymbol{\tau}_{\mathrm{dr}}^{*} = \boldsymbol{g}(\boldsymbol{q}) - \boldsymbol{J}(\boldsymbol{q})^{\mathrm{T}}(\boldsymbol{K}_{\mathrm{d}}\tilde{\boldsymbol{x}} + \boldsymbol{D}_{\mathrm{d}}\dot{\boldsymbol{x}}) \tag{26}$$

where the star-mark is used here to denote the desired torque transmitted to the robot. The actual one deviates from the desired value due to the uncompensated motor and drivetrain dynamics. Unfortunately, the link angles and the end effector coordinates are not measurable directly. Intuitively, their estimated values shall be used instead. This results in the modified control law

$$\begin{aligned}\boldsymbol{\tau}_{\mathrm{dr}}^{*} &= \boldsymbol{g}(\boldsymbol{\theta}_{qs}) - \boldsymbol{J}(\boldsymbol{\theta}_{qs})^{\mathrm{T}}\boldsymbol{K}_{\mathrm{d}}(\boldsymbol{f}(\boldsymbol{\theta}_{qs}) - \boldsymbol{x}_d) \\ &\quad - \left[\boldsymbol{J}(\boldsymbol{\theta}_{qs})^{\mathrm{T}}\boldsymbol{D}_{\mathrm{d}}(\boldsymbol{f}(\boldsymbol{\theta}_{qs}))\boldsymbol{J}(\boldsymbol{\theta}_{qs})\right]^{1/2}\boldsymbol{\vartheta} \\ &= \boldsymbol{h}(\boldsymbol{\theta}_{qs}) - \left[\boldsymbol{J}(\boldsymbol{\theta}_{qs})^{\mathrm{T}}\boldsymbol{D}_{\mathrm{d}}(\boldsymbol{f}(\boldsymbol{\theta}_{qs}))\boldsymbol{J}(\boldsymbol{\theta}_{qs})\right]^{1/2}\boldsymbol{\vartheta}\end{aligned} \tag{27}$$

where the stationary link angle from Eq. (14) is employed. The last term is the damping torque which is calculated using the designed damping matrix in Eq. (24) and the link joint velocity related term $\boldsymbol{\vartheta}$.

Since the actual link angles are not measurable, the observer for their velocities cannot be formulated. Rather, the nonmodel-based first-order differentiation filter will be employed to estimate the robot link joint velocity from the motor angle. Particularly, the term $\boldsymbol{\vartheta}$ is the estimated link joint velocity scaled by the square root of the joint space symmetric damping matrix

$$\boldsymbol{\vartheta} = s\boldsymbol{G}(s)\left[\boldsymbol{J}(\boldsymbol{\theta}_{qs})^{\mathrm{T}}\boldsymbol{D}_{\mathrm{d}}(\boldsymbol{f}(\boldsymbol{\theta}_{qs}))\boldsymbol{J}(\boldsymbol{\theta}_{qs})\right]^{1/2}\boldsymbol{T}_{q1}\boldsymbol{\theta}_0 \tag{28}$$

Here, s represents the complex argument of the Laplace transform. $\boldsymbol{G}(s)$ is a diagonal matrix of which its diagonal terms are identical and be a strictly proper and strictly positive real (SPR) filtering transfer function. The estimated link angle is acquired from $\boldsymbol{T}_{q1}\boldsymbol{\theta}_0$ rather than $\boldsymbol{\theta}_{qs}$ to secure the stability of the system. The scaling matrix may be computed through the singular value decomposition. Namely, $\left[\boldsymbol{J}^{\mathrm{T}}\boldsymbol{D}_{\mathrm{d}}\boldsymbol{J}\right]^{1/2} = \boldsymbol{U}\boldsymbol{\Sigma}^{1/2}\boldsymbol{U}^{\mathrm{T}}$ associated with the joint space damping matrix $\boldsymbol{J}^{\mathrm{T}}\boldsymbol{D}_{\mathrm{d}}\boldsymbol{J} = \boldsymbol{U}\boldsymbol{\Sigma}\boldsymbol{U}^{\mathrm{T}}$ for a diagonal matrix $\boldsymbol{\Sigma}$ of the singular values of $\boldsymbol{J}^{\mathrm{T}}\boldsymbol{D}_{\mathrm{d}}\boldsymbol{J}$ and some orthogonal matrix $\boldsymbol{U}$. This square root matrix will be denoted as $\sqrt{\boldsymbol{K}_v}$ for convenience. At the moment, it is in doubt whether the usage of such velocity estimation in the impedance controller will lead to satisfactory result. This issue is deferred to Sec. 3.4 where the stability and passivity of the controlled system will be proven.

Since the robot is actuated indirectly by the motor through the flexible transmission subsystem, the motor torque corresponding to the desirable torque of Eq. (27) applied at the robot joint must

be determined. Due to the lack of the complete system state information, the degenerated stationary model of the drivetrain, Eq. (16), shall be used to compute such motor torque. In particular

$$(\boldsymbol{\tau}_{\mathrm{m}})^{*}_{\mathrm{dr}} = \boldsymbol{T}^{\mathrm{T}}_{q1}\boldsymbol{\tau}^{*}_{\mathrm{dr}} \tag{29}$$

3.3 Motor Inertia Reduction via Transmitted Torque Estimation. Desired task space impedance behavior of Eq. (17) is hardly achieved because of the intervention from the robot and transmission dynamics that have never been perfectly cancelled, especially for the present system where most of the states are unavailable for inferring the dynamics. Motor inertia is a parameter which also deteriorates the desired impedance particularly for the system with high transmission ratio. Reference [20] firstly showed that the implication of a force feedback controller is to reduce the effective mass of the system. Reference [9] applied this means by feeding back the joint torque to reduce the reflected motor inertia and frictional torque. The reduced motor inertia subsequently helps improving the response as the transmission become lighter. Therefore, the simple impedance control law, neglecting the transmission dynamics, with additional torque feedback may be applied to the system yielding the effective impedance closer to the desired one.

Most robot systems are not equipped with the joint torque sensor. Thus, feedback of the transmitted torque may not be available. Nevertheless, it may be estimated based on the motor current and angle measurements. Consider the governing equations of the first stage of the transmission system

$$\boldsymbol{B}_1\ddot{\boldsymbol{\theta}}_0 + \boldsymbol{C}_1\mathrm{sgn}\left(\dot{\boldsymbol{\theta}}_0\right) + \boldsymbol{\tau}_1 = \boldsymbol{\tau}_{\mathrm{m}} \tag{30}$$

where $\boldsymbol{B}_1$ is the diagonal matrix containing the p-motor inertia. Loss in the DC motor may be governed by a Coulomb friction model with the constant diagonal matrix $\boldsymbol{C}_1$. $\boldsymbol{\tau}_{\mathrm{m}}$ is the actual torque generated from the electromagnetic induction force, of which the value can be deduced from the motor current by $\boldsymbol{\tau}_{\mathrm{m}} = \boldsymbol{K}_{\tau}\boldsymbol{i}$, where $\boldsymbol{K}_{\tau}$ is the motor torque constant matrix. The last term $\boldsymbol{\tau}_1$ represents the transmitted torque from the motor to the first stage of the drivetrain. Its value, which is governed by the elastic network at the first stage, will be estimated.

The method of variational integrator [21], which discretizes the system from the beginning of formulating the Lagrangian, may be applied to determine the energy conserving discrete form of Eq. (30). After identifying the discrete Lagrangian and external force, the forced discrete Euler–Lagrange formulation may be evaluated. The discretized version of Eq. (30) would be

$$\begin{aligned}&\frac{1}{h}\boldsymbol{B}_1\left(\boldsymbol{\theta}_{0(k+1)} - 2\boldsymbol{\theta}_{0k} + \boldsymbol{\theta}_{0(k-1)}\right) + \frac{h}{2}\boldsymbol{C}_1\left[\mathrm{sgn}\left(\boldsymbol{\theta}_{0(k+1)} - \boldsymbol{\theta}_{0k}\right)\right.\\ &\quad\left. + \mathrm{sgn}\left(\boldsymbol{\theta}_{0k} - \boldsymbol{\theta}_{0(k-1)}\right)\right] + \frac{h}{2}\left(\boldsymbol{\tau}_{1k} + \boldsymbol{\tau}_{1(k+1)}\right)\\ &\quad = \frac{h}{4}\boldsymbol{K}_{\tau}(\boldsymbol{i}_{k-1} + 2\boldsymbol{i}_k + \boldsymbol{i}_{k+1})\end{aligned} \tag{31}$$

with the sampling period h. Consequently, the transmitted torque at the kth-sampling may be estimated by

$$\begin{aligned}\hat{\boldsymbol{\tau}}_{1k} = &-\hat{\boldsymbol{\tau}}_{1(k-1)} - \frac{2}{h^2}\boldsymbol{B}_1\left(\boldsymbol{\theta}_{0k} - 2\boldsymbol{\theta}_{0(k-1)} + \boldsymbol{\theta}_{0(k-2)}\right)\\ &- \boldsymbol{C}_1\left[\mathrm{sgn}\left(\boldsymbol{\theta}_{0k} - \boldsymbol{\theta}_{0(k-1)}\right) + \mathrm{sgn}\left(\boldsymbol{\theta}_{0(k-1)} - \boldsymbol{\theta}_{0(k-2)}\right)\right]\\ &+ \frac{1}{2}\boldsymbol{K}_{\tau}(\boldsymbol{i}_k + 2\boldsymbol{i}_{k-1} + \boldsymbol{i}_{k-2})\end{aligned} \tag{32}$$

Negative feedback of $\hat{\boldsymbol{\tau}}_1$ may thus be used to reduce the motor inertia from $\boldsymbol{B}_1$ to $\boldsymbol{B}_{1r}$ by correcting the reference motor torque $(\boldsymbol{\tau}_{\mathrm{m}})^{*}_{\mathrm{dr}}$ to

$$\boldsymbol{\tau}^{*}_{\mathrm{m}} = \boldsymbol{B}_1\boldsymbol{B}^{-1}_{1r}(\boldsymbol{\tau}_{\mathrm{m}})^{*}_{\mathrm{dr}} + \left(\boldsymbol{I} - \boldsymbol{B}_1\boldsymbol{B}^{-1}_{1r}\right)\hat{\boldsymbol{\tau}}_1 \tag{33}$$

The resulting system dynamics of the first stage of the drivetrain becomes

$$\boldsymbol{B}_{1r}\ddot{\boldsymbol{\theta}}_0 + \boldsymbol{B}_{1r}\boldsymbol{B}^{-1}_1\boldsymbol{C}_1\dot{\boldsymbol{\theta}}_0 + \boldsymbol{\tau}_1 = (\boldsymbol{\tau}_{\mathrm{m}})^{*}_{\mathrm{dr}} \tag{34}$$

if the transmitted torque estimation is exact. Effectively, the transmitted torque and the reference motor torque are brought closer to each other, thus making the motor behave closer to an ideal torque source. This will be advantageous to the current controlled motor. In practice, motor inertia cannot be reduced arbitrarily. Saturation of the motor torque, amplification of the noise, and quantization errors restrict the lower bound of $\boldsymbol{B}_{1r}$.

Reference motor current corresponding to the motor torque of Eq. (33) may be calculated from

$$\boldsymbol{i}_{\mathrm{m}} = \boldsymbol{K}^{-1}_{\tau}\boldsymbol{\tau}^{*}_{\mathrm{m}} \tag{35}$$

If the motor is current controlled, this value may be used as the reference signal to the control unit by which the motor is thought of as an ideal effort source. However, this might be unrealistic because the actual DC motor current and hence torque depend on its rotational speed as well according to the electrical dynamics

$$\boldsymbol{L}\dot{\boldsymbol{i}} + \boldsymbol{R}\boldsymbol{i} + \boldsymbol{K}_{\mathrm{b}}\dot{\boldsymbol{\theta}}_0 = \boldsymbol{u} \tag{36}$$

where $\boldsymbol{L}$, $\boldsymbol{R}$, and $\boldsymbol{K}_{\mathrm{b}}$ are the diagonal matrix of lumped inductances, resistances, and the back-emf constants of the motors, respectively. $\boldsymbol{u}$ is the vector of the motor voltages.

The resolution is to account for its dynamics in controlling the motor current. According to Eq. (36), the current will thus be controlled to track the reference value indirectly via the motor voltage. One may choose the desired current tracking error, $\boldsymbol{e}_i = \boldsymbol{i} - \boldsymbol{i}_m$, dynamics to be

$$\boldsymbol{L}\dot{\boldsymbol{e}}_i + \boldsymbol{K}_{\mathrm{c}}\boldsymbol{e}_i = \boldsymbol{0} \tag{37}$$

where $\boldsymbol{K}_{\mathrm{c}}$ is the tunable constant diagonal matrix of the positive gains for the tracking responsiveness. To this end, the control input vector of the motor voltage must be determined as

$$\boldsymbol{u} = \boldsymbol{L}\dot{\boldsymbol{i}}_{\mathrm{m}} + \boldsymbol{R}\boldsymbol{i} + \boldsymbol{K}_{\mathrm{b}}\dot{\boldsymbol{\theta}}_0 - \boldsymbol{K}_{\mathrm{c}}(\boldsymbol{i} - \boldsymbol{i}_{\mathrm{m}}) \tag{38}$$

that relies on the exact cancellation of the motor current and angular velocity terms.

If the above scheme cannot be realized, the following tracking error dynamics:

$$\boldsymbol{L}\ddot{\boldsymbol{e}}_i + \boldsymbol{K}_{\mathrm{c}}\dot{\boldsymbol{e}}_i + \boldsymbol{K}_{\mathrm{b}}\boldsymbol{B}^{-1}_1\boldsymbol{K}_{\mathrm{b}}\boldsymbol{e}_i = \boldsymbol{0} \tag{39}$$

may be chosen instead. Here, $\boldsymbol{K}_{\mathrm{c}}$ is the positive constant diagonal matrix to regulate the damping characteristics. It can be shown that the following control input vector:

$$\boldsymbol{u} = \boldsymbol{L}\dot{\boldsymbol{i}}_{\mathrm{m}} + \boldsymbol{R}\boldsymbol{i} + \boldsymbol{K}_{\mathrm{b}}\boldsymbol{B}^{-1}_1\int_{t_i}^{t}(\boldsymbol{K}_{\mathrm{b}}\boldsymbol{i}_{\mathrm{m}} - \hat{\boldsymbol{\tau}}_{1cs})dt - \boldsymbol{K}_{\mathrm{c}}(\boldsymbol{i} - \boldsymbol{i}_{\mathrm{m}}) \tag{40}$$

shapes the closed-loop current tracking error dynamics to Eq. (39). In the equation, $\hat{\boldsymbol{\tau}}_{1cs}$ is the estimated value of $\boldsymbol{C}_1\mathrm{sgn}\left(\dot{\boldsymbol{\theta}}_0\right) + \boldsymbol{\tau}_1$ in Eq. (30) which may be determined from the discretized equation similar to Eq. (31).

In summary, captured in Fig. 3, task space impedance controller of a nonlinear flexible joint robot system, Eq. (27), is proposed based on the stationary link angles and the velocity term according to Eqs. (14) and (28), respectively. The controller allows the user to specify the desired compliance and dissipation characteristics at a set point. Then the appropriate task space damping matrix is computed by means of the matrix factorization as shown in Eq. (24). From the control law of Eq. (27), the required motor torque

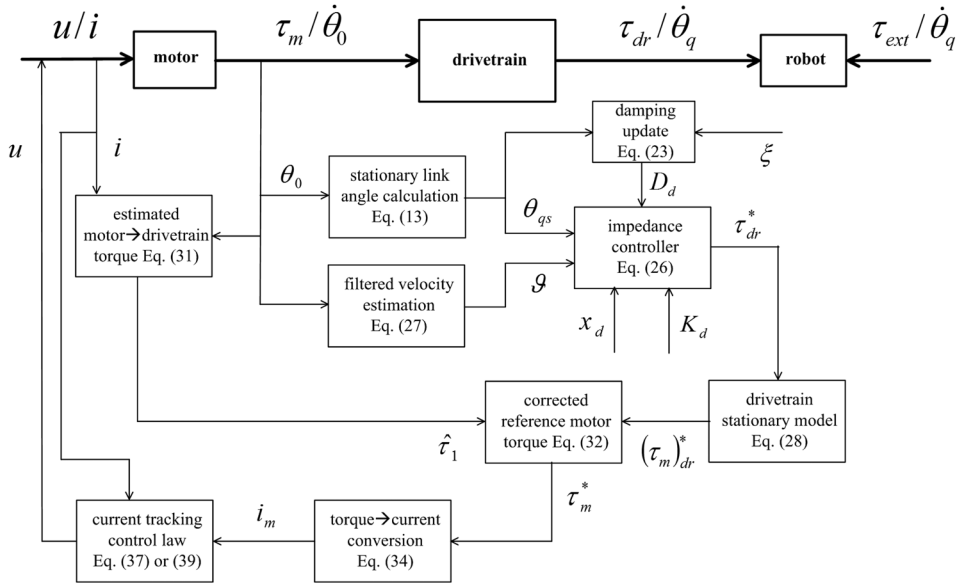

Fig. 3 Overall diagram of the task space impedance controller

corresponding to the desirable robot joint torque is calculated via Eq. (29). Additionally, feedback of the estimated transmitted torque from Eq. (32) is employed to relieve the effect of the unmodeled motor inertia. This results in the corrected reference motor torque of Eq. (33). Reference motor current which yields such torque may be commanded according to the simple relationship of Eq. (35) if it is reasonable to model the motor as an ideal torque source. Otherwise, the motor should be controlled at the voltage level where Eq. (38) provides the voltage control law. If the motor angular velocity is not available, Eq. (40) should be applied instead.

3.4 Passivity and Stability Analysis. Stability and passivity of the proposed task space impedance controller connected to the robot system driven through the multistage nonlinear flexible transmission will now be analyzed. First, the underlying energy related to the desirable robot joint torque Eq. (27) will be investigated. Positional dependent function $\boldsymbol{h}(\boldsymbol{\theta}_{qs})$ is the torque component responsible for counterbalancing the robot gravity torque and supplying the desired compliant force under the stationary condition through the network of flexible transmission elements. Therefore, $\boldsymbol{h}(\boldsymbol{\theta}_{qs})$ must be the differential of some PE $V_{\bar{h}}(\boldsymbol{\theta}_{qs})$ related to the gravitational PE of the robot, the PE of the end effector desired compliant behavior, and the elastic PE of the multistage flexible transmission subsystem. Note that the function $\boldsymbol{h}(\boldsymbol{q})$ is the differential of the PE

$$V_h(\boldsymbol{q}) = V_g(\boldsymbol{q}) - \frac{1}{2}(\boldsymbol{f}(\boldsymbol{q}) - \boldsymbol{x}_{\mathrm{d}})^{\mathrm{T}}\boldsymbol{K}_{\mathrm{d}}(\boldsymbol{f}(\boldsymbol{q}) - \boldsymbol{x}_{\mathrm{d}}) \tag{41}$$

Equation (14) may be rewritten as $\boldsymbol{T}_{q1}\boldsymbol{\theta}_0 = \boldsymbol{\theta}_{qs} + \boldsymbol{e}_{1q}^{-1}(\boldsymbol{h}(\boldsymbol{\theta}_{qs})) = \boldsymbol{l}_1(\boldsymbol{\theta}_{qs})$ or $\boldsymbol{\theta}_{qs} = \boldsymbol{l}_1^{-1}(\boldsymbol{T}_{q1}\boldsymbol{\theta}_0)$. Therefore, one can write

$$\boldsymbol{h}(\boldsymbol{l}_1^{-1}(\boldsymbol{T}_{q1}\boldsymbol{\theta}_0))^{\mathrm{T}} = \left.\frac{\partial V_{\bar{h}}(\boldsymbol{\theta}_{qs})}{\partial \boldsymbol{\theta}_{qs}}\right|_{\boldsymbol{\theta}_{qs}=\boldsymbol{l}_1^{-1}(\boldsymbol{T}_{q1}\boldsymbol{\theta}_0)} \times \frac{\partial \boldsymbol{l}_1^{-1}(\boldsymbol{T}_{q1}\boldsymbol{\theta}_0)}{\partial(\boldsymbol{T}_{q1}\boldsymbol{\theta}_0)} \tag{42}$$

Since

$$\frac{\partial \boldsymbol{l}_1(\boldsymbol{\theta}_{qs})}{\partial \boldsymbol{\theta}_{qs}} = \boldsymbol{I} + \left.\frac{\partial \boldsymbol{e}_{1q}^{-1}(\boldsymbol{h})}{\partial \boldsymbol{h}}\right|_{\boldsymbol{h}=\boldsymbol{h}(\boldsymbol{\theta}_{qs})} \times \frac{\partial \boldsymbol{h}(\boldsymbol{\theta}_{qs})}{\partial \boldsymbol{\theta}_{qs}} \quad \text{and} \quad \frac{\partial \boldsymbol{l}_1(\boldsymbol{l}_1^{-1}(\boldsymbol{T}_{q1}\boldsymbol{\theta}_0))}{\partial(\boldsymbol{T}_{q1}\boldsymbol{\theta}_0)}$$
$$= \left.\frac{\partial \boldsymbol{l}_1(\boldsymbol{\theta}_{qs})}{\partial \boldsymbol{\theta}_{qs}}\right|_{\boldsymbol{\theta}_{qs}=\boldsymbol{l}_1^{-1}(\boldsymbol{T}_{q1}\boldsymbol{\theta}_0)} \times \frac{\partial \boldsymbol{l}_1^{-1}(\boldsymbol{T}_{q1}\boldsymbol{\theta}_0)}{\partial(\boldsymbol{T}_{q1}\boldsymbol{\theta}_0)} = \boldsymbol{I}$$

$$\frac{\partial \boldsymbol{l}_1^{-1}(\boldsymbol{T}_{q1}\boldsymbol{\theta}_0)}{\partial(\boldsymbol{T}_{q1}\boldsymbol{\theta}_0)} = \left\{ \left[\boldsymbol{I} + \left.\frac{\partial \boldsymbol{e}_{1q}^{-1}(\boldsymbol{h})}{\partial \boldsymbol{h}}\right|_{\boldsymbol{h}=\boldsymbol{h}(\boldsymbol{\theta}_{qs})} \times \frac{\partial \boldsymbol{h}(\boldsymbol{\theta}_{qs})}{\partial \boldsymbol{\theta}_{qs}} \right] \Bigg|_{\boldsymbol{\theta}_{qs}=\boldsymbol{l}_1^{-1}(\boldsymbol{T}_{q1}\boldsymbol{\theta}_0)} \right\}^{-1}$$

Substituting this expression into Eq. (42), differential of $V_{\bar{h}}(\boldsymbol{\theta}_{qs})$ may thus be determined as

$$\frac{\partial V_{\bar{h}}(\boldsymbol{\theta}_{qs})}{\partial \boldsymbol{\theta}_{qs}} = \boldsymbol{h}(\boldsymbol{\theta}_{qs})^{\mathrm{T}} \left[\boldsymbol{I} + \left.\frac{\partial \boldsymbol{e}_{1q}^{-1}(\boldsymbol{h})}{\partial \boldsymbol{h}}\right|_{\boldsymbol{h}=\boldsymbol{h}(\boldsymbol{\theta}_{qs})} \times \frac{\partial \boldsymbol{h}(\boldsymbol{\theta}_{qs})}{\partial \boldsymbol{\theta}_{qs}} \right] \tag{43}$$

Consider the following differentiation:

$$\frac{\partial}{\partial \boldsymbol{\theta}_{qs}}\left[\boldsymbol{h}(\boldsymbol{\theta}_{qs})^{\mathrm{T}}\boldsymbol{e}_{1q}^{-1}(\boldsymbol{h}(\boldsymbol{\theta}_{qs}))\right] = \boldsymbol{e}_{1q}^{-1}(\boldsymbol{h}(\boldsymbol{\theta}_{qs}))^{\mathrm{T}}\frac{\partial \boldsymbol{h}(\boldsymbol{\theta}_{qs})}{\partial \boldsymbol{\theta}_{qs}} + \boldsymbol{h}(\boldsymbol{\theta}_{qs})^{\mathrm{T}}\left.\frac{\partial \boldsymbol{e}_{1q}^{-1}(\boldsymbol{h})}{\partial \boldsymbol{h}}\right|_{\boldsymbol{h}=\boldsymbol{h}(\boldsymbol{\theta}_{qs})} \times \frac{\partial \boldsymbol{h}(\boldsymbol{\theta}_{qs})}{\partial \boldsymbol{\theta}_{qs}}$$

Performing the inner product with the differential of $\boldsymbol{\theta}_{qs}$ and integrating the result yield a scalar quantity of

$$\int_{(\boldsymbol{\theta}_{qs})_i}^{\boldsymbol{\theta}_{qs}} \boldsymbol{h}(\boldsymbol{\phi})^{\mathrm{T}} \left.\frac{\partial \boldsymbol{e}_{1q}^{-1}(\boldsymbol{h})}{\partial \boldsymbol{h}}\right|_{\boldsymbol{h}=\boldsymbol{h}(\boldsymbol{\phi})} \times \frac{\partial \boldsymbol{h}(\boldsymbol{\phi})}{\partial \boldsymbol{\phi}} \cdot d\boldsymbol{\phi} = \boldsymbol{h}(\boldsymbol{\theta}_{qs})^{\mathrm{T}}\boldsymbol{e}_{1q}^{-1}(\boldsymbol{h}(\boldsymbol{\theta}_{qs})) - \int_{(\boldsymbol{\theta}_{qs})_i}^{\boldsymbol{\theta}_{qs}} \boldsymbol{e}_{1q}^{-1}(\boldsymbol{h}(\boldsymbol{\phi}))^{\mathrm{T}} \frac{\partial \boldsymbol{h}(\boldsymbol{\phi})}{\partial \boldsymbol{\phi}} \cdot d\boldsymbol{\phi} \tag{44}$$

where $(\boldsymbol{\theta}_{qs})_i$ is the stationary link angles that make $\boldsymbol{h}(\cdot)^{\mathrm{T}}\boldsymbol{e}_{1q}^{-1}(\boldsymbol{h}(\cdot)) = 0$ corresponding to the robot posture which causes no overall effective deformation of the drivetrain. Equation (44) indeed relates the elastic PE (leftmost term) of the network of

the flexible transmission elements to its co-PE (rightmost term) through the well-known Legendre transformation.

Integrating Eq. (43) and making use of Eq. (44) leads to

$$V_{\bar{h}}(\boldsymbol{\theta}_{qs}) = V_h(\boldsymbol{\theta}_{qs}) + \boldsymbol{e}_{1q}(\boldsymbol{T}_{q1}\boldsymbol{\theta}_0 - \boldsymbol{\theta}_{qs})^{\mathrm{T}}(\boldsymbol{T}_{q1}\boldsymbol{\theta}_0 - \boldsymbol{\theta}_{qs}) - \int_{(\boldsymbol{\theta}_{qs})_i}^{\boldsymbol{\theta}_{qs}} \boldsymbol{e}_{1q}^{-1}(\boldsymbol{h}(\boldsymbol{\phi}))^{\mathrm{T}} \frac{\partial \boldsymbol{h}(\boldsymbol{\phi})}{\partial \boldsymbol{\phi}} \cdot d\boldsymbol{\phi} \tag{45}$$

in which $\boldsymbol{h}(\cdot)$ is recognized as the differential of $V_h(\cdot)$ and Eq. (14) is substituted. Therefore, the underlying PE of $\boldsymbol{\tau}_{\mathrm{dr}}^*$, i.e., $V_{\bar{h}}(\boldsymbol{\theta}_{qs})$, is the difference of the gravitational plus elastic PE of the passive robot/transmission subsystems and the elastic PE of the desired task space compliance, all at the stationary link angles.

Regarding with the estimation of the link joint velocity in the control law, Eq. (28) may be understood as a filtering of the time derivative of the estimated link angles, i.e., $\boldsymbol{\vartheta} = \boldsymbol{G}(s)\sqrt{\boldsymbol{K}_v}\boldsymbol{T}_{q1}\dot{\boldsymbol{\theta}}_0$. From the linear system theory, this may be represented in the minimal realization state space $\{\boldsymbol{A}, \boldsymbol{B}, \boldsymbol{C}\}$ form

$$\begin{aligned} \dot{\boldsymbol{x}} &= \boldsymbol{A}\boldsymbol{x} + \boldsymbol{B}\sqrt{\boldsymbol{K}_v}\boldsymbol{T}_{q1}\dot{\boldsymbol{\theta}}_0 \\ \boldsymbol{\vartheta} &= \boldsymbol{C}\boldsymbol{x} \end{aligned} \tag{46}$$

where $\boldsymbol{G}(s) = \boldsymbol{C}(s\boldsymbol{I} - \boldsymbol{A})^{-1}\boldsymbol{B}$ and $\boldsymbol{x}$ is the filter states. Furthermore by the Kalman–Yakubovich (KY) lemma [22], since $\boldsymbol{G}(s)$ is a strictly proper and SPR, there exists symmetric positive definite matrices $\boldsymbol{P}$ and $\boldsymbol{Q}$ such that

$$\boldsymbol{A}^{\mathrm{T}}\boldsymbol{P} + \boldsymbol{P}\boldsymbol{A} = -\boldsymbol{Q} \tag{47}$$

$$\boldsymbol{B}^{\mathrm{T}}\boldsymbol{P} = \boldsymbol{C} \tag{48}$$

Define the error $\tilde{\boldsymbol{\theta}}_0 = \boldsymbol{\theta}_0 - \boldsymbol{\theta}_{0d}$ where $\boldsymbol{\theta}_{0d}$ is the constant target motor angles associated with the specified constant Cartesian set point $\boldsymbol{x}_{\mathrm{d}}$. With the new state vector $\boldsymbol{z}$ such that $\dot{\boldsymbol{z}} = \boldsymbol{x}$, state space representation of the velocity estimator system where the input is the regulating error $\tilde{\theta}_0$ may be expressed as

$$\begin{aligned} \dot{\boldsymbol{z}} &= \boldsymbol{A}\boldsymbol{z} + \boldsymbol{B}\sqrt{\boldsymbol{K}_v}\boldsymbol{T}_{q1}\tilde{\boldsymbol{\theta}}_0 \\ \boldsymbol{\vartheta} &= \boldsymbol{C}\boldsymbol{A}\boldsymbol{z} + \boldsymbol{C}\boldsymbol{B}\sqrt{\boldsymbol{K}_v}\boldsymbol{T}_{q1}\tilde{\boldsymbol{\theta}}_0 \end{aligned} \tag{49}$$

3.4.1 Proof of Stability. To prove the stability of the closed-loop system, consider the following function:

$$V(\boldsymbol{q}, \dot{\boldsymbol{q}}, \boldsymbol{\theta}, \dot{\boldsymbol{\theta}}, \boldsymbol{e}_i, \dot{\boldsymbol{z}}) = \frac{1}{2}\dot{\boldsymbol{q}}^{\mathrm{T}}\boldsymbol{M}(\boldsymbol{q})\dot{\boldsymbol{q}} + V_g(\boldsymbol{q}) + \frac{1}{2}\dot{\boldsymbol{\theta}}^{\mathrm{T}}\boldsymbol{B}_r\dot{\boldsymbol{\theta}} + V_e(\boldsymbol{q}, \boldsymbol{T}_{q1}\boldsymbol{\theta}_0) + \frac{1}{2}\boldsymbol{e}_i^{\mathrm{T}}\boldsymbol{L}\boldsymbol{e}_i - V_{\bar{h}}(\boldsymbol{T}_{q1}\boldsymbol{\theta}_0) + \frac{1}{2}\dot{\boldsymbol{z}}^{\mathrm{T}}\boldsymbol{P}\dot{\boldsymbol{z}} \tag{50}$$

comprising the KE and PE of the robot, modified drivetrain, motor, and the negative feedback controller

$$V_e(\boldsymbol{q}, \boldsymbol{T}_{q1}\boldsymbol{\theta}_0) = \boldsymbol{e}_{1q}(\boldsymbol{T}_{q1}\boldsymbol{\theta}_0 - \boldsymbol{q})^{\mathrm{T}}(\boldsymbol{T}_{q1}\boldsymbol{\theta}_0 - \boldsymbol{q}) - \int_{\boldsymbol{q}_i}^{\boldsymbol{q}} \boldsymbol{e}_{1q}^{-1}(\boldsymbol{h}(\boldsymbol{\phi}))^{\mathrm{T}} \frac{\partial \boldsymbol{h}(\boldsymbol{\phi})}{\partial \boldsymbol{\phi}} \cdot d\boldsymbol{\phi} \tag{51}$$

is the elastic PE of the drivetrain and $V_{\bar{h}}(\boldsymbol{T}_{q1}\boldsymbol{\theta}_0)$ denotes $V_{\bar{h}}(\boldsymbol{\theta}_{qs})$ expressed in terms of the system states $\boldsymbol{T}_{q1}\boldsymbol{\theta}_0$. The last term represents the KE-like function of the velocity estimator unit of which $\boldsymbol{P}$ is the symmetric positive definite matrix as described in Eqs. (47) and (48).

The function $V(\cdot)$ is a Lyapunov candidate function, i.e., it is a positive definite function and continuously differentiable in a neighborhood of the equilibrium point. To verify this, substitute Eqs. (41), (45), and (51) into Eq. (50) and rearrange the equation as

$$\begin{aligned} V(\cdot) = {} & \frac{1}{2}\dot{\boldsymbol{q}}^{\mathrm{T}}\boldsymbol{M}(\boldsymbol{q})\dot{\boldsymbol{q}} + \frac{1}{2}\dot{\boldsymbol{\theta}}^{\mathrm{T}}\boldsymbol{B}_r\dot{\boldsymbol{\theta}} + \frac{1}{2}\boldsymbol{e}_i^{\mathrm{T}}\boldsymbol{L}\boldsymbol{e}_i + \frac{1}{2}\dot{\boldsymbol{z}}^{\mathrm{T}}\boldsymbol{P}\dot{\boldsymbol{z}} + V_h(\boldsymbol{q}) \\ & + \frac{1}{2}(\boldsymbol{f}(\boldsymbol{q}) - \boldsymbol{x}_{\mathrm{d}})^{\mathrm{T}}\boldsymbol{K}_{\mathrm{d}}(\boldsymbol{f}(\boldsymbol{q}) - \boldsymbol{x}_{\mathrm{d}}) \\ & + \boldsymbol{e}_{1q}(\boldsymbol{T}_{q1}\boldsymbol{\theta}_0 - \boldsymbol{\theta}_{qs} + \boldsymbol{\theta}_{qs} - \boldsymbol{q})^{\mathrm{T}}(\boldsymbol{T}_{q1}\boldsymbol{\theta}_0 - \boldsymbol{\theta}_{qs} + \boldsymbol{\theta}_{qs} - \boldsymbol{q}) \\ & - \int_{\boldsymbol{\phi}_i}^{\boldsymbol{q}} \boldsymbol{e}_{1q}^{-1}(\boldsymbol{h}(\boldsymbol{\phi}))^{\mathrm{T}} \frac{\partial \boldsymbol{h}(\boldsymbol{\phi})}{\partial \boldsymbol{\phi}} \cdot d\boldsymbol{\phi} \\ & - V_h(\boldsymbol{\theta}_{qs}) - \boldsymbol{e}_{1q}(\boldsymbol{T}_{q1}\boldsymbol{\theta}_0 - \boldsymbol{\theta}_{qs})^{\mathrm{T}}(\boldsymbol{T}_{q1}\boldsymbol{\theta}_0 - \boldsymbol{\theta}_{qs}) \\ & + \int_{\boldsymbol{\phi}_i}^{\boldsymbol{\theta}_{qs}} \boldsymbol{e}_{1q}^{-1}(\boldsymbol{h}(\boldsymbol{\phi}))^{\mathrm{T}} \frac{\partial \boldsymbol{h}(\boldsymbol{\phi})}{\partial \boldsymbol{\phi}} \cdot d\boldsymbol{\phi} \end{aligned} \tag{52}$$

$\boldsymbol{\theta}_{qs} = \boldsymbol{l}_1^{-1}(\boldsymbol{T}_{q1}\boldsymbol{\theta}_0)$ is implied and the angles $\boldsymbol{\phi}_i$ be the link angles that cause no overall effective deformation of the drivetrain.

Using Taylor's series, the following expansion of

$$\begin{aligned} & \boldsymbol{e}_{1q}(\boldsymbol{T}_{q1}\boldsymbol{\theta}_0 - \boldsymbol{\theta}_{qs} + \boldsymbol{\theta}_{qs} - \boldsymbol{q})^{\mathrm{T}}(\boldsymbol{T}_{q1}\boldsymbol{\theta}_0 - \boldsymbol{\theta}_{qs} + \boldsymbol{\theta}_{qs} - \boldsymbol{q}) \\ & = \boldsymbol{e}_{1q}(\boldsymbol{T}_{q1}\boldsymbol{\theta}_0 - \boldsymbol{\theta}_{qs})^{\mathrm{T}}(\boldsymbol{T}_{q1}\boldsymbol{\theta}_0 - \boldsymbol{\theta}_{qs}) \\ & + (\boldsymbol{\theta}_{qs} - \boldsymbol{q})^{\mathrm{T}} \frac{\partial \boldsymbol{e}_{1q}(\boldsymbol{\delta})}{\partial \boldsymbol{\delta}}\bigg|_{\boldsymbol{\delta}=\boldsymbol{T}_{q1}\boldsymbol{\theta}_0 - \boldsymbol{\theta}_{qs}} (\boldsymbol{T}_{q1}\boldsymbol{\theta}_0 - \boldsymbol{\theta}_{qs}) + \ldots \\ & + \boldsymbol{e}_{1q}(\boldsymbol{T}_{q1}\boldsymbol{\theta}_0 - \boldsymbol{\theta}_{qs})^{\mathrm{T}}(\boldsymbol{\theta}_{qs} - \boldsymbol{q}) \\ & + (\boldsymbol{\theta}_{qs} - \boldsymbol{q})^{\mathrm{T}} \frac{\partial \boldsymbol{e}_{1q}(\boldsymbol{\delta})}{\partial \boldsymbol{\delta}}\bigg|_{\boldsymbol{\delta}=\boldsymbol{T}_{q1}\boldsymbol{\theta}_0 - \boldsymbol{\theta}_{qs}} (\boldsymbol{\theta}_{qs} - \boldsymbol{q}) + \ldots \end{aligned} \tag{53}$$

may be deduced. The equation has the graphical interpretation of the sum of the total elastic PE and co-PE of the transmission system. Figure 4 depicts the related area/energy of each term for one-dimensional spring. The area I-IV correspond to the first, second and its residue, third, and fourth and its residue terms on the right-hand side. Moreover, with $\boldsymbol{h}(\boldsymbol{\phi}) = \boldsymbol{e}_{1q}(\boldsymbol{T}_{q1}\boldsymbol{\theta}_0 - \boldsymbol{\phi})$, two integral terms in Eq. (52) may be summed and rewritten as the function of the deformation variable $\boldsymbol{\delta}$

$$\int_{\boldsymbol{q}}^{\boldsymbol{\theta}_{qs}} \boldsymbol{e}_{1q}^{-1}(\boldsymbol{h}(\boldsymbol{\phi}))^{\mathrm{T}} \frac{\partial \boldsymbol{h}(\boldsymbol{\phi})}{\partial \boldsymbol{\phi}} \cdot d\boldsymbol{\phi} = \int_{\boldsymbol{T}_{q1}\boldsymbol{\theta}_0 - \boldsymbol{q}}^{\boldsymbol{T}_{q1}\boldsymbol{\theta}_0 - \boldsymbol{\theta}_{qs}} \boldsymbol{\delta}^{\mathrm{T}} \frac{\partial \boldsymbol{e}_{1q}(\boldsymbol{\delta})}{\partial \boldsymbol{\delta}} \cdot d\boldsymbol{\delta} \tag{54}$$

This is the co-PE stored in changing from $\boldsymbol{T}_{q1}\boldsymbol{\theta}_0 - \boldsymbol{q}$ to $\boldsymbol{T}_{q1}\boldsymbol{\theta}_0 - \boldsymbol{\theta}_{qs}$, corresponding to the negative of the shaded area V shown in Fig. 4.

With Eqs. (53) and (54), Eq. (52) may be simplified to

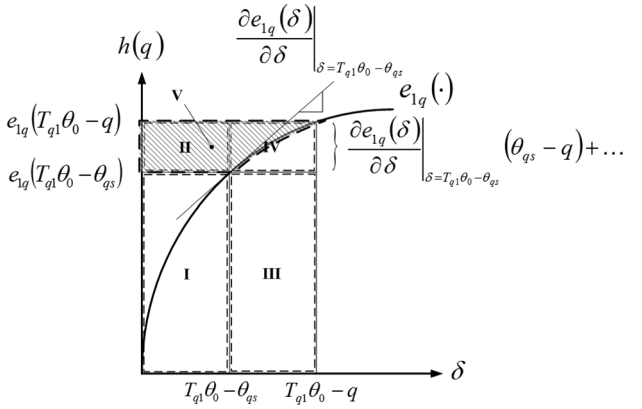

Fig. 4 Interpretation of each term in Eq. (53) as the sub areas of the elastic potential/co-PE

$$V(\cdot)=\frac{1}{2}\dot{\boldsymbol{q}}^{\mathrm{T}}\boldsymbol{M}(\boldsymbol{q})\dot{\boldsymbol{q}}+\frac{1}{2}\dot{\boldsymbol{\theta}}^{\mathrm{T}}\boldsymbol{B}_r\dot{\boldsymbol{\theta}}+\frac{1}{2}\boldsymbol{e}_i^{\mathrm{T}}\boldsymbol{L}\boldsymbol{e}_i+\frac{1}{2}\dot{\boldsymbol{z}}^{\mathrm{T}}\boldsymbol{P}\dot{\boldsymbol{z}}+\frac{1}{2}(\boldsymbol{f}(\boldsymbol{q})-\boldsymbol{x}_{\mathrm{d}})^{\mathrm{T}}\boldsymbol{K}_{\mathrm{d}}(\boldsymbol{f}(\boldsymbol{q})-\boldsymbol{x}_{\mathrm{d}})+V_h(\boldsymbol{q})-V_h(\boldsymbol{\theta}_{qs})+\int_{\boldsymbol{T}_{q1}\boldsymbol{\theta}_0-\boldsymbol{\theta}_{qs}}^{\boldsymbol{T}_{q1}\boldsymbol{\theta}_0-\boldsymbol{q}}\boldsymbol{e}_{1q}(\boldsymbol{\delta})^{\mathrm{T}}\cdot d\boldsymbol{\delta} \tag{55}$$

The last term on the right-hand side represents the incremental PE from $\boldsymbol{T}_{q1}\boldsymbol{\theta}_0-\boldsymbol{\theta}_{qs}$ to $\boldsymbol{T}_{q1}\boldsymbol{\theta}_0-\boldsymbol{q}$. For the system in which the elastic elements possess the softening-spring characteristics such as the cable-pulley driven transmission, Eq. (55) may further be arranged as

$$V(\cdot)\geq\frac{1}{2}\dot{\boldsymbol{q}}^{\mathrm{T}}\boldsymbol{M}(\boldsymbol{q})\dot{\boldsymbol{q}}+\frac{1}{2}\dot{\boldsymbol{\theta}}^{\mathrm{T}}\boldsymbol{B}_r\dot{\boldsymbol{\theta}}+\frac{1}{2}\boldsymbol{e}_i^{\mathrm{T}}\boldsymbol{L}\boldsymbol{e}_i+\frac{1}{2}\dot{\boldsymbol{z}}^{\mathrm{T}}\boldsymbol{P}\dot{\boldsymbol{z}}+\frac{1}{2}(\boldsymbol{f}(\boldsymbol{q})-\boldsymbol{x}_{\mathrm{d}})^{\mathrm{T}}\boldsymbol{K}_{\mathrm{d}}(\boldsymbol{f}(\boldsymbol{q})-\boldsymbol{x}_{\mathrm{d}})+\frac{1}{2}(\boldsymbol{\theta}_{qs}-\boldsymbol{q})^{\mathrm{T}}\frac{\partial\boldsymbol{e}_{1q}(\boldsymbol{\delta})}{\partial\boldsymbol{\delta}}\bigg|_{\boldsymbol{\delta}^*}(\boldsymbol{\theta}_{qs}-\boldsymbol{q})+V_h(\boldsymbol{q})-V_h(\boldsymbol{\theta}_{qs})+\boldsymbol{h}(\boldsymbol{\theta}_{qs})^{\mathrm{T}}(\boldsymbol{\theta}_{qs}-\boldsymbol{q}) \tag{56}$$

where

$$\frac{\partial\boldsymbol{e}_{1q}(\theta\delta)}{\partial\boldsymbol{\delta}}\bigg|_{\boldsymbol{\delta}^*}=\inf_{\forall\boldsymbol{\delta}\in\mathbb{R}^p}\frac{\partial\boldsymbol{e}_{1q}(\boldsymbol{\delta})}{\partial\boldsymbol{\delta}}\leq\frac{\partial\boldsymbol{e}_{1q}(\boldsymbol{\delta})}{\partial\boldsymbol{\delta}}\bigg|_{\boldsymbol{\delta}=\boldsymbol{T}_{q1}\boldsymbol{\theta}_0-\boldsymbol{q}}\leq\frac{\partial\boldsymbol{e}_{1q}(\boldsymbol{\delta})}{\partial\boldsymbol{\delta}}\bigg|_{\boldsymbol{\delta}=\boldsymbol{T}_{q1}\boldsymbol{\theta}_0-\boldsymbol{\theta}_{qs}}$$

To show that $V(\cdot)$ is a positive definite function, the following assumption is necessary.

Assumption 3.1.

The Hessian $\boldsymbol{H}_h(\boldsymbol{q})=(\partial\boldsymbol{h}(\boldsymbol{q})/\partial\boldsymbol{q})=(\partial^2V_h(\boldsymbol{q})/\partial\boldsymbol{q}^2)$ *of the potential function* $V_h(\boldsymbol{q})$ *satisfies the condition*

$$\alpha_h\equiv\sup_{\forall\boldsymbol{q}\in\mathbb{R}^p}\|\boldsymbol{H}_h(\boldsymbol{q})\|_K<1 \tag{57}$$

where the matrix K-norm is as defined in the Appendix.

This practical assumption is exactly the condition for the recursive evaluation of Eq. (14) to converge to the stationary link angles. An important consequence of Assumption 3.1 is the following property.

Property 3.2.

Let α_h *be the upper bound for the Hessian of* $V_h(\boldsymbol{q})$ *as defined in assumption 3.1. Then the inequality*

$$\left|V_h(\boldsymbol{q}_2)-V_h(\boldsymbol{q}_1)+h(\boldsymbol{q}_1)^{\mathrm{T}}(\boldsymbol{q}_1-\boldsymbol{q}_2)\right|\leq\frac{1}{2}\alpha_h\|\boldsymbol{q}_1-\boldsymbol{q}_2\|_K^2 \tag{58}$$

holds for all $\boldsymbol{q}_1,\boldsymbol{q}_2\in\mathbb{R}^p$ *(see Ref. [9] for the proof).*

Applying Property 3.2 and $\left\|(\partial\boldsymbol{e}_{1q}(\boldsymbol{\delta}))/\partial\boldsymbol{\delta}|_{\boldsymbol{\delta}^*}\right\|_K=1$ to Eq. (56), one would obtain

$$V(\cdot)\geq\frac{1}{2}\dot{\boldsymbol{q}}^{\mathrm{T}}\boldsymbol{M}(\boldsymbol{q})\dot{\boldsymbol{q}}+\frac{1}{2}\dot{\boldsymbol{\theta}}^{\mathrm{T}}\boldsymbol{B}_r\dot{\boldsymbol{\theta}}+\frac{1}{2}\boldsymbol{e}_i^{\mathrm{T}}\boldsymbol{L}\boldsymbol{e}_i+\frac{1}{2}\dot{\boldsymbol{z}}^{\mathrm{T}}\boldsymbol{P}\dot{\boldsymbol{z}}+\frac{1}{2}(\boldsymbol{f}(\boldsymbol{q})-\boldsymbol{x}_{\mathrm{d}})^{\mathrm{T}}\boldsymbol{K}_{\mathrm{d}}(\boldsymbol{f}(\boldsymbol{q})-\boldsymbol{x}_{\mathrm{d}})+\frac{1}{2}(1-\alpha_h)\|\boldsymbol{\theta}_{qs}-\boldsymbol{q}\|_K^2 \tag{59}$$

Recalling Assumption 3.1 and recognizing all quadratic terms in the above inequality, it can be concluded that $V(\cdot)\geq 0$.

To determine the equilibrium point where $V(\cdot)\equiv 0$, it is required that $\dot{\boldsymbol{q}}=\boldsymbol{0},\dot{\boldsymbol{\theta}}=\boldsymbol{0}$, $\boldsymbol{e}_i=\boldsymbol{0}$, and $\dot{\boldsymbol{z}}=\boldsymbol{0}$ for the quadratic terms of Eq. (50) to be zero. The remaining terms may be rearranged to show that $\boldsymbol{q}=\boldsymbol{\theta}_{qs}=\boldsymbol{f}^{-1}(\boldsymbol{x}_{\mathrm{d}})$ nullifies them. From Eq. (14), the motor angle at the equilibrium will be $\boldsymbol{\theta}_0=\boldsymbol{\theta}_{0s}=\boldsymbol{T}_{q1}^{-1}\boldsymbol{l}_1(\boldsymbol{f}^{-1}(\boldsymbol{x}_{\mathrm{d}}))$. Likewise, the equilibrium rotor angle of the drivetrain at the ith-stage is $\boldsymbol{\theta}_{(i-1)}=\boldsymbol{\theta}_{(i-1)s}=\boldsymbol{T}_{qi}^{-1}\boldsymbol{l}_i(\boldsymbol{f}^{-1}(\boldsymbol{x}_{\mathrm{d}}))$, where $\boldsymbol{l}_i(\boldsymbol{\theta}_{qs})=\boldsymbol{\theta}_{qs}+\boldsymbol{e}_{iq}^{-1}(\boldsymbol{h}(\boldsymbol{\theta}_{qs}))$ denotes the stationary rotor angle at the ith-stage reflected to the robot link angle and $\boldsymbol{e}_{iq}^{-1}(\cdot)$ is the effective nonlinear deformation function of the transmission subsystem from the ith-stage to the last qth-stage. Note that the equilibrium rotor angle at the last stage is $\boldsymbol{\theta}_{(q-1)}=\boldsymbol{\theta}_{(q-1)s}=\boldsymbol{T}_q^{-1}\boldsymbol{l}_q(\boldsymbol{f}^{-1}(\boldsymbol{x}_{\mathrm{d}}))$ where $\boldsymbol{l}_q(\boldsymbol{\theta}_{qs})=\boldsymbol{\theta}_{qs}+\boldsymbol{e}_q^{-1}(\boldsymbol{h}(\boldsymbol{\theta}_{qs}))$.

Lyapunov stability theorem and Lasalle's invariance principle [22] will now be applied to show that the system equilibrium point $(\boldsymbol{q},\dot{\boldsymbol{q}},\boldsymbol{\theta},\dot{\boldsymbol{\theta}},\boldsymbol{e}_i,\dot{\boldsymbol{z}})=(\boldsymbol{q}_s,\boldsymbol{0},\boldsymbol{\theta}_s,\boldsymbol{0},\boldsymbol{0},\boldsymbol{0})$ is (locally) asymptotically stable. Differentiating Eq. (50) along the closed-loop system trajectory results in

$$\dot{V}(\cdot)=\frac{1}{2}\dot{\boldsymbol{q}}^{\mathrm{T}}\dot{\boldsymbol{M}}(\boldsymbol{q})\dot{\boldsymbol{q}}+\dot{\boldsymbol{q}}^{\mathrm{T}}(\boldsymbol{\tau}_{\mathrm{dr}}+\boldsymbol{\tau}_{\mathrm{ext}}-\boldsymbol{C}(\boldsymbol{q},\dot{\boldsymbol{q}})\dot{\boldsymbol{q}}-\boldsymbol{g}(\boldsymbol{q}))+\dot{\boldsymbol{\theta}}^{\mathrm{T}}(\boldsymbol{\tau}_r-\boldsymbol{c}_r(\dot{\boldsymbol{\theta}})-\boldsymbol{e}(\boldsymbol{\theta}))+\boldsymbol{e}_i^{\mathrm{T}}(-\boldsymbol{K}_c\boldsymbol{e}_i)+\frac{1}{2}(\boldsymbol{A}\dot{\boldsymbol{z}}+\boldsymbol{B}\sqrt{\boldsymbol{K}_v}\boldsymbol{T}_{q1}\dot{\boldsymbol{\theta}}_0)^{\mathrm{T}}\boldsymbol{P}\dot{\boldsymbol{z}}+\frac{1}{2}\dot{\boldsymbol{z}}^{\mathrm{T}}\boldsymbol{P}(\boldsymbol{A}\dot{\boldsymbol{z}}+\boldsymbol{B}\sqrt{\boldsymbol{K}_v}\boldsymbol{T}_{q1}\dot{\boldsymbol{\theta}}_0)+\boldsymbol{g}(\boldsymbol{q})^{\mathrm{T}}\dot{\boldsymbol{q}}+\frac{\partial V_e(\boldsymbol{q},\boldsymbol{T}_{q1}\boldsymbol{\theta}_0)}{\partial\boldsymbol{q}}\dot{\boldsymbol{q}}+\frac{\partial V_e(\boldsymbol{q},\boldsymbol{T}_{q1}\boldsymbol{\theta}_0)}{\partial(\boldsymbol{T}_{q1}\boldsymbol{\theta}_0)}\boldsymbol{T}_{q1}\dot{\boldsymbol{\theta}}_0-\boldsymbol{h}(\boldsymbol{\theta}_{qs})^{\mathrm{T}}\boldsymbol{T}_{q1}\dot{\boldsymbol{\theta}}_0$$

where $\boldsymbol{\tau}_r=\left[(\boldsymbol{\tau}_{\mathrm{m}})_{\mathrm{dr}}^{\mathrm{T}}\quad\boldsymbol{0}^{\mathrm{T}}\quad\cdots\quad\boldsymbol{0}^{\mathrm{T}}\right]^{\mathrm{T}}$ and $\boldsymbol{c}_r(\cdot)$ are the modified generalized torque vector and the modified dissipative function of the drivetrain subsystem according to Eq. (34). Applying the passivity property of the robot [23], the KY lemma, and recognizing $\boldsymbol{\tau}_{\mathrm{dr}}=\boldsymbol{e}_q(\boldsymbol{T}_q\boldsymbol{\theta}_{q-1}-\boldsymbol{\theta}_q)$, $(\boldsymbol{\tau}_{\mathrm{m}})_{\mathrm{dr}}=\boldsymbol{T}_{q1}^{\mathrm{T}}(\boldsymbol{h}(\boldsymbol{\theta}_{qs})-\sqrt{\boldsymbol{K}_v}\boldsymbol{\vartheta})+\boldsymbol{K}_\tau\boldsymbol{e}_i$, $((\partial V_e(\boldsymbol{q},\boldsymbol{\theta}))/\partial\boldsymbol{\theta})\dot{\boldsymbol{\theta}}=((\partial V_e(\boldsymbol{q},\boldsymbol{T}_{q1}\boldsymbol{\theta}_0))/\partial(\boldsymbol{T}_{q1}\boldsymbol{\theta}_0))\boldsymbol{T}_{q1}\dot{\boldsymbol{\theta}}_0$, and $(\partial V_e(\boldsymbol{q},\boldsymbol{\theta}))/\partial\boldsymbol{q}=(\partial V_e(\boldsymbol{q},\boldsymbol{T}_{q1}\boldsymbol{\theta}_0))/\partial\boldsymbol{q})$, the derivative may be simplified to

$$\dot{V}(\cdot)=-\dot{\boldsymbol{\theta}}^T\boldsymbol{c}_r(\dot{\boldsymbol{\theta}})+\dot{\boldsymbol{q}}^{\mathrm{T}}\boldsymbol{\tau}_{\mathrm{ext}}-\boldsymbol{e}_i^T\boldsymbol{K}_{\mathrm{c}}\boldsymbol{e}_i-\frac{1}{2}\dot{\boldsymbol{z}}^{\mathrm{T}}\boldsymbol{Q}\dot{\boldsymbol{z}}+\dot{\boldsymbol{\theta}}_0^{\mathrm{T}}\boldsymbol{K}_\tau\boldsymbol{e}_i$$

Quadratic factorization of the last term and explicit presentation of the damping power loss at each transmission stage rearrange the equation to

$$\dot{V}(\cdot)=\dot{\boldsymbol{q}}^{\mathrm{T}}\boldsymbol{\tau}_{\mathrm{ext}}-\frac{1}{2}\dot{\boldsymbol{z}}^{\mathrm{T}}\boldsymbol{Q}\dot{\boldsymbol{z}}-\frac{1}{2}(\dot{\boldsymbol{\theta}}_0-\boldsymbol{e}_i)^{\mathrm{T}}\boldsymbol{K}_\tau(\dot{\boldsymbol{\theta}}_0-\boldsymbol{e}_i)-\sum_{k=2}^{q}\dot{\boldsymbol{\theta}}_{k-1}^{\mathrm{T}}\boldsymbol{c}_{rk}(\dot{\boldsymbol{\theta}}_{k-1})-\frac{1}{2}\boldsymbol{e}_i^{\mathrm{T}}(2\boldsymbol{K}_c-\boldsymbol{K}_\tau)\boldsymbol{e}_i-\frac{1}{2}\dot{\boldsymbol{\theta}}_0^{\mathrm{T}}(2\boldsymbol{c}_{r1}(\dot{\boldsymbol{\theta}}_0)-\boldsymbol{K}_\tau\dot{\boldsymbol{\theta}}_0) \tag{60}$$

It is practical that the drivetrain is fully damped, i.e., $\dot{\boldsymbol{\theta}}^{\mathrm{T}}\boldsymbol{c}_r(\dot{\boldsymbol{\theta}})\geq\sum_{i=1}^{pq}\alpha_i\dot{\theta}_i^2,\alpha_i>0$ and $\boldsymbol{c}_r(\boldsymbol{0})=\boldsymbol{0}$. If the matrix gain $\boldsymbol{K}_{\mathrm{c}}$ is designed to be fast enough for current tracking such that $\boldsymbol{K}_{\mathrm{c}}>(1/2)\boldsymbol{K}_\tau$ and the first-stage (the motors) has been damped enough that $\dot{\boldsymbol{\theta}}_0^{\mathrm{T}}(2\boldsymbol{c}_{r1}(\dot{\boldsymbol{\theta}}_0)-\boldsymbol{K}_\tau\dot{\boldsymbol{\theta}}_0)>0$, then it can be concluded for the case of free motion that

$$\dot{V}(\boldsymbol{q},\dot{\boldsymbol{q}},\boldsymbol{\theta},\dot{\boldsymbol{\theta}},\boldsymbol{e}_i,\dot{\boldsymbol{z}})\leq 0$$

Therefore, Eq. (50) is a Lyapunov function. From the Lyapunov stability theorem, the closed-loop system is stable. The stability is generally, however, local due to the local invertibility of the forward kinematics mapping. In addition, it can be shown that the equilibrium point is the only point (in the invariant set) which makes $\dot{V}(\cdot)\equiv 0$. Through the help of the Lasalle's invariance principle, the system is asymptotically stable to the equilibrium point. Note that the motor current will converge to the reference

value $\boldsymbol{i}_m$ of Eq. (35) and the estimated velocity related term ϑ will finally be vanished identically.

3.4.2 Proof of Passivity. Passivity is an important property for the robot system to perform interaction tasks successfully since the passive system will respond to the incoming input energy in a stable manner according to the underlying principle of energy conservation. As a result, the system will be robust to the disturbance and interact safely with the passive environment.

Figure 5 depicts the block diagram of the multistage nonlinear flexible transmission driven robot controlled system, which may be decomposed into three units representing the robot, the drivetrain, and the motor plus the controller subsystems. They are interconnecting in tandem feedback topology. The whole system is then coupled to the passive environment mapping the velocity flow $\dot{\boldsymbol{x}}$ to the action force effort $-\boldsymbol{F}_{\text{ext}}$. Since the robot moves with the same velocity, the torque acting onto the robot will then be the reaction torque $\boldsymbol{\tau}_{\text{ext}}$.

Passivity of the robot subsystem can be shown readily by the lower bounded storage function

$$S_{\text{r}}(\boldsymbol{q},\dot{\boldsymbol{q}}) = \frac{1}{2}\dot{\boldsymbol{q}}^{\text{T}}\boldsymbol{M}(\boldsymbol{q})\dot{\boldsymbol{q}} + V_g(\boldsymbol{q}) \tag{61}$$

with $|V_g(\boldsymbol{q})| < \beta$, for some $\beta > 0$. Its time derivative along the trajectory of the robot dynamics is $\dot{S}_{\text{r}} = \dot{\boldsymbol{q}}^{\text{T}}(\boldsymbol{\tau}_{\text{dr}} + \boldsymbol{\tau}_{\text{ext}})$. Hence, the robot subsystem is the lossless system mapping $(\boldsymbol{\tau}_{dr} + \boldsymbol{\tau}_{ext}) \mapsto \dot{\boldsymbol{q}}$. Passivity of the modified drivetrain subsystem may be analyzed with the storage function

$$S_{\text{dr}}(\boldsymbol{q},\boldsymbol{\theta},\dot{\boldsymbol{\theta}}) = \frac{1}{2}\dot{\boldsymbol{\theta}}^{\text{T}}\boldsymbol{B}_r\dot{\boldsymbol{\theta}} + V_e(\boldsymbol{q},\boldsymbol{\theta}) \tag{62}$$

of which its derivative along the trajectory of the drivetrain dynamics is $\dot{S}_{\text{dr}} = \dot{\boldsymbol{\theta}}_0^{\text{T}}(\boldsymbol{\tau}_{\text{m}})_{\text{dr}} - \dot{\boldsymbol{q}}^{\text{T}}\boldsymbol{\tau}_{\text{dr}} - \dot{\boldsymbol{\theta}}^{\text{T}}\boldsymbol{c}_r(\dot{\boldsymbol{\theta}})$. Therefore, if the transmission subsystem is fully damped, it will be the state strictly passive system mapping $\dot{\boldsymbol{q}} \mapsto -\boldsymbol{\tau}_{\text{dr}}$ at the port connecting the drivetrain to the robot, and $(\boldsymbol{\tau}_{\text{m}})_{\text{dr}} \mapsto \dot{\boldsymbol{\theta}}_0$ at the port connecting to the motor electrical dynamics and the controller.

Pertaining equations of the motor current dynamics plus the controller are displayed in Fig. 5. With the comprehension in the underlying energy previously analyzed, one may select the following storage function:

$$S_{\text{mc}}(\boldsymbol{e}_i,\dot{\boldsymbol{z}},\boldsymbol{\theta}_0) = \frac{1}{2}\boldsymbol{e}_i^{\text{T}}\boldsymbol{L}\boldsymbol{e}_i + \frac{1}{2}\dot{\boldsymbol{z}}^{\text{T}}\boldsymbol{P}\dot{\boldsymbol{z}} - V_{\bar{h}}(\boldsymbol{T}_{q1}\boldsymbol{\theta}_0) \tag{63}$$

Time derivative along the trajectory of the current tracking and velocity estimator dynamics after some additional manipulation is thus

$$\dot{S}_{\text{mc}} = -\dot{\boldsymbol{\theta}}_0^{\text{T}}(\boldsymbol{\tau}_{\text{m}})_{\text{dr}} - \boldsymbol{e}_i^{\text{T}}\boldsymbol{K}_c\boldsymbol{e}_i - \frac{1}{2}\dot{\boldsymbol{z}}^{\text{T}}\boldsymbol{Q}\dot{\boldsymbol{z}} - \frac{1}{2}(\dot{\boldsymbol{\theta}}_0 - \boldsymbol{e}_i)^{\text{T}}\boldsymbol{K}_\tau(\dot{\boldsymbol{\theta}}_0 - \boldsymbol{e}_i) + \frac{1}{2}\dot{\boldsymbol{\theta}}_0^{\text{T}}\boldsymbol{K}_\tau\dot{\boldsymbol{\theta}}_0 + \frac{1}{2}\boldsymbol{e}_i^{\text{T}}\boldsymbol{K}_\tau\boldsymbol{e}_i$$

Because the last two terms are always non-negative, passivity and passive mapping $\dot{\boldsymbol{\theta}}_0 \mapsto -(\boldsymbol{\tau}_{\text{m}})_{\text{dr}}$ of this subsystem solely cannot be concluded. Nevertheless, one may combine the drivetrain, motor, and controller subsystems (second and third units) altogether. Consequently, the storage function of this integral unit may be proposed as the sum of the storage functions of the subsystems

$$S_{\text{dr,mc}}(\boldsymbol{q},\boldsymbol{\theta},\dot{\boldsymbol{\theta}},\boldsymbol{e}_i,\dot{\boldsymbol{z}}) = S_{\text{dr}}(\cdot) + S_{\text{mc}}(\cdot) \tag{64}$$

The time derivative will merely be the sum of the derivative of these subsystem storage functions

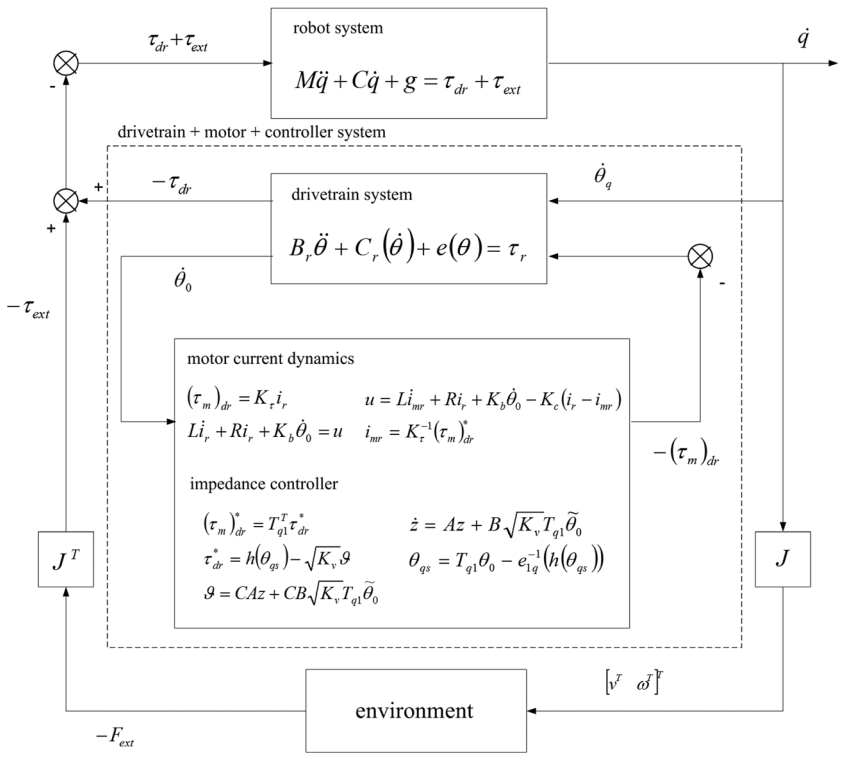

Fig. 5 Feedback interconnection of three subsystems of the nonlinear flexible joint robot controlled system interacting with the passive environment. The system as a whole is passive.

$$\dot{S}_{\mathrm{dr,mc}}(\cdot) = \dot{S}_{\mathrm{dr}}(\cdot) + \dot{S}_{\mathrm{mc}}(\cdot) = -\dot{\boldsymbol{q}}^{\mathrm{T}}\boldsymbol{\tau}_{\mathrm{dr}} - \frac{1}{2}\dot{\boldsymbol{z}}^{\mathrm{T}}\boldsymbol{Q}\dot{\boldsymbol{z}} - \frac{1}{2}\left(\dot{\boldsymbol{\theta}}_0 - \boldsymbol{e}_i\right)^{\mathrm{T}}\boldsymbol{K}_{\tau}\left(\dot{\boldsymbol{\theta}}_0 - \boldsymbol{e}_i\right) - \sum_{k=2}^{q}\dot{\boldsymbol{\theta}}_{k-1}^{\mathrm{T}}\boldsymbol{c}_{rk}\left(\dot{\boldsymbol{\theta}}_{k-1}\right) - \frac{1}{2}\boldsymbol{e}_i^{\mathrm{T}}(2\boldsymbol{K}_{\mathrm{c}} - \boldsymbol{K}_{\tau})\boldsymbol{e}_i - \frac{1}{2}\dot{\boldsymbol{\theta}}_0^{\mathrm{T}}\left(2\boldsymbol{c}_{r1}\left(\dot{\boldsymbol{\theta}}_0\right) - \boldsymbol{K}_{\tau}\dot{\boldsymbol{\theta}}_0\right) \tag{65}$$

Under the conditions of $\boldsymbol{K}_{\mathrm{c}} > (1/2)\boldsymbol{K}_{\tau}$ and $\dot{\boldsymbol{\theta}}_0^{\mathrm{T}}\left(2\boldsymbol{c}_{r1}\left(\dot{\boldsymbol{\theta}}_0\right) - \boldsymbol{K}_{\tau}\dot{\boldsymbol{\theta}}_0\right) > 0$, and fully damped transmission system, the state strictly passive mapping $\dot{\boldsymbol{q}} \mapsto -\boldsymbol{\tau}_{\mathrm{dr}}$ at the port connecting to the robot of the integrated drivetrain, motor, and controller subsystems is ensured. As a result, Fig. 5 may be viewed as the negative feedback interconnection of two passive systems. Further, it is possible that the robot is coupled to the passive environment.

Theorem 3.3.

FEEDBACK INTERCONNECTION OF THE SYSTEMS: [24] The negative feedback interconnection of two passive systems is passive.

Applying the stated Theorem 3.3, proof of the passivity of the multistage nonlinear flexible transmission driven robot controlled system interacting with the passive environment is thus completed.

4 Simulation, Experiments, and Discussions

In this section, a 2DOF cable-pulley driven flexible joint robot with the developed task space impedance control law in Sec. 3 is studied. The system has been constructed as a prototype supporting the fundamental study of the cable-pulley driven robot which will further be useful in developing the whole arm of the ongoing service robot project. As depicted in Fig. 6, the rigid robot is driven through the multistage nonlinear flexible cable-pulley transmission unit. Its shoulder link is capable of moving along the pitch and yaw directions emulating the principal motion performed by the human shoulder.

Figure 7 illustrates the winches and pulleys arrangement of the four-stage transmission subsystem. Two motors are used to drive the system symmetrically along the left and right segregating paths. Motor axle is coupled to winch#1, which then drives winch#2 through the properly wrapped cables. It in turn drives pulley#1 and pulley#2. With pulley#3 and the cable circuits, these pulleys form the differential mechanism producing the pitching and yawing motion of the output shoulder link. It is the place where two transmission paths meet. Additional pulley#4 is not attached with any cable and its purposes are to counter pulley#3 and to strengthen the structure.

According to the manipulator design, output motion of the system is not measurable as there is no any motion sensor directly

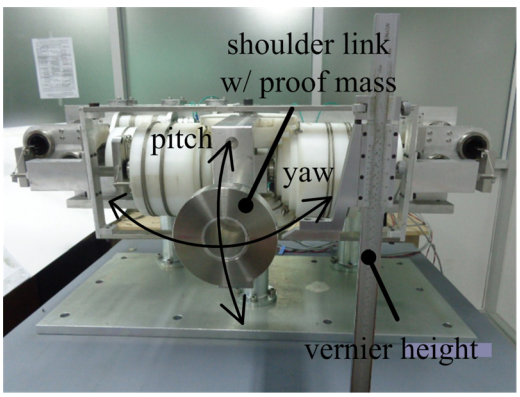

Fig. 6 A 2DOF multistage cable-pulley driven flexible joint robot. In the figure, the proof mass of 1.0 kg is placed at the link end tip with a vernier height gauge used to measure the position in *Y*-direction.

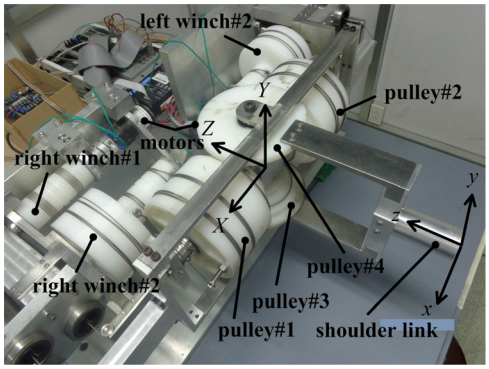

Fig. 7 Winches and pulleys arrangement in the drivetrain unit of the flexible joint robot. Relevant coordinate frames are shown. Left winch#1 is occluded.

equipped to the robot linkage. Rather, collocated sensors of the motor encoders are used to deduce the stationary pitch and yaw output motion $\boldsymbol{\theta}_{qs}$ following Eq. (14). It is observed from the experiment that they may well be used as the estimation of the actual robot motion if it performs smoothly at low speed. The actual end tip motion might also be acquired through the dedicated separate sensor such as the optical tracking system. In the meantime, a simpler means of employing the vernier height gauge (0.02 mm of resolution) to measure only the static *Y*-position of the robot end tip is adopted. See Fig. 6 for the system setup.

Task space impedance control law is applied to this system with the specified task space stiffness matrix ${}^{\{xyz\}}\boldsymbol{K}_{\mathrm{d}} = \mathrm{diag}\left(k_{dx}, k_{dy}\right)$ and the damping ratio ξ. Accordingly, the damping matrix of Eq. (24) may be expressed

$$\boldsymbol{D}_{\mathrm{d}}\left(\boldsymbol{f}\left(\boldsymbol{\theta}_q\right)\right) = \begin{bmatrix} \dfrac{2\xi\sqrt{k_{dx}I_{yy_{py}}}}{l_o} & 0 \\ 0 & \dfrac{2\xi\sqrt{k_{dy}\left(I_{xx_{py}}c_y^2 + I_{zz_{py}}s_y^2 + I_{xx_p}\right)}}{l_o c_y} \end{bmatrix} \tag{66}$$

as a function of the robot joint angles $\boldsymbol{\theta}_q = [\,\theta_p \quad \theta_y\,]^{\mathrm{T}}$. In the simulation, the nominal stiffness and damping values are set to 10×10^3 N/m and 4.0, while for the real system the typical values are tuned to 500 N/m and 0.6. These lower values are in accordance with the passivity limitation, i.e., energy generation, cursed by the sampling rate and quantization of the sampled-data control system [25]. Stiffer robot may be achieved if the system is implemented with faster sampling rate and higher resolution. Unmodeled dynamics degrades the expected performance as well. Also, a simple first-order low-pass filter of $G(s) = \lambda/(s+\lambda)$ is employed in filtering the estimated link joint velocity. The cutoff frequency λ is selected to be 500 rad/s in the simulation, while it has been reduced to just 65 rad/s in the real system. This is to avoid picking up the signal with frequency higher than 10 Hz that is too fast for the typical robot motion. Motor current safety limit is set to 3.5 A.

In the simulation, the designed controller is performed in MATLAB® connected to 20-sim© [26]. This simulator program is employed to model the whole system in details using the bond graph modeling framework. Since the system is quite stiff, the adaptive backward differentiation formula integration method with the step size of 1 ms is used in all simulations. For the real system, the controller and the supporting processes are programmed entirely in C# language. The controller is implemented with the rate of 1 kHz. At each sampling, $\boldsymbol{\theta}_{qs}$ is determined recursively where the value is further used to compute other terms of $\boldsymbol{g}$, $\boldsymbol{J}$, $\boldsymbol{f}$, $\boldsymbol{D}_{\mathrm{d}}$, and ϑ for which Tustin approximation is employed to

discretize $s\boldsymbol{G}(s)$. $\hat{\tau}_1$ is also updated by the motor current and angle. These variables are thus prepared for calculating the robot control signal as delineated in Fig. 3. It should be mentioned that this fully damped system satisfies the Assumption 3.1. Hence, the convergence of $\boldsymbol{\theta}_{qs}$ and the system stability/passivity are assured. Figure 8 depicts the signal interconnection between the system and the controller where the motor current and angle are fed back to the controller unit for processing the commanded current. In the following, some simulation and experiments are performed to investigate the effect of several control parameters on the system response and to illustrate the effectiveness of the proposed control law.

4.1 Task Space Stiffness and Damping. To verify that the desired task space stiffness is actually achieved, the robot is regulated at the center of the workspace and the external force of 10 N is applied in the *X*- and *Y*-direction, respectively. For the simulation, the end tip deflection responses using the nominal stiffness value of 10×10^3 N/m are shown in Fig. 9 for a set of different damping ratios. It is observed that larger damping makes the motion be more sluggish. For a wide range of damping ratios, the end tip eventually reaches the point corresponding to the deflection of about 1 mm that agrees with the desired stiffness and the applied force.

For the actual system, the proof mass of 1.0 kg is placed at the far end of the robot shoulder link to realize the constant external force in the negative *Y*-direction as shown in Fig. 6. The default stiffness of 500 N/m and a set of moderate damping ratios are set to perform the experiment. Figure 10 depicts its estimated deflection responses. It can be seen that with the use of low damping value, the response exhibits an overshoot before settling down to the static deflection value. On the other hand, too high damping makes the end tip to deflect slowly and prevents it from reaching the expected deviation. Hence, the environment may feel the robot be stiffer than its actual value. Note that the effective stiffness is higher than the set value due to the friction in the mechanism. Simulation result under the same conditions is displayed along with. Qualitatively, the response of the real system agrees with that of the simulated one. The desired task space stiffness and damping characteristics is therefore accomplished.

As the currently available method for cross-checking, the vernier height gauge is applied to acquire the actual static end tip deflection from the position measurement before and after applying the weight. The actual deflections are 17.54, 17.38, and 16.26 mm for the damping ratio of 0.2, 0.6, and 1.0 in turn, while the estimated deflections as seen from Fig. 10 are 16.76, 16.71, and 15.01 mm under the default stiffness and 1.0 kg load. Hence the estimation error (less than 2 mm for the 315 mm-long robot, or 1% of the robot size) is small enough for the service robot performing daily tasks and therefore the stationary position may legitimately be used as the replacement for the actual value.

4.2 Tracking Response Subject to External Force. A circular trajectory is generated for the tracking simulation. The starting point is at the right of the robot caused by rotating the shoulder link in the yaw direction for −40 deg from the center of the hemispherical workspace. Then the trajectory is made by rotating the link around the *Z*-axis for a complete round in 6 s. Finally, the desired position is held constant at the starting point for 0.5 s. Task space stiffness and damping ratio are set to their nominal values while the intrinsic motor inertia value is unchanged. Figure 11 displays the tracking result when the robot is subject to the 10 N force acting in the *X*- and *Y*-direction throughout the path, respectively. It is seen that the proposed controller, which is designed for the regulation objective, may be used in the tracking task as well. The end tip follows the reference trajectory closely because of the high stiffness value compared to the magnitude of the applied force. As depicted in the figure, finally the end point deviates from the desired location by 0.6 and 0.86 mm along the *X*- and *Y*-direction for each case in turn.

When the end point is at its final position, nominal task space stiffness matrix expressed in the local frame parallel to the reference frame $\{XYZ\}$ is determined by [27]

$$ {}^{\{XYZ\}}\boldsymbol{K}_{\mathrm{d}} = {}^{\{xyz\}}R_{\{XYZ\}}^{\mathrm{T}}\{xyz\}\boldsymbol{K}_{\mathrm{d}}^{\{xyz\}}R_{\{XYZ\}} \tag{67} $$

where the numerical value of $k_{\mathrm{d}z}$ is selected to be 1000×10^3 N/m as the robot cannot move along the *z*-direction. The associated deflections, determined from

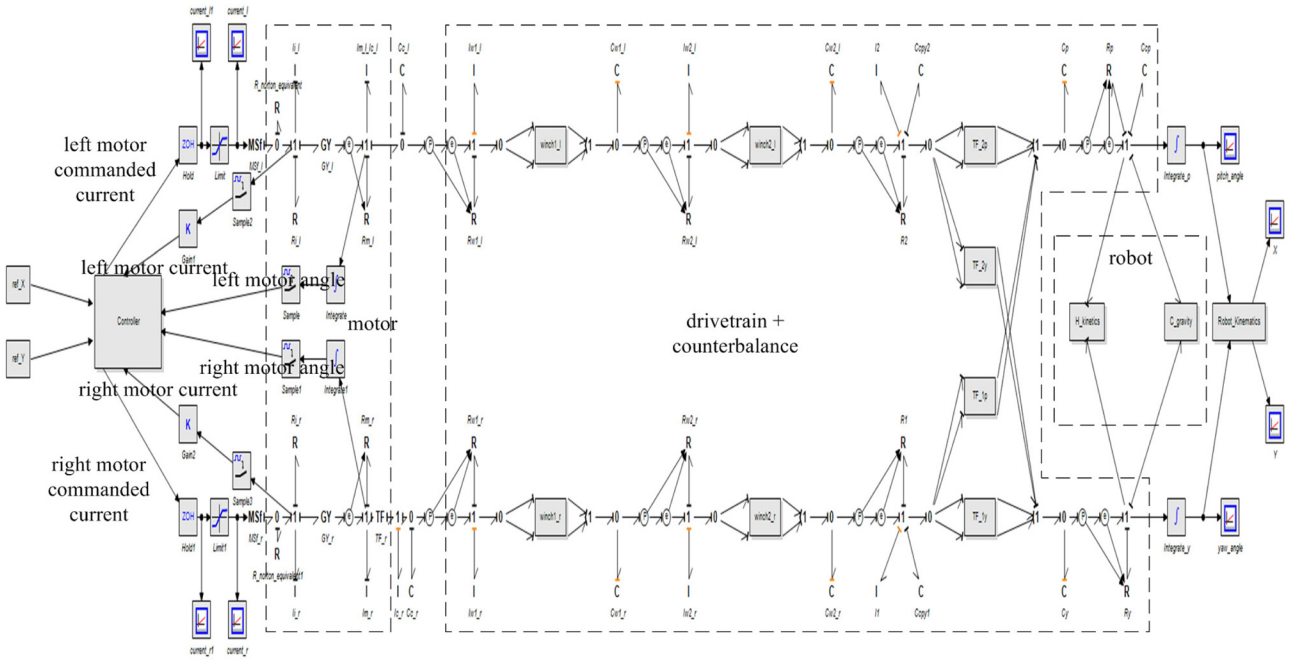

Fig. 8 Detailed bond graph diagram of the 2DOF cable-pulley driven flexible joint robot controlled system. The diagram displays the interconnection of the controller, motor, drivetrain, counterbalance, and robot units. In addition, physical systemlike couplings of the lumped model of the system components ease the understanding of the overall dynamics.

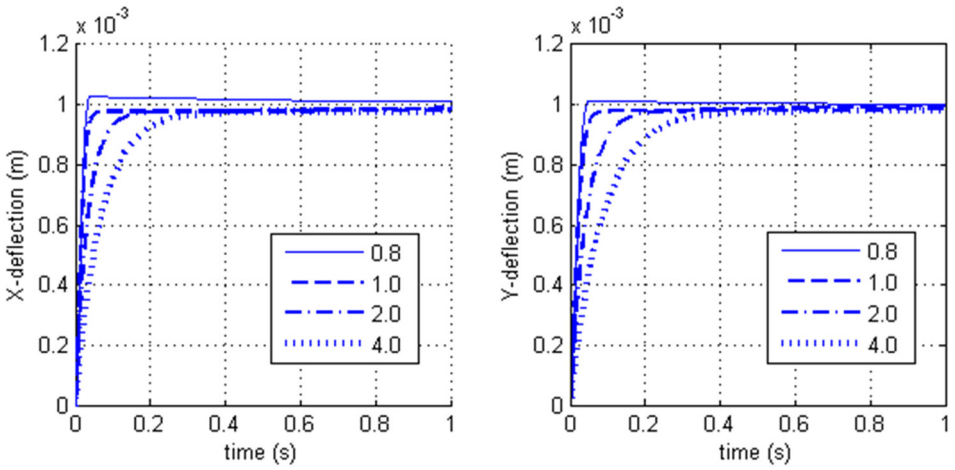

Fig. 9 Simulation of the flexible robot end tip deflection with the nominal stiffness value of 10×10^3 N/m and a set of damping ratios subject to 10 N force in the *X*- and *Y*-direction, respectively

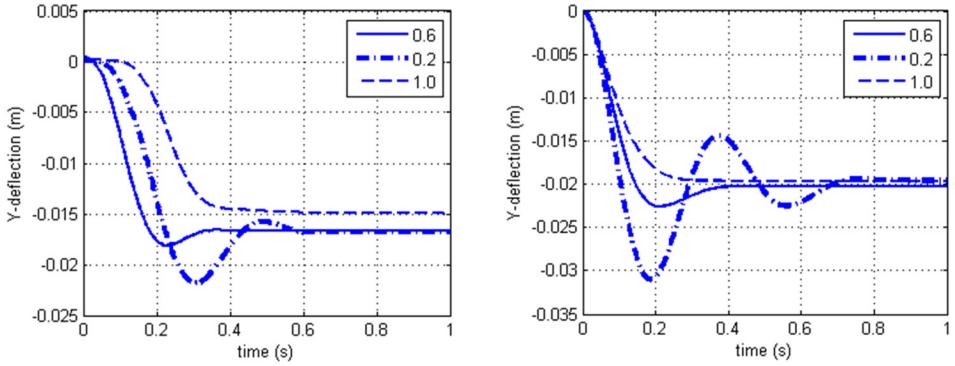

Fig. 10 Deflection responses of the real (left) and simulated (right) robot end tip under 1.0 kg proof mass with the stiffness value of 500 N/m

$$^{\{XYZ\}}\boldsymbol{\delta} = {}^{\{XYZ\}}\boldsymbol{K}_{\mathrm{d}}^{-1}\{XYZ\}\boldsymbol{F} \tag{68}$$

along the direction of the applied force will be 0.59 and 1.0 mm for each case in order. Hence, actual deviations agree with the theoretical values. Therefore, the desired end effector stiffness is achieved. It should be noted that large application of the external force requires large current to keep the robot end tip staying in the track. If such current cannot be supplied, the tracking will fail and the motion will be unstable. For the typical limit ± 10 A of the motor supply current, the external force of 40 N or more will drive the system unstable.

Similar experiment is implemented with the real system. The reference trajectory starts from the center point of the robot workspace. Then it moves leftward by executing the yaw rotation for 40 deg in 3 s and idles for 2 s. Next, the trajectory completes the clockwise circular path around the *Z*-axis in 20 s. After that, it idles for 2 s before traveling rightward back to the starting point and finally staying there for 2 s. Tracking result of the real system with the attached 1.0 kg deadweight is depicted in Fig. 12. Because of much weaker stiffness value of 500 N/m, the actual motion clearly deviates more from the reference path. At the end of the tracking, the tip departs from the workspace center by -17.6 mm along the *Y*-direction. This agrees with the static deflection in Sec. 4.1. The tracking performance, indicating the deflection during the motion, may be computed from the average of the integral of absolute error $I = (1/N)\sum_{k=0}^{N} \|\boldsymbol{x}_k - \boldsymbol{x}_{dk}\|_2$. Its value is 16.8 mm while for the simulated system using the same control parameters this error would be 18.0 mm. The corresponding plot is shown alongside. Therefore, with the proposed controller, the flexible robot system is capable of displaying the desired impedance behavior during the general task execution.

4.3 Motor Inertia Reduction. Nominal reduced motor inertia value is adjusted to investigate its effect to the controlled system. In the experiment, the stiffness of 500 N/m and the damping ratio of 0.6 are used in both the simulated and the real system. First, the robot end tip is regulated at the center of the workspace, which is also its initial position. Three different values of the effective motor inertia are set. Figure 13 displays the current consumption in case of the simulation. When the 150 g cm^2 effective motor inertia (40% reduction) is tuned, the motor current exponentially oscillates during the transient before settling down to a constant value of 0.346 A. On the other hand, if the 248 g cm^2 or the original motor inertia value is used, the current reaches the final value in a first-order system fashion with fast time constant of 11 ms. From the graph, the choice of unmodified inertia yields the cleanest response. However, difference in the motion responses of these three cases is imperceptible due to small motor inertia portion compared to the inertia of the whole drivetrain. It may be concluded that the reduction of a small motor inertia in a small gear ratio system does not improve the dynamics meaningfully. If the inertia is reduced further, the current will be saturated, hitting its limits in a bang–bang manner. In turn, the end point motion starts to exhibit the oscillatory drift from the set value. Current consumption of the real system is shown in

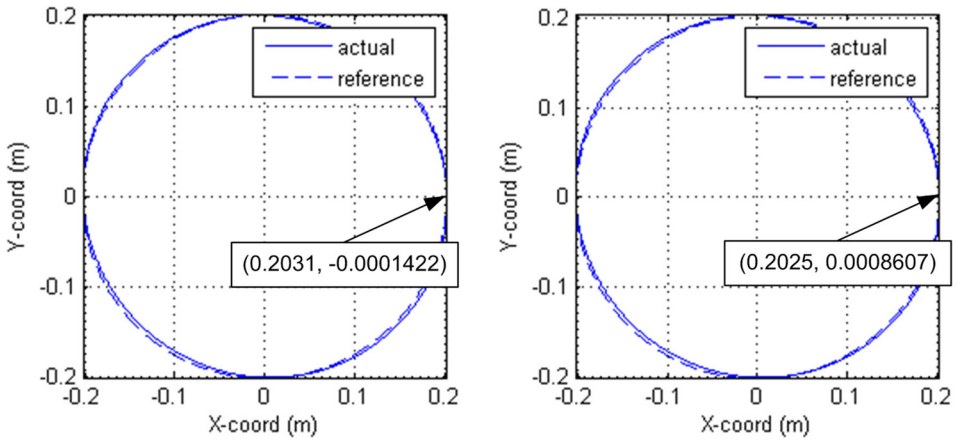

Fig. 11 Tracking simulation with the stiffness of 10×10^3 N/m subject to the 10 N force applied along the *X*- (left) and *Y*- (right) direction

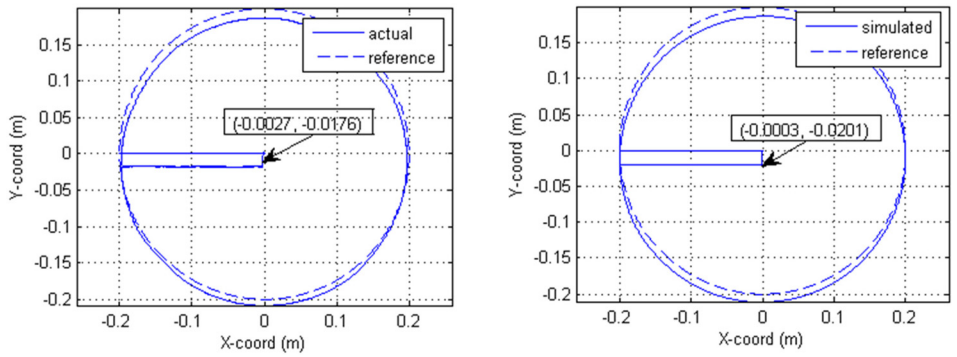

Fig. 12 Circular path tracking with the stiffness of 500 N/m under the 10 N force applied along the *Y*-direction for the real (left) and simulated (right) system

Fig. 14. The result is qualitatively similar; the lower value the effective motor inertia be, the more oscillatory response the motor current is.

Same modulation of the motor inertia is performed when the robot end tip tracks the circular trajectory in Sec. 4.2 with no load. Comparison of the current consumption during the course for different effective motor inertias is depicted in Figs. 15 and 16 for the simulated and real system, respectively. The real system draws larger and more noisy current than the simulated one accountable to the model parameter mismatch and unmodeled dynamics. As observed in the regulation case, the modulated inertia value draws more aggressive and fluctuating current than the natural one. In the tracking case, the lowest motor inertia value that can be reduced is increased to 170 g cm^2 (30% reduction). Percentage of admissible inertia reduction is decreased because larger current is involved in the tracking motion. The real system becomes unstable by exhibiting the oscillatory tracking when the inertia value of 150 g cm^2 is used. Essentially the inertia reduction is equivalent to

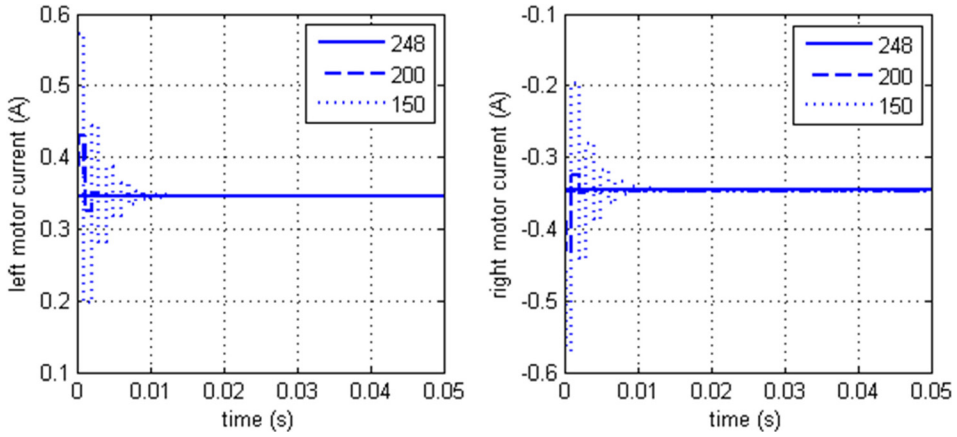

Fig. 13 Current consumption of the simulated system for the regulation task under three different values of the effective motor inertia (150, 200, and 248 g cm^2)

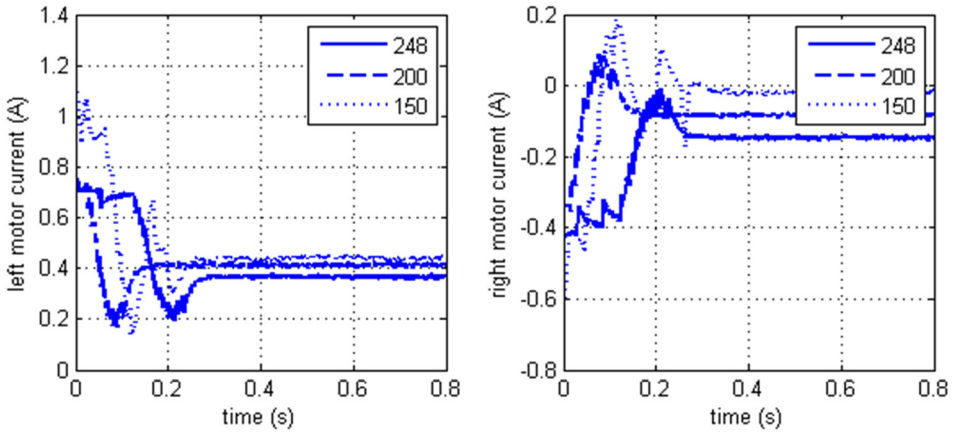

Fig. 14 Current consumption of the real system for the regulation task under three different values of the effective motor inertia (150, 200, and 248 g cm^2)

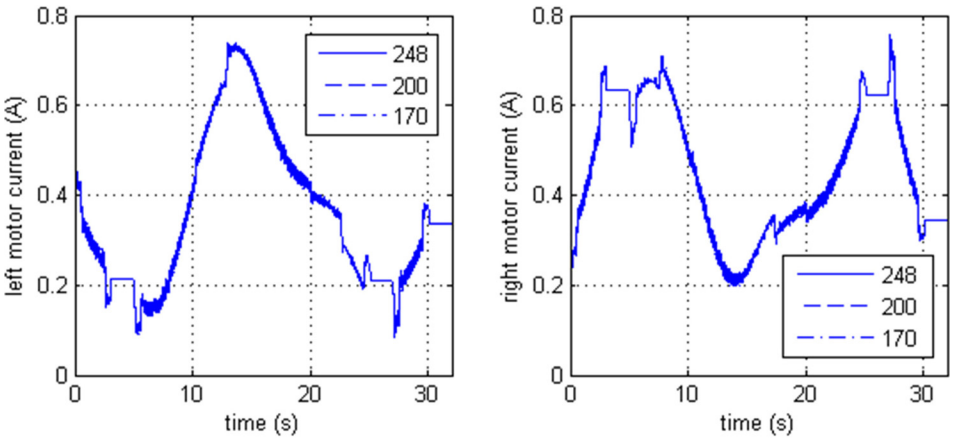

Fig. 15 Current consumption of the simulated system for the circular tracking task under three different values of the effective motor inertia (170, 200, and 248 g cm^2)

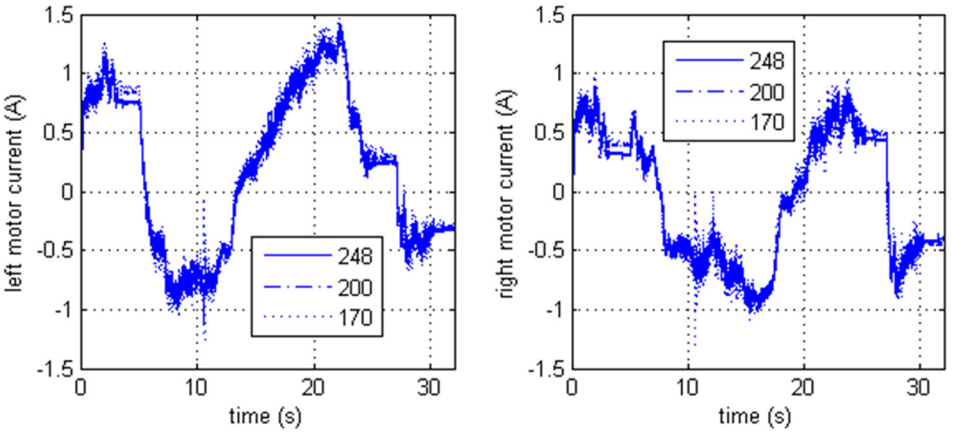

Fig. 16 Current consumption of the real system for the circular tracking task under three different values of the effective motor inertia (170, 200, and 248 g cm^2)

the increase in control loop gain. Therefore, too large inertia reduction makes the system become unstable. If the physical motor inertia value is retained (no inertia reduction), there will be no feedback of the transmitted torque. Implicitly, natural dynamics of the drivetrain is employed. The original system will draw less energy and be more stable than the modulated one, on the price of contaminated desired dynamics. This is evident from the reduction in the tracking error of the real system from 6.7 to 5.4 and to 4.6 mm corresponding to the motor inertia value of 248 (original), 200, and 170 g cm^2.

5 Conclusions

This work develops a task space impedance control of the manipulator driven through the generally multiple stages of the nonlinear softening-spring flexible transmission unit, such as the embodiment of the belt-pulley or cable-pulley transmission. The proposed controller regulates the stiffness and damping of the end effector at the specified position to the desired values based on the only available feedback signal of the motor current and angle. Robot link angle and joint velocity in the traditional impedance control law are substituted by the estimated values computed from the motor angle recursively using the stationary model of the drivetrain and robot system. Furthermore, estimation of the transmitted torque from the motor current is fed back to reduce the motor inertia. Effectively, the motor dynamics distorting the desired transmitted torque is attenuated. Thus, the actual robot characteristics behave closer to the ideal target impedance. Implementation of the control law via the current or the voltage mode of the motor system is discussed. Thorough passivity and stability analysis of the controlled system are presented, in companion with a couple of realistic assumptions. The proofs yield an insight in the underlying energy of the controller that attempts to shape the system PE to the one corresponding to the desired task space compliance.

The controller is applied to a system of 2DOF cable-pulley driven flexible joint robot. It exhibits satisfactory results in standard tasks including trajectory tracking subject to externally applied force. The end effector stiffness matches the desired value in the simulation while the friction force contributes to the higher value in the actual system. Experimenting with several reduced motor inertia values to improve the system dynamics suggests that good practice in mechanical system design at the beginning is preferable to using the torque or current feedback in shaping the inertia to the desired value later. This is to preserve the stability margin of the controlled system.

Overall, the proposed controller is capable of regulating the task space impedance of the manipulator driven through the multistage, constant transmission ratio matrix, nonlinear flexible transmission unit. Examples of applicable systems range from the traditional robots driven through stages of geartrains, flexible belts, or cable-pulley, to novel robots actuated by arrays of piezoelectric or polymer actuators, from which their structures are also created. It is impractical for these systems to gain access to the feedback signals apart from the actuators. This research has demonstrated that the desired impedance may be accomplished using merely the actuator motion and current signals together with the appropriate flexible transmission model. This controller may further be incorporated with the higher-level control system to accomplish the advanced manipulation tasks in general.

Acknowledgment

The author is grateful for valuable comments from the reviewers. This work was generously supported by the grants from the Ratchadaphiseksomphot Endowment Fund of Chulalongkorn University (No. RES560530224-AS), the Thailand Research Fund (Nos. MRG5580227 and MSD56I0018), the ISUZU Research Foundation, and Department of Mechanical Engineering, Chulalongkorn University.

Appendix: Convergence of the Stationary Link Angles Calculation

To determine whether the numerical evaluation of $\boldsymbol{\theta}_{qs}$ in Eq. (14) converges or not, the contraction mapping theorem [24], which guarantees the existence and uniqueness of the fixed point, is employed. Accordingly, to conclude that the recursive evaluation of Eq. (14) converges, it is sufficient to show that the mapping function

$$\boldsymbol{P}(\boldsymbol{q}) = \boldsymbol{T}_{q1}\boldsymbol{\theta}_0 - \boldsymbol{e}_{1q}^{-1}(\boldsymbol{h}(\boldsymbol{q})) \tag{A1}$$

is a contraction mapping.

The distance function

$$\begin{aligned} d_K(\boldsymbol{q}_1,\boldsymbol{q}_2) &= \|\boldsymbol{q}_1-\boldsymbol{q}_2\|_K = \|\boldsymbol{U}(\boldsymbol{q}_1-\boldsymbol{q}_2)\|_2 \\ &= \left[(\boldsymbol{q}_1-\boldsymbol{q}_2)^{\mathrm{T}}\boldsymbol{K}_{1q}(\boldsymbol{q}_1-\boldsymbol{q}_2)\right]^{1/2} \end{aligned} \tag{A2}$$

is defined based on the robot joint effective stiffness matrix $\boldsymbol{K}_{1q}$-weighted vector norm $\|\boldsymbol{q}\|_K = \|\boldsymbol{U}\boldsymbol{q}\|_2$ where $\boldsymbol{K}_{1q} = \boldsymbol{U}^{\mathrm{T}}\boldsymbol{U} = \inf_{\forall\boldsymbol{\delta}\in\mathbb{R}^p}\left(\partial\boldsymbol{e}_{1q}(\boldsymbol{\delta})/\partial\boldsymbol{\delta}\right)$ is the minimum deformation-dependent nonlinear effective stiffness of the drivetrain. The corresponding matrix norm is defined as $\|\boldsymbol{A}\|_K = \left\|\boldsymbol{U}^{-T}\boldsymbol{A}\boldsymbol{U}^{-1}\right\|_2$.

The mapping $\boldsymbol{P}(\boldsymbol{q})$ is a contraction mapping if

$$\|\boldsymbol{P}(\boldsymbol{q}_2)-\boldsymbol{P}(\boldsymbol{q}_1)\|_K \le \rho\|\boldsymbol{q}_2-\boldsymbol{q}_1\|_K \tag{A3}$$

holds for any $\boldsymbol{q}_1$ and $\boldsymbol{q}_2$, with some $\rho \in [0, 1)$. Since the mapping $\boldsymbol{P}(\boldsymbol{q})$, for specific motor angles $\boldsymbol{\theta}_0$, at $\boldsymbol{q}_2$ is related to the value at $\boldsymbol{q}_1$ by

$$\begin{aligned} \boldsymbol{P}(\boldsymbol{q}_2) &= \boldsymbol{P}(\boldsymbol{q}_1) + \int_{\boldsymbol{q}_1}^{\boldsymbol{q}_2}\frac{\partial\boldsymbol{P}(\boldsymbol{q})}{\partial\boldsymbol{q}}d\boldsymbol{q} \\ &= \boldsymbol{P}(\boldsymbol{q}_1) - \int_{\boldsymbol{q}_1}^{\boldsymbol{q}_2}\frac{\partial\boldsymbol{e}_{1q}^{-1}(\boldsymbol{\tau})}{\partial\boldsymbol{\tau}}\Big|_{\boldsymbol{\tau}=\boldsymbol{h}(\boldsymbol{q})}\times\frac{\partial\boldsymbol{h}(\boldsymbol{q})}{\partial\boldsymbol{q}}d\boldsymbol{q} \end{aligned}$$

Manipulate the expression to suit Eq. (A3) as

$$\begin{aligned} \|\boldsymbol{U}(\boldsymbol{P}(\boldsymbol{q}_2)-\boldsymbol{P}(\boldsymbol{q}_1))\|_2 &= \left\| -\int_{\boldsymbol{q}_1}^{\boldsymbol{q}_2}\boldsymbol{U}\frac{\partial\boldsymbol{e}_{1q}^{-1}(\boldsymbol{\tau})}{\partial\boldsymbol{\tau}}\Big|_{\boldsymbol{\tau}=\boldsymbol{h}(\boldsymbol{q})}\times\frac{\partial\boldsymbol{h}(\boldsymbol{q})}{\partial\boldsymbol{q}}d\boldsymbol{q}\right\|_2 \\ &\le \left\|\int_{\boldsymbol{q}_1}^{\boldsymbol{q}_2}\boldsymbol{U}^{-T}\frac{\partial\boldsymbol{h}(\boldsymbol{q})}{\partial\boldsymbol{q}}\boldsymbol{U}^{-1}d\boldsymbol{U}\boldsymbol{q}\right\|_2 \end{aligned}$$

using the fact that the positive definite load-dependent compliance matrix $\left(\partial\boldsymbol{e}_{1q}^{-1}(\boldsymbol{\tau})/\partial\boldsymbol{\tau}\right) \le \boldsymbol{K}_{1q}^{-1} = \boldsymbol{U}^{-1}\boldsymbol{U}^{-T}$. The inequality may be elaborated further so that

$$\|\boldsymbol{P}(\boldsymbol{q}_2)-\boldsymbol{P}(\boldsymbol{q}_1)\|_K \le \sup_{\forall\boldsymbol{q}\in\mathbb{R}^p}\left\|\frac{\partial\boldsymbol{h}(\boldsymbol{q})}{\partial\boldsymbol{q}}\right\|_K\|\boldsymbol{q}_2-\boldsymbol{q}_1\|_K \tag{A4}$$

Consequently, the recursive evaluation of $\boldsymbol{\theta}_{qs}$ in Eq. (14) will converge to the stationary link angles for any starting iteration value if

$$\sup_{\forall\boldsymbol{q}\in\mathbb{R}^p}\left\|\frac{\partial\boldsymbol{h}(\boldsymbol{q})}{\partial\boldsymbol{q}}\right\|_K < 1 = \left\|\boldsymbol{K}_{1q}\right\|_K \tag{A5}$$

Physically, the condition requires the robot joint effective stiffness, or the effective stiffness of the drivetrain, to be larger than the joint stiffness induced by the gravity and the desired compliant forces. This implies the transmission stiffness is capable of preventing the robot "after-the-joint" motion caused by its own weight and the position-mismatch induced compliant force. Hence, the robot structure should be lightweight enough and the desired end effector stiffness should not be set too high, otherwise the effective joint stiffness must be very stiff.

References

[1] Guthart, G. S., and Salisbury, J. K., 2000, "The Intuitive® Telesurgery System: Overview and Application," Proceedings of the IEEE International Conference on Robotics and Automation, San Francisco, California, Apr. 24–28, pp. 618–621.

[2] Wyrobek, K. A., Berger, E. H., Van der Loos, H. F. M., and Salisbury, J. K., 2008, "Towards a Personal Robotics Development Platform: Rationale and Design of an Intrinsically Safe Personal Robot," Proceedings of the IEEE

International Conference on Robotics and Automation, Pasadena, CA, May 19–23, pp. 2165–2170.
[3] Hogan, N., 1985, "Impedance Control: An Approach to Manipulation," ASME J. Dyn. Syst., Meas., Control, **107**(1), pp. 1–24.
[4] Chiaverini, S., Siciliano, B., and Villani, L., 1999, "A Survey of Robot Interaction Control Schemes With Experimental Comparison," IEEE/ASME Trans. Mechatronics, **4**(3), pp. 273–285.
[5] Spong, M., 1987, "Modeling and Control of Elastic Joint Robots," ASME J. Dyn. Syst., Meas., Control, **109**(4), pp. 310–319.
[6] Zollo, L., Siciliano, B., de Luca, A., and Dario, P., 2005, "Compliance Control for an Anthropomorphic Robot With Elastic Joints: Theory and Experiments," ASME J. Dyn. Syst., Meas., Control, **127**(3), pp. 321–328.
[7] Tomei, P., 1991, "A Simple PD Controller for Robots With Elastic Joints," IEEE Trans. Autom. Control, **36**(10), pp. 1208–1213.
[8] Albu-Schaffer, A., Ott, C., Frese, U., and Hirzinger, G., 2003, "Cartesian Impedance Control of Redundant Robots: Recent Results With the DLR-Light-Weight-Arms," Proceedings of the IEEE International Conference on Robotics and Automation, Taipei, Taiwan, Sept. 14–19, pp. 3704–3709.
[9] Ott, C., Albu-Schaffer, A., Kugi, A., and Hirzinger, G., 2008, "On the Passivity-Based Impedance Control of Flexible Joint Robots," IEEE Trans. Rob., **24**(2), pp. 416–429.
[10] Chien, M. C., and Huang, A. C., 2012, "Adaptive Impedance Controller Design for Flexible-Joint Electrically-Driven Robots Without Computation of the Regressor Matrix," Robotica, **30**(1), pp. 133–144.
[11] Pratt, G., and Williamson, M., 1995, "Series Elastic Actuators," Proceedings of the IEEE/RSJ International Conference on Intelligent Robots and Systems, Pittsburg, PA, Aug. 5–9, pp. 399–406.
[12] Zinn, M., Roth, B., Khatib, O., and Salisbury, J. K., 2004, "A New Actuation Approach for Human Friendly Robot Design," Int. J. Rob. Res., **23**(4–5), pp. 379–398.
[13] Wolf, S., and Hirzinger, G., 2008, "A New Variable Stiffness Design: Matching Requirements of the Next Robot Generation," Proceedings of the IEEE International Conference on Robotics and Automation, Pasadena, CA, May 19–23, pp. 1741–1746.
[14] Grebenstein, M., Albu-Schaer, A., Bahls, T., Chalon, M., Eiberger, O., Friedl, W., Gruber, R., Haddadin, S., Hagn, U., Haslinger, R., Hoppner, H., Jorg, S., Nickl, M., Nothhelfer, A., Petit, F., Reill, J., Seitz, N., Wimbock, T., Wolf, S., Wustho, T., and Hirzinger, G., 2011, "The DLR Hand Arm System," Proceedings of the IEEE International Conference on Robotics and Automation, Shanghai, China, May 9–13, pp. 3175–3182.
[15] Xu, Q., 2013, "Adaptive Discrete-Time Sliding Mode Impedance Control of a Piezoelectric Microgripper," IEEE Trans. Rob., **29**(3), pp. 663–673.
[16] Karnopp, D. C., Margolis, D. L., and Rosenberg, R. C., 2006, *System Dynamics: Modeling and Simulation of Mechatronic Systems*, Wiley, New York.
[17] Spong, M. W., 1997, "Underactuated Mechanical Systems," *Control Problems in Robotics and Automation*, Springer-Verlag, London, UK.
[18] Anderson, R. J., 1989, "Passive Computed Torque Algorithms for Robots," Proceedings of the 28th IEEE Conference on Decision and Control, Tampa, FL, Dec. 13–15, pp. 1638–1644.
[19] Meirovitch, L., 2001, *Fundamentals of Vibrations*, McGraw-Hill, New York.
[20] Colgate, J. E., 1988, "The Control of Dynamically Interacting Systems," Ph.D. thesis, MIT, Cambridge, MA.
[21] Marsden, J. E., and West, M., 2001, "Discrete Mechanics and Variational Integrators," Acta Numer., **10**, pp. 357–514.
[22] Slotine, J.-J. E., and Li, W., 1991, *Applied Nonlinear Control*, Prentice-Hall, Englewood Cliffs, NJ.
[23] Koditschek, D., 1984, "Natural Motion for Robot Arms," Proceedings of the 23rd IEEE Conference on Decision and Control, Las Vegas, NV, Dec. 12–14, pp. 733–735.
[24] Khalil, H. K., 2001, *Nonlinear Systems*, 3rd ed., Prentice-Hall, Englewood Cliffs, NJ.
[25] Diolaiti, N., Niemeyer, G., Barbagli, F., and Salisbury, J. K., 2006, "Stability of Haptic Rendering: Discretization, Quantization, Time Delay, and Coulomb Effects," IEEE Trans. Rob., **22**(2), pp. 256–268.
[26] 20-sim Simulation Program, Controllab Products B.V., http://www.20sim.com
[27] Loncaric, J., 1987, "Normal Forms of Stiffness and Compliance Matrices," IEEE J. Rob. Autom., **3**(6), pp. 567–572.

International Journal of Advanced Robotic Systems

OPEN ACCESS
ARTICLE

Modelling and Control of the Multi-stage Cable Pulley-driven Flexible-joint Robot

Regular Paper

Phongsaen Pitakwatchara[1,*]

1 Department of Mechanical Engineering, Faculty of Engineering, Chulalongkorn University, Bangkok, Thailand
* Corresponding author E-mail: phongsaen.p@chula.ac.th

Received 7 Oct 2013; Accepted 20 May 2014

DOI: 10.5772/58697

Abstract This work is concerned with the task space impedance control of a robot driven through a multi-stage nonlinear flexible transmission system. Specifically, a two degrees-of-freedom cable pulley-driven flexible-joint robot is considered. Realistic modelling of the system is developed within the bond graph modelling framework. The model captures the nonlinear compliance behaviour of the multi-stage cable pulley transmission system, the spring effect of the augmented counterbalancing mechanism, the major loss throughout the system elements, and the typical inertial dynamics of the robot. Next, a task space impedance controller based on limited information about the angle and the current of the motors is designed. The motor current is used to infer the transmitted torque, by which the motor inertia may be modulated. The motor angle is employed to estimate the stationary distal robot link angle and the robot joint velocity. They are used in the controller to generate the desired damping force and to shape the potential energy of the flexible joint robot system to the desired configuration. Simulation and experimental results of the controlled system signify the competency of the proposed control law.

Keywords Cable Pulley-driven Robot, Multi-stage Flexible Transmission System, Task Space Impedance Control

1. Introduction

Impedance plays an important role in the performance of tasks by manipulators that require interaction with the environment [1]. For example, a laparoscopic surgical robotic system, such as [2], typically works inside the human abdomen, packed with vital organs of which their precise location and geometry are not known. The motion of the forceps is controlled and supervised by a skilful surgeon. Nevertheless, erroneous motion is possible, as a result of which the surrounding organs may be injured. If the forceps are equipped with proper compliance, the severity of wounds can be mitigated. As another example, a service robot system, such as [3], among the others, is able to perform general daily tasks. It is inevitable that such a robot has limited and imprecise information about the environment it interacts with. To successfully implement tasks, the robot must possess appropriate compliance characteristics. A specific impedance model implemented through the mass, spring and damping parameters is popular among the more general functions between the motion and force variables. This representation is intuitive to the human operator and it may be used to shape the behaviour of wheeled inverted pendulum vehicles for better riding experiences [4].

Many efforts have been made in shaping robot compliance to the desired values. However, only a few works have attempted to control the impedance of flexible joint robots. [5] presented a simplified model of a flexible joint robot on which most of the proposed controllers, such as [6] and [7], are based. A tracking impedance controller for the DLR-II arm [8] was proposed using singular perturbation analysis. In contrast, [9] applied a passivity analysis to design a robust and stable impedance control law. Recently, an adaptive impedance controller based on the function approximation technique (FAT) [10] was applied to a flexible joint robot system with motor dynamics included. Impedance behaviour may also be acquired indirectly through admittance control by generating the reference motion from the interaction force error. This idea is applied using an adaptive fuzzy control technique to manipulate the non-rigid environment of the multiple mobile manipulators [11].

The contribution of this research is a passive task space impedance controller for a flexible joint robot system driven through multi-stage nonlinear flexible transmission based only on the motor angle signal. Motor current feedback may optionally be used to improve the system response time. In particular, an embodiment of a prototypical two degrees-of-freedom (DOF) cable pulley-driven flexible joint robot is investigated. Section 2 develops the detailed model of the robot, its counterbalance and its flexible drivetrain subsystems. A model of the complete system is then obtained by integrating these together using the bond graph framework. Based on this model and the available feedback signals of the motor current and angle, in section 3 a task space impedance controller is designed to accomplish the desired viscoelastic behaviour at the specified set point. The stability of the closed-loop system is proven. In order to validate the effectiveness of the control law, various simulations and experiments of the system are conducted and the results are discussed accordingly in section 4. Finally, section 5 concludes the study.

2. System Modelling

A two-DOF cable pulley-driven flexible joint robot, shown in Figure 1, is constructed as a prototype serving as a fundamental study of the multi-stage cable pulley-driven robot class, which will further be employed in developing the entire arm of our ongoing service robot project. It comprises three subsystems, namely a rigid robot, a flexible transmission and a counterbalance. The robot shoulder link is capable of moving in the pitch and yaw directions, emulating the principal motion performed by the human shoulder. Generalized coordinates describing the position of its end-tip may naturally be chosen as the pitch and yaw angles, denoted as θ_p and θ_y respectively.

Figure 2 depicts the winch and pulley arrangement of the robot's multi-stage transmission subsystem. Starting from the input side, the motor axle is coupled to winch#1, which then drives winch#2 through the wrapped cables. Winch#2 in turn drives pulley#1 (for the right winch) and pulley#2 (for the left winch). Together with pulley#3, these pulleys form the differential mechanism which produces

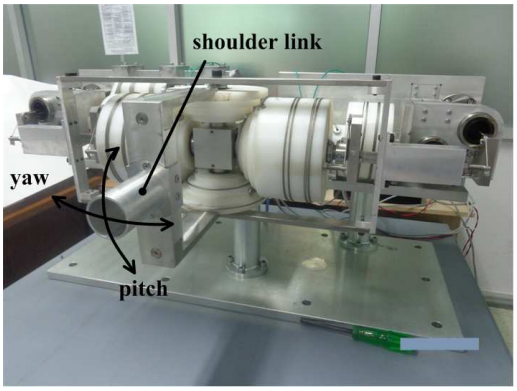

Figure 1. A two-DOF multi-stage cable pulley-driven flexible joint robot

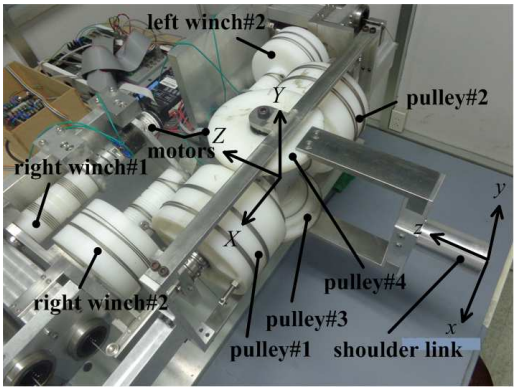

Figure 2. Winch and pulley arrangement in the drivetrain unit of the flexible joint robot. Left winch#1 is occluded.

the rotational motion of the output shoulder link around two mutually perpendicular axes, causing the motion of the shoulder link end-tip in the pitch and yaw directions. A differential mechanism is implemented in this work through the cables and stepped pulleys. In addition, the additional pulley#4 is not attached to any cable - its purpose is to counter pulley#3 and to strengthen the structure.

Furthermore, the robot is equipped with a patented (pending) counterbalancing mechanism [12], invented to reduce the amount of torque commonly supplied by the motors to sustain weight and, hence, to improve the safety of the robot. Basically, the motions of pulley#1 and pulley#2 are transmitted via the cable routing to elongate a set of springs. With an appropriate spring stiffness selected, the generated torque can match the configuration-dependent gravitational torque. Such considerations may apply from the viewpoint of maintaining the total potential energy of the system.

2.1. The Robot System

Referring to Figure 2, the position vector of the shoulder link end-point relative to the origin of $\{XYZ\}$ described in $\{xyz\}$ is ${}^{\{xyz\}}\boldsymbol{r} = \begin{bmatrix} 0 & 0 & -l_o \end{bmatrix}^T$, for which l_o is the shoulder link length measured from the centre of rotation. Besides, the relative rotation between $\{xyz\}$ and $\{XYZ\}$ is described by the rotation matrix ${}^{\{XYZ\}}R_{\{xyz\}} = R_{x,\theta_p} R_{y,\theta_y}$. Therefore, the position vector $\boldsymbol{r}$ described in the reference frame $\{XYZ\}$ is:

$$
\begin{aligned}
{}^{\{XYZ\}}\boldsymbol{r} &= {}^{\{XYZ\}}R_{\{xyz\}}\,{}^{\{xyz\}}\boldsymbol{r} \\
&= \begin{bmatrix} -l_o s_y & l_o s_p c_y & -l_o c_p c_y \end{bmatrix}^T . \qquad (1)
\end{aligned}
$$

For the spherical configuration of the robot, the velocity of the end point may be determined simply from the fact that its motion comprises pure rotation around the origin of the fixed frame $\{XYZ\}$. If $\boldsymbol{\omega}$ is the link angular velocity, the end-point velocity expressed in the moving frame $\{xyz\}$ is ${}^{\{xyz\}}\boldsymbol{v}_e = \boldsymbol{\omega} \times \boldsymbol{r} = \begin{bmatrix} -l_o\dot{\theta}_y & l_o\dot{\theta}_p c_y & 0 \end{bmatrix}^T$. Consequently, the Jacobian matrix represented in $\{xyz\}$ becomes:

$$
{}^{\{xyz\}}J = \begin{bmatrix} 0 & -l_o \\ l_o c_y & 0 \\ 0 & 0 \end{bmatrix} . \qquad (2)
$$

The main moving parts of the robot are pulley#3, pulley#4 and the output shoulder link. For convenience, the rectangular frame of the counterbalancing mechanism subject to the pitch motion will be included as well. These components may be grouped into two categories: one undergoing pitching motion alone, and the other undergoing a composite pitching and yawing motion. CAD drawings of these two collections are depicted in Figure 3. Their related parameters will thus be subscripted as 'p' and 'py', respectively. The reference and moving coordinate frames employed are the same as those shown in Figure 2.

For the first collection undergoing pitching motion, its compound centre of gravity (C.G.) is evaluated by the CAD program to be at ${}^{\{xyz\}}(\boldsymbol{r}_G)_p = \begin{bmatrix} 0 & 0 & r_{z_p} \end{bmatrix}^T$ relative to the origin of $\{XYZ\}$. Because its motion is a rotation around the fixed pitch axis with the angular velocity ${}^{\{xyz\}}\boldsymbol{\omega}_p = \begin{bmatrix} \dot{\theta}_p & 0 & 0 \end{bmatrix}^T$, the associated kinetic energy may be determined as:

$$
T_p = \frac{1}{2}\boldsymbol{\omega}_p^T \boldsymbol{I}_{o_p}\boldsymbol{\omega}_p = \frac{1}{2} I_{xx_p}\dot{\theta}_p^2, \qquad (3)
$$

where $\boldsymbol{I}_{o_p}$ is the pitch-collection inertia matrix, with the inertia around the x-x axis denoted by I_{xx_p}. The potential energy may be derived simply as:

$$
V_p = -m_p \boldsymbol{g} \cdot (\boldsymbol{r}_G)_p = -m_p g r_{z_p} s_p, \qquad (4)
$$

for which m_p is the mass of this collection and $\boldsymbol{g}$ is the vector of gravitational acceleration.

Similarly, the kinetic and potential energy of the pitch/yaw collection may be derived as follows. From the geometry, the compound C.G. location is at ${}^{\{xyz\}}(\boldsymbol{r}_G)_{py} = \begin{bmatrix} 0 & 0 & r_{z_{py}} \end{bmatrix}^T$. However, its angular velocity is due to both the pitch and yaw motions. In the body's fixed frame, this may be written as ${}^{\{xyz\}}\boldsymbol{\omega}_{py} = \begin{bmatrix} \dot{\theta}_p c_y & \dot{\theta}_y & \dot{\theta}_p s_y \end{bmatrix}^T$. Therefore, the kinetic energy expression, with some simplification, may be expressed as:

$$
\begin{aligned}
T_{py} &= \frac{1}{2}\boldsymbol{\omega}_{py}^T \boldsymbol{I}_{o_{py}}\boldsymbol{\omega}_{py} \\
&= \frac{1}{2}\left[\left(I_{xx_{py}} c_y^2 + I_{zz_{py}} s_y^2 \right)\dot{\theta}_p^2 + I_{yy_{py}}\dot{\theta}_y^2 \right], \qquad (5)
\end{aligned}
$$

for which the careful design of the shape of the parts makes the off-diagonal elements of the inertia matrix $\boldsymbol{I}_{o_{py}}$ negligible. In other words, $\boldsymbol{I}_{o_{py}} = \text{diag}\left(I_{xx_{py}}, I_{yy_{py}}, I_{zz_{py}} \right)$. The potential energy may be calculated as:

$$
V_{py} = -m_{py}\boldsymbol{g} \cdot (\boldsymbol{r}_G)_{py} = -m_{py} g r_{z_{py}} s_p c_y, \qquad (6)
$$

with m_{py} denoting the mass of this collection. The parameter values of the robot are summarized in Table 1.

2.2. The Counterbalance System

The counterbalancing mechanism contributes to the robot dynamics by maintaining the constant potential energy of the augmented system. The mechanism may be divided into two parts. Figure 4 illustrates a part of the mechanism [12] where the cable (20) is routed through the set of idlers (21-24) to convey the tension force from the spring (12) to the stud (18) embedded in pulley#2. The generated torque will counter the gravitational torque of the pitch/yaw collection. The other simple part of the mechanism accounts for the pitch-collection. Note that, due to the (generally) non-zero initial tension of the spring, the cable routing over non-zero radius idlers and the travelling limitation hit of the mechanism, the compensator departs from theory. Nevertheless, the current consumption of the motor in holding the robot statically is reduced dramatically; the current is now bounded within the band of ± 0.1 [A] as compared with the average value of 1.5 [A], when there is no assistance from the counterbalance.

The force and induced moment produced by the mechanism may be analysed indirectly via the spring potential energy of the counterbalance. The cabling of the mechanism enforces the elongated length of the springs in relation to the robot configuration through its generalized coordinates θ_p and θ_y. For the springs accounting for the gravity force of the pitch and pitch/yaw collection, their elongations δ_p and δ_{py} are:

$$
\delta_p = 2h_p\sqrt{2\left[1 - \sin\left(\theta_p + \frac{25\pi}{180}\right)\right]} \qquad (7)
$$

$$
\begin{aligned}
\delta_{py} = h_{py}\Bigg[&\sqrt{2\left[1 - s\left(\theta_p + \theta_y\right)\right]} \\
&+ \sqrt{2\left[1 - s\left(\theta_p - \theta_y\right)\right]} \Bigg], \qquad (8)
\end{aligned}
$$

where h_p and h_{py} are the shortest distance of the cable terminal at the rectangular frame and at pulley#1/#2 measured from the X-X axis, respectively. The constant angle of $\frac{25\pi}{180}$ [rad] reflects the safety limit of the mechanism at 65°. Consequently, the potential energy of the counterbalance for the pitch- and pitch/yaw collection may be determined from the area under the force-elongation linear relationship:

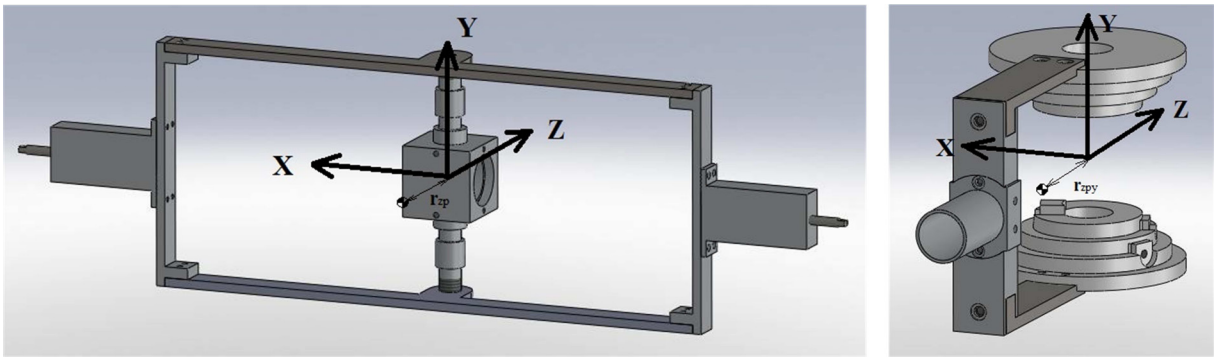

Figure 3. (left) Collection of mechanical parts undergoing pitching motion. (right) Collection of mechanical parts undergoing pitching and yawing motion.

robot parameter	value
shoulder link length, l_o	0.315 [m]
z-coordinate of the C.G. of the pitch-collection, r_{z_p}	-0.0288 [m]
pitch-collection inertia about C.G. along x-x axis, I_{xx_p}	276.0 [kg $\cdot$ cm^2]
mas of the pitch-collection, m_p	3.55 [kg]
z-coordinate of the C.G. of the pitch/yaw collection, $r_{z_{py}}$	-0.1202 [m]
pitch/yaw collection inertia about C.G. along x-x axis, $I_{xx_{py}}$	932.0 [kg $\cdot$ cm^2]
pitch/yaw collection inertia about C.G. along y-y axis, $I_{yy_{py}}$	761.5 [kg $\cdot$ cm^2]
pitch/yaw collection inertia about C.G. along z-z axis, $I_{zz_{py}}$	205.2 [kg $\cdot$ cm^2]
mass of the pitch/yaw collection, m_{py}	3.07 [kg]

Table 1. Robot parameter values

$$V_{C_p} = 2k_p h_p^2 \left[1 - \sin\left(\theta_p + \frac{25\pi}{180}\right)\right] + 2h_p T_{i_p} \sqrt{2\left[1 - \sin\left(\theta_p + \frac{25\pi}{180}\right)\right]} \tag{9}$$

$$V_{C_{py}} = 2k_{py} h_{py}^2 \left(1 - s_p c_y\right) + h_{py} T_{i_{py}} \left[\sqrt{2\left[1 - s\left(\theta_p + \theta_y\right)\right]} + \sqrt{2\left[1 - s\left(\theta_p - \theta_y\right)\right]}\right], \tag{10}$$

in which T_{i_p} and $T_{i_{py}}$ are the respective spring initial tensions, and k_p and k_{py} are the spring stiffnesses designed based on the perfect gravitational torque cancellation of the ideal counterbalancing mechanism:

$$k_p = \frac{m_p g r_{z_p}}{2h_p^2} \tag{11}$$

$$k_{py} = \frac{m_{py} g r_{z_{py}}}{2h_{py}^2}. \tag{12}$$

Additionally, the friction force F_f developed at the linear bushing, guiding the stroke of the spring, should be taken into account to provide for realistic simulation. It is modelled simply by a nonlinear switching function:

$$F_f = \begin{cases} -\mathrm{sgn}\,(v)\, F_m, & v \neq 0 \\ 0, & v = 0, \end{cases} \tag{13}$$

where v is the signed velocity of the slider and F_m is the constant sliding friction limit value. In this regard, the friction force is comparable to the extra initial dynamic tension force of the spring. Table 2 collects all the parameter values of the counterbalancing mechanism.

According to the above energy analysis, the Lagrangian of the robot plus its counterbalances may be determined as:

$$L\left(\boldsymbol{q}, \dot{\boldsymbol{q}}\right) = T_p + T_{py} - V_p - V_{py} - V_{C_p} - V_{C_{py}}, \tag{14}$$

where $\boldsymbol{q} = \begin{bmatrix}\theta_p & \theta_y\end{bmatrix}^T$ denotes the vector of the robot's generalized coordinates. Applying and evaluating the Lagrangian formulation along $\boldsymbol{q}$, the robot dynamics may be manipulated into the modified standard form of its joint space model, which includes the frictional torque $\boldsymbol{f}$:

$$\boldsymbol{M}\left(\boldsymbol{q}\right)\ddot{\boldsymbol{q}} + \boldsymbol{C}\left(\boldsymbol{q}, \dot{\boldsymbol{q}}\right)\dot{\boldsymbol{q}} + \boldsymbol{f} + \boldsymbol{g}\left(\boldsymbol{q}\right) = \boldsymbol{\tau}_{dr} + \boldsymbol{\tau}_{ext}, \tag{15}$$

with:

$$\boldsymbol{M}\left(\boldsymbol{q}\right) = \begin{bmatrix} I_{xx_{py}} c_y^2 + I_{zz_{py}} s_y^2 + I_{xx_p} & 0 \\ 0 & I_{yy_{py}} \end{bmatrix}$$

$$\boldsymbol{C}\left(\boldsymbol{q}, \dot{\boldsymbol{q}}\right) = \begin{bmatrix} \left(I_{zz_{py}} - I_{xx_{py}}\right) s_y c_y \dot{\theta}_y & \left(I_{zz_{py}} - I_{xx_{py}}\right) s_y c_y \dot{\theta}_p \\ \left(I_{xx_{py}} - I_{zz_{py}}\right) s_y c_y \dot{\theta}_p & 0 \end{bmatrix}$$

$$\boldsymbol{f}\left(\boldsymbol{q}, \dot{\boldsymbol{q}}\right) = \begin{bmatrix} \frac{2h_p \mathrm{sgn}\left(\dot{\theta}_p\right) F_m \cos\left(\theta_p + \frac{25\pi}{180}\right)}{\sqrt{2\left[1 - \sin\left(\theta_p + \frac{25\pi}{180}\right)\right]}} + \frac{h_{py}\mathrm{sgn}\left(\dot{\theta}_p + \dot{\theta}_y\right) F_m c\left(\theta_p + \theta_y\right)}{\sqrt{2\left[1 - s\left(\theta_p + \theta_y\right)\right]}} + \frac{h_{py}\mathrm{sgn}\left(\dot{\theta}_p - \dot{\theta}_y\right) F_m c\left(\theta_p - \theta_y\right)}{\sqrt{2\left[1 - s\left(\theta_p - \theta_y\right)\right]}} \\ \frac{h_{py}\mathrm{sgn}\left(\dot{\theta}_p + \dot{\theta}_y\right) F_m c\left(\theta_p + \theta_y\right)}{\sqrt{2\left[1 - s\left(\theta_p + \theta_y\right)\right]}} - \frac{h_{py}\mathrm{sgn}\left(\dot{\theta}_p - \dot{\theta}_y\right) F_m c\left(\theta_p - \theta_y\right)}{\sqrt{2\left[1 - s\left(\theta_p - \theta_y\right)\right]}} \end{bmatrix}. \tag{16}$$

In Eq. 15, $\boldsymbol{g}(\boldsymbol{q})$ is the resulting torque vector of the robot gravity torque compensated by the counterbalancing spring torque. Their components along the generalized coordinates θ_p and θ_y are:

$$g_p(\boldsymbol{q}) = -m_p g r_{z_p} c_p - 2k_p h_p^2 \cos\left(\frac{25\pi}{180}\right) c_p + 2k_p h_p^2 \sin\left(\frac{25\pi}{180}\right) s_p - \frac{2h_p T_{i_p} \cos\left(\theta_p + \frac{25\pi}{180}\right)}{\sqrt{2\left[1 - \sin\left(\theta_p + \frac{25\pi}{180}\right)\right]}}$$
$$- m_{py} g r_{z_{py}} c_p c_y - 2k_{py} h_{py}^2 c_p c_y - \frac{h_{py} T_{i_{py}} c(\theta_p + \theta_y)}{\sqrt{2\left[1 - s(\theta_p + \theta_y)\right]}} - \frac{h_{py} T_{i_{py}} c(\theta_p - \theta_y)}{\sqrt{2\left[1 - s(\theta_p - \theta_y)\right]}} \quad (17)$$

$$g_y(\boldsymbol{q}) = m_{py} g r_{z_{py}} s_p s_y + 2k_{py} h_{py}^2 s_p s_y - \frac{h_{py} T_{i_{py}} c(\theta_p + \theta_y)}{\sqrt{2\left[1 - s(\theta_p + \theta_y)\right]}} + \frac{h_{py} T_{i_{py}} c(\theta_p - \theta_y)}{\sqrt{2\left[1 - s(\theta_p - \theta_y)\right]}}. \quad (18)$$

The external force caused by the robot interacting with the environment at the end of the shoulder link may naturally be described in the task space frame as ${}^{\{xyz\}}\boldsymbol{F}_{ext} = \begin{bmatrix} F_x & F_y \end{bmatrix}^T$. Therefore, the torque vector $\boldsymbol{\tau}_{ext}$ reflected to the robot's generalized coordinates is determined by:

$$\boldsymbol{\tau}_{ext} = {}^{\{xyz\}}J^{T\{xyz\}}\boldsymbol{F}_{ext} = \begin{bmatrix} F_y l_o c_y \\ -F_x l_o \end{bmatrix}, \quad (19)$$

as can also be verified by inspecting the robot geometry directly. Finally, $\boldsymbol{\tau}_{dr}$ is the actuated generalized torque vector from the transmission unit.

2.3. The Transmission System

The pulley and winch arrangement of the multi-stage flexible transmission is illustrated in Figure 2. It can be seen that the drivetrain is designed to have four stages for compactness. In the 1st-stage, the motor is connected to winch#1 via the disk coupling. For the 2nd- and 3rd-stages, the transmission is realized by the wound cables around winch#1-winch#2 and winch#2-pulley#1/2 respectively. The 4th-stage connects the drivetrain unit to the robot via the cable pulley differential mechanism.

Let θ_m, θ_w, θ_1, θ_2, θ_p and θ_y be the angular positions of the motor, winch, pulley#1, pulley#2 and the pitch and yaw angles of the shoulder link, respectively. The structural interconnection between these parts by the cables poses the following kinematic constraints:

$$\begin{aligned} \dot{\theta}_{w1r} &= -\dot{\theta}_{mr} & \dot{\theta}_{w1l} &= \dot{\theta}_{ml} \\ \dot{\theta}_{w2r} &= n_{2r}\dot{\theta}_{w1r} & \dot{\theta}_{w2l} &= n_{2l}\dot{\theta}_{w1l} \\ \dot{\theta}_1 &= n_{3r}\dot{\theta}_{w2r} & \dot{\theta}_2 &= n_{3l}\dot{\theta}_{w2l} \\ \dot{\theta}_p &= \frac{1}{2}(\dot{\theta}_1 + \dot{\theta}_2) & \dot{\theta}_y &= \frac{1}{2}(\dot{\theta}_1 - \dot{\theta}_2). \end{aligned} \quad (20)$$

This particular system is designed such that the transmission ratio, n, at the 2nd- and 3rd-stages are all $\frac{1}{3}$.

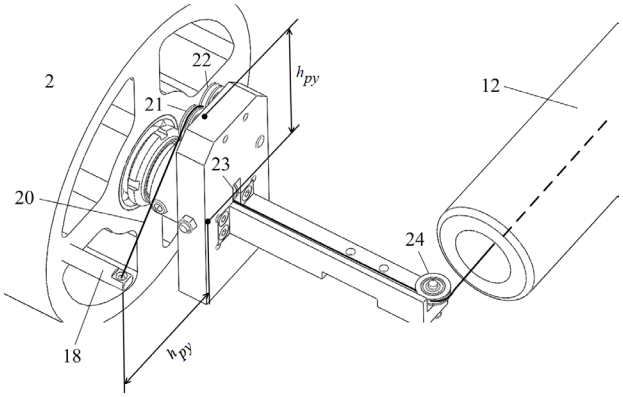

Figure 4. Counterbalancing mechanism for the pitch/yaw collection of the robot [12]. The shortest distance of the cable terminal at pulley#2 measured from the X-X axis, h_{py}, is depicted.

Since the mechanism employs the cables as the means for transmitting power, its inherent compliance characteristics should be taken into account. Assuming the cables have been securely wrapped around the pulleys with proper pretension, such that the total slippage between the cable and the pulley groove over the circuit is negligible, the explicit torque-angle deflection equation of a stiff simple cable pulley drive unit may be determined [13] as:

$$\theta = \frac{T_o}{EA\mu_{\text{eff}}}\left[\left(\frac{me^m}{e^m - 1} - 1\right)(1 + GF) - \log\frac{me^m}{e^m - 1}\right] \quad (21)$$

where the cable, with a Young modulus E and an effective cross-sectional area A, has been pre-tensioned to T_o. $m = \frac{M}{rT_o}$ is the dimensionless torque of the loaded torque M applied at the loaded pulley of radius r. μ_{eff} is the effective coefficient of friction. Finally, $GF = \frac{L\mu_{\text{eff}}}{r}$ is the geometric friction number in which L is the cable length of the unwrapped portion on each side. The current drivetrain is designed so that it possesses a low GF value, indicating stiff but softening spring transmission characteristics. Equation 21 governs the compliance behaviour for the 2nd- and 3rd-stages. The numerical values of the pertinent parameters from the design are tabulated in Table 3.

The compliance analysis in [13] can be extended to handle the cable pulley differential mechanism at the 4th-stage of the drivetrain. As a result, the torque-angle deflection equation along the pitch or yaw DOF may be expressed as:

$$\theta = \frac{T_o}{EA\mu_{\text{eff}}}\left[\left(\frac{me^{m/2}}{2\left(e^{m/2} - 1\right)} - 1\right)(1 + GF) - \log\frac{me^{m/2}}{2\left(e^{m/2} - 1\right)}\right]. \quad (22)$$

counterbalance parameter	value
spring stiffness for the pitch collection counterbalance, k_p	311.88 [N/m]
distance between the cable terminal for the pitch collection counterbalance and the X-X axis, h_p	0.04 [m]
spring initial tension for the pitch collection counterbalance, T_{i_p}	5.10 [N]
spring stiffness for the pitch/yaw collection counterbalance, k_{py}	426.9 [N/m]
distance between the cable terminal for the pitch/yaw collection counterbalance and the X-X axis, h_{py}	0.06 [m]
spring initial tension for the pitch/yaw collection counterbalance, $T_{i_{py}}$	7.94 [N]
sliding friction limit, F_m	0.005 [N]

Table 2. Parameter values of the counterbalancing mechanism

parameter	2^{nd}-stage	3^{rd}-stage	4^{th}-stage
pretension, T_o	74 [N]	185 [N]	238 [N]
Young modulus, E	200 [GPa]	200 [GPa]	200 [GPa]
cable cross-sectional area, A	1.767 [mm^2]	3.534 [mm^2]	7.069 [mm^2]
effective coeff. friction, μ_{eff}	0.1	0.1	0.1
loaded pulley radius, r	67.5 [mm]	81.0 [mm]	63 [mm]
geometric friction number, GF	0.045	0.041	0

Table 3. Numerical values of the parameters for the flexible cable pulley-driven transmission system

In this case, m is the dimensionless torque of the loaded torque M applied along the pitch or yaw directions. Since there is no unwrapped segment of the cable for the differential drive unit, effectively $GF = 0$. For the 1^{st}-stage, the transmission compliance is simply the inverse of the coupling constant stiffness value of 5700 [N/m] from the data sheet.

Major loss in transmission happens at the bearing units. The complexity of the friction phenomenon at the support leads us to propose a friction model as a combination of the simple Coulomb's friction torque when the relative velocity of the mating surfaces is virtually zero, and the empirical formulation of the frictional torque for the standard sealed deep-grooved ball bearing [14] when relative motion occurs. Mathematically:

$$M_f = \begin{cases} \text{sat}\,(M_{\text{in}})\,, & \omega = 0 \text{ and } M_{\min} \leq \text{sat}\,(M_{\text{in}}) \leq M_{\max} \\ 35812.5\frac{Hd}{nr}, & \omega \neq 0, \end{cases} \tag{23}$$

where M_{in} [Nmm] and H [kW] are the torque and the power transmitted through the cable pulley mechanism, M_f [Nmm] is the developed frictional torque, d [mm] r [mm] is the shaft diameter and the pulley radius, and n [rpm] is the angular velocity of the pulley. $M_{\min}$ and $M_{\max}$ limit the maximum amount of power loss that can occur at the bearing. Their typical values, experimentally chosen, are $M_{\min} = -10$ [Nmm] and $M_{\max} = 10$ [Nmm]. Table 4 depicts the designed values of the shaft diameter and pulley radius. Moreover, see the bond graph diagram of the system in Figure 5 for the location of the bearing losses in the transmission system.

The inertias of the rotational parts in the transmission unit are summarized in Table 5. Hence, the complete dynamics of the drivetrain may now be determined by combining the inertial, the dissipating and the elastic torques according to the system's kinematic configuration, together with the externally applied torque of the motors. Unfortunately, the explicit form of the equations for motion is barely achieved due to the inversion problem of the complicated nonlinear deformation functions in Eqs. 21 and 22. This, however, does not affect the simulation or the control law implementation.

2.4. The Complete System

A realistic model of the two-DOF multi-stage cable pulley-driven flexible joint robot which captures its important behaviours may be acquired through the bond graph technique [15]. With this approach, the system model is constructed by identifying the governing equations of the subsystems, comprising the bond graph basic elements of one-port inertance, compliance, resistance and two-port transformer and gyrator.

Nevertheless, the robot dynamics are modelled using the customized nonlinear two-port inertance and compliance elements. In particular, the equation of motion Eq. 15 is expressed in the Hamiltonian form with the generalized coordinates $\boldsymbol{q} = \begin{bmatrix} \theta_p & \theta_y \end{bmatrix}^T$ and generalized momentum $\boldsymbol{p} = \begin{bmatrix} p_p & p_y \end{bmatrix}^T$ as the system state variables:

$$\begin{aligned} \dot{\theta}_p &= \frac{p_p}{I_{xx_{py}} c_y^2 + I_{zz_{py}} s_y^2 + I_{xx_p}} \\ \dot{\theta}_y &= \frac{p_y}{I_{yy_{py}}} \\ \dot{p}_p &= m_p g r_{z_p} c_p + m_{py} g r_{z_{py}} c_p c_y + \tau_{ext_p} \\ \dot{p}_y &= \frac{\left(I_{zz_{py}} - I_{xx_{py}}\right) s_y c_y}{\left(I_{xx_{py}} c_y^2 + I_{zz_{py}} s_y^2 + I_{xx_p}\right)^2} p_p^2 \\ &\quad - m_{py} g r_{z_{py}} s_p s_y + \tau_{ext_y}. \end{aligned} \tag{24}$$

parameter	winch#1	winch#2	pulley#1 and #2	pitch	yaw
shaft diameter, d	17	17	25	30	20
pulley radius, r	22.5	27	45	63	63

Table 4. Shaft diameter and pulley radius values in [mm] at each rotor-bearing support

All of these elements are then combined through the power bonds and the effort/flow ports. The complete bond graph diagram is given in Figure 5.

3. Task Space Impedance Control

3.1. The Controller

A task space impedance control for the robot driven through a multi-stage nonlinear flexible transmission system has been developed in [16]. The controller uses the available feedback information of merely the motor current and angles, which is frequently encountered in practice. In particular, if the desired task space compliance and dissipative damping ratio, $\boldsymbol{K}_d$ and $\boldsymbol{\zeta}$, are specified accompanied with a set point $\boldsymbol{x}_d$, the control law:

$$\begin{aligned}\boldsymbol{\tau}_m^* = \boldsymbol{B}_1\boldsymbol{B}_{1r}^{-1}\boldsymbol{T}_{q1}^T\Big[&\boldsymbol{g}\left(\boldsymbol{q}_s\right) - J\left(\boldsymbol{q}_s\right)^T\boldsymbol{K}_d\left(\boldsymbol{f}\left(\boldsymbol{q}_s\right) - \boldsymbol{x}_d\right)\\ &- \left(J\left(\boldsymbol{q}_s\right)^T\boldsymbol{D}_d\left(\boldsymbol{f}\left(\boldsymbol{q}_s\right)\right)J\left(\boldsymbol{q}_s\right)\right)^{1/2}\boldsymbol{\vartheta}\Big]\\ &+ \left(\boldsymbol{I} - \boldsymbol{B}_1\boldsymbol{B}_{1r}^{-1}\right)\hat{\boldsymbol{\tau}}_1 \end{aligned} \tag{25}$$

computes the motor reference torque $\boldsymbol{\tau}_m^*$ that imposes such behaviour at the robot end-effector. In the equation, for conciseness, $\boldsymbol{T}_j$ is the transmission ratio matrix of the j^{th}-stage reducer in the drivetrain and $\boldsymbol{T}_{qj}$ denotes the compound transmission ratio $\boldsymbol{T}_q\boldsymbol{T}_{q-1}\cdots\boldsymbol{T}_j$. $\boldsymbol{f}\left(\cdot\right)$ is the forward kinematics mapping of the robot. The specified damping ratio determines the task space damping matrix $\boldsymbol{D}_d\left(\cdot\right)$, which asymptotically stabilizes the system. Furthermore, the controller utilizes the motor current $\boldsymbol{i}$ feedback to estimate the torque transmitted to the drivetrain, $\hat{\boldsymbol{\tau}}_1$, which can then be used to reduce the motor inertia from $\boldsymbol{B}_1$ to $\boldsymbol{B}_{1r}$.

The controller is based on the estimated stationary robot link angles $\boldsymbol{q}_s$. They are determined *recursively* from the motor angles $\boldsymbol{\theta}_0$ by:

$$\begin{aligned}\boldsymbol{e}_{1q}^{-1}\left(\boldsymbol{\tau}\right) = &\boldsymbol{T}_{q2}\boldsymbol{e}_1^{-1}\left(\boldsymbol{T}_{q2}^T\boldsymbol{\tau}\right) + \boldsymbol{T}_{q3}\boldsymbol{e}_2^{-1}\left(\boldsymbol{T}_{q3}^T\boldsymbol{\tau}\right) + \ldots\\ &+ \boldsymbol{T}_{q(q-1)}\boldsymbol{e}_{q-2}^{-1}\left(\boldsymbol{T}_{q(q-1)}^T\boldsymbol{\tau}\right)\\ &+ \boldsymbol{T}_q\boldsymbol{e}_{q-1}^{-1}\left(\boldsymbol{T}_q^T\boldsymbol{\tau}\right) + \boldsymbol{e}_q^{-1}\left(\boldsymbol{\tau}\right)\end{aligned} \tag{26}$$

$$\begin{aligned}\boldsymbol{q}_s = \boldsymbol{T}_{q1}\boldsymbol{\theta}_0 - \boldsymbol{e}_{1q}^{-1}\big(&\boldsymbol{g}\left(\boldsymbol{q}_s\right)\\ &- J\left(\boldsymbol{q}_s\right)^T\boldsymbol{K}_d\left(\boldsymbol{f}\left(\boldsymbol{q}_s\right) - \boldsymbol{x}_d\right)\big).\end{aligned} \tag{27}$$

rotor	inertia value [g · cm^2]
motor	248
winch#1	344.6
winch#2	16728
pulley#1 and #2	48440

Table 5. Inertia of the rotational parts in the drivetrain around their own fixed rotating axes

$\boldsymbol{e}_{1q}^{-1}\left(\cdot\right)$ is the overall effective nonlinear deformation function of the transmission unit contributed by the deformation $\boldsymbol{e}_j^{-1}\left(\cdot\right)$ of each stage. The estimated link joint velocity scaled by the square root of the joint space symmetric damping matrix, $\boldsymbol{\vartheta}$, is then computed as:

$$\boldsymbol{\vartheta} = s\boldsymbol{G}\left(s\right)\left[J\left(\boldsymbol{q}_s\right)^T\boldsymbol{D}_d\left(\boldsymbol{f}\left(\boldsymbol{q}_s\right)\right)J\left(\boldsymbol{q}_s\right)\right]^{1/2}\boldsymbol{T}_{q1}\boldsymbol{\theta}_0. \tag{28}$$

The argument s represents the complex argument of the Laplace transform. $\boldsymbol{G}\left(s\right)$ is a diagonal matrix of a strictly proper and strictly positive real filtering transfer function. A simple first-order low-pass filter of $G\left(s\right) = \frac{\lambda}{s+\lambda}$ may be employed.

The estimated transmitted torque may be achieved by discretizing the motor equation of motion with the variational integrator method [17], which guarantees the energy conservation at every sampling. As a result, the transmitted torque at the k^{th}-sampling with the sampling period h may be estimated sequentially by:

$$\begin{aligned}\hat{\boldsymbol{\tau}}_{1k} = &-\hat{\boldsymbol{\tau}}_{1(k-1)} - \frac{2}{h^2}\boldsymbol{B}_1\left(\boldsymbol{\theta}_{0k} - 2\boldsymbol{\theta}_{0(k-1)} + \boldsymbol{\theta}_{0(k-2)}\right)\\ &-\boldsymbol{C}_1\left[\operatorname{sgn}\left(\boldsymbol{\theta}_{0k} - \boldsymbol{\theta}_{0(k-1)}\right)\right.\\ &\left.+\operatorname{sgn}\left(\boldsymbol{\theta}_{0(k-1)} - \boldsymbol{\theta}_{0(k-2)}\right)\right]\\ &+\frac{1}{2}\boldsymbol{K}_\tau\left(\boldsymbol{i}_k + 2\boldsymbol{i}_{k-1} + \boldsymbol{i}_{k-2}\right),\end{aligned} \tag{29}$$

where $\boldsymbol{B}_1$, $\boldsymbol{C}_1$ and $\boldsymbol{K}_\tau$ are the diagonal matrix of the motor inertias, frictional torques and torque constants. It should be mentioned that this controller is valid only for a practical system with a transmission stiff enough to withstand the robot's 'after-the-joint' motion, caused by its own weight and the position-mismatch compliant force.

For this two-DOF cable pulley-driven flexible joint robot, Eq. 26 is tailored to:

$$\begin{aligned}\boldsymbol{e}_{1q}^{-1}\left(\boldsymbol{\tau}\right) = &\boldsymbol{T}_{q2}\boldsymbol{e}_1^{-1}\left(\boldsymbol{T}_{q2}^T\boldsymbol{\tau}\right) + \boldsymbol{T}_{q3}\boldsymbol{e}_2^{-1}\left(\boldsymbol{T}_{q3}^T\boldsymbol{\tau}\right)\\ &+\boldsymbol{T}_q\boldsymbol{e}_3^{-1}\left(\boldsymbol{T}_q^T\boldsymbol{\tau}\right) + \boldsymbol{e}_q^{-1}\left(\boldsymbol{\tau}\right),\end{aligned} \tag{30}$$

with the following compound transmission ratios:

$$\boldsymbol{T}_q = \begin{bmatrix}\frac{1}{2} & \frac{1}{2}\\ \frac{1}{2} & -\frac{1}{2}\end{bmatrix} \qquad \boldsymbol{T}_{q3} = \begin{bmatrix}\frac{1}{6} & \frac{1}{6}\\ \frac{1}{6} & -\frac{1}{6}\end{bmatrix}$$

$$\boldsymbol{T}_{q2} = \begin{bmatrix}\frac{1}{18} & \frac{1}{18}\\ \frac{1}{18} & -\frac{1}{18}\end{bmatrix} \qquad \boldsymbol{T}_{q1} = \begin{bmatrix}-\frac{1}{18} & \frac{1}{18}\\ -\frac{1}{18} & -\frac{1}{18}\end{bmatrix}.$$

The individual deformations at each stage are determined from the coupling stiffness and the cable pulley compliance relationship of Eqs. 21 and 22:

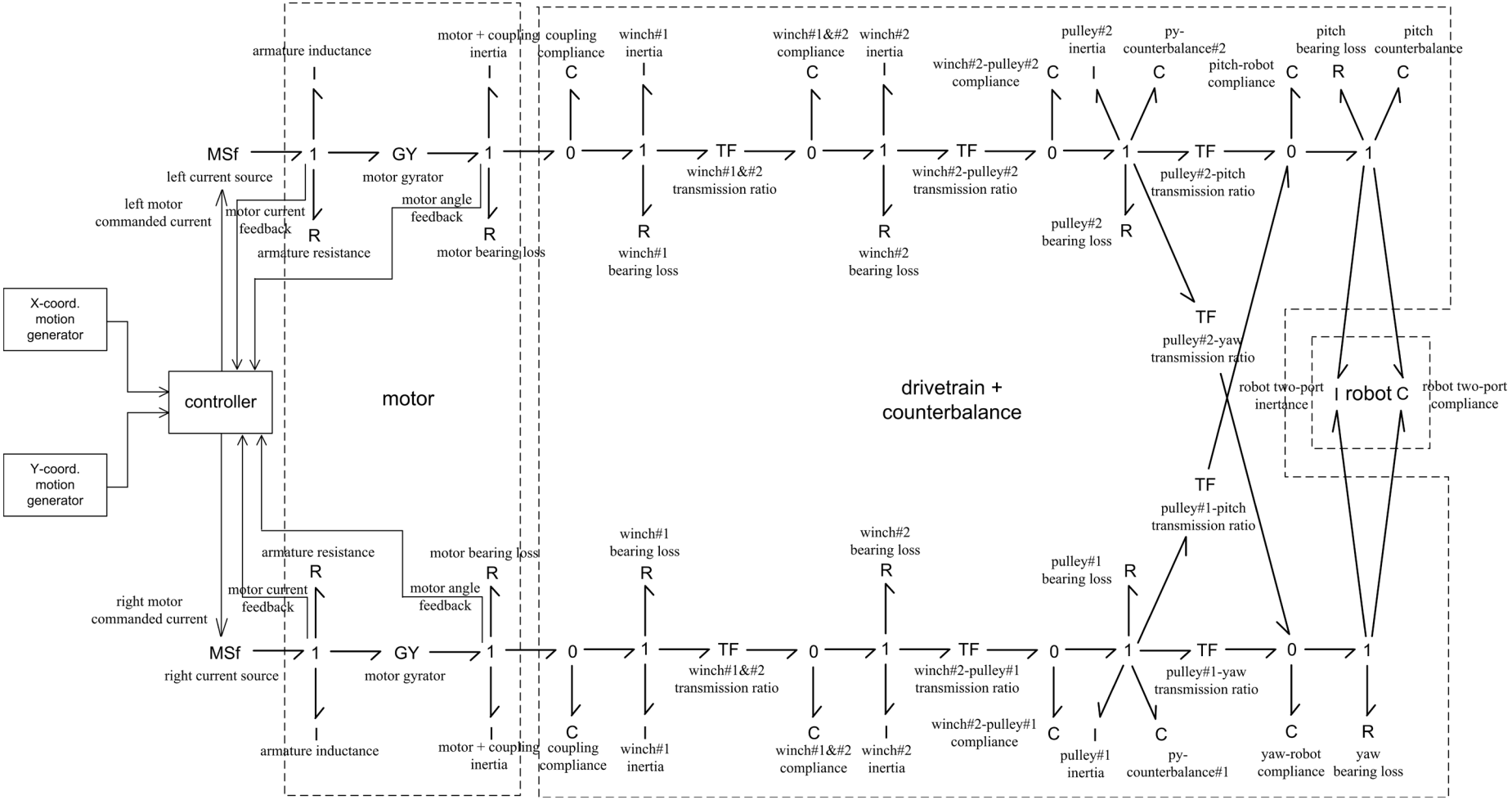

Figure 5. Detailed bond graph diagram of the two-DOF cable pulley-driven flexible joint robot-controlled system. The diagram displays the interconnection of the controller, motor, drivetrain, counterbalance and robot subsystems. The physical system-like couplings of the lumped model of the system's components ease the understanding of the overall dynamics.

$$
\begin{aligned}
\boldsymbol{e}_1^{-1}(\boldsymbol{\tau}_{w1}) &= \begin{bmatrix} 175.44\times10^{-6}\tau_{w1r} \\ 175.44\times10^{-6}\tau_{w1l} \end{bmatrix} \\
\boldsymbol{e}_2^{-1}(\boldsymbol{\tau}_{w2}) &= \begin{bmatrix} \frac{T_o}{EA\mu_{\text{eff}}}\left[\left(\frac{m_{w2r}e^{m_{w2r}}}{e^{m_{w2r}}-1}-1\right)(1+GF)-\log\frac{m_{w2r}e^{m_{w2r}}}{e^{m_{w2r}}-1}\right] \\ \frac{T_o}{EA\mu_{\text{eff}}}\left[\left(\frac{m_{w2l}e^{m_{w2l}}}{e^{m_{w2l}}-1}-1\right)(1+GF)-\log\frac{m_{w2l}e^{m_{w2l}}}{e^{m_{w2l}}-1}\right] \end{bmatrix} \\
\boldsymbol{e}_3^{-1}(\boldsymbol{\tau}_{d}) &= \begin{bmatrix} \frac{T_o}{EA\mu_{\text{eff}}}\left[\left(\frac{m_1e^{m_1}}{e^{m_1}-1}-1\right)(1+GF)-\log\frac{m_1e^{m_1}}{e^{m_1}-1}\right] \\ \frac{T_o}{EA\mu_{\text{eff}}}\left[\left(\frac{m_2e^{m_2}}{e^{m_2}-1}-1\right)(1+GF)-\log\frac{m_2e^{m_2}}{e^{m_2}-1}\right] \end{bmatrix} \\
\boldsymbol{e}_q^{-1}(\boldsymbol{\tau}_{dr}) &= \begin{bmatrix} \frac{T_o}{EA\mu_{\text{eff}}}\left[\left(\frac{m_pe^{m_p/2}}{2\left(e^{m_p/2}-1\right)}-1\right)(1+GF)-\log\frac{m_pe^{m_p/2}}{2\left(e^{m_p/2}-1\right)}\right] \\ \frac{T_o}{EA\mu_{\text{eff}}}\left[\left(\frac{m_ye^{m_y/2}}{2\left(e^{m_y/2}-1\right)}-1\right)(1+GF)-\log\frac{m_ye^{m_y/2}}{2\left(e^{m_y/2}-1\right)}\right] \end{bmatrix},
\end{aligned}
\tag{31}
$$

where:

$$
\begin{aligned}
\boldsymbol{\tau}_{w1} &= \begin{bmatrix} \tau_{w1r} & \tau_{w1l} \end{bmatrix}^T & \boldsymbol{\tau}_{w2} &= \begin{bmatrix} \tau_{w2r} & \tau_{w2l} \end{bmatrix}^T \\
\boldsymbol{\tau}_{d} &= \begin{bmatrix} \tau_1 & \tau_2 \end{bmatrix}^T & \boldsymbol{\tau}_{dr} &= \begin{bmatrix} \tau_p & \tau_y \end{bmatrix}^T
\end{aligned}
$$

are the torque vectors transmitted over the elastic couplings and cable pulley mechanisms to winch#1, winch#2, pulley#1, pulley#2 and the pitch and yaw joints of the robot. Also:

$$
\begin{aligned}
m_{w2r} &= \tfrac{\tau_{w2r}}{(rT_o)_{w2r}} & m_{w2l} &= \tfrac{\tau_{w2l}}{(rT_o)_{w2l}} \\
m_1 &= \tfrac{\tau_1}{(rT_o)_1} & m_2 &= \tfrac{\tau_2}{(rT_o)_2} \\
m_p &= \tfrac{\tau_p}{(rT_o)_p} & m_y &= \tfrac{\tau_y}{(rT_o)_y}
\end{aligned}
$$

are their dimensionless values.

For this system with the desired task space stiffness matrix ${}^{\{xyz\}}\boldsymbol{K}_d = \text{diag}\left(k_{dx}, k_{dy}\right)$ and the damping ratio ζ, the damping matrix may be determined by solving the eigenproblem of the desired impedance dynamics at the end-effector. The result is:

$$
\boldsymbol{D}_d\left(\boldsymbol{f}\left(\boldsymbol{q}_s\right)\right) = \begin{bmatrix} \frac{2\zeta\sqrt{k_{dx}I_{yypy}}}{l_o} & 0 \\ 0 & \frac{2\zeta\sqrt{k_{dy}\left(I_{xxpy}c_{ys}^2+I_{zzpy}s_{ys}^2+I_{xxp}\right)}}{l_oc_{ys}} \end{bmatrix} \tag{32}
$$

as a function of the stationary robot joint angle θ_{ys} computed from Eq. 27.

The designed controller is integrated with the developed model of the two-DOF cable pulley-driven flexible joint robot. Figure 5 depicts the signal interconnection between the system and the controller, where the motor current and angle are fed back to the controller unit to process the commanded current. The controller is digitally implemented at a frequency of 1 kHz. For the simulation, the controller computation is done in MATLAB® connected to the 20-sim© [18]. This simulation program is based on the bond graph modelling language, which does not require the explicit formulation of the complete system's differential equations. At each sampling, $\boldsymbol{q}_s$ is determined recursively by Eq. 27, whereby the value is further used to update other terms of $\boldsymbol{g}$, J, $\boldsymbol{f}$, $\boldsymbol{D}_d$ and $\boldsymbol{\vartheta}$. All of these terms and the estimated transmitted torque $\hat{\boldsymbol{\tau}}_1$ are used to compute the motor reference torque by Eq. 25. Tustin approximating discretization method is used to obtain the discrete equivalent of the continuous transfer function $s\boldsymbol{G}(s)$. For the real system, the controller and the peripheral tasks are programmed in C#. Typical control parameters used in the simulations and experiments are depicted in Table 6.

3.2. Stability of the Closed-loop System

Proposition. *The task space impedance control law Eq. 25 asymptotically stabilizes the robot system Eq. 15 driven through the multi-stage nonlinear flexible transmission unit to the desired set point* $\boldsymbol{x}_d$.

Proof. Before proving the stability of the closed-loop system, let us consider the estimated link joint velocity of Eq. 28. It may be viewed as the stable linear filtering of the time derivative of the estimated link angles $\boldsymbol{T}_{q1}\dot{\boldsymbol{\theta}}_0$. Hence, this velocity estimator might be represented in the minimal realization state space $\{\boldsymbol{A}, \boldsymbol{B}, \boldsymbol{C}\}$ form:

$$
\begin{aligned}
\dot{\boldsymbol{x}} &= \boldsymbol{A}\boldsymbol{x} + \boldsymbol{B}\sqrt{\boldsymbol{K}_v}\boldsymbol{T}_{q1}\dot{\boldsymbol{\theta}}_0 \\
\boldsymbol{\vartheta} &= \boldsymbol{C}\boldsymbol{x},
\end{aligned}
\tag{33}
$$

where $\sqrt{\boldsymbol{K}_v}$ denotes the square root of the joint space damping matrix $J^T\boldsymbol{D}_dJ$, $\boldsymbol{G}(s) = \boldsymbol{C}\left(s\boldsymbol{I}-\boldsymbol{A}\right)^{-1}\boldsymbol{B}$, and $\boldsymbol{x}$ denotes the filter states. Applying the Kalman-Yakubovich (KY) lemma [19], since $\boldsymbol{G}(s)$ is a strictly proper and strictly positive real (SPR) transfer function, there exist symmetric positive definite matrices $\boldsymbol{P}$ and $\boldsymbol{Q}$ such that $\boldsymbol{A}^T\boldsymbol{P}+\boldsymbol{P}\boldsymbol{A} = -\boldsymbol{Q}$ and $\boldsymbol{B}^T\boldsymbol{P} = \boldsymbol{C}$.

Define the new state vector $\boldsymbol{z}$ such that $\dot{\boldsymbol{z}} = \boldsymbol{x}$. Furthermore, define the motor set point error $\tilde{\boldsymbol{\theta}}_0 = \boldsymbol{\theta}_0 - \boldsymbol{\theta}_{0d}$ where $\boldsymbol{\theta}_{0d}$ denotes the constant target motor angles according to the desired constant Cartesian set point $\boldsymbol{x}_d$. Then, Eq. 28 or Eq. 33 might be expressed in terms of the new state $\boldsymbol{z}$:

$$
\begin{aligned}
\dot{\boldsymbol{z}} &= \boldsymbol{A}\boldsymbol{z} + \boldsymbol{B}\sqrt{\boldsymbol{K}_v}\boldsymbol{T}_{q1}\tilde{\boldsymbol{\theta}}_0 \\
\boldsymbol{\vartheta} &= \boldsymbol{C}\boldsymbol{A}\boldsymbol{z} + \boldsymbol{C}\boldsymbol{B}\sqrt{\boldsymbol{K}_v}\boldsymbol{T}_{q1}\tilde{\boldsymbol{\theta}}_0,
\end{aligned}
\tag{34}
$$

where the input is now the regulation error $\tilde{\boldsymbol{\theta}}_0$.

Let $\boldsymbol{\theta} = \begin{bmatrix} \boldsymbol{\theta}_0^T & \boldsymbol{\theta}_1^T & \cdots & \boldsymbol{\theta}_{q-1}^T \end{bmatrix}^T$ be the vector of the q-stages of the transmission system generalized coordinates in which

parameter	simulation	experiment
cut-off frequency of low-pass filter, λ	500 [rad/s]	65 [rad/s]
desired stiffness, k_d	10000 [N/m]	500 [N/m]
desired damping ratio, ζ	1.0	0.6
reduced motor inertia, b_{1r}	200 [g $\cdot$ cm^2]	248 [g $\cdot$ cm^2]

Table 6. Nominal control parameters adopted in the simulations and experiments

the rotor angles are naturally adopted. Note that $\boldsymbol{\theta}_0$ is the vector of the motor angles. Consider the following function of the closed-loop system states $\left[\boldsymbol{q}, \dot{\boldsymbol{q}}, \boldsymbol{\theta}, \dot{\boldsymbol{\theta}}, \dot{\boldsymbol{z}}\right]^T$:

$$V(\cdot) = \frac{1}{2}\dot{\boldsymbol{q}}^T \boldsymbol{M}(\boldsymbol{q})\dot{\boldsymbol{q}} + V_g(\boldsymbol{q}) + \frac{1}{2}\dot{\boldsymbol{\theta}}^T \boldsymbol{B}_r \dot{\boldsymbol{\theta}} + V_e\left(\boldsymbol{q}, \boldsymbol{T}_{q1}\boldsymbol{\theta}_0\right) - V_{\bar{h}}\left(\boldsymbol{T}_{q1}\boldsymbol{\theta}_0\right) + \frac{1}{2}\dot{\boldsymbol{z}}^T \boldsymbol{P}\dot{\boldsymbol{z}} \quad (35)$$

consisting of the kinetic energy (KE) and potential energy (PE) of the robot, the KE of the reduced inertia drivetrain according to its dynamics (rotor inertia matrix $\boldsymbol{B}_r$ and vector of dissipating and elastic torques $\boldsymbol{c}_r\left(\dot{\boldsymbol{\theta}}\right)$ and $\boldsymbol{e}(\boldsymbol{\theta})$ subject to the input torque vector $\boldsymbol{\tau}_r$):

$$\boldsymbol{B}_r\ddot{\boldsymbol{\theta}} + \boldsymbol{c}_r\left(\dot{\boldsymbol{\theta}}\right) + \boldsymbol{e}(\boldsymbol{\theta}) = \boldsymbol{\tau}_r, \quad (36)$$

the elastic PE of the drivetrain:

$$V_e\left(\boldsymbol{q}, \boldsymbol{T}_{q1}\boldsymbol{\theta}_0\right) = \boldsymbol{e}_{1q}\left(\boldsymbol{T}_{q1}\boldsymbol{\theta}_0 - \boldsymbol{q}\right)^T\left(\boldsymbol{T}_{q1}\boldsymbol{\theta}_0 - \boldsymbol{q}\right) - \int_{\boldsymbol{q}_i}^{\boldsymbol{q}} \boldsymbol{e}_{1q}^{-1}\left(\boldsymbol{h}(\boldsymbol{\phi})\right)^T \frac{\partial \boldsymbol{h}(\boldsymbol{\phi})}{\partial \boldsymbol{\phi}} \cdot d\boldsymbol{\phi}, \quad (37)$$

the negative PE of the controller:

$$V_{\bar{h}}(\boldsymbol{q}_s) = V_g(\boldsymbol{q}_s) - \frac{1}{2}\left(\boldsymbol{f}(\boldsymbol{q}_s) - \boldsymbol{x}_d\right)^T \boldsymbol{K}_d\left(\boldsymbol{f}(\boldsymbol{q}_s) - \boldsymbol{x}_d\right) + \boldsymbol{e}_{1q}\left(\boldsymbol{T}_{q1}\boldsymbol{\theta}_0 - \boldsymbol{q}_s\right)^T\left(\boldsymbol{T}_{q1}\boldsymbol{\theta}_0 - \boldsymbol{q}_s\right) - \int_{(\boldsymbol{q}_s)_i}^{\boldsymbol{q}_s} \boldsymbol{e}_{1q}^{-1}\left(\boldsymbol{h}(\boldsymbol{\phi})\right)^T \frac{\partial \boldsymbol{h}(\boldsymbol{\phi})}{\partial \boldsymbol{\phi}} \cdot d\boldsymbol{\phi}, \quad (38)$$

and the KE-like function of the velocity estimator unit. According to Eq. 27, $\boldsymbol{q}_s$ is indeed the function of $\boldsymbol{T}_{q1}\boldsymbol{\theta}_0$. Hence, in Eq. 35, $V_{\bar{h}}(\cdot)$ may be explicitly written as the function of the system state $\boldsymbol{\theta}_0$. $\boldsymbol{h}(\boldsymbol{\phi}) = \boldsymbol{e}_{1q}\left(\boldsymbol{T}_{q1}\boldsymbol{\theta}_0 - \boldsymbol{\phi}\right)$ is the elastic torque from the drivetrain transmitted to the robot joint. Assuming that the system operates smoothly at a low enough speed, this torque quasi-statically balances the gravity and the desired task space compliance force, namely:

$$\begin{aligned}\boldsymbol{h}(\boldsymbol{q}_s) &= \boldsymbol{e}_{1q}\left(\boldsymbol{T}_{q1}\boldsymbol{\theta}_0 - \boldsymbol{q}_s\right) \\ &= \boldsymbol{g}(\boldsymbol{q}_s) - \boldsymbol{J}(\boldsymbol{q}_s)^T \boldsymbol{K}_d\left(\boldsymbol{f}(\boldsymbol{q}_s) - \boldsymbol{x}_d\right).\end{aligned} \quad (39)$$

It can be shown that the function $V(\cdot)$ is a Lyapunov candidate function if the transmission unit is moderately stiff [16]. At the equilibrium, $V(\cdot) = 0$. From Eq. 35, this requires $\dot{\boldsymbol{q}} = \boldsymbol{0}$, $\dot{\boldsymbol{\theta}} = \boldsymbol{0}$, and $\dot{\boldsymbol{z}} = \boldsymbol{0}$. The remaining terms may be rearranged to show that $\boldsymbol{q} = \boldsymbol{q}_s = \boldsymbol{f}^{-1}(\boldsymbol{x}_d)$ nullifies them. The corresponding values of the equilibrium rotor angles $\boldsymbol{\theta}_s$ may be determined from the quasi-static equilibrium conditions of the transmission system.

The above equilibrium point $\left(\boldsymbol{q}, \dot{\boldsymbol{q}}, \boldsymbol{\theta}, \dot{\boldsymbol{\theta}}, \dot{\boldsymbol{z}}\right) = \left(\boldsymbol{q}_s, \boldsymbol{0}, \boldsymbol{\theta}_s, \boldsymbol{0}, \boldsymbol{0}\right)$ is indeed (locally) asymptotically stable. Differentiating Eq. 35 along the closed-loop system trajectory with further manipulation yields:

$$\begin{aligned}\dot{V}(\cdot) = &\frac{1}{2}\dot{\boldsymbol{q}}^T \dot{\boldsymbol{M}}(\boldsymbol{q})\dot{\boldsymbol{q}} + \dot{\boldsymbol{q}}^T\left(\boldsymbol{\tau}_{dr} + \boldsymbol{\tau}_{ext} - \boldsymbol{C}(\boldsymbol{q}, \dot{\boldsymbol{q}})\dot{\boldsymbol{q}} - \boldsymbol{g}(\boldsymbol{q})\right) + \dot{\boldsymbol{\theta}}^T\left(\boldsymbol{\tau}_r - \boldsymbol{c}_r\left(\dot{\boldsymbol{\theta}}\right) - \boldsymbol{e}(\boldsymbol{\theta})\right) \\ &+\frac{1}{2}\left(\boldsymbol{A}\dot{\boldsymbol{z}} + \boldsymbol{B}\sqrt{\boldsymbol{K}_v}\boldsymbol{T}_{q1}\dot{\boldsymbol{\theta}}_0\right)^T \boldsymbol{P}\dot{\boldsymbol{z}} + \frac{1}{2}\dot{\boldsymbol{z}}^T \boldsymbol{P}\left(\boldsymbol{A}\dot{\boldsymbol{z}} + \boldsymbol{B}\sqrt{\boldsymbol{K}_v}\boldsymbol{T}_{q1}\dot{\boldsymbol{\theta}}_0\right) \\ &+\boldsymbol{g}(\boldsymbol{q})^T\dot{\boldsymbol{q}} + \frac{\partial V_e\left(\boldsymbol{q}, \boldsymbol{T}_{q1}\boldsymbol{\theta}_0\right)}{\partial \boldsymbol{q}}\dot{\boldsymbol{q}} + \frac{\partial V_e\left(\boldsymbol{q}, \boldsymbol{T}_{q1}\boldsymbol{\theta}_0\right)}{\partial\left(\boldsymbol{T}_{q1}\boldsymbol{\theta}_0\right)}\boldsymbol{T}_{q1}\dot{\boldsymbol{\theta}}_0 - \boldsymbol{h}(\boldsymbol{q}_s)^T\boldsymbol{T}_{q1}\dot{\boldsymbol{\theta}}_0,\end{aligned}$$

where $\boldsymbol{\tau}_r = \left[\left(\boldsymbol{T}_{q1}^T\left(\boldsymbol{h}(\boldsymbol{q}_s) - \sqrt{\boldsymbol{K}_v}\boldsymbol{\vartheta}\right)\right)^T \boldsymbol{0}^T \cdots \boldsymbol{0}^T\right]^T$ is the generalized input torque vector of the modified drivetrain Eq. 36. Applying the passivity property of the robot, the KY lemma and recognizing:

$$\begin{aligned}&\boldsymbol{\tau}_{dr} = \boldsymbol{e}_q\left(\boldsymbol{T}_q\boldsymbol{\theta}_{q-1} - \boldsymbol{q}\right) = \boldsymbol{e}_{1q}\left(\boldsymbol{T}_{q1}\boldsymbol{\theta}_0 - \boldsymbol{q}\right) \\ &\frac{\partial V_e\left(\boldsymbol{q}, \boldsymbol{T}_{q1}\boldsymbol{\theta}_0\right)}{\partial \boldsymbol{q}} = -\boldsymbol{e}_{1q}^T\left(\boldsymbol{T}_{q1}\boldsymbol{\theta}_0 - \boldsymbol{q}\right) \\ &\boldsymbol{e}(\boldsymbol{\theta}) = \left(\frac{\partial V_e(\boldsymbol{q}, \boldsymbol{\theta})}{\partial \boldsymbol{\theta}}\right)^T \\ &\frac{\partial V_e(\boldsymbol{q}, \boldsymbol{\theta})}{\partial \boldsymbol{\theta}}\dot{\boldsymbol{\theta}} = \frac{\partial V_e\left(\boldsymbol{q}, \boldsymbol{T}_{q1}\boldsymbol{\theta}_0\right)}{\partial\left(\boldsymbol{T}_{q1}\boldsymbol{\theta}_0\right)}\boldsymbol{T}_{q1}\dot{\boldsymbol{\theta}}_0,\end{aligned}$$

the derivative may be simplified to:

$$\dot{V}(\cdot) = -\dot{\boldsymbol{\theta}}^T\boldsymbol{c}_r\left(\dot{\boldsymbol{\theta}}\right) - \frac{1}{2}\dot{\boldsymbol{z}}^T\boldsymbol{Q}\dot{\boldsymbol{z}} + \dot{\boldsymbol{q}}^T\boldsymbol{\tau}_{ext}. \quad (40)$$

The realistic transmission system is fully damped, making $\dot{\boldsymbol{\theta}}^T\boldsymbol{c}_r\left(\dot{\boldsymbol{\theta}}\right) \geq \sum_{i=1}^{pq}\alpha_i\dot{\theta}_i^2 \geq 0$, $\alpha_i > 0$ and $\boldsymbol{c}_r(\boldsymbol{0}) = \boldsymbol{0}$. Therefore, in the free motion case, it can be concluded that $\dot{V}(\cdot) \leq 0$ and $V(\cdot)$ denote the Lyapunov function. Given the Lyapunov stability theorem, the closed-loop system is then locally stable. Since this equilibrium point is the only point which makes $\dot{V}(\cdot) \equiv 0$, the closed-loop system is asymptotically stable at the equilibrium point thanks to the Lasalle's invariance principle. □

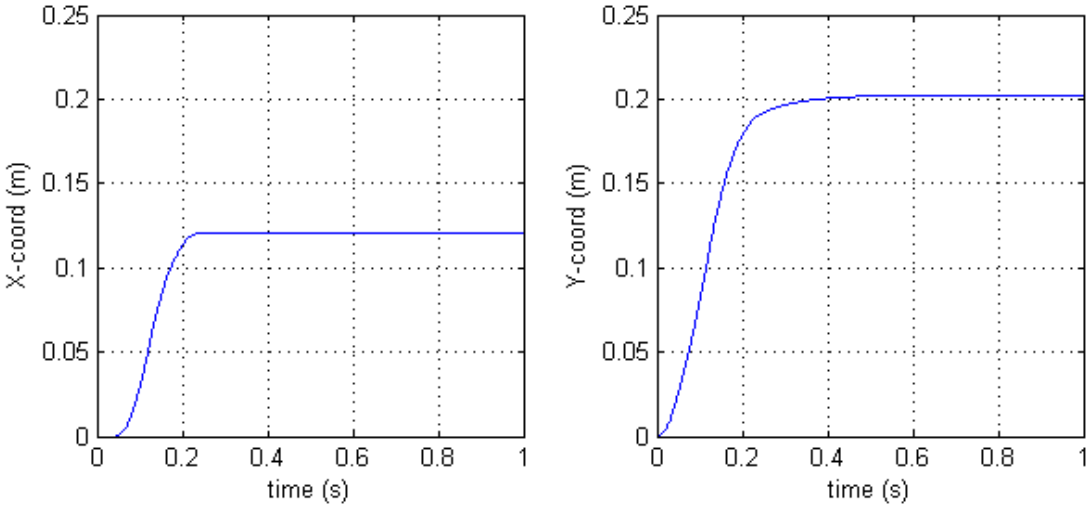

Figure 6. Motion response of the end point X/Y-coordinates for a constant set point simulation

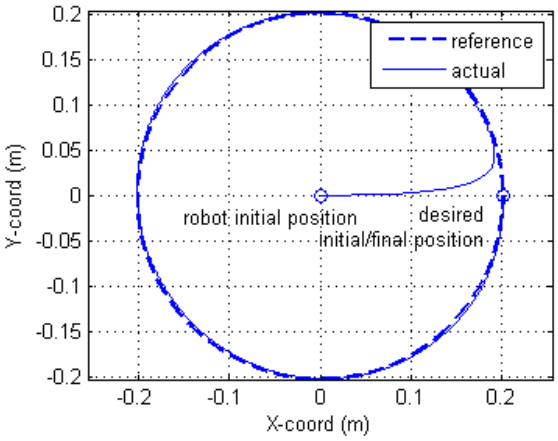

Figure 7. Simulated trajectory-tracking of the robot with initial position mismatch

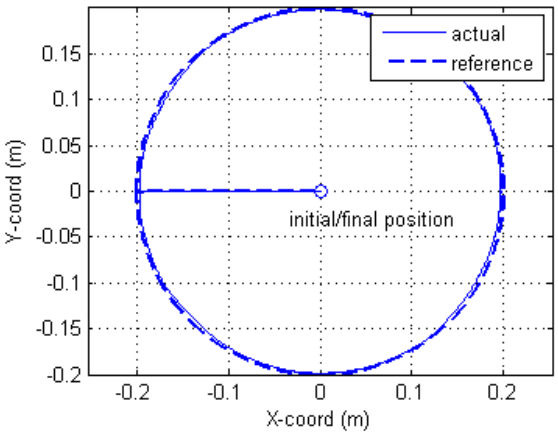

Figure 8. Circular trajectory-tracking of the real system under no external force

4. Simulations and Experiments

In what follows, various simulations and experiments are performed to investigate the effect of several control parameters on the system response and to illustrate the effectiveness of the control law. Since the system is rather stiff, an adaptive backward differentiation formula integration method with a step size of 1 [ms] is used in all simulations. In the real system, due to the discrete implementation of the controller and the unmodelled dynamics, the achievable desired stiffness and damping ratio are reduced to the values shown in Table 6. Additionally, the motor current has been limited to 3.5 [A] for safety reasons.

4.1. Constant Set Point

Let the initial position of the robot end-point be at the centre of its hemispherical workspace, i.e., ${}^{\{XYZ\}}\boldsymbol{x}\,(0) = \begin{bmatrix}0 & 0 & -0.315\end{bmatrix}^T$ [m]. This corresponds to $\theta_p = 0°$ and $\theta_y = 0°$. The desired position is set to be at ${}^{\{XYZ\}}\boldsymbol{x}_d = \begin{bmatrix}0.1207 & 0.2025 & -0.2090\end{bmatrix}^T$ [m], caused by rotating the shoulder link from the initial posture for $40°$ around the X-axis followed by $-30°$ around the Y-axis. The nominal values of the task space stiffness matrix, the damping ratio and the desired motor inertia are used. Figure 6 shows the simulation result of the measured X/Y-coordinates at the end-point. The response reaches the desired position $\boldsymbol{x}_d$ in 0.5 [sec] with no overshoot thanks to a large damping ratio. It should be noted that the controlled system is not destabilized despite the magnitude of the step input (0.2663 [m] of path distance); only the current is saturated in the transient phase.

4.2. Trajectory-tracking

A circular trajectory is generated for the free-tracking simulation. The starting point is at the rightmost, ${}^{\{XYZ\}}\boldsymbol{x}_d\,(0) = \begin{bmatrix}0.2025 & 0 & -0.2413\end{bmatrix}^T$ [m], caused by rotating the shoulder link in the yaw direction for $-40°$. Next, the trajectory is made by rotating the link around the Z-axis for a complete rotation in 6 [sec] with a moderate constant speed of 0.212 [m/s]. Finally, the desired position is held constant at the starting point for 0.5 [sec]. The initial position of the robot end-point is intentionally placed at the centre of the workspace to create a large position

mismatch (0.22 [m] of path distance) at the beginning. The controller and its parameters are the same as used in the constant set point case.

Figure 7 displays the trajectory-tracking of the robot along with the reference trajectory. It can be seen that the proposed controller - which was designed for the regulation objective - may well be used in the tracking task, since it can tolerate a moderate speed and accuracy. The initial mismatch does not effect the tracking performance or destabilize the system. It merely causes current saturation of the motor during a large position error. Once the end-tip enters its track, the current consumption is quite low (0.45 [A] average) thanks to the energy restoration from the truly passive control of the augmented counterbalancing mechanism.

A similar experiment is implemented with the real system. The reference trajectory, which may be divided into three parts, starts from the centre point of the robot workspace. Then, it moves leftwards by executing the yaw rotation for 40° in 3 [sec] and idles for 2 [sec]. Next, the trajectory completes the clockwise circular path around the Z-axis in 20 [sec] with a speed of 0.0636 [m/s]. Afterwards, it idles for the next 2 [sec] before reversing the motion of the first part; travelling rightwards back to the starting point and staying there for 2 [sec]. The total time spent is thus 32 [sec].

Figure 8 displayed the estimated stationary path of the robot end-tip and its reference. It is seen that the actual robot motion tracks the desired trajectory faithfully. The average of the integral of the absolute error $I = \frac{1}{N}\sum_{k=0}^{N} \|\boldsymbol{x}_k - \boldsymbol{x}_{dk}\|_2$ may be used as an indication of the tracking-error, of which its value is 0.0065 [m]. This error might further be reduced by fine tuning the task space stiffness and damping parameters. The average current consumption is found to be 0.59 and 0.65 [A] for the right and left motors. The peak values are 0.99 and 1.41 [A] respectively.

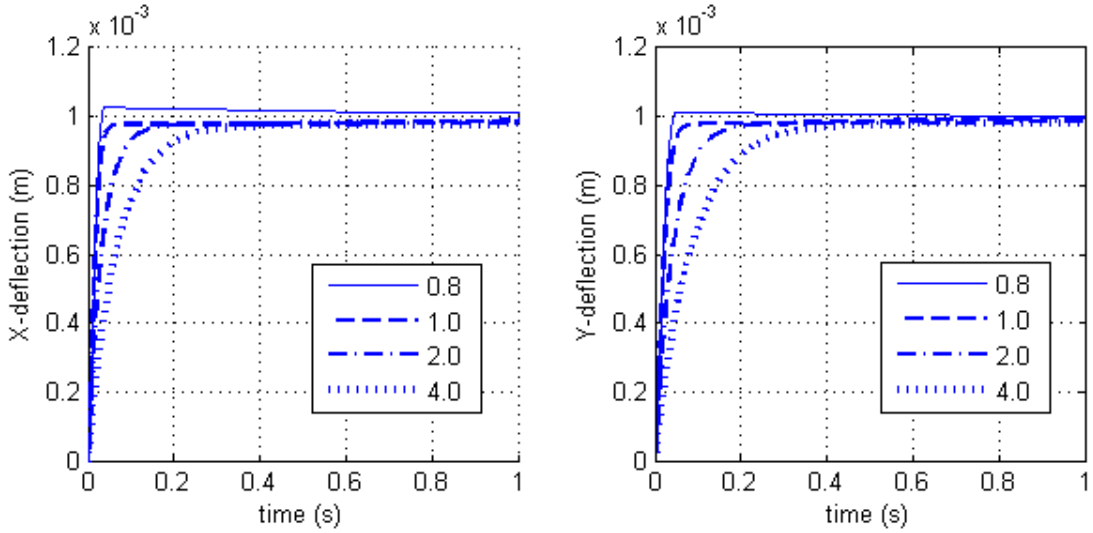

Figure 9. Simulation of the robot end-tip deflection with the nominal stiffness value subject to the external force of 10 [N] for a set of damping ratios

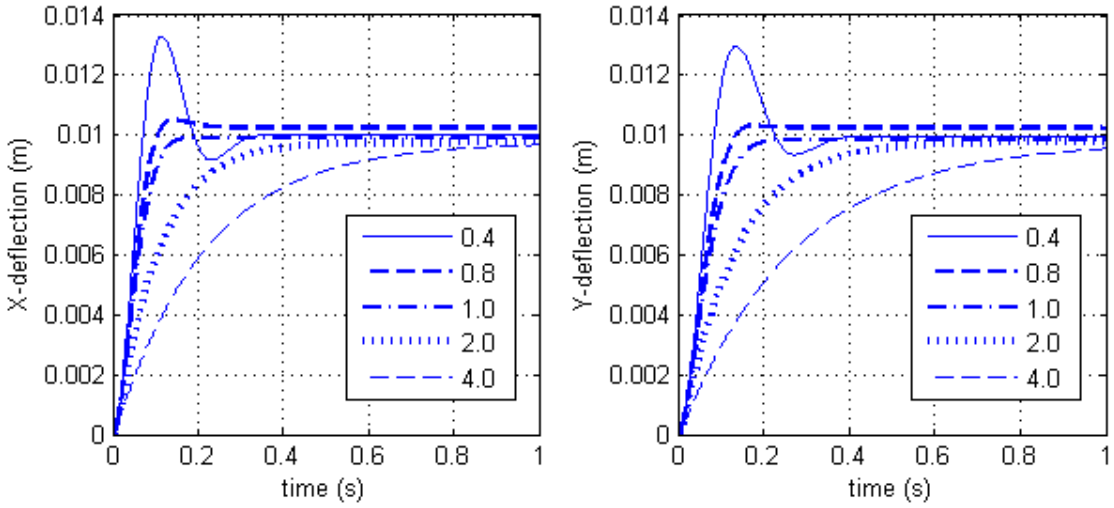

Figure 10. Simulation of the robot end-tip deflection with a stiffness value of 1000 [N/m] subject to an external force of 10 [N] for a set of damping ratios

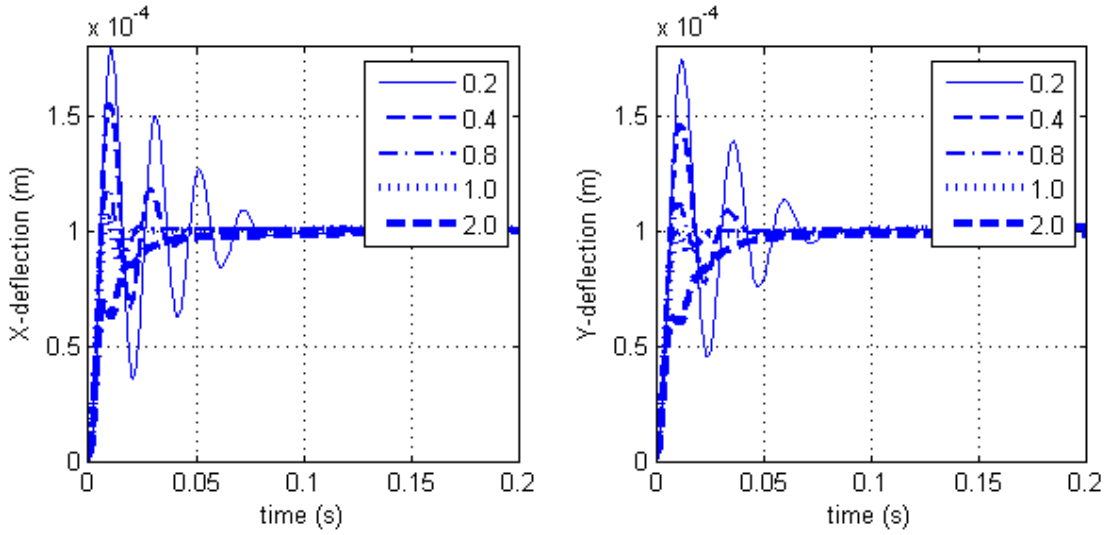

Figure 11. Simulation of the robot end-tip deflection with a stiffness value of 100,000 [N/m] subject to an external force of 10 [N] for a set of damping ratios. The system will be unstable if a ratio value of 4.0 or higher is used.

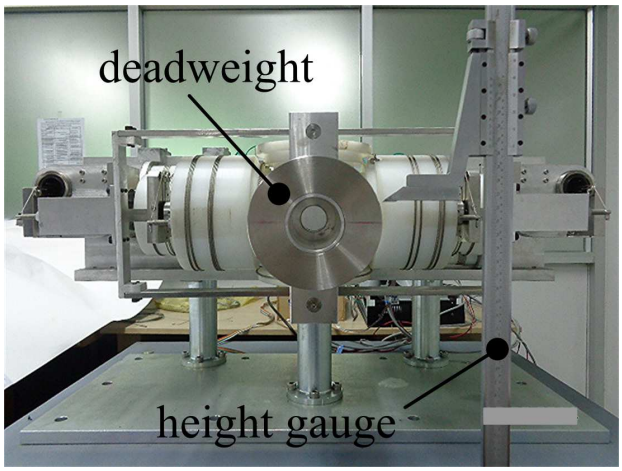

Figure 12. Robot setup for experiments with varying end-tip stiffnesses and damping values

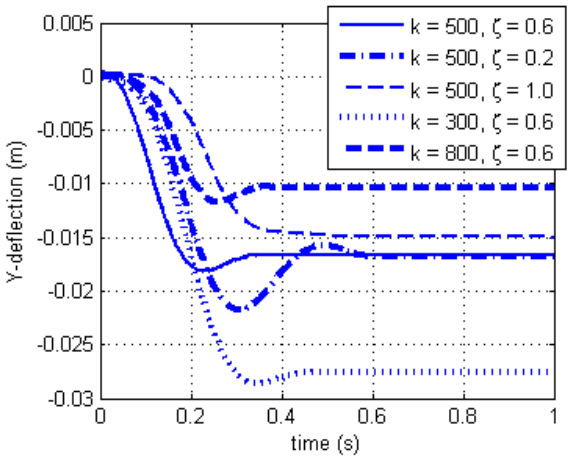

Figure 13. Actual responses of the robot end tip deflection subject to 1.0 [kg] deadweight

compliance parameters	actual deflection [m]	actual stiffness [N/m]	predicted deflection [m]	friction force [N]
$k = 500, \zeta = 0.2$	0.01738	565	0.0196	1.13
$k = 500, \zeta = 0.6$	0.01754	560	0.0196	1.05
$k = 500, \zeta = 1.0$	0.01626	603	0.0196	1.67
$k = 300, \zeta = 0.6$	0.02738	358	0.0325	1.59
$k = 800, \zeta = 0.6$	0.01154	850	0.0122	0.58

Table 7. Static deflection of the robot end point subject to 1.0 [kg] deadweight with different compliance behaviours

4.3. Task Space Stiffness and Damping

To verify that the desired task space stiffness is actually achieved, the robot is set at the centre of the workspace and an external force of 10 [N] is applied in the X- and Y-directions, respectively. For the simulation, the end-tip deflection responses using the nominal stiffness value are shown in Figure 9 for a set of damping ratios of 0.8, 1.0, 2.0 and 4.0. It is observed that, in practice, increased damping makes the motion more sluggish, while the current drawn (not shown) becomes more responsive. Together with a larger stiffness (order of 10^5 [N/m]), this can make the system unstable. In any case of Figure 9, eventually, the end-tip reaches the point corresponding to a deflection of about 1 mm, which agrees with the desired stiffness and the applied force.

Figure 10 and 11 show the deflection plots for stiffness values of 1000 and 100,000 [N/m]. A lower stiffness with high damping causes the end-tip to deflect slowly and prevents it from reaching the expected deviation. Subsequently, the environment will feel the robot become stiffer than its actual value. The deflection of the system with high stiffness and light damping will largely oscillate around the steady value long before it dies out. On the other hand, if too high a damping ratio is selected, the responsive motor current will suppress the deflection aggressively such that the undershoot may be detected. If the damping is further increased, it can cause the system to become unstable.

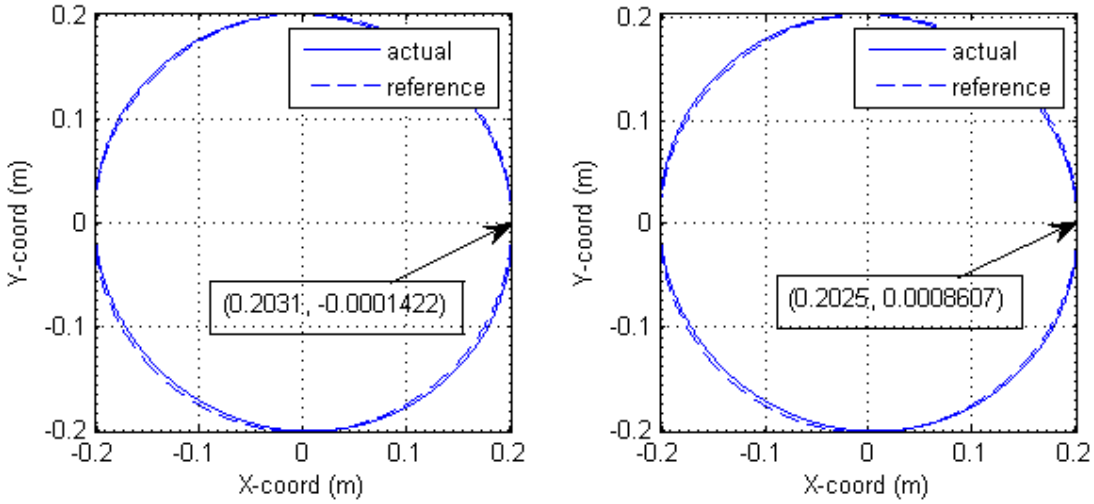

Figure 14. Tracking simulation with nominal stiffness subject to a 10 [N] force applied along the X- (left) and Y- (right) directions

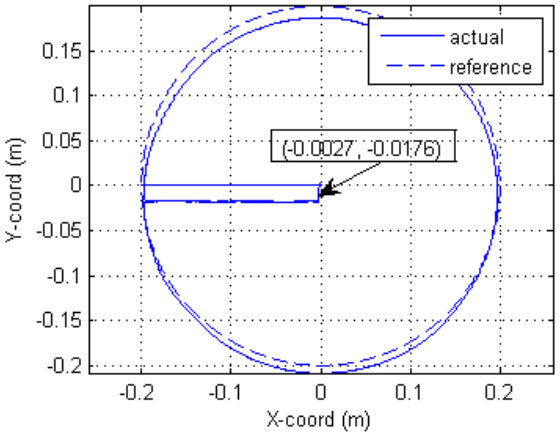

Figure 15. Trajectory-tracking of the real system subject to 1.0 [kg] deadweight at the end-tip

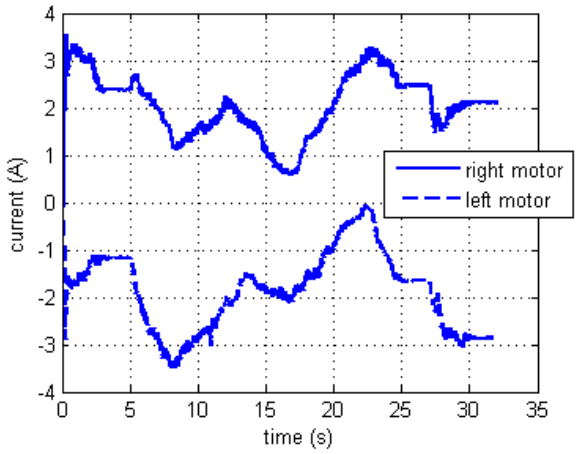

Figure 16. Motor current consumption during circular path-tracking subject to 1.0 [kg] deadweight

For the actual system, a proof mass of 1.0 [kg] is placed at the end of the robot shoulder link to realize a constant external force in the negative Y-direction, as illustrated in Figure 12. A set of stiffness and damping ratio values, as depicted in Table 7, are tuned to perform the experiment. Figure 13 depicts the estimated end-tip deflections with different impedances. The responses of the real system agree with the simulation results. The static position of the robot end-tip is measured by a vernier height gauge (0.02 [mm] of resolution) before and after applying the weight to obtain the actual deflection value, as recorded in Table 7. Using the commanded stiffness and the estimated stationary pitch and yaw angles, the predicted deflection may be determined from Eqs. 41 and 42. It is observed that the actual deflection is less than the predicted value. This is due to the friction in the mechanism, which causes the effective stiffness to be higher than the desired value.

It should be mentioned that motor inertia reduction will increase the effective stiffness, since it has the effect of increasing the control loop gain and thus the resultant stiffness becomes larger than the desired value. Therefore, motor inertia reduction should not be implemented if the exact desired stiffness is of concern.

4.4. Application of an External Force

For the last experiment, an external force is applied to the end point while the robot is tracking the same trajectory as in subsection 4.2. The task space stiffness and damping ratio are set to their nominal values. Figure 14 displays the tracking simulation result when the robot is subject to the 10 [N] force acting in the X- and Y-directions throughout the circular path. It was observed that the end-tip follows the reference trajectory closely because of the high stiffness value compared to the magnitude of the applied force. As depicted in the figure, ultimately the end-point deviates from the desired location by 0.6 and 0.86 [mm] along the X- and Y-directions respectively.

When the end-point is at its final position, the nominal task space stiffness matrix expressed in the local frame parallel to the reference frame $\{XYZ\}$ is determined by:

$$ {}^{\{XYZ\}}\boldsymbol{K}_d = {}^{\{xyz\}}R^T_{\{XYZ\}}\, {}^{\{xyz\}}\boldsymbol{K}_d\, {}^{\{xyz\}}R_{\{XYZ\}} \quad (41) $$

where the numerical value of k_{dz} is set to 1000×10^3 [N/m], as the robot cannot move along the z-direction. The associated deflections, determined by:

$$^{\{XYZ\}}\boldsymbol{\delta} = {}^{\{XYZ\}}\boldsymbol{K}_d^{-1}\,{}^{\{XYZ\}}\boldsymbol{F}, \tag{42}$$

along the direction of the applied force will be 0.59 and 1.0 [mm] for each case in turn. Hence, the actual deviations agree with the theoretical values with only a slight mismatch because of friction. Therefore, the desired end-effector stiffness is achieved.

The tracking result of the real system with a constant force in a negative Y-direction supplied by the attached 1.0 [kg] deadweight is depicted in Figure 15. Due to a weaker nominal stiffness value, the actual motion deviates more from the reference path. Following tracking, the end-point departs from the workspace centre by -0.0176 [m] along the Y-direction while the predicted value is -0.0196 [m]. This agrees with the result in the previous subsection. The tracking performance via the average of the integral of absolute error is 0.0168 [m], which is approximately 2.5 times larger than that of the free-tracking case. The current consumption during the course is plotted in Figure 16. The average values are 2.05 and 1.87 [A] for the right and left motors respectively. From the graph, both motors are saturated for a short period during tracking. It should be noted that the controller exhibits robustness in relation to the unmodelled inertia of the deadweight.

5. Conclusions

A prototypical system of a two-DOF cable pulley-driven flexible joint robot is designed and analysed. Important characteristics of the system components are modelled using the Lagrangian energy method. They are organized and integrated using the bond graph modelling technique to accomplish a realistic model of the whole system. A task space impedance controller for a robot driven through a multi-stage nonlinear flexible transmission system is proposed. This regulates the stiffness and damping of the end-effector at the specified position in accordance with the desired values based on just the motor current and angle feedback. The stability of the overall system is proven.

From the simulation, the controller exhibits satisfactory results for standard tasks, such as regulation or trajectory-tracking, both with and without the application of external force. An additional simulation is performed to verify that the specified task space stiffness is indeed achieved. The effects of the damping ratio value on the motion response are studied. Overly high stiffness and light damping cause the robot to oscillate significantly before settling down. On the other hand, the robot moves sluggishly if too low stiffness and high damping are selected. Experiments with the real system further ensure the simulation results. From the investigation, it is evident that the proposed controller is capable of regulating the task space impedance of the manipulator coupling with a multi-stage nonlinear flexible transmission unit in a stable and robust manner. This development will be of great benefit to advanced manipulators in accomplishing challenging missions amidst complex environments.

6. Acknowledgements

The author is grateful for the generous support from many sources, including the Ratchadaphiseksomphot Endowment Fund of Chulalongkorn University (RES560530224-AS), the Thailand Research Fund (MRG5580227 and MSD56I0018), the ISUZU Research Foundation, and the Department of Mechanical Engineering, Chulalongkorn University.

7. References

[1] Hogan N (1985) Impedance Control: An Approach to Manipulation. Trans. ASME J. Dynamic Systems, Measurement, and Control. 107 (1): 1-24.

[2] Guthart GS and Salisbury JK (2000) The Intuitive® Telesurgery System: Overview and Application. In: Proc. IEEE International Conference on Robotics and Automation; pp. 618-621.

[3] Wyrobek KA et al (2008) Towards a Personal Robotics Development Platform: Rationale and Design of an Intrinsically Safe Personal Robot. In: Proc. IEEE International Conference on Robotics and Automation; pp. 2165-2170.

[4] Yang C et al (2013) Trajectory Planning and Optimized Adaptive Control for a Class of Wheeled Inverted Pendulum Vehicle Models. IEEE Trans. Cybernetics. 43 (1): 24-36.

[5] Spong M (1987) Modeling and Control of Elastic Joint Robots. Trans. ASME J. Dynamic Systems, Measurement, and Control. 109 (4): 310-319.

[6] Tomei P (1991) A Simple PD Controller for Robots with Elastic Joints. IEEE Trans. Automatic Control. 36 (10): 1208-1213.

[7] Zollo L (2005) Compliance Control for an Anthropomorphic Robot with Elastic Joints: Theory and Experiments. Trans. ASME J. Dynamic Systems, Measurement, and Control. 127 (3): 321-328.

[8] Albu-Schaffer A et al (2003) Cartesian Impedance Control of Redundant Robots: Recent Results with the DLR-Light-Weight-Arms. In: Proc. IEEE International Conference on Robotics and Automation; pp. 3704-3709.

[9] Ott C et al (2008) On the Passivity-Based Impedance Control of Flexible Joint Robots. IEEE Trans. on Robotics. 24 (2): 416-429.

[10] Chien MC and Huang AC (2012) Adaptive Impedance Controller Design for Flexible-Joint Electrically-Driven Robots without Computation of the Regressor Matrix. Robotica. 30 (1): 133-144.

[11] Li Z et al (2013) Decentralized Adaptive Fuzzy Control of Coordinated Multiple Mobile Manipulators Interacting with Nonrigid Environments. IET Control Theory & Applications. 7 (3): 397-410.

[12] Pitakwatchara P (2012) Spring-Cable Counter-Balancing System for Pitch-Yaw Compound Joint Mechanism. Thailand Patent Office. Patent Pending Application #1201002792. Filed on 12 June 2012.

[13] Snow ER (1993) The Load/Deflection Behavior of Pretensioned Cable/Pulley Transmission Mechanisms [SM thesis]. M.I.T.

[14] Nippon System Kaihatsu (2007) NSK Rolling Bearing Catalog. CAT #E1102e.
[15] Karnopp DC et al (2006) System Dynamics: Modeling and Simulation of Mechatronic Systems. New York: John Wiley & Sons.
[16] Pitakwatchara P (2014) Task Space Impedance Control of the Manipulator Driven Through the Multi-Stage Nonlinear Flexible Transmission. The ASME J. Dynamic Systems, Measurement, and Control. Accepted.
[17] Marsden JE and West M (2001) Discrete Mechanics and Variational Integrators. Acta Numerica. 10: 357-514.
[18] Controllab Products B.V. the Netherlands. 20-sim© simulation program [Internet]. Available from: http://www.20sim.com Accessed on 5 July 2013.
[19] Slotine JJE and Li W (1991) Applied Nonlinear Control. New Jersey: Prentice-Hall.

เลขที่อนุสิทธิบัตร 9201

อสป/200 - ข

อนุสิทธิบัตร

อาศัยอำนาจตามความในพระราชบัญญัติสิทธิบัตร พ.ศ. 2522
แก้ไขเพิ่มเติมโดยพระราชบัญญัติสิทธิบัตร (ฉบับที่ 3) พ.ศ. 2542
บดีกรมทรัพย์สินทางปัญญาออกอนุสิทธิบัตรฉบับนี้ให้แก่

จุฬาลงกรณ์มหาวิทยาลัย

สำนักงานกองทุนสนับสนุนการวิจัย

สำนักงานคณะกรรมการการอุดมศึกษา

สำหรับการประดิษฐ์ตามรายละเอียดการประดิษฐ์ ข้อถือสิทธิ และรูปเขียน (ถ้ามี)
ที่ปรากฏในอนุสิทธิบัตร

เลขที่คำขอ	1303001330
วันขอรับอนุสิทธิบัตร	21 ตุลาคม 2556
ผู้ประดิษฐ์	ผู้ช่วยศาสตราจารย์ ดร.พงศ์แสน พิทักษ์วัชระ และ นายฉัตรชัยวัฒน์ โลวะกิจ
ชื่อที่แสดงถึงการประดิษฐ์	กลไกปรับแรงตึงในลวดสลิง

ให้ผู้ทรงอนุสิทธิบัตรนี้มีสิทธิหน้าที่ตามกฎหมายว่าด้วยสิทธิบัตรทุกประการ

ออกให้ ณ วันที่ 8 เดือน ตุลาคม พ.ศ. 2557

หมดอายุ วันที่ 20 เดือน ตุลาคม พ.ศ. 2562

(ลงชื่อ) .....

(นายสมศักดิ์ พณิชยกุล)

รองอธิบดี ปฏิบัติราชการแทน

อธิบดีกรมทรัพย์สินทางปัญญา

ผู้ออกสิทธิบัตร

พนักงานเจ้าหน้าที่

หมายเหตุ
1. ผู้ทรงอนุสิทธิบัตรต้องชำระค่าธรรมเนียมรายปีเริ่มแต่ปีที่ 5 ของอายุสิทธิบัตร มิฉะนั้น อนุสิทธิบัตรจะสิ้นอายุ
2. ผู้ทรงอนุสิทธิบัตรจะขอชำระค่าธรรมเนียมรายปีล่วงหน้าโดยชำระทั้งหมดในคราวเดียวก็ได้
3. ภายใน 90 วันก่อนวันสิ้นอายุอนุสิทธิบัตร ผู้ทรงสิทธิบัตรมีสิทธิขอต่ออายุอนุสิทธิบัตรได้ 2 คราว มีกำหนดคราวละ 2 ปี โดยยื่นคำขอต่ออายุ
4. การอนุญาตให้ใช้สิทธิตามอนุสิทธิบัตรและการโอนอนุสิทธิบัตรต้องทำเป็นหนังสือและจดทะเบียนต่อพนักงานเจ้าหน้าที่

019237

รายละเอียดการประดิษฐ์

ชื่อที่แสดงถึงการประดิษฐ์

กลไกปรับแรงตึงในลวดสลิง

ลักษณะและความมุ่งหมายของการประดิษฐ์

กลไกปรับแรงตึงในลวดสลิงตามการประดิษฐ์นี้ เป็นกลไกที่สังเคราะห์แรงตึงในลวดสลิง ประกอบด้วย ตัวจับยึดลวดสลิงซึ่งสามารถเคลื่อนที่ในทิศทางตามความยาวของลวดสลิงได้ด้วยระยะทางที่จำกัดโดยการขันสลักเกลียวซึ่งฝังอยู่กับรูเกลียวของตัวจับยึดลวดสลิง การเคลื่อนที่ของตัวจับยึดลวดสลิงจะทำให้ปลายด้านที่ถูกจับยึดของลวดสลิงเคลื่อนที่ตามไปด้วย อันจะก่อให้เกิดการยืดตัวของลวดสลิงและเหนี่ยวนำให้เกิดแรงตึงในลวดสลิง

ความมุ่งหมายของการประดิษฐ์นี้ คือ การพัฒนากลไกซึ่งสามารถปรับแรงตึงในลวดสลิงได้ตามความต้องการ โดยที่กลไกมีขนาดกะทัดรัดและไม่ซับซ้อนเพื่อให้สามารถประยุกต์ใช้ในกลไกต่างๆ ที่มีการส่งผ่านแรงและการเคลื่อนที่ด้วยลวดสลิง

สาขาวิทยาการที่เกี่ยวข้องกับการประดิษฐ์

วิศวกรรมเครื่องกลในส่วนที่เกี่ยวกับกลไกปรับแรงตึงในลวดสลิง

ภูมิหลังของศิลปะหรือวิทยาการที่เกี่ยวข้อง

ลวดสลิงเป็นส่วนประกอบที่สำคัญของกลไกต่างๆ สำหรับการส่งผ่านแรงและการเคลื่อนที่จากที่หนึ่งไปยังอีกที่หนึ่ง ยกตัวอย่างเช่น ระบบการเคลื่อนที่ของลิฟท์ ระบบการเปลี่ยนเกียร์หรือระบบรอก เป็นต้น ในระบบเหล่านี้ ลวดสลิงจะต้องมีความตึงพอเหมาะเพื่อที่จะให้การส่งผ่านแรงและการเคลื่อนที่ด้วยลวดสลิงเป็นไปอย่างมีประสิทธิภาพ หากลวดสลิงหย่อนเกินไป มันจะไม่สามารถทำหน้าที่ส่งผ่านแรงและการเคลื่อนที่ได้ หากลวดสลิงตึงเกินไป มันจะทำให้ระบบเกิดการสั่นขณะที่มีการเคลื่อนที่ ในกรณีเลวร้ายที่สุด แรงตึงที่มากเกินไปจะทำให้ลวดสลิงขาดได้

ที่ผ่านมา ได้มีการประดิษฐ์คิดค้นกลไกปรับแรงตึงในลวดสลิง เพื่อประโยชน์ในงานต่างๆ มากมาย ตัวอย่างของงานที่เกี่ยวข้อง เช่น ระบบปรับและรักษาอัตราส่วนของแรงตึงในลวดสลิงด้วยกลไกคานหรือกลไกรอก (US. PAT. NO. 7,802,658) ระบบสร้างและปรับแรงตึงในลวดสลิงโดยอาศัยแรงน้ำหนักถ่วง (US. PAT. NO. 3,838,752) หรือแรงสปริง (US. PAT. NO. 6,193,017) เป็นต้น อย่างไรก็ตาม กลไกเหล่านี้มีความซับซ้อนและต้องการเนื้อที่มากในการติดตั้ง ซึ่งแตกต่างจากกลไกปรับแรงตึงในลวดสลิงของการประดิษฐ์นี้ ที่ไม่ซับซ้อน กินเนื้อที่ไม่มาก และมีชิ้นส่วนเพียงชิ้นเดียวเท่านั้น เพราะฉะนั้นจึงสามารถนำไปใช้ปรับแรงตึงในลวดสลิงในงานที่มีเนื้อที่จำกัดและไม่ต้องมีการบำรุงรักษามาก

คำอธิบายรูปเขียนโดยย่อ

รูปที่ 1 แสดงลักษณะของกลไกปรับแรงตึงในลวดสลิงตามการประดิษฐ์นี้

การเปิดเผยการประดิษฐ์โดยสมบูรณ์

ตามรูปที่ 1 แสดงลักษณะของกลไกปรับแรงตึงในลวดสลิงตามการประดิษฐ์นี้ ซึ่งประกอบด้วย ตัวจับยึดลวดสลิง (2) ซึ่งถูกบังคับให้มีการเคลื่อนที่แบบเลื่อนขนานในร่องเลื่อน (3) ณ ตัวจับยึดลวดสลิง (2) มีรูซึ่งทำเกลียวตัวเมีย (6) ไว้ เพื่อให้สลักเกลียว (7) ร้อยผ่านรูผ่าน (5) ของชิ้นส่วนของกลไกตัวขับ (4ข) ไปสู่รูเกลียวตัวเมีย (6) ซึ่งรูทั้งสองรูนี้ตรงศูนย์กันพอดี

ปลายด้านหนึ่งของลวดสลิง (1) ที่ต้องการปรับแรงตึง ถูกยึดติดกับตัวจับยึดลวดสลิง (2) ส่วนปลายอีกด้านหนึ่งของลวดสลิง (1) ถูกยึดติดกับชิ้นส่วนของกลไกตัวตาม (4ก) ซึ่งเคลื่อนที่ตามชิ้นส่วนของกลไกตัวขับ (4ข)

การทำงานของกลไกปรับแรงตึงในลวดสลิง

ในการประกอบชิ้นส่วนของกลไกปรับแรงตึงในลวดสลิงนี้ ตัวจับยึดลวดสลิง (2) จะถูกจัดให้อยู่ในตำแหน่งซึ่งทำให้ลวดสลิง (1) เกิดแรงตึงเบื้องต้นในระดับหนึ่ง ตลอดการทำงานของกลไกปรับแรงตึงในลวดสลิง หัวของสลักเกลียว (8) จะต้องยันกับชิ้นส่วนของกลไกตัวขับ (4ข) ตลอดเวลา สำหรับเกลียววนขวา เมื่อขันสลักเกลียว (7) ในทิศทางวนซ้ายจะทำให้ตัวจับยึดลวดสลิง (2) เคลื่อนที่แบบเลื่อนขนานในร่องเลื่อน (3) ในทิศทางเข้าหาหัวของสลักเกลียว (8) อันจะก่อให้เกิดการยืดตัวของลวดสลิง (1) และเหนี่ยวนำให้เกิดแรงตึงในลวดสลิง (1) เพิ่มขึ้น เมื่อขันสลักเกลียว (7) ในทิศทางวนขวาจะทำให้ตัวจับยึดลวดสลิง (2) เคลื่อนที่แบบเลื่อนขนานในร่องเลื่อน (3) ในทิศทางออกจากหัวของสลักเกลียว (8) อันจะก่อให้เกิดการหดตัวของลวดสลิง (1) และทำให้แรงตึงในลวดสลิง (1) ลดลง

วิธีการในการประดิษฐ์ที่ดีที่สุด

เหมือนกับที่ได้กล่าวมาแล้วในหัวข้อการเปิดเผยการประดิษฐ์โดยสมบูรณ์

ข้อถือสิทธิ

1. กลไกปรับแรงตึงในลวดสลิง ซึ่งประกอบด้วย ตัวจับยึดลวดสลิง (2) ซึ่งถูกบังคับให้มีการเคลื่อนที่แบบเลื่อนขนานในร่องเลื่อน (3) ณ ตัวจับยึดลวดสลิง (2) มีรูซึ่งทำเกลียวตัวเมีย (6) ไว้เพื่อให้สลักเกลียว (7) ร้อยผ่านรูผ่าน (5) ของชิ้นส่วนของกลไกตัวขับ (4ข) ไปสู่รูเกลียวตัวเมีย (6) ซึ่งรูทั้งสองรูนี้ตรงศูนย์กันพอดี

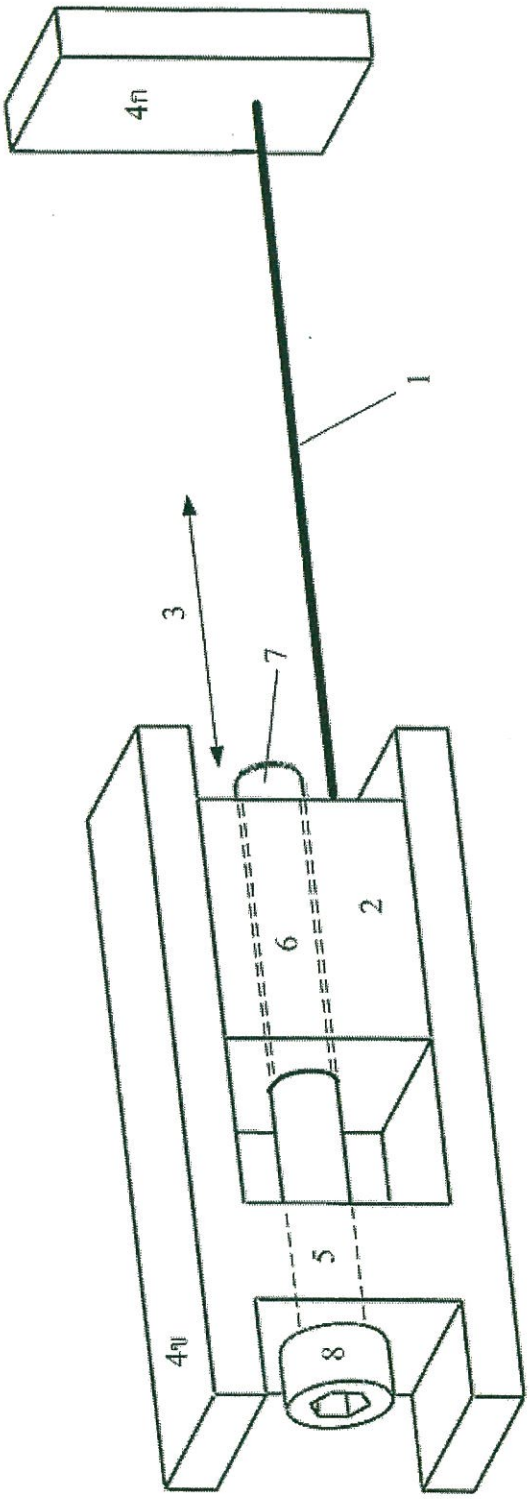

รูปที่ 1

บทสรุปการประดิษฐ์

การประดิษฐ์นี้เกี่ยวข้องกับกลไกซึ่งสามารถปรับแรงตึงในลวดสลิงได้ตามความต้องการ กลไกนี้ประกอบด้วยตัวจับยึดลวดสลิงซึ่งสามารถเคลื่อนที่ในร่องเลื่อน ในทิศทางตามความยาวของลวดสลิงได้ด้วยระยะทางที่จำกัดโดยการขันสลักเกลียวซึ่งฝังอยู่กับรูเกลียวของตัวจับยึดลวดสลิง การเคลื่อนที่ของตัวจับยึดลวดสลิงทำให้ปลายด้านที่ถูกจับยึดของลวดสลิงเคลื่อนที่ตามไปด้วย อันจะก่อให้เกิดการยืดตัวของลวดสลิงและเหนี่ยวนำให้เกิดแรงตึงในลวดสลิง

DRC011

Task Space Impedance Control of the Multi-Stage Cable-Pulley Driven Flexible Joint Robot System

Phongsaen Pitakwatchara

Department of Mechanical Engineering, Chulalongkorn University
Phyathai Road, Pathumwan, Bangkok 10330, THAILAND
phongsaen.p@chula.ac.th

Abstract

A task space impedance control law of the manipulator driven through the multi-stage flexible transmission unit is proposed. The controller utilizes the limited, yet mostly found in practice, information of the motor angle and current readouts only. With the elastic model of transmission system, motor current may be used to infer the transmitted torque to the robot. At the same time, its joint angle and joint velocity will be estimated via the stream of motor angle values. Altogether, they are used in the controller to generate the desired damping force and to shape the potential energy of the flexible joint robot system to the desired one. Experimental results are presented to validate the theoretical work.

Keywords*:* task space impedance control, flexible transmission, flexible joint robot, cable-pulley driven robot

1. Introduction

Appropriate impedance has an important role for the manipulators to successfully perform the tasks which require close interaction with the environment [1]. A famous Da Vinci® surgical robotic system [2] or most of the advanced robotic arms such as [3-5] employ the impedance control strategy in dealing with the imperfect information about the environment. An impedance model after the discrete mass-spring-damper system is popular among the more general functions between the motion and force variables.

There are many works reported about shaping the robot compliance to the desired values. However, only few works have attempted to control the impedance of the flexible joint robots. Reference [6] presented a simplified model of the flexible joint robot on which most of the proposed controllers are based. Early works such as [7] used a simple PD controller to tune the stiffness and damping behavior. The online gravity compensation was proposed instead of the constant set-point gravity compensation [8].

A tracking impedance controller based on singular perturbation analysis for the flexible DLR-II arm was proposed [9]. Later, a robust and stable impedance controller design using the passivity analysis was reported [10]. Recently, an adaptive impedance controller based on the function approximation technique (FAT) was applied to a flexible joint robot system with motor dynamics included [11]. However the controller requires measurement of the interaction force

other than the position and velocity of both the motors and the robot joints.

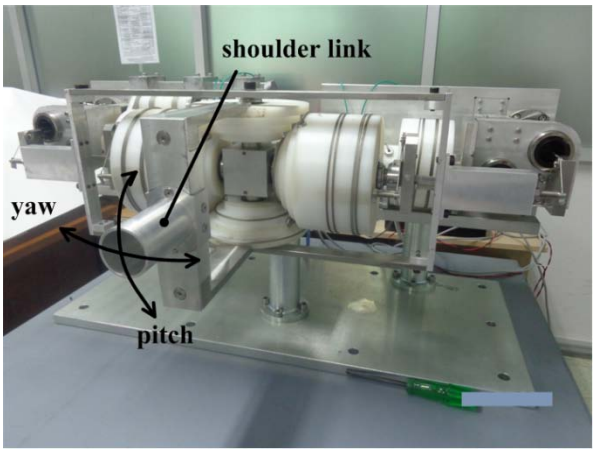

Fig. 1 A two-DOF multi-stage cable pulley-driven flexible joint robot

This research proposes a passive task space impedance controller for a flexible joint robot system driven through multi-stage nonlinear flexible transmission. A distinct feature is that it uses only the motor angle signal to regulate the stiffness and damping characteristics at the end effector. Motor current feedback may optionally be used to improve the system response time. The controller is implemented on a prototypical two DOFs cable-pulley driven flexible joint robot. The article is organized as follow. Section 2 describes the robot and develops its detailed model. Section 3 presents the task space impedance controller which enforces the desired viscoelastic behavior at the specified set point. The effectiveness of the controller is shown through several experiments in section 4. Finally, the conclusion is provided in section 5.

2. System Modeling

A two-DOF cable pulley-driven flexible joint robot, shown in Fig. 1, is constructed as a prototype to study the shoulder joint design of the whole arm for the ongoing service robot project. It comprises three mechanical subsystems; a rigid robot, a flexible transmission, and a counterbalance. The robot shoulder link is capable of moving in the pitch and yaw directions emulating the principle motion performed by the human shoulder. Hence the pitch and yaw angles, θ_p and θ_y, may be selected as the generalized coordinates describing the position of its end-tip. Figure 2 depicts the winch and pulley arrangement of the robot's multi-stage transmission subsystem conveying the motors' rotational motion to the pitch and yaw motion of the output shoulder link.

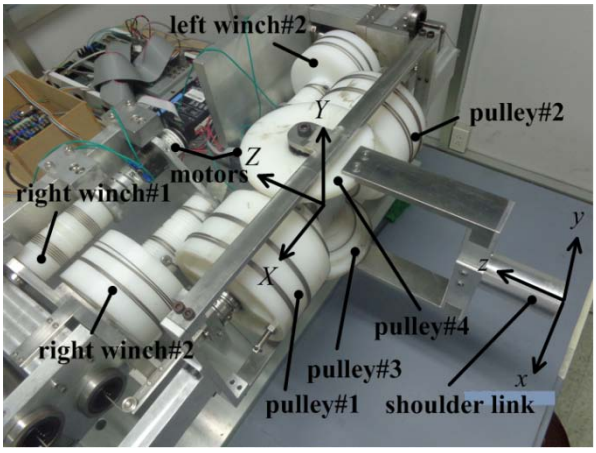

Fig. 2 Winch and pulley arrangement of the transmission unit for the flexible joint robot

Position vector of the shoulder link end-point relative to the origin of $\{XYZ\}$ described in $\{xyz\}$ is ${}^{\{xyz\}}r = [0 \quad 0 \quad -l_0]^T$, where l_0 is the shoulder link length. It may also be described in $\{XYZ\}$ as

$${}^{\{XYZ\}}r = [-l_0 s_y \quad l_0 s_p c_y \quad -l_0 c_p c_y]^T. \qquad (1)$$

The end-point velocity may then be determined readily as

$${}^{\{xyz\}}v_e = \left[-l_0\dot{\theta}_y \quad l_0\dot{\theta}_p c_y \quad 0\right]^T, \qquad (2)$$

which implies the Jacobian matrix

$$ {}^{\{xyz\}}J = \begin{bmatrix} 0 & -l_0 \\ l_0 c_y & 0 \\ 0 & 0 \end{bmatrix}. \quad (3) $$

Moving parts of the robot are pulley#3, pulley#4, and the shoulder link. They may be grouped into two categories for those undergoing pitching motion alone and the others undergoing a composite pitching and yawing motion. The associated kinetic and gravitational potential energy of each collection is determined. Furthermore, the elastic potential energy of the counterbalancing spring [12] has been accounted to form the Lagrangian of the whole system

$$ L(q, \dot{q}) = T_p + T_{py} - V_p - V_{py} - V_{sp}. \quad (4) $$

Detailed expression of each term is reported in [13]. Evaluating the Lagrangian formulation along the generalized coordinates q, dynamical model of the robot may be obtained in the following form:

$$ M(q) + C(q, \dot{q}) + f + g(q) = \tau_{dr} + \tau_e. \quad (5) $$

The model includes the frictional torque f and explicitly splits the interaction torque on the robot by the environment, τ_e, from the actuated torque by the transmission unit, τ_{dr}.

Flexibility of the transmission system might be governed by the torque-angle $(m - \theta)$ deflection equation of the simple cable-pulley unit [13];

$$ \theta = \frac{T_0}{EA\mu}\left[\left(\frac{me^m}{e^m - 1} - 1\right)(1 + GF) - \log\frac{me^m}{e^m - 1}\right]. \quad (6) $$

This basic model is further elaborated to handle the flexibility of the differential unit [13]. Recognizing the cascading interconnection of the cable-pulley units, the overall flexibility may be obtained by adding these compliances together. Moreover, the significant frictional torque developed at the bearings have been taken into consideration as well. With the knowledge of these sub-models, the realistic model of the robot may be derived using the bond graph modeling technique [14]. The complete bond graph diagram is depicted in Fig. 3.

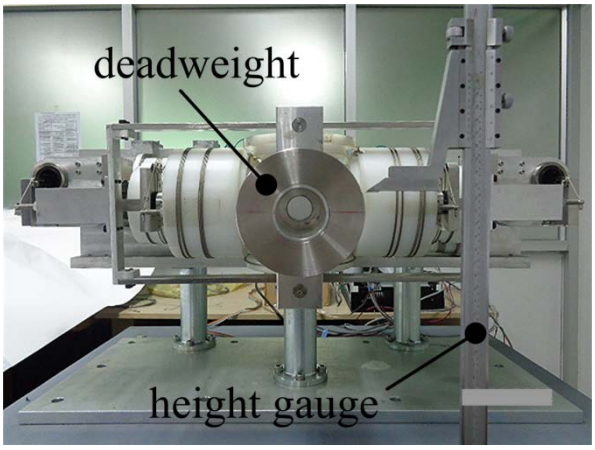

Fig. 4 Robot with the 1.0 kg proof mass attached

3. Task Space Impedance Control

The proposed impedance controller will modulate the robot end effector impedance to achieve the following task space impedance dynamics;

$$ \Lambda(x)\ddot{\tilde{x}} + (\mu(x, \dot{x}) + D_d)\dot{\tilde{x}} + K_d\tilde{x} = F_e, \quad (7) $$

where x is the task space coordinates and $\tilde{x}$ the coordinate errors of x from the set point x_d. D_d and K_d are the desired task space damping and stiffness. According to the robot dynamics Eq. 5, the desired impedance dynamics may be achieved with the control law

$$ \tau^*_{dr} = g(q) - J(q)^T(K_d\tilde{x} + D_d\dot{x}), \quad (8) $$

where the star-mark denotes the desired value deviating from the actual one due to the uncompensated motor and drivetrain dynamics.

Unfortunately, the link angles and the end effector coordinates are not measurable. Rather, the estimated stationary value of the link angles q_s and the end effector coordinates $f(q_s)$ shall be used instead. This results in the modified control law [13]

$$ \tau^*_{dr} = g(q_s) - J(q_s)^T K_d(f(q_s) - x_d) $$

$$-\left[J(q_s)^T D_d\big(f(q_s)\big)J(q_s)\right]^{\frac{1}{2}}\vartheta, \quad (9)$$

in which q_s are determined recursively from the measured motor angles θ_0 through the quasi-static model of the drivetrain by

$$q_s = T_{q1}\theta_0 - e_{1q}^{-1}\big(g(q_s) - J(q_s)^T K_d\big(f(q_s) - x_d\big)\big). \quad (10)$$

$e_{1q}^{-1}(\cdot)$ is the overall effective nonlinear deformation function of the transmission unit, T_{q1} is its compound transmission ratio, and $f(\cdot)$ denotes the forward kinematics mapping of the robot. The term

$$\vartheta = sG(s)\left[J(q_s)^T D_d\big(f(q_s)\big)J(q_s)\right]^{\frac{1}{2}} T_{q1}\theta_0 \quad (11)$$

represents the estimation of the filtered link joint velocity scaled by the square root of the joint space symmetric damping matrix.

Due to the lack of the complete system state information, the motor torque corresponding to the desirable torque may be computed by

$$(\tau_m)_{dr}^* = T_{q1}^T\,\tau_{dr}^*. \quad (12)$$

Furthermore, if the value of the transmitted torque from the drivetrain to the robot τ_1 is available, the following motor torque

$$\tau_m^* = B_1 B_{1r}^{-1}(\tau_m)_{dr}^* + (I - B_1 B_{1r}^{-1})\,\tau_1 \quad (13)$$

will effectively reduce the motor torque inertia from B_1 to B_{1r} in addition to modulating the end effector impedance. If the torque measurement is not available, the value may be estimated from the motor angle and current measurement. Passivity and stability of the closed loop system comprised of Eq. 5, 9, 10, 11, 12, and 13 have been shown in [15].

4. Experiments

Various experiments have been conducted to investigate the effect of the control parameters on the system response and to illustrate the effectiveness of the control law. Due to the discrete implementation of the controller and the unmodeled dynamics, the achievable desired stiffness and damping ratio are 500 N/m and 0.6 using the simple low-pass filter $G(s) = \frac{65}{s+65}$ for the robot joint velocity estimation. Moreover, the motor current has been limited to 3.5 A for safety reason.

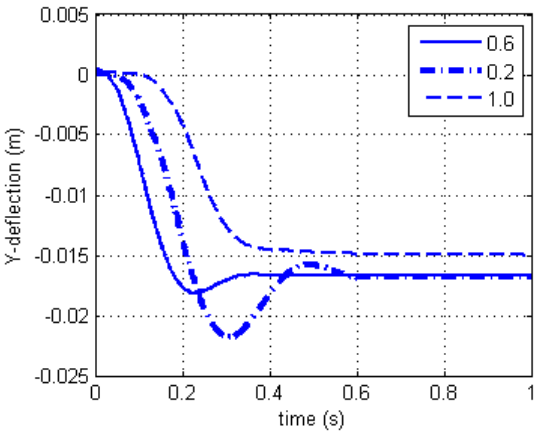

Fig. 5 Deflection of the robot end tip subject to 1.0 kg proof mass with the stiffness of 500 N/m

4.1 Task Space Stiffness and Damping

To verify that the desired task space stiffness is actually achieved, the robot is regulated using the proposed controller and the proof mass of 1.0 kg is placed at the end of the shoulder link to realize a constant external force in the negative Y-direction, as shown in Fig. 4. The default stiffness with a family of damping ratios are set to perform the experiment. Figure 5 depicts the estimated deflection responses. The behavior conforms to that of a typical mass-spring-damper system. From the graph, the environment may feel the robot be stiffer than the actual value when too high damping is tuned. Note the actual end tip static deflection is measured by the vernier height gauge. The values are closed to the estimated one with small error bound of ±1.25 mm for the 315 mm link length. Hence the

stationary position estimation can practically be used as the replacement for the actual value.

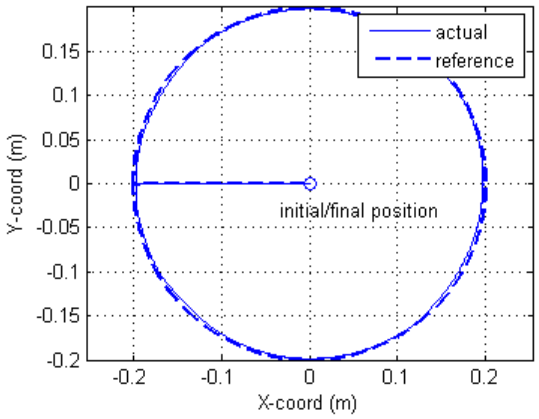

Fig. 6 Free motion tracking of a circular path

4.2 Trajectory Tracking

Although the controller is synthesized to handle for only the regulation task, the following experiment demonstrates that it also works quite well for the tracking task with moderate speed. A circular path of 20.25 cm is generated for the robot to follow with the constant speed of 6.36 cm/s; thus the tracking is completed in 20 seconds. Figure 6 displays the tracking of the robot against the reference path. It is seen that the actual robot motion is capable of tracking the desired trajectory faithfully. The average of the integral of the absolute error (ITAE) is used to measure the tracking error quantitatively. The value is 6.5 mm, which might further be reduced by fine tuning the task space stiffness and damping parameters.

Practically with this controller, the flexible robot system is capable of displaying the desired impedance behavior during the tracking motion as well. Previous circular path is commanded to the robot with the 1.0 kg proof mass attached to the end. Tracking result is depicted in Fig. 7. According to relatively weak stiffness of 500 N/m against the constant 10 N load, apparent deviation from the reference path is observed. Tracking error degrades to 16.8 mm. At the end of the tracking, the end effector departs from the reference by 17.6 mm while the ideal value is 19.6 mm. Hence the controlled robot exhibits the desired impedance characteristics during the general motion.

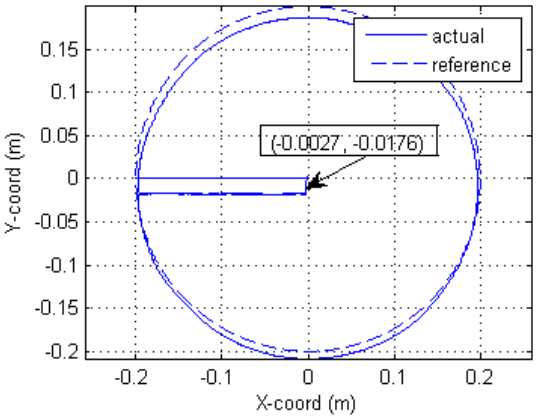

Fig. 7 Circular path tracking subject to 1.0 kg proof mass with the stiffness of 500 N/m

5. Conclusions

This work develops a task space impedance control of the manipulator driven through the multi-stage flexible transmission unit. The controller regulates the stiffness and damping of the end effector at the specified position based on the available feedback signal of the motor angle and current. Motor angle is used to compute the estimation of the robot link angle and joint velocity based on the stationary elastic model. These values are employed in the traditional impedance control law. Optionally, the motor current might be used to determine the transmitted torque, which helps reducing the motor inertia. It can be shown that the controller effectively shapes the system potential energy to the one of the desired task space compliance.

A two DOF cable-pulley driven flexible joint robot as the embodiment of the manipulator driven through the multiple stages flexible transmission unit is regulated with the proposed controller. Detailed model of the robot is derived for the purpose of system simulation. From the experiments, the controlled system yields satisfactory results of displaying the desired impedance during general task execution. Therefore this practical controller will be helpful in accomplishing real-world manipulation of the flexible robot system.

6. Acknowledgement

This work is partially supported by the grants from the Ratchadaphiseksomphot Endowment Fund of Chulalongkorn University (RES560530224-AS), the Thailand Research Fund (MRG5580227 and MSD56I0018), the ISUZU Research Foundation, and Department of Mechanical Engineering, Chulalongkorn University.

7. References

[1] Hogan, N. (1985). Impedance Control: An Approach to Manipulation, *Trans. ASME J. Dynamic Systems, Measurement, and Control*, 107(1), pp. 1-24.

[2] Guthart, G. S. and Salisbury, J. K. (2000). The Intuitive® Telesurgery System: Overview and Application, *Proc. IEEE Int. Conf. Robotics and Automation*, pp. 618-621.

[3] Rooks, B. (2006). The Harmonious Robot, *Int. J. Industrial Robot*, 33(2), pp. 125-130.

[4] Albu-Schaffer, A., et al. (2007). The DLR Lightweight Robot – Design and Control Concepts for Robots in Human Environments, *Int. J. Industrial Robot*, 34(5), pp. 376-385.

[5] Wyrobek, K. A., et al. (2008). Towards a Personal Robotics Development Platform: Rationale and Design of an Intrinsically Safe Personal Robot, *Proc. IEEE Int. Robotics and Automation*, pp. 2165-2170.

[6] Spong, M. W. (1987) . Modeling and Control of Elastic Joint Robots, *Trans. ASME J. Dynamic Systems, Measurement, and Control*, 109(4), pp. 310-319.

[7] Tomei, P. (1991). A Simple PD Controller for Robots with Elastic Joints, *IEEE Trans. Automatic Control*, 36(10), pp. 1208-1213.

[8] Zollo, L., et al. (2005). Compliance Control for an Anthropomorphic Robot with Elastic Joints: Theory and Experiments, *Trans. ASME J. Dynamic Systems, Measurement, and Control*, 127(3), pp. 321-328.

[9] Albu-Schaffer, A., et al. (2003). Cartesian Impedance Control of Redundant Robots: Recent Results with the DLR-Light-Weight-Arms, *Proc. IEEE Int. Conf. Robotics and Automation*, pp. 3704-3709.

[10] Ott, C., et al. (2008). On the Passivity-Based Impedance Control of Flexible Joint Robots, *IEEE Trans. Robotics*, 24(2), pp. 416-429.

[11] Chien, M. C. and Huang, A. C. (2012). Adaptive Impedance Controller Design for Flexible-Joint Electrically-Driven Robots without Computation of the Regressor Matrix, *Robotica*, 30(1), pp. 133-144.

[12] Pitakwatchara, P. (2012). Spring-Cable Counter-Balancing System for Pitch-Yaw Compound Joint Mechanism, *Thailand Patent Office*, Pat. Pend. #1201002792, Filed on June 12, 2012.

[13] Pitakwatchara, P. (2014). Modelling and Control of the Multi-stage Cable Pulley-driven

Flexible-joint Robot, *Int. J. Adv. Robotic Systems*, 11:118, pp. 1-16. (doi: 10.5772/58697)

[14] Karnopp, D. C., et al. (2006). System Dynamics: Modeling and Simulation of Mechatronic Systems, John Wiley & Sons, NY.

[15] Pitakwatchara, P. (2015). Task Space Impedance Control of the Manipulator Driven Through the Multi-Stage Nonlinear Flexible Transmission, *The ASME J. Dynamic Systems, Measurement, and Control*, 137(2), pp. 1-17. (doi: 10.1115/1.4028252)

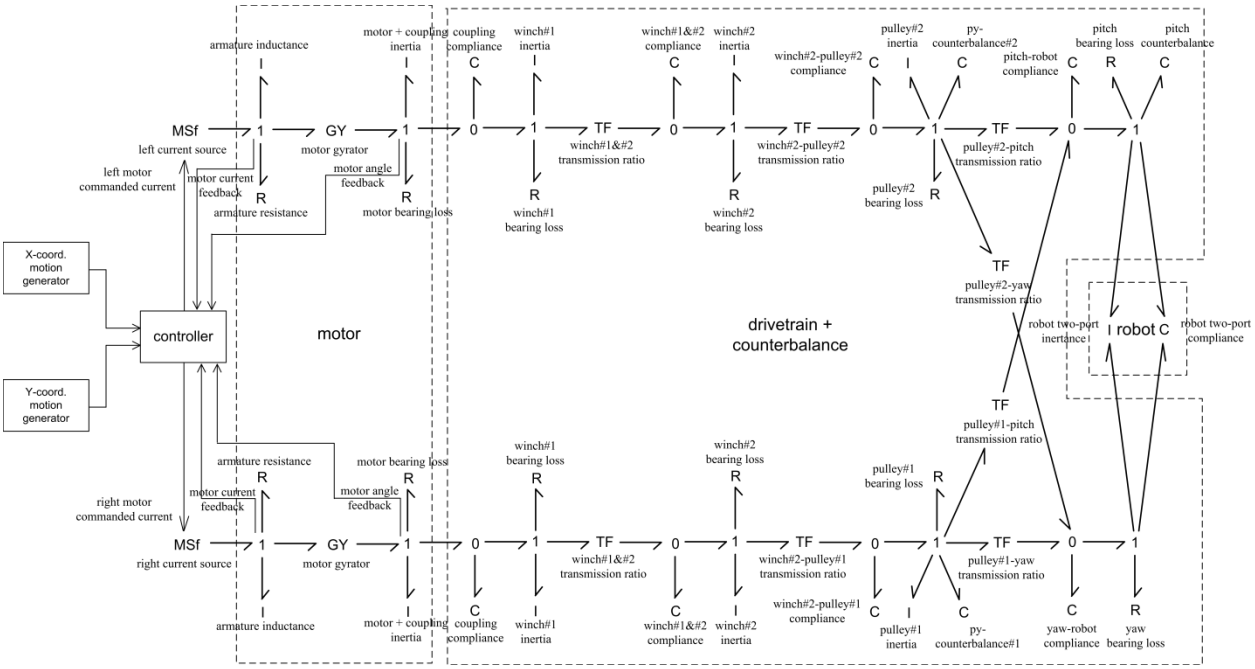

Fig. 3 Complete bond graph diagram of the two-DOF cable pulley-driven flexible joint robot controlled system

The 4th TSME International Conference on Mechanical Engineering
16-18 October 2013, Pattaya, Chonburi
sea of Innovation TSME-ICoME 2013
DRC-1004

Kinematical Design of a General-Purpose Service Robot Arm Based on the Mobility Consideration

Chatchaiwat Lowakij and Phongsaen Pitakwatchara*

Department of Mechanical Engineering, Faculty of Engineering
Chulalongkorn University, Bangkok, THAILAND 10330
*Corresponding Author: E-mail: phongsaen.p@chula.ac.th

Abstract

An aspect in the design and analysis of a four degrees-of-freedom (DOF) anthropomorphic arm is described in this paper. Major parts of the arm, which is affixed to the trunk, are the three DOF shoulder joint, the upper arm, the one DOF elbow joint, and the lower arm. Inspired by the anatomy of the human arm, kinematic structure of the robot arm may be designed with the joint arrangement of yaw-pitch-roll-pitch (YPRP) or roll-pitch-roll-pitch (RPRP). Accordingly, the kinematic manipulability and the kinematic isotropy indices are employed as one guideline in designing the arm structure that is most suitable for the prescribed task. Furthermore, these indices suggest the optimal ratio of the arm's link lengths.

Keywords: anthropomorphic arm, kinematic Isotropy, kinematic manipulability

1. Introduction

Current usage of the robots has been gradually shifted from the industrial to the service sector. Regarding to the statistical data from the IFR: "In 2011, about 2.5 million service robots for personal and domestic use were sold, 15% more than in 2010. The value of sales increased by 19% to US$636 million", Moreover, IFR has estimated that service robots for personal use could be sold 15.6 million units in 2012-2015 [1].

Although Thailand in today is still far from the practical demand of the service robots, mainly because of the rather inexpensive labor payment. Nevertheless, the percentage of the aging people in the country is increasing. By 2030, the number of the elderly is expected to be at 25% of the country population [2]. Therefore, it is foreseen that Thailand is turning toward the shortage of the working class and high wages very soon. The situation will eventually lead to the use of the service robots in general daily tasks.

Service robots are designed to perform daily tasks for human. Therefore the robot arm should be designed based on the human arm, both the size and the structural configuration.

Section 2 describes two types of the anthropomorphic arms, i.e. the yaw-pitch-roll-pitch (YPRP) and the roll-pitch-roll-pitch (RPRP) joint configurations. Accordingly in section 3, two indices of the manipulability index and the inverse condition number index are evaluated on each type of arm. These indices are related to the end effector mobility which show how well the arm can perform the various tasks of daily service. In the following section, MATLAB script files are written to determine the best indices based on the proposed indices. Additionally, the best arm

configuration and its optimal length ratios can be drawn. Lastly, section 5 concludes the study.

2. Arm Configuration

This research describes an aspect in the kinematical design and analysis of a four-degree-of-freedom (DOF) anthropomorphic structured service robot arm. Anthropomorphic arm has the structure which resembles that of the human arm. Major components of the human arm, in order from top to bottom, are the shoulder, the upper arm, the elbow, the lower arm, the wrist and the hand. This preliminary investigation focuses on the gross motion of the arm. Hence the wrist and the hand will be excluded, resulting in a four-DOF arm. The shoulder joint is simplified to a compound three-DOF joint implemented by a revolute joint and a differential cable-pulley mechanism. For the elbow joint, it is accounted by a simple revolute joint.

Three DOF shoulder joint may be implemented in several ways, of which two arrangements are studied as follow.

2.1 Yaw-Pitch-Roll-Pitch (YPRP)

YPRP is the arm in which the first three revolute joints, arranged in yaw-pitch-roll (YPR) direction, replicate the shoulder joint motion and the last revolute joint for the elbow one. Fig. 1 illustrates the conceptual YPRP arm. The arm of the PR2 robot from Willow Garage [3] is an example that employs this kinematical structure.

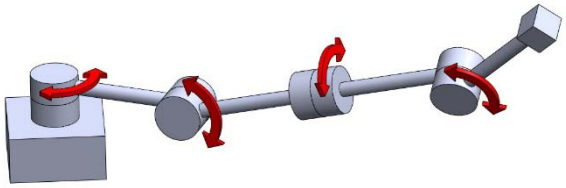

Fig. 1 YPRP-arm configuration

2.2. Roll-Pitch-Roll-Pitch (RPRP)

RPRP is the arm in which the first three revolute joints, arranged in roll-pitch-roll (RPR) direction, replicate the shoulder joint motion and the last revolute joint for the elbow one. Fig. 2 illustrates the conceptual RPRP arm. Several robots such as the ASIMO humanoid robot from Honda [4] are designed with this joint arrangement.

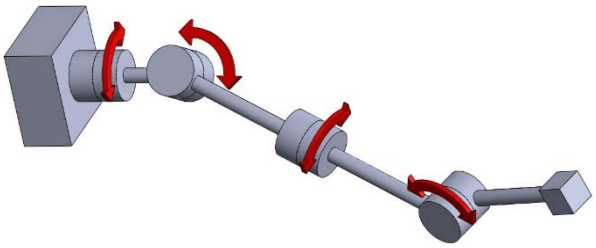

Fig. 2 RPRP-arm configuration

3. Mobility Evaluation

Robot arm may be evaluated by several criteria such as capable payload, precision, repeatability, manipulability, and kinematic isotropy. As a consequence, which index will be used for depends on a particular employment of the robot.

Since the arm is to be designed for performing the general household tasks, e.g. writing, picking and placing an object, or house cleaning, it should have ability to move in any direction equally well. This is quite difficult to realize, however. By observation, human tends to maintain the motion in the horizontal plane rather than to change the height level during the task execution. Thus, it is preferable for the arm to easily move in the horizontal direction more than in others. Accordingly, the robot manipulability [5] and kinematic isotropy [6] indices shall be used to evaluate such desired capability. In brief, the manipulability index

describes the ability of the arm to move in each direction. Closely related, the kinematic isotropy indicates the ability of the arm to move in arbitrary direction equally well.

Evaluation of both indices require computing the singular values of the robot Jacobian matrix. This can be achieved by the singular value decomposition (SVD). Because the elements in the 3x4 Jacobian matrix are rather complex, it is not possible to solve for the singular values in closed form. Thus, numerical method will be used to determine the singular values. Specifically, the MATLAB scripts are written to evaluate both indices at samples of the points in the robot workspace. Details of the algorithm are explained in section 4.

Generally, the SVD decomposed any matrix J into the multiplication of three matrices, i.e.

$$\mathrm{J} = \mathrm{U}\Sigma\mathrm{V}^{\mathrm{T}}, \qquad (1)$$

where the matrix U contain the eigenvectors corresponding to the singular values that are placed in the matrix Σ along its diagonal elements

$$\Sigma = \begin{bmatrix} \sigma_1 & 0 & 0 & 0 \\ 0 & \sigma_2 & 0 & 0 \\ 0 & 0 & \sigma_3 & 0 \end{bmatrix},$$

sorting in the descending order.

Singular values of the Jacobian matrix indicate the mobility along the principal directions of the rotated ellipsoid corresponding to the eigenvectors. These two quantities may be used to construct the ellipsoid which represent the manipulability of the end effector at a particular point. Image of the ellipsoid is good for qualitative comparison. Several indices which reflect different characteristics of the robot motion are proposed. Two commonly used indices are

1. Robot manipulability (w) is defined as

$$w = \sigma_1\sigma_2\sigma_3, \qquad (2)$$

representing the volume of the ellipsoid. Thus it reflects the overall mobility of the end effector.

2. Inverse condition number (icn) is defined as

$$icn = \frac{\sigma_3}{\sigma_1}, \qquad (3)$$

this index indicates the roundness of the ellipsoid. In effect, the closer the value to one (from below), the closer the ellipsoid become the sphere, showing the ability of the end effector to move in any direction equally well.

4. Analysis and Evaluation

4.1 Manipulability

Manipulability and inverse condition number may be used as the criteria in selecting the appropriate joint arrangement of the robot arm. Both indices will be evaluated at various arm postures throughout the workspace. This is achieved by varying the joint angles at every 15°-step and determine the indices according to the changing Jacobian matrix. Following is the pseudo-code of such calculation.

```
Define all link length
for t1 = limit-:15deg:limit+
   for t2 = limit-:15deg:limit+
      for t3 = limit-:15deg:limit+
         for t4 = limit-
         :15deg:limit+
            Calculate Jacobian(J)
            Calculate SVD(J)
            Calculate W
            Calculate Icn
            Draw Arm
            Label Indexes
            Save the picture
         End
      End
   End
End
```

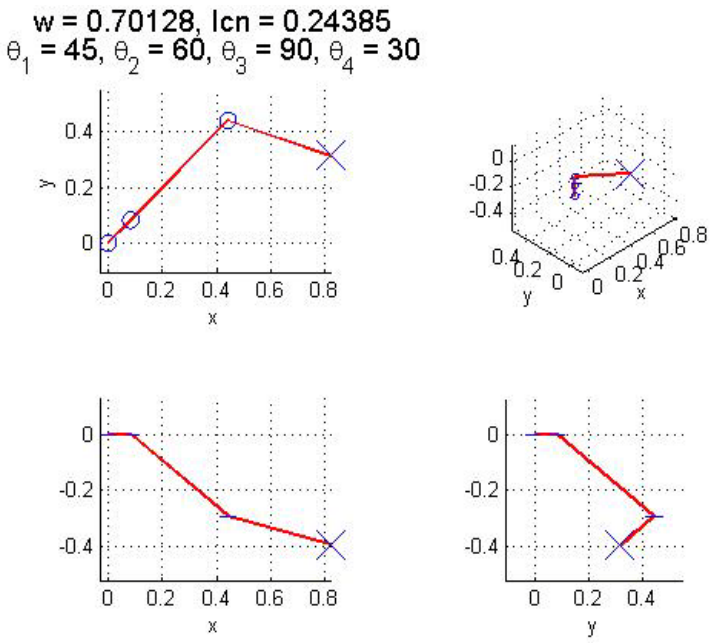

Fig. 3 Example Result

After that, the SVD is performed to determine its singular values and the eigenvectors. The manipulability and the inverse condition number indices are calculated along with. The arm posture is drawn as well. The algorithm reruns at the new joint angles varying by 15° step for the entire workspace. An example of the arm posture along with its indices and joint angle values is shown in Fig. 3.

From the analysis, it is seen that the mobility of both RPRP and YPRP are very similar. Therefore, the average values of the indices for both arms over their workspace are determined. Average values of w for the YPRP and RPRP are 0.6731 and 0.6733, while the averages of Icn are 0.3852 and 0.3683, respectively.

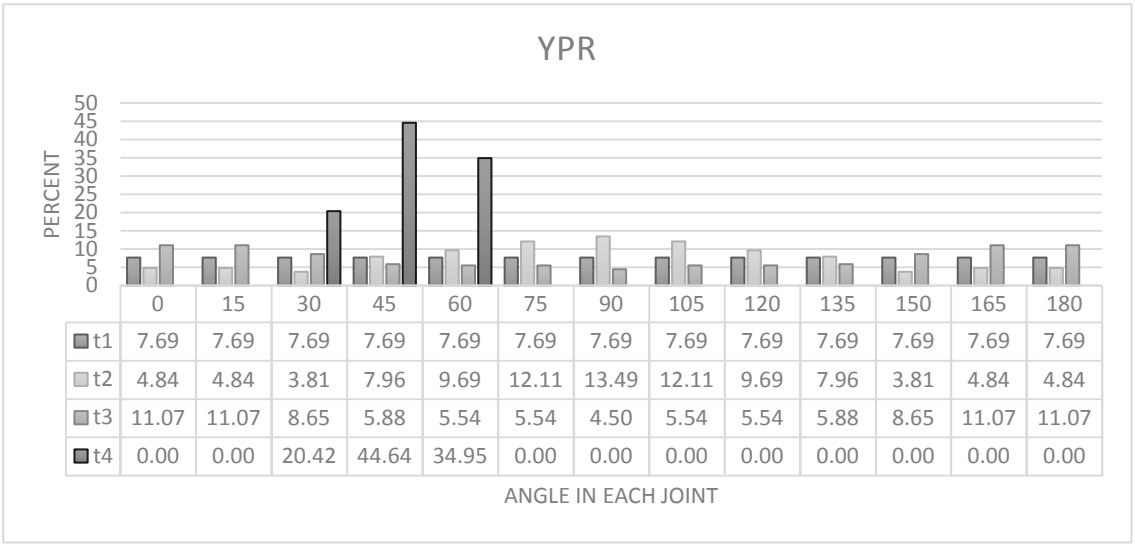

	0	15	30	45	60	75	90	105	120	135	150	165	180
t1	7.69	7.69	7.69	7.69	7.69	7.69	7.69	7.69	7.69	7.69	7.69	7.69	7.69
t2	4.84	4.84	3.81	7.96	9.69	12.11	13.49	12.11	9.69	7.96	3.81	4.84	4.84
t3	11.07	11.07	8.65	5.88	5.54	5.54	4.50	5.54	5.54	5.88	8.65	11.07	11.07
t4	0.00	0.00	20.42	44.64	34.95	0.00	0.00	0.00	0.00	0.00	0.00	0.00	0.00

Fig. 4 Histogram of YPRP-arm four joint angles that provide both indices bigger than 60% of its maximum at various posture

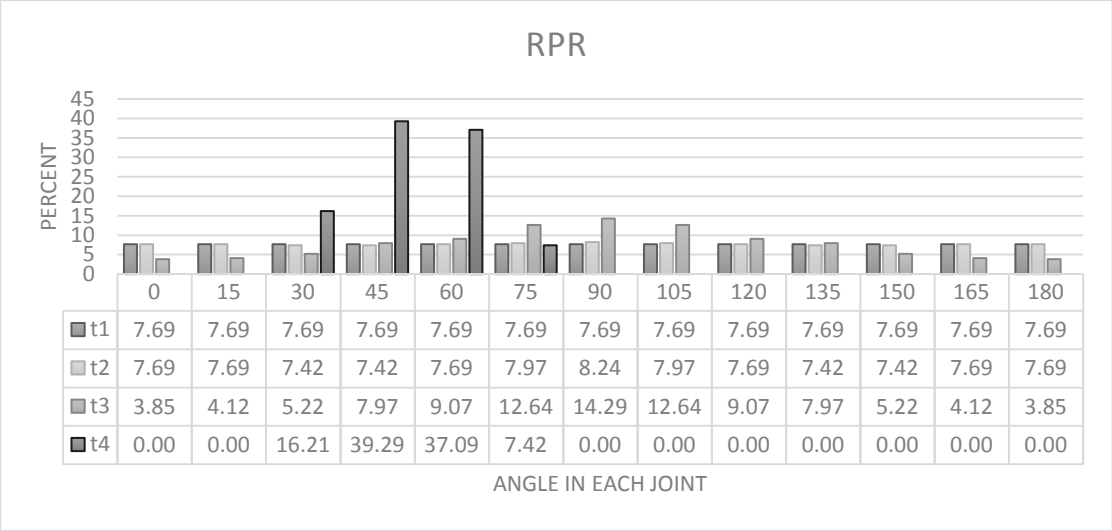

Fig. 5 Histogram of RPRP-arm four joint angles that provide both indices bigger than 60% of its maximum at various posture

Hence it is difficult to decide which arm configuration will be more agile. To resolve the problem, a detailed analysis in determining the set of the joint angles which produce the index values greater than 60% of the maximum has been performed. Histogram charts are depicted in Fig. 4-5. to show the frequency of such joint angles

From the graph, frequency of θ_1 is equally spread over its range. Hence the angle of the first joint has no effect to both indices. However, for the YPRP arm to possess good mobility, θ_2 should fall in the range of about $75°$ to $105°$, while θ_3 be around $0°$ and $180°$. Good mobility for the RPRP, on the other hand, will occur when θ_2 is about $90°$ and θ_3 falls in the range of about $75°$ to $105°$. For the angle θ_4, the histogram shows that it is highly concentrated around $45°$ to $60°$ for both arms. Therefore the elbow angle θ_4 is the most influential parameter among the joint angles.

According to the above results, it can't conclude which arm will perform better. Most of the take perform by the service robot have the end-effector motion executed in the horizontal plane, e.g. household work or the table-top work. By the serial configuration of the arm, the first joint will make the end-effector move with the longest range, due to the longest length from joint to end effector. For the RPRP, the first joint axis is in the horizontal direction hence the rotation from this joint will cause the end-effector to move mainly in the vertical plane. On the other hand, that first joint of YPRP lies in the vertical direction. Therefore, its rotation will make the end-effector to move in the horizontal plane corresponding to the major plane of many service tasks. (Fig. 6-7)

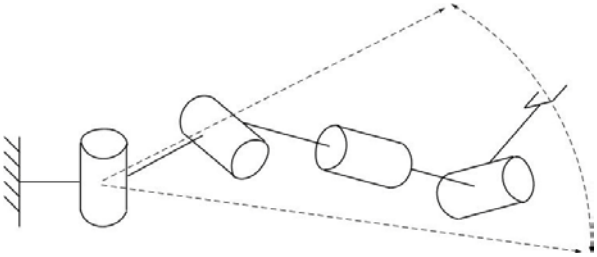

Fig. 6 Motion range of RPRP when the first joint is actuated

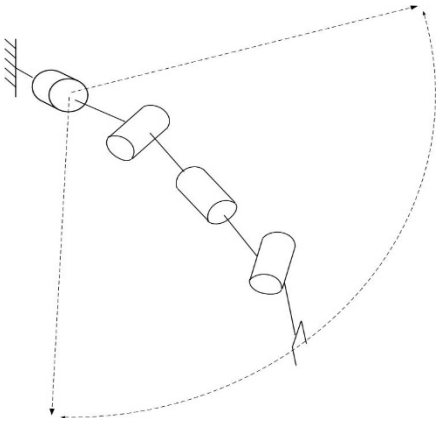

Fig. 7 Motion range of RPRP when the first joint is actuated

4.2 Arm length ratio

After the arm configuration of YPRP is chosen, it is then necessary to determine the appropriate lengths for the shoulder, the upper arm, and the forearm section. Partially, they are constrained by the desirable workspace. Additionally, they should be designed to provide the arm with good mobility. For the latter purpose, previous indicators as the manipulability and inverse condition number indices may be used.

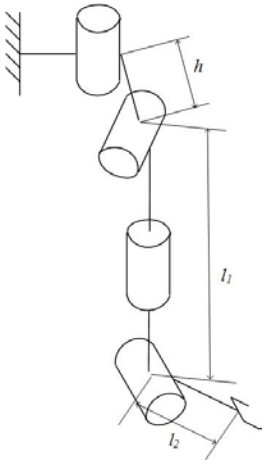

Fig. 8 YPRP-arm showing the symbolic lengths of each segment

In the following, the arm length ratio (Fig. 8) of $h:l_1:l_2$, that provides the highest overall index values, will be determined. Here, the representative index for the whole workspace is chosen to be the average of the sum of the index at every point in the workspace. A MATLAB script has been written to determine such values.

The script starts by assigning the length ratios of the arm segments h, l_1, and l_2, with l_1 preset to be 1. Next the actual lengths of h', l_1' and l_2', according to these ratios are determined from the constraint that the total length of the arm is 0.6m. With the arm lengths completely specified, the algorithm runs at discrete locations of the end effector throughout the workspace. For each position, the inverse kinematics is performed to determine the corresponding joint angles. Since the robot is redundant, the first joint angle θ_1 will be assigned to be a value varying from 0 to π at $15°$ step. In addition, the robot Jacobian is determined and the SVD is performed. Thus, the manipulability and the inverse condition number may then be calculated. These values are compared to determine the peak. Also, they are summed over the workspace to obtain their average values. The whole calculation is repeated for a new arm segment ratios. For visualization purpose, both index values are plotted on the surface over the range of h and l_2 in Fig. 9-10.

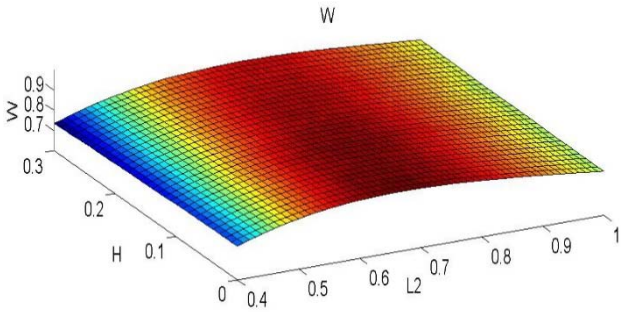

Fig. 9 Index W against h and l_2

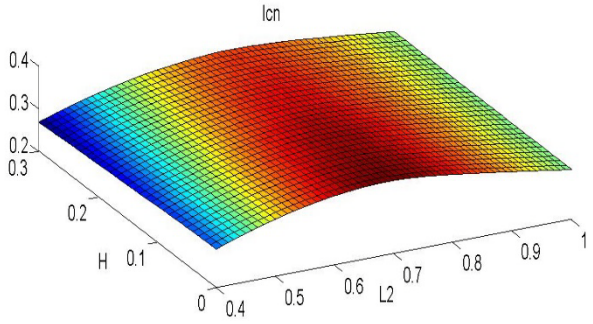

Fig. 10 Index Icn against h and l_2

From Fig. 9-10 the increase in h affect the index values, making them decrease by a small value. However the change of l_2 influence the index value significantly. At l_2 = 0.66 the value of W is maximized to 0.90335 while Icn index is 0.37227, and at l_2 = 0.71, the value of Icn is maximized to 0.37289 while W index is dropped 0.90064. The result show that both index values are nearly the same in either case. Therefore, it may be concluded that the round-off arm length ratio of 0:1:0.7 will optimize the mobility of the manipulator.

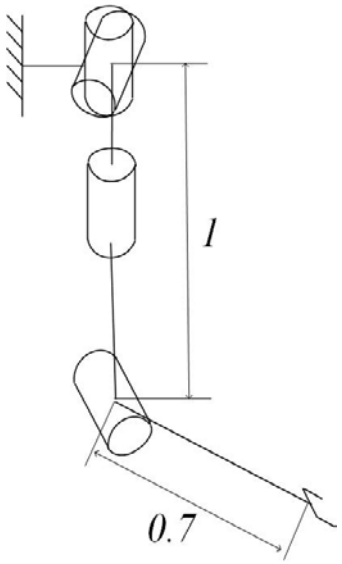

Fig. 8 YPRP-arm viewed from the side, drawn with the actual length ratios.

5. Conclusion

Mobility study of the RPRP and YPRP arm configurations does not yield the conclusive result of which arm performs better. However, the YPRP arm structure can produce the gross motion in the horizontal plane by the first joint rotation. Therefore, the YPRP arm configuration is employed in designing the arm for general service tasks.

Appropriate lengths for the shoulder, the upper arm, and the forearm section are designed based on the maximization of the mobility indices throughout the workspace. From the analysis, the appropriate ratio is 0:1:0.7.

In summary, this work presents the kinematical design of the general-purpose service robot arm. The YPRP configuration is selected and the arm consists of two main joints: the shoulder and the elbow joint. The complex shoulder joint is kinematically equivalent to the three consecutive revolute joints arranged in the yaw-pitch-roll configuration. The elbow joint is simply a revolute joint connecting the upper arm and the forearm. The arm length ratio for the shoulder to the upper arm to the forearm of 0:1:0.7 yields superior mobility than other designs.

Acknowledgements

This work is generously supported by the grants from the Ratchadaphiseksomphot Endowment Fund of Chulalongkorn University (RES560530224-AS), the Thailand Research Fund (MRG5580227 and MSD56I0018), the ISUZU Research Foundation, and Department of Mechanical Engineering, Chulalongkorn University.

6.Reference

[1] IFR International Federation of Robotics, statistic data, URL: http://www.ifr.org/service-robots/statistics/ , access on 28/06/2013

[2] Foundation of Thai Gerontology Research and development institute (TGRI), Situation of the Thai elderly (2010), *Annual Report 2010*

[3] Willow Garage, Spec Sheet, URL: http://www.willowgarage.com/pages/pr2/specs, access on 28/06/2013

[4] American Honda Motor Co. Inc. Corporate affairs & Communication, “Asimo the Honda humanoid robot,”American Honda Motor Co. Inc., Technical Information, 2003.

[5] Yoshikawa, T.: Manipulability of robotic mechanisms, Int. J. Robotics Res. Vol. 4(2), June 1985, pp. 3-9.

[6] Angeles, J. and Lopez-Cajtin, C. S.: Kinematic isotropy and the conditioning index of serial robotic manipulators, Int. J. Robotics Res. Vol. 11(6), December 1992, pp. 560-571.

Paper ID
DRC1009

The 3rd TSME International Conference on Mechanical Engineering
October 2012, Chiang Rai

Control of a Two-Degree of Freedom Cable Driven Compound Joint System: Preliminary Results

Phongsaen Pitakwatchara

Department of Mechanical Engineering, Faculty of Engineering
Chulalongkorn University, Bangkok, THAILAND 10330
Email: phongsaen.p@chula.ac.th

Abstract

This is an ongoing work on the two-degree of freedom cable driven compound joint system. Construction of the prototype has been completed and currently the work on controlling this system has just begun. Here some preliminary results are reported. Namely, a simple Proportional-Derivative (PD) controller on the individual motor is designed and tuned based on the motor's model solely. Then, this same controller is applied to drive the compound joint system according to the desired motion. The resulting response from even such this simple controller is quite satisfactory, not surprisingly thanks to the well-designed of the system dynamics. Overall, the closed loop system is passively stable and hence can interact with the passive environment safely. Friction in the system induces the constant offset of the tracking task, however. For this purpose, two strategies, the supervisory correction command and the drift error correction control law, have been proposed. The latter approach leads to the Proportional-Integral-Derivative (PID) controller. A friendly graphical user interface (GUI) has been developed along with; allowing the user to specify his/her desired motion intuitively.

Keywords*:* PD controller, PID controller, GUI for motion control, cable driven robot

1. Introduction

Prior work of the author [1-3] reported the analysis and design of a two-degree of freedom (DOF) cable driven compound joint system. It is intended to be a study prototype of a cable-driven robotic system, in particular the anthropomorphic arm. At present, the prototype was constructed, as shown in Fig. 1. The system possesses two DOF, hence making the output linkage able to travel in the pitching and yawing directions. This motion grossly mimics the major rotations of the human shoulder joint. The travel range is approximately $\pm 65^{\circ}$ for each, hence with the output link length of $315\,\text{mm}$ covering the working area of approximately $3{,}700\,\text{cm}^2$. Further details of the robot specifications are stated in [2, 3].

Preliminary work on control of the robot has been addressed in this work. Specifically, a simple controller on each motor is designed and tuned based on its model solely. Then these servo motors are equipped to the robot and used to drive the system according to the desired motion. In other words, the robot dynamics is not taken into consideration.

Section 2 explained the design of a simple Proportional-Derivative (PD) controller for the motor unit. Together with the gravity compensator, they form the simple controller for the robot. Modifications of this controller to solve the constant offset problem of the tracking task are presented in section 3, where the experimental verifications are shown along with. Development of a friendly graphical user interface (GUI) is mentioned in section 4. Finally, discussion of this preliminary work and future research direction are given in section 5.

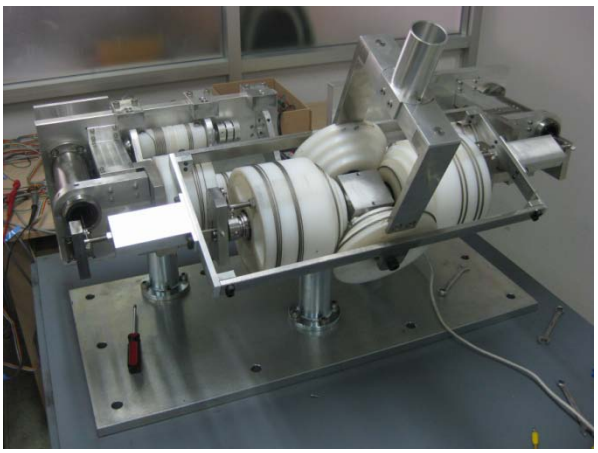

Fig. 1: Photo of the two DOF cable driven compound joint system

2. Simple Control of the Robot

2.1 Model of the DC motor

Motor may be viewed as the instrument which transforms the electrical power into the

mechanical power. Here the inertia effects and losses in both domains will be considered in its modeling. Referring to the DC motor schematic diagram in Fig. 2, R_e and I_e are the lumped resistance and inductance in the armature coil and R_m and I_m are the mechanical viscous friction and inertia of the rotor. κ is the motor torque constant. If the motor is operated under current mode, its dynamics is governed by the following equation

$$I_m\ddot{\theta} + R_m\dot{\theta} = \kappa i \qquad (1)$$

where i is the supplied current to the motor and θ is the rotor angle.

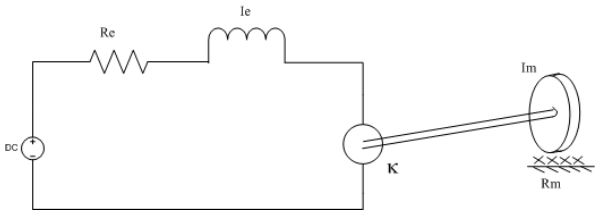

Fig. 2: Schematic diagram of the DC motor

2.2 A simple PD controller

The following PD control law

$$i = -\frac{1}{\kappa}\left[R_m'\dot{\theta} + K_d(\theta - \theta_d)\right] \qquad (2)$$

is proposed. Using this controller, the closed loop system equation becomes

$$I_m\ddot{\theta} + R_d\dot{\theta} + K_d(\theta - \theta_d) = 0 \qquad (3)$$

where $R_d = R_m + R_m'$ is the desired damping value and K_d the desired stiffness. It can be easily shown that this closed loop motor system has the globally asymptotically stable equilibrium point at $\theta = \theta_d$ and $\dot{\theta} = 0$.

From the motor's data sheet, $I_m = 13.8 \times 10^{-6}\ \text{kg}\cdot\text{m}^2$, $R_m = 4.14 \times 10^{-3}\ \text{Nm}\cdot\text{s/rad}$, and $\kappa = 60.3 \times 10^{-3}\ \text{Nm/A}$. If the value of R_m' and K_d are selected to be $1 \times 10^{-3}\ \text{Nm}\cdot\text{s/rad}$ and $1.43 \times 10^{-1}\ \text{Nm/rad}$, the closed loop motor system theoretically behaves according to the following second order linear ODE:

$$13.8 \times 10^{-6}\ddot{\theta} + 4.14 \times 10^{-3}\dot{\theta} + 1.43 \times 10^{-1}(\theta - \theta_d) = 0. \qquad (4)$$

Hence the closed loop system has the characteristics of $\omega_n = 16.2\ \text{Hz}$ and $\zeta = 1.83$, indicating a fast enough and well damped system.

The designed controller is implemented digitally on a desktop computer with Intel® Core™ 2 Quad processor. The control loop runs at the average speed of 1 kHz. For a given set point value, the cycloidal curve is used to generate a transitional profile which has smooth velocity to prevent the control saturation. If the set point A is required to be reached within T seconds, the motion profile θ during $0 \le t \le T$ is described by

$$\theta = \frac{A}{T}\left(t - \frac{\sin\frac{2\pi}{T}t}{\frac{2\pi}{T}}\right). \qquad (5)$$

2.3 Gravity torque and compensation

Mass and inertia of the robot's parts account for the gravity force, which, in turn, induces the gravity torque. A convenient way to derive such term is to determine it from the potential energy. Referring to the parameters and bond graph model of the system [2, 3], the total potential energy V_r of the robot can be written as

$$V_r = -m_p g r_{z_p} s_p - m_{py} g r_{z_{py}} s_p c_y, \qquad (6)$$

where m_p and m_{py} are the aggregated mass of the parts that undergo the pure pitching motion and the compound pitching and yawing motion, respectively. r_{z_p} and $r_{z_{py}}$ are the distance of the compound center of gravity of the parts that undergo the pure pitching motion and the compound pitching and yawing motion, measured from the center point of rotation.

Gravity torque may be compensated by the motor torque. This, however, requires the suitable motor sizing, otherwise motor saturation will happen. Additionally, this approach assumes proper operation of the motors. Violation might occur due to the power blackout or the malfunction of the control system. The robot motion will then be overruled by the gravity effect, which may cause the accident that cannot be compromised for the service robots.

Therefore, this robot is equipped with the patented pending spring-based counter-balancing mechanism [4]. This mechanism theoretically generates the torque, based on the current posture of the robot, which is oppositely equal to the gravity torque. As a result, no motor torque is required for the gravity compensation and hence the robot is inherently safe.

Unfortunately, mechanical compensation of the gravity torque is not perfect as desired. This is due mainly to the mismatch between the designed spring stiffness and the actual one obtained from the available off-the-shelf spring. Therefore, a small motor torque is needed in addition to completely cancel the gravity torque. This torque is associated with the potential energy V_m that makes the total potential of the system be constant. Mathematically,

$$V_m = -V_r - V_c, \qquad (7)$$

where V_c is the potential energy of the counter-balancing mechanism. Development of the required motor torque expression is rather lengthy and shall be excluded from the paper. With this

gravity compensation system, the PD controller will be responsible for the tracking of the desired motion solely.

2.4 Simple control of the robot

Two of the controlled motors, as described in section 2.2, and the gravity compensation system are now used for positioning control of the robot. As for the initial work, the controlled motors acting as the servo motors, are equipped to the robot. Then, the inverse kinematics will be performed to transform the coordinates of the set point specified in the task space (pitch and yaw angles, θ_p and θ_y) to the coordinates in the joint space (two motor angles, θ_{w1_l} and θ_{w1_r}). Particularly,

$$\begin{bmatrix}\theta_{w1_l}\\ \theta_{w1_r}\end{bmatrix} = \begin{bmatrix}9 & -9\\ 9 & 9\end{bmatrix}\begin{bmatrix}\theta_p\\ \theta_y\end{bmatrix}, \qquad (8)$$

provided the initial angles are all reset to zero. These motor angles set point are regarded as the desired angle θ_d for the motor controller. In other words, the robot dynamics is not taken into consideration.

Figure 3 displays the response of the controlled system to a sequence of pitch and yaw set points; that is, $(0°, 0°)$, $(10°, 0°)$, $(20°, 0°)$, $(10°, 0°)$, $(0°, 0°)$, $(-10°, 0°)$, $(-20°, 0°)$, $(-10°, 0°)$, $(0°, 0°)$, $(0°, 10°)$, $(0°, 20°)$, $(0°, 10°)$, $(0°, 0°)$, $(0°, -10°)$, $(0°, -20°)$, $(0°, -10°)$, and $(0°, 0°)$ are given to the controller manually with enough settle time interval for each of them. It is observed that the response tracks the reference quite well, but with the exception of constant steady state error (less than 2°) due to some imperfect cancellation of the gravity torque and the underestimated stiction in the system. Overall, the closed loop system is passively stable and hence can interact with the environment safely.

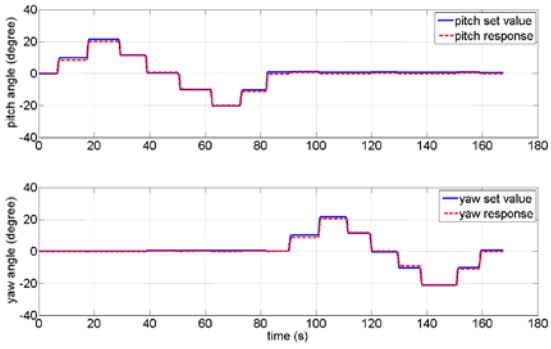

Fig. 3: Response of the robot motion
to a sequence of pitch and yaw set points
under a simple PD controller

3. Controller Modification

Simple PD controller does not respond to the zero-order steady state error. To correct this problem, two strategies are proposed.

3.1 Supervisory correction command

For the previous controller, single cycloidal step is used to generate the desired motion profile. However, fraction of the associated supplied energy must be given to the compliance and resistance effects of the gravity and friction. Therefore, the available energy to drive the robot is less than what has been expected, which causes the mismatch between the actual and the desired position. A simple notion of providing extra amount of energy to bring the robot to the desired position should solve this problem.

The scheme for the first approach is as follow. After the cycloidal motion profile is supplied for a certain time where the system may be assumed to be in the equilibrium, a supervisory program monitors the position error. The mismatch will then be used as a new relative set point A to generate an additional cycloidal step. In other words, a high level of the controller is employed to generate appropriate command to the low level controller. The use of such a simple strategy can be found in biological livings. Blind people use haptic queue to help manipulating the objects successfully, for example.

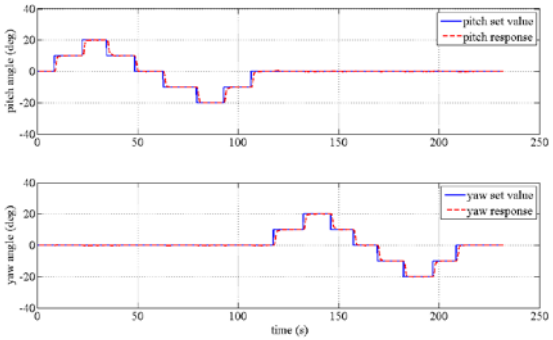

Fig. 4: Response of the robot motion
using the simple PD controller
and the simple supervisory controller

Figure 4 shows the response of the system under the simple PD controller with the adjunct supervisory controller. In this experiment, parameter T of the motion profile has been set to 2 seconds, which is the same as the update time of the supervisory controller. Position error of the robot becomes zero after one or two corrective pulse. Again, since the controller and the robot are passive systems, therefore the interconnecting closed loop is also passive system.

3.2 Drift error correction control law

The second approach continually monitors the position error, which is then used to modify the original control law for the purpose of zero steady state error [5].

Let $d(t) = \theta(t) - \theta_d(t)$ denotes the tracking error. Therefore the original tracking PD control law $\hat{u}$ may be written as

$$\hat{u} = -R_m' \dot{d} - K_d d. \quad (9)$$

This control law must be corrected by $\Delta u(t)$, resulting in a new control law

$$u(t) = \hat{u}(t) + \Delta u(t). \quad (10)$$

At steady state, Eq. (9) reduces to

$$d(t) = -\frac{\hat{u}(t)}{K_d}. \quad (11)$$

The control value at steady state should be unchanged, i.e. $\dot{u}(t) = 0$. Differentiating Eq. (11) and applying this fact result in the following relation;

$$\dot{d}(t) = \frac{\Delta\dot{u}(t)}{K_d}. \quad (12)$$

For the error $d(t)$ to be zero asymptotically,

$$\Delta\dot{u}(t) = -\lambda K_d d(t) \quad (13)$$

should be applied. Integrating Eq. (13) to obtain the corrective term as

$$\Delta u(t) = \lambda K_d \int_0^t (\theta_d - \theta) d\tau. \quad (14)$$

Therefore the modified controller is

$$u = R_m'(\dot{\theta}_d - \dot{\theta}) + K_d(\theta_d - \theta) + \lambda K_d \int_0^t (\theta_d - \theta) d\tau, \quad (15)$$

which is actually a PID controller that employs the integrator to provide the constant control input in solving the steady state error problem. Nevertheless, it should be mentioned that the PID controller itself is not passive, which makes the closed loop less stable than the PD one.

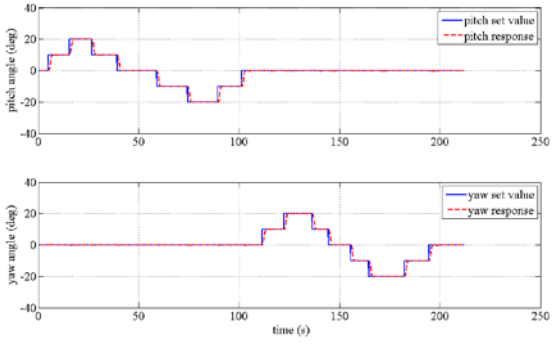

Fig. 5: Response of the robot motion using the PID controller

Previous experiment is now re-executed with the PID controller. With the value of the integral gain of 1.43×10^{-1} Nm/rad · s, the response of the system is depicted in Fig. 5. Without the external interacting force to the robot, the response is cleaner and faster compared to using the supervisory correction command.

4. GUI for the Motion Command

A friendly graphical user interface (GUI) has been developed to allow the user in specifying his/her desired motion intuitively. Since the end effector of the robot, i.e. the end tip of the output linkage, is constrained to be on the spherical surface, the user should be allowed to specify the robot motion only on the virtual spherical surface as well. For this reason, a spherical workspace is drawn on the two dimensional monitor, as shown in Fig. 6. This picture corresponds to the front view of the robot.

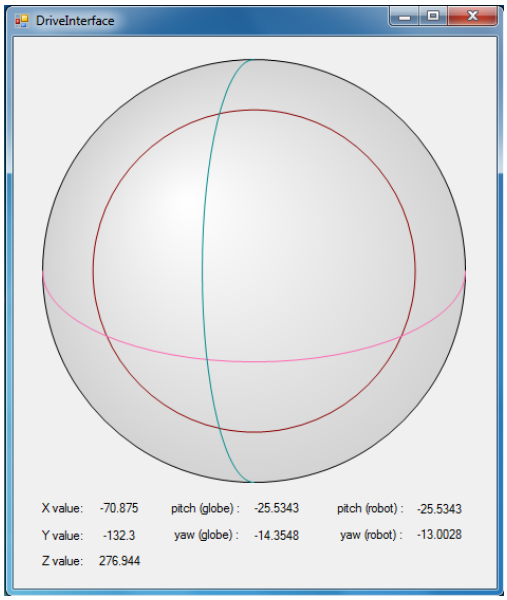

Fig. 6: A snapshot of the GUI for specifying the desired motion to the robot

The user indicates the desired motion by moving the mouse over the workspace. The program will then calculate the corresponding pitch and yaw angles of the differential joint from the x and y coordinates of the cursor as followed. Consider Fig. 7 which shows the top, front, and right side view of the workspace with its reference frame. With the known output link length, r, the z coordinate of the end effector will be

$$z = \sqrt{r^2 - x^2 - y^2}. \quad (16)$$

Pitch angle of the robot may now be calculated simply by

$$\theta_p = \tan^{-1}\left(\frac{y}{z}\right). \quad (17)$$

To calculate the yaw angle, it must be viewed along the y_r axis, which is moving according to

the changing pitch angle. See Fig. 7. In this view, the output link will always be seen as a true line. Therefore, the yaw angle can be calculated by

$$\theta_y = \sin^{-1}\left(\frac{x}{r}\right). \quad (18)$$

Additionally, the latitudinal and longitudinal curves of the current position are drawn in the GUI to provide the visual appearance of moving over the spherical surface. These curves can be constructed from the associated latitude and longitude angles, which, referring to Fig. 7, may be calculated from the coordinates of the point as

$$\theta_{lat} = \tan^{-1}\left(\frac{y}{z}\right), \quad (19)$$

$$\theta_{long} = \tan^{-1}\left(\frac{x}{z}\right). \quad (20)$$

Updated numerical values of these three coordinates are displayed in the bottom of the interface.

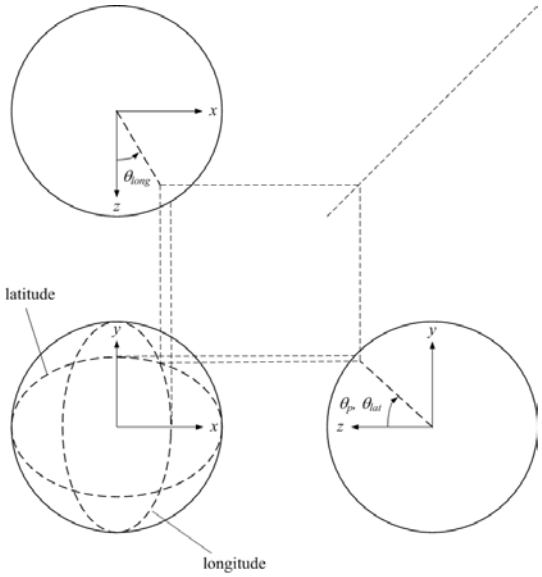

Fig. 7: Geometry for coordinate transformation of the robot

An experiment of the robot tracking task using the PID and the gravity compensation controller with the reference trajectory specified in real time from the user through the developed GUI is performed. Protocol of this experiment are as followed. The robot starts from rest at the middle point of the workspace. The user then moves the cursor horizontally to the right until the limiting brown circle is reached. The GUI will prevent any cursor movement that exceeds the limit. In effect, this is the soft limit of the robot.

After that, the user manipulates the cursor in the manner that it tracks the boundary of the limit in the counterclockwise direction for one round. Next the user moves the cursor horizontally to the left until the limit is reached again, at the left hand side for this time. In turn, the user manipulates the cursor in the manner that it tracks the boundary of the limit in the clockwise direction for one round. Finally the user moves the cursor horizontally to the right until it reaches the home position.

Plots of the reference and the response in the robot's pitch and yaw coordinates are depicted in Fig. 8. Tracking result is satisfactory for such a simple controller. An observable tracking delay of about 0.5 second is due to the tracking velocity limit set indirectly via the settling time of the updated point-to-point motion.

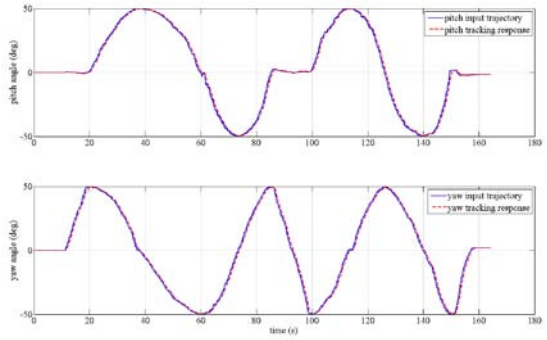

Fig. 8: Tracking response of the robot using the PID controller and gravity compensator

5. Discussions and Conclusions

In this paper, preliminary control of a two DOF cable driven robot using a simple PD and PID control laws are presented. Gravity compensation is conducted mainly by the counter-balancing mechanism. The remainder is taken care by the motor effort. Overall response of the system is fairly good. The robot can follow the specified trajectory closely.

The developed control law is based solely on the motor's dynamics. In particular, knowledge of the robot dynamics has not been exploited in designing the controller. This simplification will adversely affect the response of more demanding tasks. Since the power from the motors is transmitted mechanically through the cables and pulleys that inherently possess the compliance characteristics [1, 2], the robot naturally will exhibit a degree of vibration in its motion. This phenomenon may be evident during rapid movement, which causes the overshoot and the recurring oscillation. Worse yet, ignorance of flexibility in the robot may result in the unstable system.

Therefore in the next phase, a rigorous investigation on designing the controller based on the flexible robot model will be pursued. Moreover, since the robot is intended to perform collaborative tasks with humans, the controller should be designed based on the interaction control framework. Topics on determining the suitable impedance, the utilization of the inherent joint flexibility, and the impedance alteration are among our interest.

6. Acknowledgement

This work is generously supported by grants from the Engineering Faculty Research Funding, A Centennial Chulalongkorn University Research Funding, and the ISUZU Research Foundation.

7. References

[1] Pitakwatchara, P. (2010). Analysis and Modeling of the Cable-Pulley Power Transmission System in Robot, paper presented in *The 2010 IASTED International Conference on Robotics (ROBO 2010)*, Phuket, Thailand.

[2] Pitakwatchara, P. (2011). Design and Analysis of a Two-Degree of Freedom Cable Driven Compound Joint System, paper presented in *The Second TSME International Conference on Mechanical Engineering (TSME-ICOME)*, Krabi, Thailand.

[3] Pitakwatchara, P. (2012). A Two-Degree of Freedom Cable Driven Compound Joint System, Research Report No. 207-ME-2553, Faculty Research Fund, Faculty of Engineering, Chulalongkorn University.

[4] Pitakwatchara, P. (2012). Spring-Cable Counter-Balancing System for Pitch-Yaw Compound Joint Mechanism, Thailand Patent Pending, Patent Application No. 1201002792.

[5] Niemeyer, G. and Slotine, J. (2004). Telemanipulation with Time Delays, *International Journal of Robotics Research*, Vol. 23 (9), pp. 873-890.

Faculty of **ENGINEERING** | Chulalongkorn University
THAILAND
Pillar of the Kingdom

Task Space Impedance Control of the Multi-Stage Cable-Pulley Driven Flexible Joint Robot System

Phongsaen PITAKWATCHARA
Department of Mechanical Engineering, Chulalongkorn University
phongsaen.p@chula.ac.th

Background

Impedance plays a vital role for the manipulators to successfully perform the tasks which requires close interaction with the environment [1-5]. Only few works of impedance control have been attempted on the flexible joint robots. For example, a simple PD controller was used to tune the stiffness and damping parameters [6], and the online gravity compensation was proposed to reduce the error caused by the constant set-point gravity controller [7]. Sophisticated methods are employed on the design of the tracking impedance controllers such as the singular perturbation analysis [8], robust passivity analysis [9], and the adaptive techniques [10]. However, these controllers require measurements of the robot joint position, velocity, and interaction force, of which they are usually not available in common systems.

Objectives

This research therefore proposes a passive impedance controller for the flexible joint robot system. The controller requires only the motor angle to regulate the stiffness and damping characteristics at the end effector. Moreover, the development is generalized so it can be applied to the robot driven through multi-stage nonlinear flexible transmission system. Additionally, motor current feedback may be used to improve the system response time. Detailed information are reported in [11-13].

System modeling

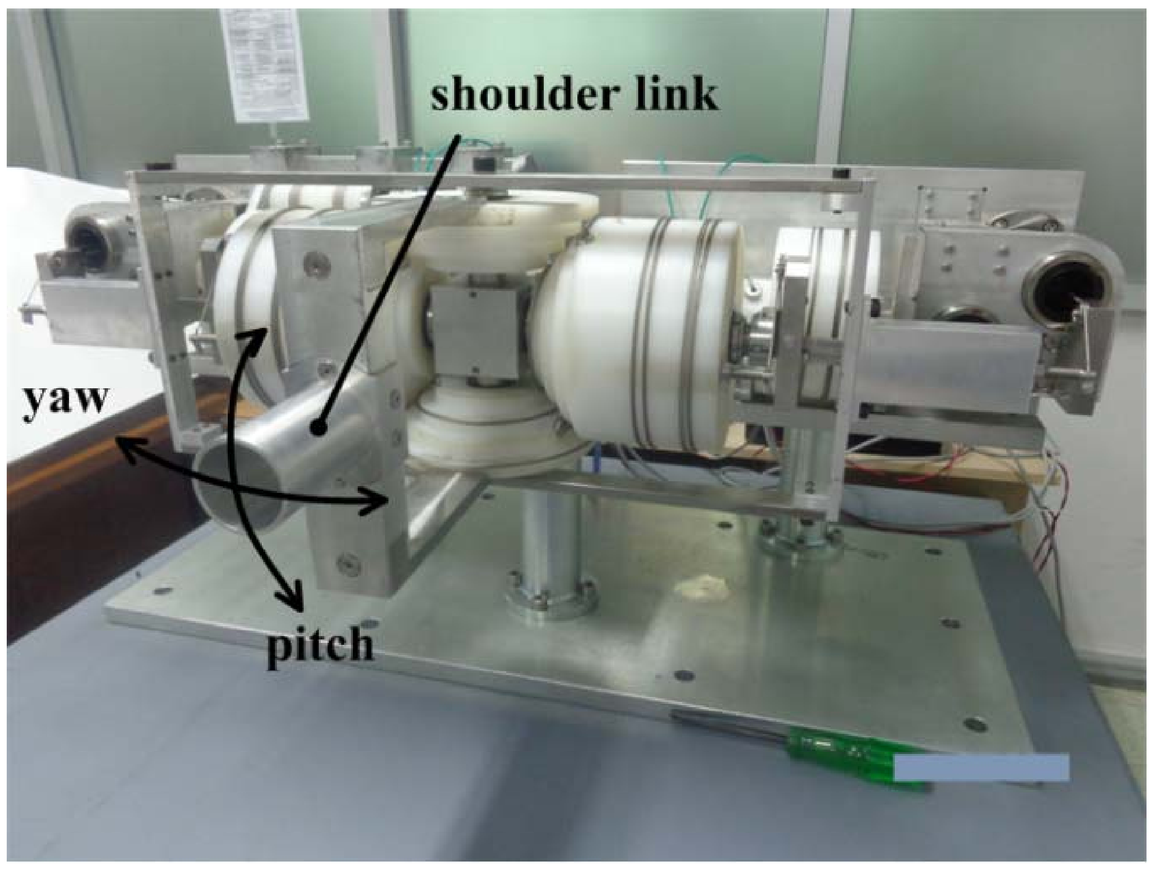

The figure depicts a 2-DOF pitch-yaw cable-pulley driven flexible joint robot as a platform for the study. Dynamics of the rigid robot system is developed in the joint space governed by

$$M(q)+C(q,\dot{q})+f+g(q)=\tau_{dr}+\tau_{e}.$$

Flexibility of the transmission system may be derived from the torque-angle deflection equation of the simple cable-pulley unit [12].

$$\theta=\frac{T_0}{EA\mu}\left[\left(\frac{me^m}{e^m-1}-1\right)(1+GF)-\log\frac{me^m}{e^m-1}\right].$$

Task Space Impedance Controller

The proposed controller will modulate the robot end effector impedance to the following task space impedance dynamics

$$\Lambda(x)\ddot{\tilde{x}}+\left[\mu(x,\dot{x})+D_d\right]\dot{\tilde{x}}+K_d\tilde{x}=F_e$$

where $\tilde{x}$ is the coordinate error. According to the system dynamics, the control law is

$$\tau_{dr}^{*}=g(q_s)-J(q_s)^T K_d(f(q_s)-x_d)-\left[J(q_s)^T D_d J(q_s)\right]^{\frac{1}{2}}\vartheta$$

in which q_s is the stationary value of the link angle determined from

$$q_s=T_{q1}\theta_0-e_{1q}^{-1}(g(q_s)-J(q_s)^T K_d(f(q_s)-x_d),$$

and ϑ the estimation of the filtered and scaled link joint velocity;

$$\vartheta=sG(s)\left[J(q_s)^T D_d J(q_s)\right]^{\frac{1}{2}}T_{q1}\theta_0.$$

Experiments & Results

The figure depicts an experimental result in which the robot tracks a circular path with the 1.0 kg proof mass attached. Actual tracking deviates from the reference path according to the applied load and the desired end effector stiffness of 500 N/m.

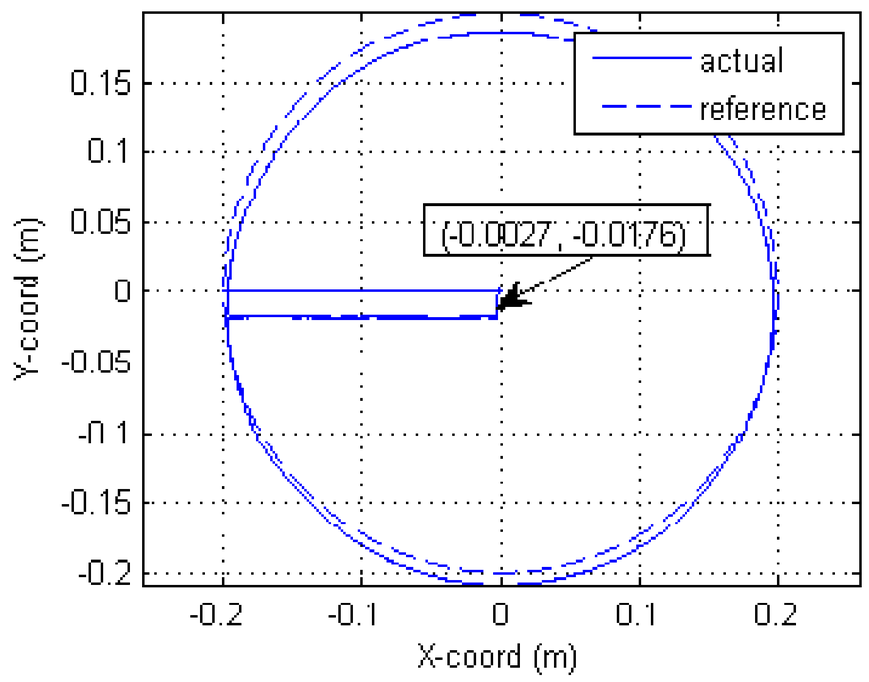

References

[1] Hogan, N (1985) Impedance Control: An approach to Manipulation, *Trans. ASME J. Dynamic Systems, Measurement, and Control*, 107(1), pp. 1-24.
[2] Guthart, GS and Salisbury, JK (2000) The Intuitive Telesurgical System: Overview and Application, *Proc. IEEE ICRA*, pp. 618-621.
[3] Rooks, B (2006) The Harmonious Robot, *Int. J. Ind. Robot*, 33(2), pp. 125-130.
[4] Albu-Schaffer, A, et al (2007) The DLR Lightweight Robot, *Int. J. Ind. Robot*, 34(5), pp. 376-385.
[5] Wyrobek, KA, et al (2008) Towards a Personal Robotics Development Platform: Rationale and Design of an Intrinsically Safe Personal Robot, *Proc. IEEE ICRA*, pp. 2165-2170.
[6] Tomei, P (1991) A Simple PD Controller for Robots with Elastic Joints, *IEEE Trans. Automatic Control*, 36(10), pp. 1208-1213.
[7] Zollo, L, et al (2005) Compliance Control for an Anthropomorphic Robot with Elastic Joints, *Trans. ASME J. Dynamic Systems, Measurement, and Control*, 127(3), pp. 321-328.
[8] Albu-Schaffer, A, et al (2003) Cartesian Impedance Control of Redundant Robots: Recent Results with the DLR Light-Weight-Arms, *Proc IEEE ICRA*, pp. 3704-3709.
[9] Ott, C, et al (2008) On Passivity-Based Impedance Control of Flexible Joint Robots, *IEEE Trans. Robotics*, 24(2), pp. 416-429.
[10] Chien, MC and Huang, AC (2012) Adaptive Impedance Controller for Flexible-Joint Electrically-Driven Robots without Computation of the Regressor Matrix, *Robotica*, 30(1), pp. 133-144.
[11] Pitakwatchara, P (2012) Spring-Cable Counter-Balancing System for Pitch-Yaw Compound Joint Mechanism, *Thailand Patent Office*, Pat. Pend. #1201002792, filed on June 12, 2012.
[12] Pitakwatchara, P (2014) Modeling and Control of the Multi-stage Cable Pulley-driven Flexible-joint Robot, *Int. J. Adv. Robotic Systems*, 11:118, pp. 1-16. (doi: 10.5772/58697)
[13] Pitakwatchara, P (2015) Task Space Impedance Control of the Manipulator Driven Through the Multi-Stage Nonlinear Flexible Transmission, *The ASME J. Dynamic Systems, Measurement, and Control*, 137(2), pp. 1-17. (doi:10.1115/1.4028252)